

**Erosion and Rolling Contact Wear Mechanisms in
Silicon Nitride Hybrid Bearings**

BALAMURUGAN KARUNAMURTHY

**A thesis submitted in partial fulfilment of the requirements of Bournemouth
University for the degree of Doctor of Philosophy**

July 2009

Bournemouth University
In collaboration with
SKF Engineering and Research centre, The Netherlands.

This copy of the thesis has been supplied on condition that anyone who consults it is understood to recognise that its copyright rests with its author and due acknowledgement must always be made of the use of any material contained in, or derived from, this thesis.

ABSTRACT

One remarkable advantage of hybrid bearings over all steel bearings is the elimination of separate oil lubricant system in applications, such as compressors and pumps in refrigeration and air conditioning units. High speed test runs restricted increase in speed due to material wear, which eventually affected the life of bearings. Being low saturation temperature fluids, change of phase is very common in refrigerants and cryogenic liquids, which lead to cavitation. Silicon nitride rolling elements with different sintering additives, properties and microstructure were experimentally studied to understand the nature of cavitation erosion.

Advanced surface analysis technique was used study the erosive wear correlation to microstructure of test materials. Cavitation erosion wear initiated by multiple intergranular and transgranular fracture, leading to erosion pit formation. Grain size and grain boundary composition have shown to be the dominant factors for providing resistance to cavitation. Effect of surface defects and lubricant viscosity on cavitation erosion was investigated and is detailed in this thesis. A rotary specimen method was designed to study the effect of cavitation on rolling bodies. Computational modelling of acoustically generated cavitation was attempted and is also reported in this work.

A novel test methodology was designed and manufactured by modifying a rotary tribometer to allow controlled experimental testing of two different phenomena rolling contact fatigue and cavitation erosion. This testing made it possible to study rolling and erosive wear mechanisms of rolling elements. Cavitation created far away in this new system is shown to be transported to the rolling contacts. The mechanism of material damage was by surface weakening due to mechanical impact of bubbles, which enhance fluid entrance and hydrodynamic pressure leading to wear initiation. Micro erosion pits formed in the rolling contact, which accelerated the damage by dislodging grains and bunch of grains. This testing method is suitable for a qualitative assessment of cavitation-RCF damage for different fluids with varying viscosities, and operating conditions.

PUBLICATIONS RESULTING FROM THESIS

Journal Publications:

1. B Karunamurthy and M Hadfield, *Mechano-Erosion: A Novel test methodology to accelerate Erosion in Rolling Contact Fatigue Experiments*. The Annals of 'Dunarea de Jos university of Galati Fascicle IX Metallurgy and Materials Science. ISSN 1453-083X. 2007.
2. B Karunamurthy, M Hadfield, C Vieillard and G Morales. *Cavitation erosion in silicon nitride: Experimental investigations on the mechanism of material Degradation*. Journal of European Ceramic Society (Submitted 2009)
3. B Karunamurthy, M Hadfield, C Vieillard and G Morales. *Cavitation and Rolling Wear in Silicon Nitride*, Materials and Design (Submitted 2009)

LIST OF CONTENTS

Abstract.....	iii
List of Publications.....	iv
List of Figures.....	x
List of Tables.....	xvi
Acknowledgement.....	xvii
Abbreviations.....	xix
Nomenclature.....	xx
CHAPTER 1.....	1
1. INTRODUCTION.....	1
1.1 Motivation	2
1.2 Hybrid Bearings and River Marks.....	5
1.2.1 Oil-free Lubrication.....	6
1.2.2 Wear in Refrigerant Lubrication.....	10
1.3 Background work.....	12
1.3.1 Cavitation and Erosion.....	13
1.3.1.1 Cavitation in Bearings.....	15
1.3.1.2. Erosion in ceramics.....	18
1.3.2. Rolling Contact Fatigue.....	20
1.3.3.1. Lubrication Oils.....	22
1.3.3.2. Refrigerant-Oil mixtures.....	24
1.3.3.3. Refrigerants.....	24
1.3.3.4. Cryogenic Fluids.....	25

1.4 Aims and Objectives.....	27
1.5 Overview of Thesis.....	28
CHAPTER 2.....	30
2. EXPERIMENTAL METHODOLOGY.....	30
2.1. Test Materials.....	30
2.1.1 Silicon Nitride.....	31
2.1.2 Bearing Steel.....	34
2.1.3. Test Specimen Preparation.....	34
2.1.3.1. Indentation and Crack generation.....	35
2.2. Cavitation Erosion.....	37
2.2.1. Vibratory Cavitation.....	39
2.2.1.1 Apparatus.....	40
2.2.1.2. Experiment Setup.....	42
2.2.1.3. Test Procedure.....	45
2.3. Rolling Contact Fatigue Experiments.....	46
2.3.1. Rotary Tribometer.....	46
2.3.1.1. Contact Stress Calculations.....	48
2.3.1.2. Defect Positing.....	49
2.3.1.3. Test Procedure.....	50
2.4. Surface Analysis.....	51
2.4.1 Optical Microscopy.....	52
2.4.2. Scanning electron microscopy.....	54
2.4.3. 3D Surface Optical Profiling and Measurement System...56	

CHAPTER 3.....	59
3. EROSION WEAR: THE MECHANISM OF MECHANICAL DEGRADATION...	59
3.1 Erosion Initiation.....	59
3.1.1 Transgranular fracture.....	61
3.1.2. Intergranular fracture.....	63
3.1.3. Micro Cracks.....	70
3.2. Erosion Pitting.....	73
3.2.1. Pit Inception.....	74
3.2.2. Pit Growth.....	78
3.2.3. Wear Sheet.....	86
3.3 Surface Analysis.....	88
3.3.1 Average Roughness.....	90
3.3.2 Volume Loss.....	91
3.4 Erosion Attenuation.....	92
3.5 Stages of Erosion.....	95
3.6. Heterogeneous Surface.....	97
3.6.1. Polished flat specimens.....	98
3.6.2. Surface Defects.....	101
3.6.2.1 Indents.....	101
3.6.2.2 Cracks.....	105
3.6.2.3. Star Defect.....	107
3.7. Cavitation Conditions.....	109
3.7.1. Effect of Magnitude of vibration.....	109
3.7.2. Effect of Viscosity.....	110
3.7.3. Effect of Fluid Thickness.....	112

3.8 Erosion in Steel.....	113
CHAPTER 4.....	115
4. Mechano-Erosion.....	115
4.1 Cavitation Erosion and Rolling contact Fatigue.....	115
4.2 Rotating Specimen.....	117
4.2.1 Testing Methodology.....	118
4.2.2 Results and Discussion.....	120
4.3 RCF Experiments on Eroded specimens.....	122
4.3.1 Testing Approach.....	122
4.3.2 Wear Results.....	124
4.4 Mechano-Erosion Experiments.....	126
4.4.1 Test Rig Design	126
4.4.2 Experimental Procedure.....	132
4.5 Erosion in rolling elements.....	137
4.5.1. Erosion on contact track	139
4.5.1.1 Ceramic contact.....	140
4.5.1.2 Hybrid Contact.....	144
4.5.2 Wear mechanism in rolling contact.....	149
4.5.2.1 Formation of micro pits.....	149
4.5.2.2 Erosion pits and material failure.....	151
4.5.2.3 Delamination wear.....	154

4.6 Wear conditions.....	155
4.6.1 Effect of contact stress.....	155
4.6.2 Effect of rotational speed.....	157
4.6.3 Effect of Lubricant.....	157
4.6.4 Effect cavitation conditions.....	159
Chapter 5.....	160
5. Conclusions and Future recommendations.....	160
5.1. Conclusions.....	160
5.2. Recommendations for future.....	163
APPENDIX A.....	164
APPENDIX B.....	171
APPENDIX C.....	173
APPENDIX D.....	183
REFERENCES.....	207

LIST OF FIGURES

Figure 1.1 3D CAD of Hybrid bearing with steel races and Si ₃ N ₄ balls.....	3
Figure 1.2 River marks seen on silicon nitride balls and rollers run in cryogenic environments.....	8
Figure 1.3 Superficial micro cracks on silicon nitride balls.....	9
Figure 1.4 River marks on silicon nitride balls.....	11
Figure 1.5 A classic photograph by Crum showing micro jet development during bubble collapse.....	13
Figure 1.6 Journal bearing showing lubricant cavitation zone.....	16
Figure 1.7 (a) Cavitation erosion of diesel engine main bearing and (b) wear on hydrodynamic bearing surface.....	17
Figure 1.8 (a) Erosion rate against temperature (b) shows eroded area of silicon nitride.....	19
Figure 1.9 (a) Schematic of contact profile of rolling element on raceway (b) SEM image of a spall on Si ₃ N ₄ after 16 million stress cycles.....	21
Figure 1.10 Rolling contact fatigue life in various lubricants and contact stresses.....	23
Figure 1.11 A detailed description of four ball-on-disk high speed cryo-tribometer.....	26
Figure 1.12 Cracks on wear track on test materials in liquid nitrogen.....	27
Figure 2.1 Plasma etched images of test samples.....	33
Figure 2.2 Indent generation and resulting indent.....	35
Figure 2.3 Crack generation using a Plint impact pendulum	36
Figure 2.4 (a) Vickers Indent and (b) Surface crack on test samples.....	36
Figure 2.5 Different Types of Cavitation.....	38
Figure 2.6 Pre-stressed sandwich transducer	41
Figure 2.7 Cavitation Erosion experiment setup.....	43
Figure 2.8 Schematic of test set up.....	44
Figure 2.9 Rolling contact fatigue testing.....	47

Figure 2.10 Loading configuration of the rotary Tribometer.....	49
Figure 2.11 Optical Microscopy.....	52
Figure 2.12 Magnified surface Images using Optical Microscope.....	53
Figure 2.13 (a) and (b) SEM Images of Silicon Nitride balls.....	55
Figure 2.14 EDX Spectrum of point analysis.....	56
Figure 2.15 3D Optical Profilometer.....	57
Figure 2.16 3D Interactive surface display.....	58
Figure 3.1 (a) and (b) Material B showing Transgranular fracture after 3 minutes of erosion testing.....	61
Figure 3.2 Transgranular fracture images.....	62
Figure 3.3 Material B showing advanced stages of Transgranular fracture after 10 minutes of testing.....	63
Figure 3.4 (a) and (b) Pore formation at grain boundaries in material C.....	64
Figure 3.5 (a) and (b) pores in material C and (c) and (d) in material B.....	65
Figure 3.6 Pore formation material A after 10 minutes of testing without any grain fracture.....	66
Figure 3.7 Schematic of a triple junction grain boundary in silicon nitride.....	66
Figure 3.8 Material B showing pore formation stage after 45 minutes of testing with low powered transducer.....	67
Figure 3.9 SEM and plasma etched Material B with initial pores next to coarser grains.....	68
Figure 3.10 (a) and (b) SEM and plasma etched image of material B showing both grain fracture and pore formation at boundaries.....	69
Figure 3.11 (a) and (b) show SEM an etched image of pore formed surrounding a large grain. (c) and (d) show pore formation circling a bunch of small grains.....	69
Figure 3.12 Micro crack formation at microstructure on material B at different scales...	71
Figure 3.13 (a) and (b) Broader cracks in material A. (c) and (d) micro cracks propagating in material A.....	71
Figure 3.14 Micro thin cracks transformed to broader cracks by displacing nearby material as observed in material C.....	73

Figure 3.15 Micro crack growth retardation as seen in material A.....	73
Figure 3.16 Pit formation in Material A.....	74
Figure 3.17 Sharp and narrow pits in material A.....	75
Figure 3.18 Erosion pit inception in material B.....	76
Figure 3.19 (a) and (b) SEM and plasma etched image of Material C with cavitation pits.....	76
Figure 3.20 Very few Erosion pits after one hour testing with low powered transducer.....	77
Figure 3.21 (a) Pit bridging and (b) pit enlargement.....	78
Figure 3.22 Pit bridging of two large pits.....	79
Figure 3.23 SEM images showing pit growth by linking up pits.....	80
Figure 3.24 Cavitation pits of different shapes in two materials.....	80
Figure 3.25 (a) and (b) Cavitation pits in material C and A.....	81
Figure 3.26 Light microscope images of erosion pits at different stages.....	82
Figure 3.27 (a) and (b) Erosion pits developed into large crater.....	83
Figure 3.28 (a) Erosion pits at the edge of the centre wear scar and (b) Pit growth at the edges.....	83
Figure 3.29 SEM images on severely eroded areas.....	84
Figure 3.30 SEM images of final stages of erosion pit growth.....	85
Figure 3.31 (a) Pit bridge and (b) erosion wear bridging between two test areas.....	86
Figure 3.32 Wear sheet formation in material B after 5 hours of testing using low powered transducer.....	87
Figure 3.33 EDAX spectra of wear sheet on material B.....	87
Figure 3.34 Wear sheet formation in material C.....	88
Figure 3.35 (a) Pits in material A and (b) pits in material B after 5 hours of testing. (c) a plot of pit count.....	89
Figure 3.36 (a) Eroded surface after 3 hours of testing and (b) after 5 hours.....	90
Figure 3.37 Average roughness plot of test materials over time.....	91
Figure 3.38 Volume loss measurements over time.....	91
Figure 3.39 (a) Light microscope image of severely eroded surface and (b) SEM image of the same area.....	92

Figure 3.40 (a) Observed crater in material C after 45 hours of cavitation testing and (b) close up.....	93
Figure 3.41 EDAX spectra comparison inside and outside of the crater.....	93
Figure 3.42 Attenuation stage images on material A and B showing deep craters.....	94
Figure 3.43 Different stages of cavitation erosion in silicon nitride.....	96
Figure 3.44 Surface Average roughness over cavitation exposed time.....	98
Figure 3.45 Average Maximum Height over cavitation exposed time.....	99
Figure 3.46 Peak-to-Peak value over cavitation exposed time.....	99
Figure 3.47 Volume loss over cavitation exposed time.....	100
Figure 3.48 10 Kg Vickers's Hardness Indent.....	101
Figure 3.49 (a) & (b) Eroded Indent after 30 and 60 minutes.....	102
Figure 3.50 Eroded Indent after 240 minutes.....	102
Figure 3.51 (a) SEM images of Indent eroded after 60 minutes and (b) visible cracks.....	103
Figure 3.52 (a) SEM image of the eroded indent edge and (b) crack.....	103
Figure 3.53 EDAX spectrum comparison of inside and outside of Indent.....	104
Figure 3.54 Surface crack (a) Light Microscope image of crack before testing, (b) after 2 hrs of erosion testing and (c) SEM image of eroded crack.....	106
Figure 3.55 Surface microscopy images (a) Surface crack and (b) eroded crack and surrounded by pit inception.....	106
Figure 3.56 SEM image of eroded star pattern and (b) Surface parameters.....	107
Figure 3.57 Surface profilometer measurements on the STAR defect.....	108
Figure 3.58 Influence of Vibration amplitude on erosive wear.....	109
Figure 3.59 Erosion rate dependence on fluid thickness.....	112
Figure 3.60 (a) and (b) Light and scanning electron microscope images of erosion initiation in bearing steel.....	113
Figure 3.61 Surface layer damage in steel due to erosion.....	114
Figure 3.62 SEM images of erosion pits in bearing steel.....	114
Figure 4.1 Typical spherical particle debris reported in rolling contact.....	116
Figure 4.2 (a) River marks in application balls and	

(b) Erosion marks obtained in laboratory.....	117
Figure 4.3 Rotating test specimen set up.....	119
Figure 4.4 Eroded rotating specimen at various magnifications.....	120
Figure 4.5 Erosion mark comparison with application rolling elements.....	121
Figure 4.6 (a) Test specimen after 2 hrs of RCF testing and (b) close up of the contact track	124
Figure 4.7 Erosion progression in rolling contact.....	125
Figure 4.8 Surface scan of the contact path.....	125
Figure 4.9 Ultrasonic transducer in RCF test chamber.....	128
Figure 4.10 Schematic of test configuration.....	129
Figure 4.11 Stainless steel test chamber to accommodate steel cup.....	130
Figure 4.12 Mechano-Erosion test set up (a) Before loading (b) after loading and (c) complete set up.....	131
Figure 4.13 Erosion marks on lower balls of S-1.....	137
Figure 4.14 Microscope image of erosion mark on rolling element.....	138
Figure 4.15 Erosion pits on contact track of S-2.....	139
Figure 4.16 Edge of contact track.....	140
Figure 4.17 Erosion pits in ceramic to ceramic contact.....	141
Figure: 4.18 Light microscope images of material C eroded contact track (a) full view of the eroded track and (b) High magnification of the contact track.....	142
Figure: 4.19. Contact track and adjacent area.....	143
Figure: 4.20 Surface measurements on the contact track region.....	143
Figure: 4.21 Comparison of erosion pits in rolling contact and bench testing (a) Eroded contact track and (b) erosion pits on stationary specimen.....	144
Figure: 4.22 Erosion marks on ceramic rolling element with hybrid contact.....	145
Figure: 4.23 (a) Contact track eroded on steel lower balls and (b) close up.....	146
Figure: 4.24 High magnification of steel ball contact track (a) showing sharp erosion pits and (b) high density of erosion marks.....	146

Figure: 4.25 (a) Bird's eye view of contact track of steel lower ball and (b) Area with bunch of erosion pits.....	147
Figure: 4.26 (a) Ring edge of lower steel ball and (b) ring mouth.....	148
Figure: 4.27 Material flaking at the edge of the ring in bearing steel.....	148
Figure: 4.28. Bubbling out of surface layer in rolling contact.....	150
Figure: 4.29 Wear initiations in rolling contact after 40 minutes.....	150
Figure: 4.30 (a) Micro pit formation and (b) C-shaped damage initiation.....	151
Figure: 4.31 Material A erosion marks (a) after 2 hours (b) after 4 hours and (c) close up of erosion marks.....	152
Figure: 4.33 Formation of C-shaped erosion marks on contact track.....	153
Figure: 4.34 Final stages of material failure showing severe erosion.....	154
Figure: 4.35 Delamination wear on material C on lower balls.....	155
Figure: 4.36 Effect of contact stress (a) contact track at high load of 5.2 GPa and (b) Contact track at low load of 3.5 GPa.....	156
Figure: 4.37 (a) Large pit formation due to high load and (b) Close up of erosion pit.....	156
Figure: 4.38 Contact track after 3 hours of testing at speed of (a) 2000 rpm and (b) 3000 rpm	157

LIST OF TABLES

Table 2.1 Mechanical properties of test samples.....	33
Table 2.2 Properties of Bearing steel.....	34
Table 3.1 Incubation periods in minutes.....	92
Table 3.2 Description of stages in cavitation erosion.....	95
Table 3.3 Properties of flat and polished silicon nitride test specimens.....	98
Table 3.4 Viscosity influence on the rate of erosion.....	111
Table 4.1 Test conditions for eroded specimen.....	123
Table 4.2 Mechano-erosion test programme.....	136
Table 4.3 Effect of test lubricant.....	158

ACKNOWLEDGEMENTS

I thank everybody who helped me during this period of stay at Bournemouth University. Most of all, sincere gratitude to my first supervisor Professor Mark Hadfield for providing continuous support, advice, encouragement, and freedom to work on this individualized nature of PhD.

Financial support from SKF is much appreciated. Sincere thanks to my SKF supervisor Dr Guillmero Morales Espejel for his time, organizing meetings, inviting experts for project discussions and for his valuable comments and suggestions throughout my PhD. I appreciate the help provided by Charlotte Viellard for surface analysis at SKF and providing test samples on time; her expertise in material science helped me learn more in this field. Thanks to Dr Robin Cundil and Dr Goran Lindsten for their kind advices, time and effort to participate in these project discussions at SKF. I also thank Professor Stathis Ioannides, the director of SKF ERC. Other colleagues at SKF, Dr Georghie Popovaci, Dr H R Pasaribu made my stay more enjoyable and I am grateful to them.

I also thank the technical staff here at Bournemouth University, in particular Brian Wright, Ken Millard, Kevin Smith, Gary Toms and Dave Kennedy for their help in the workshop.

I thank the Graduate school for the series of Research Methodology and skills programme, which without doubt helped to successfully plan and manage my PhD.

Thanks to Mrs Nita Verma at Experimental Testing Centre, Brunel University for her help on surface analysis. I am grateful to Gavin Butcher and Richard Evans of ANSYS Inc for their advices, technical support and for arranging a training session in Oxford, which made me more comfortable in writing codes to run fluid, thermal and structural simulations.

I thank Dr Ying Wang for his help and support in the lab during the initial stages of my PhD.

Thanks to Rob Perkins and Simon Denley of Sonic Systems, Pukington for their very kind co-operation to manufacture our design of piezoelectric transducer for cavitation experiments.

My special thanks to Jo Sawyer, who helped me in all administrative tasks, and also Jackie Holmes for her kind help. Also I thank my colleagues, Ben Thomas, Wei Wang and Ping Zhao for their cooperation in the laboratory. My housemates Gurtej Grewal and Manish Bharara, and friends Sami and Sarath helped me to have a good fun during these three years in Bournemouth. Pursuing higher studies in England would not have been possible without the love, care, support and encouragement from my family members.

ABBREVIATIONS

rpm	revolutions per minute
HPOTP	High Pressure Turbo Pump
CFC	Chlorofluorocarbon
HC	Hydrocarbon
HFC	Hydro fluorocarbon
EHL	Elasto-Hydrodynamic Lubrication
HPSN	Hot Pressed Silicon Nitride
SSN	Sintered Silicon Nitride
HIPSN	Hot Iso-statically Pressed Silicon Nitride
RBSN	Reaction Bonded Silicon Nitride
RCF	Rolling Contact Fatigue
SEM	Scanning Electron Microscope
OI	Optical Interferometry
LM	Light Microscope
UV	Ultraviolet
EDX	Energy Dispersive X-ray
HV	Vickers hardness
CFD	Computational Fluid Dynamics
CE	Cavitation Erosion
FEM	Finite Element Method
FEA	Finite Element Analysis

NOMENCLATURE

DN	(Bearing bore mm) X (rotating speed rpm)	
L	Bearing fatigue life in million revolutions	n
C	Dynamic load capacity rating	N
P	Bearing equivalent dynamic load	N
n	Stress life exponent	
R_a	Average roughness	m
P_{ac}	Acoustic power	watts
ρ	Density of load	kg/m ³
c	Sound velocity in the load	m/s
a	Amplitude of transducer/Horn vibration.	m
P_c	Contact load	N
L_s	Applied shaft load	N
θ	angle	Degree
E	Young's Modulus	N/m ²
ν	Poisson's ratio	
P_o	Maximum contact pressure	N/m ²
ρ	Density	kg/m ³
p	Probability of contact path	
a	area of contact	m ²
R_z	Average maximum height	m
R_t	Peak-to-peak value	m
P_v	Gas pressure	N/m ²
P_o	Ambient liquid pressure	N/m ²
σ	surface tension	N/m
R_o	bubble radius	m
R_c	Critical radius	m
N	Bubble number	

\dot{M}	Mass transfer	
$\frac{dm_o}{dt}$	Rate of change of bubble mass	kg/s
$\frac{dV_o}{dt}$	Rate of change of bubble volume	m ³ /s
$\frac{dR_o}{dt}$	Rate of change of bubble radius	m/s
r	Volume fraction	
d _i	Initial distance	m
d _f	Final distance	m
v	Frequency	Hz
ω	Angular frequency	Hz
T _p	Time period	s
d _y	Displacement in Y-direction	m
T _{tot}	Total time	s
T _{step}	Total step	s
F _v	Vertical force	N

Chapter 1

INTRODUCTION

Bearings have played an undeniable role in all stages, from building simple machines to the high-tech equipment we use today. This invention made it possible to achieve almost all of the engineering advances in the last few centuries. Bearings reduce friction and thus greatly increase the efficiency of the moving part. The earliest known evidence of a bearing dates back to the construction of pyramids. Wooden cylinders were used to reduce friction for motion translation: the simplest form of bearing. This was followed by the usage of animal fat and olive oil to reduce friction in the early human civilization. A ball thrust bearing dated 40 AD was found in Lake Nemi near Rome (Leibensperger 2003). Thus, the science of friction, wear and lubrication is not new, but started very early and is now termed as tribology. Invention of machines and industrial advancements increased the knowledge and importance of tribology. Nowadays, it's impossible to ignore friction, wear and lubrication, and is hard to imagine an engineering world without bearings, lubrication, gears or cams.

Another important field that has seen significant advancement over the past centuries is ceramics. Although they were known to humankind around 30,000 years ago, the greatest advance in this field begun since humans have been capable of conceptual thinking. The invention of furnace accelerated the improvement of ceramics properties and the invention of new ceramics and composites (Sentence 2004). Now they are widely used in almost all fields of engineering because of their high hardness, stiffness and chemical inertness. One of the most important of these applications is hybrid bearings, constructed of steel inner and outer rings, with ceramic rolling elements in place of steel. Hybrid bearings offer many advantages over all-steel bearings: These advantages make them well suitable for high speed and temperature applications such as machine spindles, turbines, and rocket engines. Generally, machinery speed is restricted by the DN of the bearings, but with hybrid bearings it is possible to achieve high speeds of up to 3 million DN and high operating temperatures of 1700⁰C (Anon 2006). A recent advance in hybrid

bearings has been their use in compressors and pumps where the bearings run in refrigerants, which results in better performance, longer life and lower manufacturing and running costs. Refrigerant lubrication is advantageous where lubrication, maintenance and environmental issues are a concern (Fischbach et al 2007). The work presented in this thesis is an effort to provide more insight on the failure mechanisms of these bearings and thus providing support in the continuing investigation and development of hybrid bearings.

1.1 Motivation:

Bearings are everywhere from space shuttles to household appliances, automobiles, dentist drills, roller skates, and computer disk drives e.t.c. The bearing, a device that allows two parts to rotate or move in contact with each other, is directly related to the performance of all moving parts in a machine. Although, invention of bearings could date back to few thousand years, Leonardo da Vinci was the first to publish a manuscript on bearings in 1490-99 and show the precursor of a thrust ball bearing. These manuscripts describe the development of systems to reduce friction on rotating axles which resulted in disk and roller bearings made of wood and bronze (Morton 1965). Following this, cast iron was used as a material of choice for roller bearings for bucket pumps in 1556 (Zaretsky 1971). One major breakthrough in bearing development was de Mondran's carriage built in 1710, in which the wheels were supported by rolling bearings. The first rolling bearing industry was established in 1868 as a result of pedal bicycles. Galileo Galilei, John Harrison, Philip Vaughan and Friedrich Fischer were the major contributors of the bearings we use today. The modern, self-aligning design of ball bearing is attributed to Sven Winquist of the SKF ball-bearing manufacturer in 1907.

Continuing advances in the bearing industry mainly result from technological innovations such as offering variety of choices of materials, self-lubricating, more efficient bearings and bearing design for specialized applications. Steel was considered to be best choice for bearings because of its strength and the existing technology to produce and machine it. Bearing steel is typically high carbon chromium steel which also contains small amounts of manganese and silicon. However, applications of all-steel bearings are limited due to

their physical properties. For example, use of all-steel bearings for high temperature, corrosive and hostile environment, high speed and precision applications is not possible because of unsatisfactory performance. Ceramics and polymers can replace steel components in bearings and offer several advantageous over all-steel bearings. It is often said that “the most significant advance in ball bearings since the invention of bearings is the hybrid bearing”. Hybrid bearings have rings of steel and silicon nitride rolling elements as shown in Figure 1.1

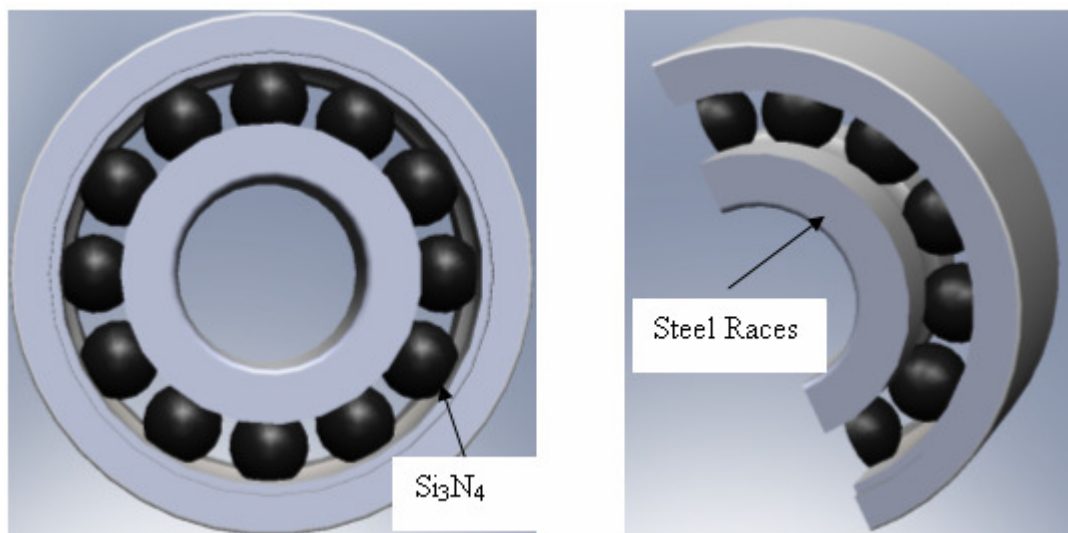


Fig: 1.1 Model of Hybrid bearing with steel races and Si_3N_4 balls.

It was Dee, in 1970, who first proposed hot pressed silicon nitride for rolling element bearings as well as journal bearings (Dee 1970). Silicon nitride has low density and high stiffness as required for gas turbine and machine tool applications. Moreover, the high hardness, low coefficient of thermal conductivity and higher temperature capabilities of this material are well suited for rolling contact applications. Some of the advantages of hybrid bearings over all-steel bearings are as follows:

- 30 to 50% higher running speed with less lubrication.
- Increased bearing life of up to 10 times compared to that of all-steel bearings
- Higher modulus of elasticity provides higher accuracy
- Lower wear, corrosion resistant, non-magnetic and non-conductive.

One drawback of silicon nitride is that it is not easy to manufacture. But, over the past few decades, much research was devoted to the manufacturing methods of this material which achieved promising results. This has resulted in the replacement of all-steel bearings for several applications. Hence, much research work was carried out on studying the rolling contact fatigue (RCF) of hybrid bearings, which is responsible for failure of rolling contact bearings. Thus, several publications on rolling contact fatigue experiments on silicon nitride are available (Wang 2000, 2002, Stewart 2002). Understanding RCF behaviour of rolling contact of materials and the influence of lubricants is a key factor to ensure good life of bearings.

One of the promising applications of hybrid bearings is in refrigeration and air-conditioning applications. Fluid contamination and poor bearing lubrication is a big challenge in compressors and pumps used in refrigeration and air conditioning units. The working fluid (refrigerant) often mixes with the lubricant, saturating it enough to cause lubricant starvation. With poor lubrication, severe rolling wear accelerates which leads to the failure of bearings causing reliability problems. Previously, this problem was tackled by installing better bearing housings and seals to control the lubricant mixing with the working fluid. In 2002, SKF, a bearing manufacturer, made a breakthrough by replacing these all-steel bearings with hybrid bearings. This replacement allowed the use of the working fluid as lubricant instead of a separate oil-lubricant system. This enabled significant improvements in the compressor pump design, operating performance, reliability and service life. Marshall Space Flight Center, NASA, USA and National Aerospace Laboratory of Japan tested hybrid bearings for space transportation systems. Advanced liquid hydrogen and nitrogen turbo pumps are used in rocket engines. The rotor speeds of these turbo pumps are restricted by the DN limits of bearings. Hybrid bearings are ideal for these applications and showed good performance of up to 3 million DN. However, performance can be limited due to a severe wear formation in this cryogenic environment. The cause, its mechanism and the influence of this wear damage on the life of bearings is not yet known. Any continuing success in this field of oil-free lubrication relies on understanding this failure mechanism and that is what motivated the work reported in this project.

1.2. Hybrid Bearings and River marks:

Silicon nitride rolling elements are made from silicon nitride powder, compressed under high pressure and baked in a furnace. This homogenous material then undergoes lapping and several cycles of polishing to achieve the high-precision smooth surface required by the duty and design. Si_3N_4 on its own does not form a dense strong material when sintered with high mechanical pressure, but rather it decomposes into silicon and nitrogen. The discovery of fabricating silicon nitride and silicon carbide by reaction sintering was made in Great Britain in the 1960s (Richerson 1997). Without the aid of additives, silicon nitride cannot be made into a high strength pore free material. Different types of silicon nitride are available which are obtained through different manufacturing methods and sintering additives. Detailed material information of this material is presented in section 2.1.1 and in Appendix A. The original reason to develop silicon nitride was for use in gas turbine engines; where material must survive temperatures over 1100°C for several thousands of hours when subjected to high thermal stresses, thermal shocks, corrosion, creep and fatigue. Although silicon nitride is not yet widely used in gas turbines, its greatest commercial success is in hybrid bearings.

As hybrid bearings provide several advantages over all-steel bearings, they made a successful entry into the refrigeration and air conditioning industry. Running hybrid bearings with pure refrigerant as lubricant is now possible. Surface examination of rolling elements subjected to this running conditions exhibit a unique type of wear, which is now termed as “river marks”. These river marks have also been found on hybrid bearings run in cryogenic fluids. This type of wear is unusual and was never found on hybrid bearings run under normal lubricating oils. This encourages looking at the running conditions in compressors and pumps in refrigeration and air-conditioning applications. A mechanism which can clearly describe this wear damage process and its initiation and progression under a contact load is required, for which a clear understanding of this working condition is necessary. This section presents a detailed review on the running conditions and the resulting damage that has been found in various applications.

1.2.1 Oil-free Lubrication:

Efforts to increase the life of bearings in space shuttle engines are always challenging due to their unique operating conditions. This includes short duration runs for several minutes of high speed rocket turbo pumps and long duration runs for several hours of cooling system pumps at moderate speed and loads. A series of reports were published by NASA on the reliability of bearings used in space shuttles. One classic paper on bearings and seals for cryogenic fluids was by Scibbe (1967) which showed the results of bearing and seal performance in cryogenic fluids. Severe wear was found on the bearings, which he concluded was due to excessive heat generation. The source of local heating was found to be the rubbing of balls against the cage. They concluded that sufficient lubrication could eliminate the bearing wear, which would allow running bearings for several hours. In a later report by the same author (Scibbe 1968), a modified bearing design which had smaller ball diameters and more open raceway curvatures to minimize heat generation at high operating speeds was described.

Following this, many studies were carried out on the effect of lubrication in cryogenic running conditions, thereby allowing a proper selection of lubricant for these applications (Dietrich 1969, 1970, 1975; Coe 1978). Bearing testing was carried out using a modified five-ball fatigue tester for cryogenic temperature testing (Dietrich 1969). Rolling elements were SAE 52100 (carbon chromium) steel balls with fluorinated polyether fluids as lubricants. These tests were carried at a maximum Hertz contact stress of 3.4 to 5.5 GPa and speeds up to 4750 rpm. The results were quite promising as they showed that fluorinated ethers could form elastohydrodynamic lubrication (EHL) films at a temperature range of 80 to 227 degree Kelvin. Although, using this lubricant was promoted for cryogenic fluid applications, the service life of bearings, however, remained unsatisfactory.

A NASA technical paper (Armstrong 1988) clearly described the problems of bearing life in space shuttle main engines. It reported that the bearings used in high-pressure turbo pumps (HPOTP) in space shuttle main engines had shown severe wear after only 10

percent of their design service time. This encouraged NASA to investigate these bearings with the aim of increasing their service life. They identified the reason for short service life was due to large thermally induced internal loads and the high speeds at which bearings were run. The bearing life was further increased by changes in raceway curvatures and contact angles, variations in lubrication method and variations in the coolant flow rate. But, the major breakthrough in this bearing application came when hybrid bearings replaced all-steel bearings. The primary reason for this is the low centrifugal force offered by hybrid bearings which reduced bearing loads at high speeds.

Initial testing of hybrid bearings for more than 280 starts and 135,000 seconds of hot fire test and flight time of HPOTP was achieved without any notable wear on the ceramic balls and steel raceways (Burse 1996). Nosaka et al (1999) studied the tribo-characteristics of hybrid and all-steel bearings for rocket turbo pumps. They investigated the self-lubricating performance of hybrid bearings and compared them with all-steel bearings. Testing was carried out to maximum of 60 minutes at a constant speed of 50,000 rpm with a relatively low thrust load of 784 N, which was further increased up to 2840 N. Hybrid bearings showed good wear resistance compared to all-steel bearings, but exhibited poor self lubricating characteristics.

Marshall Space Flight Center, USA (Gibson et al 2000) built a bearing test rig to evaluate and develop rolling element bearings used in high speed cryogenic turbo pumps. This test was configured to run ball/ball/hydrostatic, ball/roller/hydrostatic or all hydrostatic bearings. Speeds of up to 35000 rpm were possible with this rig, which could operate in liquid nitrogen, hydrogen and oxygen. With the advancement in new bearing technologies, they found the best improvement was in hybrid bearings, which improved the baseline from 15 minutes to 420 minutes in the design. They carried out hybrid bearing testing in liquid hydrogen for approximately 75,000 seconds. After each test series, surface inspection revealed the presence of river marks as shown in Figure 1.2. These river marks are characterized by large width to depth ratios and run on the surface of the ball with small tributaries leaving the main line. They measured the width and depth of these marks and found a typical width and depth values of 0.14 mm and

0.005mm. They ruled out the possibility of fracture as none was noted until then. They also found that river marks did not grow further, rather as smaller tributaries branched out from the main lines. They concluded that the surface anomaly that has been called as river marks exists on some silicon nitride balls and their effect on bearing life needed to be studied.

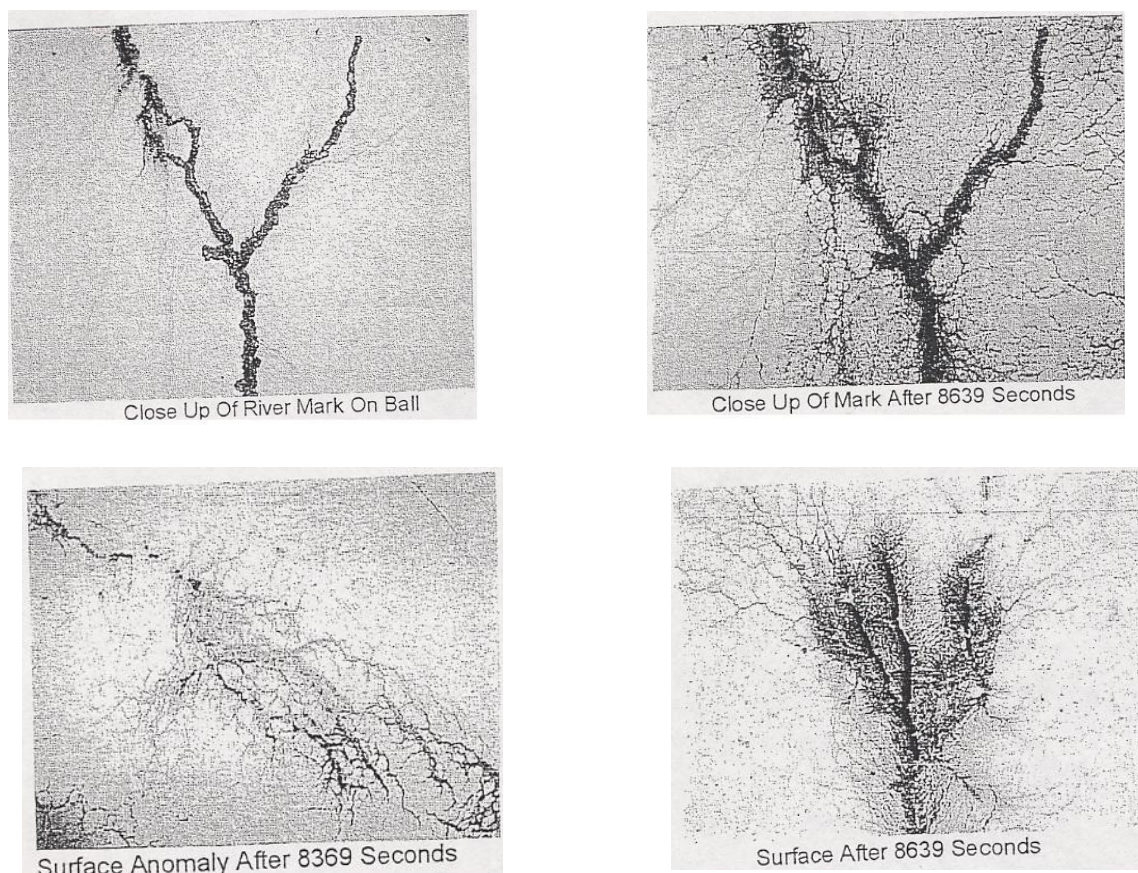


Fig: 1.2 River marks seen on silicon nitride balls and rollers run in cryogenic environments (Gibson 2000).

Another report on this type of material degradation was published by National Aerospace Laboratory of Japan (Nosaka et al 2004). They reported on the successful testing of hybrid bearings run at a very high speed of 3 million DN (120,000 rpm) in liquid hydrogen. A bearing-seal tester was built to achieve high speeds and loads. They found

that hybrid bearings had relatively lower sensitivity in bearing load capacity and bearing torque than all-steel bearing in liquid hydrogen due to the formation of thick transfer films on the silicon nitride balls which could withstand high bearing load. Testing included hybrid bearings with silicon nitride balls, all-steel bearings and martensitic stainless steel (SUS 440C) bearings. All test materials were macroscopically examined after testing which ran for a total time of 20.4 minutes at a speed level of 113,000 to 120,000 rpm with thrust loads applied from 980 N to 3140 N. Hybrid bearings showed no damage compared to the other two types, which exhibited severe wear. However, microscopic examination of silicon nitride balls showed presence of river marks, what they called as “superficial micro-cracks” as shown in Figure.1.3. These micro-cracks varied at depths with the maximum of 3 μm . They also found fractures with flaking occurred near those micro-cracks. Inspection after sectioning the balls showed that these superficial micro-cracks extended very little inside the ball. Their hypothesis on this damage formation was that it was due to a spike in the bearing temperature at a thrust load of 3,140 N, and concluded that the formation of superficial micro-cracks in silicon nitride was due to local frictional heating. This paper also cited work on high-DN bearing test conducted for VINCI engine (Bosson et al 1999), where similar surface damage was reported on silicon nitride balls, but nothing was reported about the cause and its effect on the life of bearings.

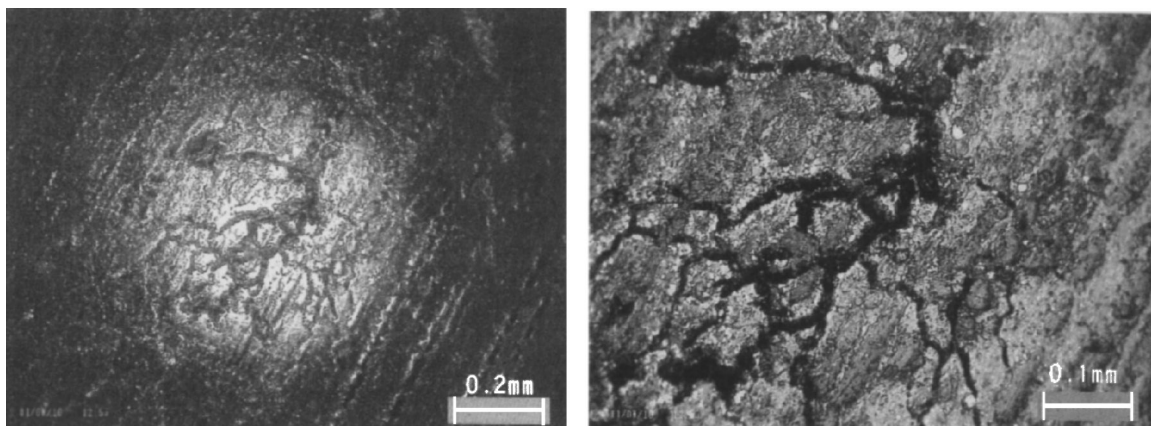


Fig: 1.3. Superficial micro cracks on silicon nitride balls (Nosaka et al 2004)

1.2.2. Wear in Refrigerant Lubrication:

In 1990s, several tests were carried out to test the implications of diluting oils with refrigerants in conventional all-steel bearings. Although there was a good progress in lubrication issues with oil/refrigerant mixtures, major progress was not made until SKF successfully evaluated hybrid bearings run in pure refrigerant (Wallin 2002). Compressor designs make it difficult to avoid dilution of oils by refrigerants and they found that conventional all-steel bearings exhibited inadequate lubrication at dilution levels of 20% to 30%. With difficulties in improving the bearing performance, they tested hybrid bearings running in pure refrigerant and found that they not only eliminated the need for a separate oil lubrication system, but also enhanced the bearing performance. They also reported that refrigerants can actually form an elasto-hydrodynamic lubricant film due to viscosity increase under the very high pressures developed in the contact areas. This thin film formation is sufficient to lubricate hybrid bearings but not all-steel bearings.

One promising application of oil-free lubrication reported by them was in centrifugal and screw compressors in chillers, which produce cold water for use in large air-conditioning systems and industrial processes. Different types of compressors are used for chillers; one good example is in centrifugal compressors, where oil is only used to lubricate bearings. By eliminating the oil lubrication completely, the following advantages were reported:

- Design simplifications and cost savings
- Eradicating failure modes associated with oil-based chiller lubrication systems
- Associated problems with oil and refrigerant mixing can be avoided
- Increased efficiency and environmental benefits.

These advantages then lead to the concept of hybrid bearings to running in pure refrigerants in different applications. The advantage of hybrid bearing with oil-free concept was also proved to improve pump efficiency by completely eliminating the need of oil lubrication system (Mikalonis 2003). These findings put hybrid bearings in several

applications where pure refrigerant was used as lubricant. Although a good success rate was achieved with the expected service life, some silicon nitride balls exhibited the presence of river marks as shown in Figure 1.4. These bearings were operated in pure refrigerant environment in an air-conditioning application. Failure analysis study on these samples revealed the river mark patterns as a main line with small tributaries running all over the ball. Until then, these river marks were only observed on silicon nitride balls run in cryogenic fluids such as liquid oxygen, hydrogen or nitrogen.

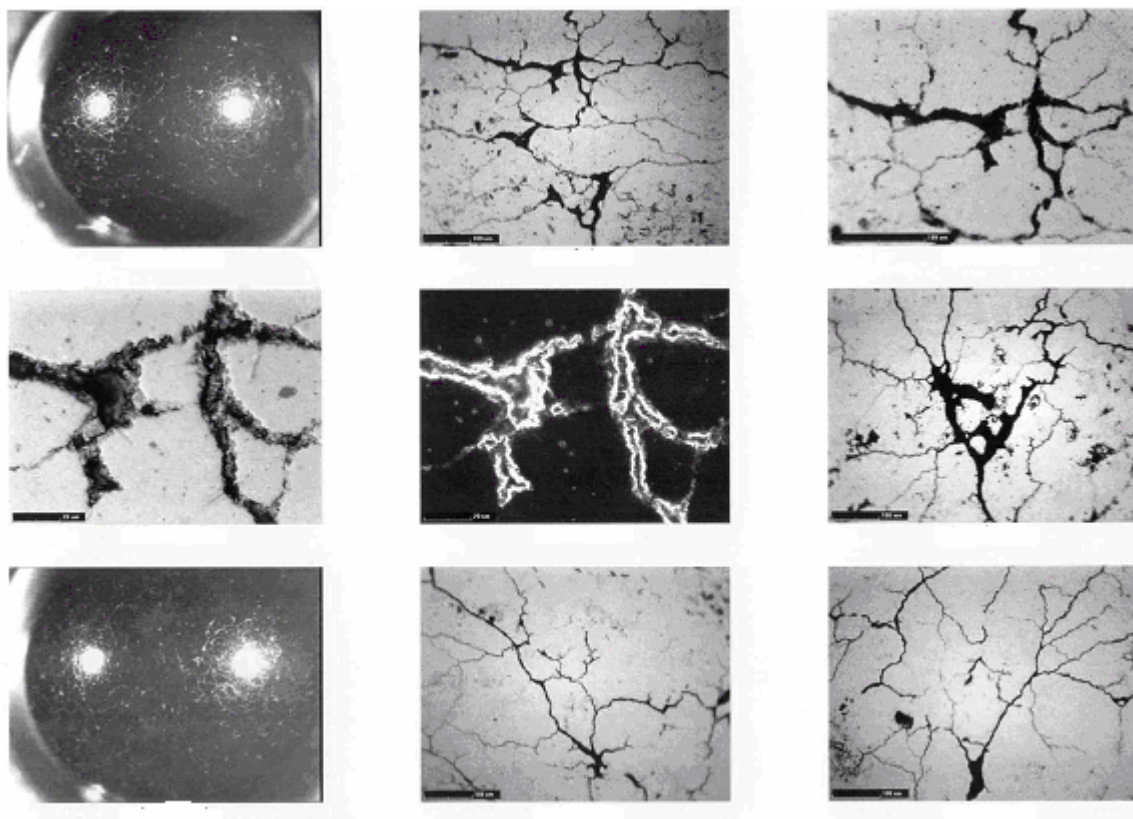


Fig: 1.4. River marks on Silicon nitride balls (SKF)

Surface measurements on river marks showed the deepest was almost 7 microns. EDAX analysis did not reveal any clear chemical attack and thus it was concluded that the river marks were formed by erosion. However, there is no clear proof to support this hypothesis.

1.3 BACKGROUND WORK:

This section summarizes the necessary and relevant literature supporting the work reported in this thesis. During the start of this project, silicon nitride with river marks obtained from various applications was supplied by the project sponsor for surface examination. To rule out that river marks are not surface cracks, a surface examination was carried out in the laboratory. Surface cracks are hard to observe on ceramic surface even under very powerful microscopes. Some non-destructive techniques like X-ray radiography and ultrasonics can be used, but for a quick and effective screening, a fluorescent dye penetration technique is often used. This is done by cleaning the sample in acetone and soaking it in fluorescent penetrant post-emulsifiable solution for approximately 1 hour. The sample is then immersed in diethyl glycol mono-butyl ether to clean the surface of any traces of penetrant, which is then followed by a gentle rinse in tap water. The prepared specimen when observed under an optical microscope with an ultraviolet light source would reveal any presence of surface cracks. This method was followed for river mark specimens. The microscopic observations showed no surface cracks on the surface which proved that river marks are different.

Being a low viscous and low saturation temperature fluid, refrigerant can undergo phase changes with drop in pressure due to geometry variations through the flow, possibly choked flow in bearings and seals. This phase changes are likely to cause cavitation and thus degrading the material by erosion. Also, silicon nitride balls in hybrid bearings have been extensively tested in various lubricating oils with no reports of the formation of river marks. Moreover, the cavitation erosion characteristics of silicon nitride are not clearly understood. Erosion coupled with rolling contact and its effect on the life of rolling elements is not yet known. These factors motivated the investigation of a cavitation erosion mechanism for silicon nitride and the effect of cavitation in rolling contact fatigue experiments. Thus, a profound knowledge on cavitation, cavitation in bearings, lubrication and rolling contact fatigue experiments is required for this work. A short summary and review on these topics are covered in the following sections.

1.3.1 Cavitation and Erosion:

Cavitation became a major concern during the late nineteenth century with increased difficulties with ship propellers in achieving required speeds. The Thornycroft torpedo boat destroyer, Daring, built in 1894 in Britain did not reach the expected speed of 27 knots but only 24 (Thornycroft 1895). An investigation showed that harmful propeller behaviour was the cause and it was called as “cavitation” derived from a Latin word Cavus meaning hollow. Sir Charles Parsons became the first to study the effects of cavitation, namely erosion and pitting of propeller blades, for which he built a cavitation tunnel (Burrill 1951). But, well before this, in 1886, Reynolds clearly recognized the possible influence of cavitation on bearing behaviour (Osborne 1886). Nowadays, there is a good understanding on this concept of cavitation, which provides a safeguard in designing hydraulic structures, among engineers and scientists after continued examinations over a century. The phenomenon of cavitation can be defined as the formation and collapse of bubbles or cavities. A classic photograph of a collapsing bubble is shown in Figure 1.5 producing a micro jet. These cycles of bubble collapse on solid structures could lead to a progressive loss of material by surface fatigue mechanism. In short, cavitation is an abnormal condition in hydraulic structures resulting in loss of production, equipment damage and even personnel injury. Components that have proved to be susceptible to damage due to cavitation erosion include marine propellers, bearings, pump impellers, valves, pipes and cylinder liners.



Fig: 1.5. A classic photograph by Crum showing micro jet development during bubble collapse. Bubble diameter approx. 1mm (Crum 1996)

The theoretical tensile strength of water at room temperature is approximately 101.3 MPa (Young 1999), but cavitation is observed at pressure amplitudes of 0.1 MPa. This implies that bubble formation due to pressure drop is merely the growth of pre-existing minute bubbles, called bubble nuclei. Hence, bubble formation means both creation of new bubbles or expansion of bubble nuclei. Cavitation can be initiated by any of the following three ways when pressure is reduced to a negative value (Young 1999):

- Presence of large number of minute spherical gas bubbles
- Solid impurities or particles with gas trapped in
- Trapped gas in the tiny cracks or splits of the vessel containing the liquid.

This cavitation initiation process can be accomplished by either creating tension or by depositing energy into the liquid. Cavitation can be gaseous or vaporous depending on whether a gas or vapour is contained in the bubble. Bubbles can grow steadily oscillating in the liquid until it becomes unstable and collapse called as stable cavitation. On the other hand, bubble growth and collapse can be rapid and violent which is called as transient cavitation. This cavitation process has four major characteristics as follows (Chen 2002):

- High pressure: During cavitation, pressures can reach up to hundreds of MPa or even GPa, which is higher than the elastic limit of most engineering materials.
- High temperature: The temperature during collapse is estimated as several thousand degrees centigrade. Experiments were made to measure the temperature during bubble collapse, using a similar system to measure star temperatures which revealed that the temperature could be four times that of the sun's surface (Flint 1991, Flannigan 2005 and Crum 1995)
- Small dimension: The impact on the solid surface caused by bubble collapse is very small in the order of microns
- Short time: The duration of this collapse process is very short often in microseconds.

These high pressures and temperatures result in material damage and noise. If the resulting stresses exceed the elastic limit of the material, this will lead to plastic deformation. The collapse of bubbles results in shockwaves and micro jets, and from various studies made in the past decades, it seems that both contribute to material damage (Brennen 1995). Once a bubble collapses on to a solid surface, it breaks down into smaller parts as minute bubbles or nuclei, which again grows and get collapsed as the previous one. Lindau investigated the effects of counter jet development on material damage after bubble collapse (Lindau 2001). He concluded that this counter jet consists of micro bubbles with two to three times less magnitude of the micro jet developed during collapse and contribute to material erosion. Laboratory studies of cavitation and erosion are plenty (Young 1999, Brennan 1995, Lin 2005, Tao 1971). Chapter 2 of this thesis describes the available testing methods and the one chosen for this study. The mechanism of cavitation erosion and the effect of material properties and cavitation conditions on silicon nitride are detailed in Chapter 3.

Along with all these disadvantages, there is also a good side to cavitation. Scientists are working on ways to make use of cavitation for useful purposes, which resulted in supercavitation (Kirschner 2001, Rowe 2000). This is a hydrodynamic process, in which a cavity is used to transport undersea objects at high mach numbers, such as underwater supersonic projectile and is of particular interest to navies. The major applications of supercavitation are in underwater body motion for very high speeds and supercavitating water jets (Savchenko 2001). This flow investigation started early in the 20th century for guiding missiles and underwater vehicle. A supercavitating torpedo which reaches 800 km/hr was reported (DIEHL 2006). The super cavitation was also proposed as a method to suppress noise (Grinchenko 1998).

1.3.1.1 Cavitation in Bearings:

In order to reduce friction and wear, lubricants and process liquids are used in bearings. Fluids in bearings are forced to flow due to shearing forces of mechanical surfaces which generates hydrodynamic pressure. This pressure is non-uniform and varies at different

regions in the bearing. When the film thickness increases locally at certain areas, the fluid pressure may drop below its vapour pressure and lead to release of dissolved gases which results in cavitation. The form of cavitation in bearings is due to the ventilation from the surrounding atmosphere or, as mentioned earlier, due to surface crevices. Figure 1.6 shows a lubricant cavitation in journal bearing. Cavitation in lubricant thin films can not only cause material damage due to erosion but also affect the load carrying capacity of bearings. Thus, cavitation effects on bearings and their stability have been extensively studied and are well documented in literature (Dowson 1974, 1979, Garner 1980, Berthe 1975, Hamrock 1994, Heshmat 1988)

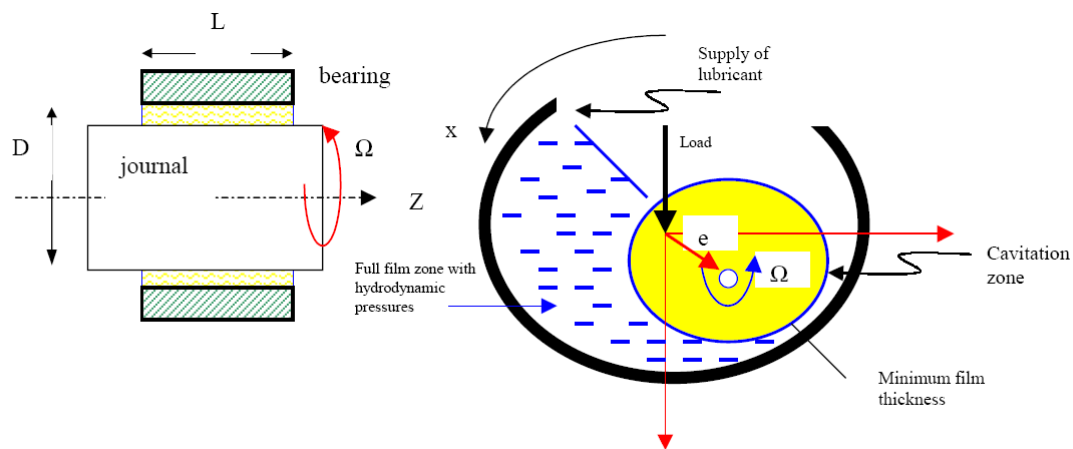


Fig: 1.6. Journal bearing showing lubricant cavitation zone (Andreas 2000).

From observations, different forms of cavitation erosion have been postulated in bearings. (Dowson 1979) lists them as following:

- Suction erosion: this occurs when the journal of a bearing recedes rapidly from a bearing surface. Examples: crankshaft or crankpin.
- Discharge erosion: this results from the displacement of oil ahead of a shaft moving radially
- Flow erosion: this is due to the flow of lubricant across discontinuities i.e. liquid jet and particles immersed in the lubricant causing particle erosion.

- Impact erosion: this can arise due to oil supplying from a main to a big end bearing which passes from grooved to an ungrooved portion of the bearing surface
- Dispersed erosion: this type of erosion can occur due to rippling of top layers in the lubricant.

Gaseous or vaporous cavitation can occur in bearings depending on the steady or dynamic loading bearing conditions. Vapour cavitation in a dynamically loaded journal bearing was first recorded by Hamrock using high speed photography techniques (Jacobson 1983). The effect of shaft frequency on the cavitation formation and damage was also investigated and concluded that the increase in shaft frequency caused a delay in cavitation onset (Brewer 1987). Theoretical studies on cavitation in bearings are extensive and are well documented in literature (Elrod 1974, 1981, Floberg 1961, Zeiden 1989, Feng 1989, Vincent 1996, Rapposelli 2001). Due to variations in the speed, load and designs it is not always easy to identify the exact cause of cavitation. However, cavitation does occur and cause material damage thereby affecting the efficiency of the hydraulic structure. Below Figure 1.7 shows an example of damage caused by cavitation in bearings.



Fig: 1.7. (a) Cavitation erosion of diesel engine main bearing and (b) wear on hydrodynamic bearing surface (Chen 2005).

1.3.1.2 Erosion in Ceramics:

Ceramics form a wide class of materials and, like metals, have a broad range of applications including body armour and hip implants. They are also used as coatings in many cases due to their excellent wear and temperature resistant properties. Glasses, traditional and engineering ceramics, cement and concrete, rocks and minerals, and ceramic composites all belong to this class. Ceramics are characterized as highly brittle solids with a typical fracture toughness range of 1 to 12 MPam^{1/2}, high elastic modulus (usually much greater than metals), high compressive strength and very high hardness. Other properties like creep and wear resistance, chemical inertness and high melting point make them very attractive for engineers and designers for applications such as nozzles, turbine blades, heat exchangers, steam pipes and with fluids and/or particles dispersed in liquids. Erosion characteristics of these ceramics must be clearly understood to use them in such applications and hence plenty of work has been reported in this field as well (Wang 1996, Khalil 1996, Lathabai 2000, Wakuda 2003).

Silicon nitride is very difficult to manufacture and is expensive too. Commercially produced silicon nitride ceramics are available with a wide variety of compositions and microstructures. This makes it possible to test this material with different composition and microstructures. (Hyeon-Ju Choi et al 2003) have tested three different types of silicon nitride, which different microstructures and have concluded that microstructure has a large influence on the wear rate. Erosion was created by impacting with silicon carbide abrasives of 130 µm size at an incident angle of 90°.

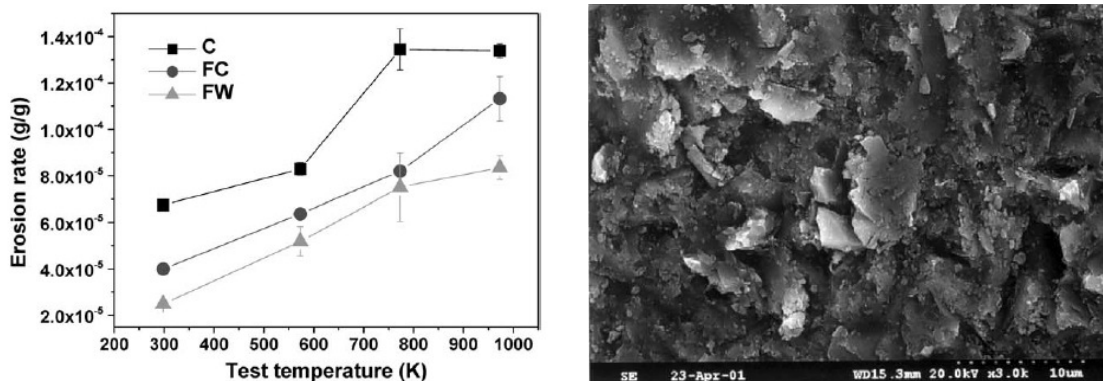
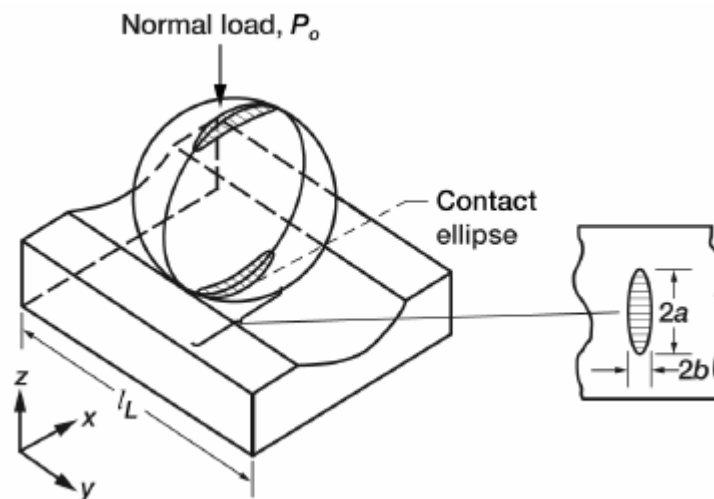


Fig: 1.8 (a) Erosion rate against temperature and (b) shows eroded area of silicon nitride (Hyeon-Ju Choi et al, 2003).

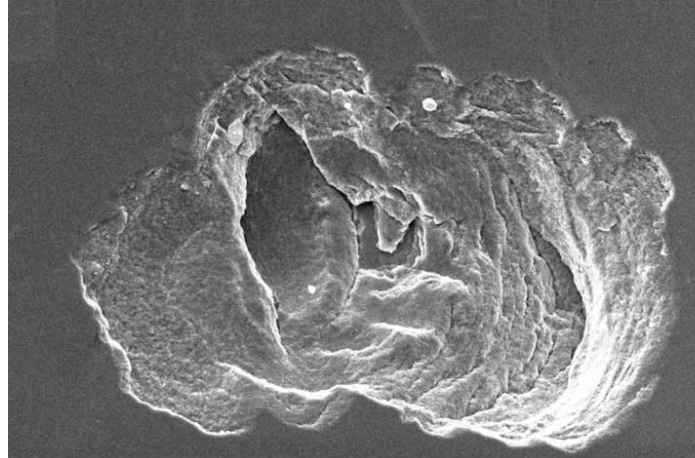
Their results showed that coarser the microstructure the higher the rate of erosion and that the rate depended on the grain size more than on mechanical properties including hardness and the fracture toughness. Erosion occurred mainly by grain dislodgment following inter-granular fracture. Figure 1.8 (a) shows erosion rate plotted against temperature and 1.8 (b) an eroded area. Another paper published in the same field by (Lim et al, 2003) showed similar results, but concluded that the eroded region exhibited extensive plastic deformation and grain pullout. They also showed that loss of binding strength between debris with increase in temperature that resulted in higher wear rate. Three times increase in cavitation resistance due to LASER surface alloying of silicon nitride coating was reported because of high fracture toughness (Man 2000). Niebuhr (Niebuhr 2007) investigated cavitation erosion of ceramics in aqueous solution and concluded that silicon nitride had the highest resistance to cavitation compared to that of other ceramics tested. Also, the mechanism of material failure reported in his paper was consistent among all materials and was due to intergranular fracture. Cavitation erosion on silicon nitride materials apart from coatings was not reported, and so the wear mechanism in this material due to cavitation was not understood. Moreover, cavitation erosion and their relation to rolling contact wear, and their combined influence on rolling elements was not reported.

1.3.2 Rolling Contact Fatigue:

Rolling contact fatigue (RCF) is the major cause of failure in components subjected to rolling or rolling/sliding contacts (Stewart 2002). Apart from bearings, gears and cam/tappet arrangements are some of the examples which undergo rolling contact fatigue. RCF is a surface damage process on rolling bodies which roll on each other and are subjected to repeated stress cycles; a schematic is shown in Figure 1.9. This section covers only the RCF review on bearings, in particular hybrid bearings, mainly due its interest and relation to this project. Among different bearings, RCF occurs in ball bearings in contact with the inner and outer raceways, in shafts in contact with sliding bearings and in roller or needle bearings in contact with the outer raceways (Fernandes 1997). The failure due to rolling contact fatigue involves crack initiation and propagation leading to material removal. In the case of conventional all-steel bearings, microscopic pits or micro-pits form first, which act as stress concentrators for further damage. These pits over time grow into macro-pitting due to flaking. These finally end up as a large craters or deep pits called as spalls as significant material is removed (Stewart 2002). In ceramics, crack initiation and propagation is the mechanism which then leads to delamination (Wang 2002).



(a)



(b)

Fig: 1.9 (a) Schematic of contact profile of rolling element on raceway (Zaretsky et al 2005) and (b) SEM image of a spall on Si₃N₄ after 16 million stress cycles (Wang 2002).

Rolling contact life of bearings can be expressed using the theory of Lundberg and Palmgren put forward in 1940s as (Wang et al 2000):

$$L = (C / P)^{n/3}$$

Where,

L – Bearing fatigue life in million revolutions

C – Dynamic load capacity rating

P – Bearing equivalent dynamic load

n – Stress life exponent

In general, rolling contact fatigue life of rolling elements largely depends on the surface quality, lubrication conditions and stress distributions. In order to predict the rolling contact fatigue life of rolling elements, laboratory RCF testing is commonly done. To date, there are several different testing methods available, variations in the RCF tester itself (Kang 2003, Manoj 2007). RCF testers which can directly assess the rolling element ball samples are Four-ball rolling tester (Tourret and Wright 1977), Five-ball rolling tester (Parker and Zaretsky 1975), Rolling element on flat tester (Dalal 1975), Three-ball on rod tester (Chao et al 1998) and V-Groove ball tester (Galbato et al 1992).

Apart from these, Disk on disk RCF tester is also used to study RCF behaviour of rolling elements (Effner and Woydt 1998). The main difference among these testers is the configuration they provide, which reproduces the actual running conditions. The rolling fatigue tester used for this project is described in Chapter 2. Since erosion in hybrid bearings is the main focus topic of this project, the effect of lubricant in the rolling contact fatigue wear is important. Therefore, the following sections review the findings of silicon nitride with steel contact in different lubricants resulted from various laboratory testing.

1.3.3.1 Lubrication Oils:

Tribological behaviour of hybrid bearings is hugely influenced by the type of lubricant used. Since rolling contact bearings are widely used in numerous applications, it becomes necessary to evaluate the rolling contact life in various lubricating fluids. Most importantly, understanding the role of lubricant in the rolling contact life of bearings is required. Hence, several investigations were made in the past and their results were published (Stewart 2002, Wang et al 2000, Zhao 2004, Bower 1988 and Wang 2000). It was found that the lubricant not only plays a role in the life of hybrid bearings, but also has a vital role in the rolling contact fatigue failure mechanism. Example situations include the lubricant pressure acting as a crack opening force (Keer 1983, Kaneta et al 1985), lubricating the crack faces which increase the shear stress intensity factor (Bryant 1984) and the fluid entrapment mechanism (Bower 1988).

Noteworthy contributions on the effect of lubricant on RCF life and failure mechanisms in hybrid bearings have been made by Ping Zhao and Mark Hadfield (Zhao et al 2004, 2006). They reported on the role of the lubricant on the life of hybrid bearings, precisely explaining the lubricant role in the formation of secondary surface cracks. These studies were made on silicon nitride balls with pre-existing cracks. This allowed them to understand the formation of secondary cracks and subsequent failures under various lubricants. Test lubricants were grease, gearbox and traction oil, with a wide variation in their properties. RCF tests with traction oil showed decreased fatigue life relative to

grease indicating the effect of lubricant on the rolling contact life of hybrid bearings under the same operating conditions. Results of their findings are shown in Figure 1.10.

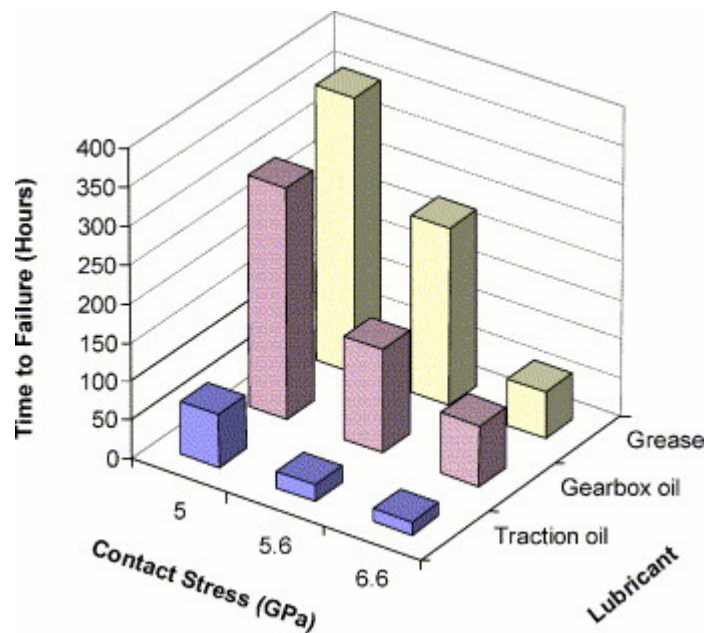


Fig: 1.10. Rolling contact fatigue life with various lubricants and contact stresses (Zhao et al 2004)

The above Figure 1.10 shows no fatigue failure with gearbox oil and grease when the maximum contact pressure was less than 5 GPa for 20.2×10^7 cycles. But, on the other hand, traction oil showed fatigue failure after a short period of testing for about 68.5 hours. This is a clear proof that lubricating oils have a significant effect on the life of hybrid bearings. With these results, they have concluded that the use of grease might prevent oil penetration in the crack or at least delay its penetration. Also, they stated that increasing the surface tangential traction decreases the rolling contact life and hence the reason why RCF performance was less satisfactory with traction oil which increased the surface tangential traction. All failure mechanisms reported were due to secondary crack formation leading to spalling. However, no difference in the failure mechanism with regard to lubricant was reported in their findings.

1.3.3.2 Refrigerant-Oil Mixtures:

Following the Montreal protocol on substances that deplete the ozone layer, chlorofluorocarbons (CFCs) were substituted by hydrofluorocarbon (HFCs). There is no technical reason to replace CFCs if the system does not leak refrigerant to the atmosphere and operate properly. Anyway, the change has been made and it has put pressure on compressor manufacturers to design the equipments to accommodate HFCs. Since the most important property of a lubricant is to form a film that separates surfaces in contact, HFCs were extensively investigated to determine and enhance their lubrication properties. Refrigerant-oil mixture lubrication studies are plenty, but only pure refrigeration is reviewed here due to close relevance to this work.

1.3.3.3 Refrigerants:

Khan et al published a series of papers on rolling contact fatigue of ceramic/steel contact in pure refrigerant lubrication (Khan 2005A, 2005B, 2006). A pressurized chamber was used for their study, which allowed them to achieve liquid state of the refrigerant in RCF experiments satisfying the boundary lubrication conditions. A high speed four-ball rotary tribometer used for this project was then adapted for their refrigeration experiments. These were aimed at evaluating the influence of refrigerants HC (R600a) and HFC (R134a) on rolling wear of hybrid contacts. Shaft speeds up to maximum 5000 rpm and contact pressure of about 7 GPa was tested. Test specimens were commercial silicon nitride balls with pre-existing surface defects such as indents and cracks. They reported higher fatigue life in R134a than in R600a, supported by the possible reason that fluoride layer formation in sliding surfaces in the former environment.

The gaseous phase of the refrigerant was reported to result in severe wear. Time for specimen failure varied from less than 3 minutes to several hours. The mechanism of failure was crack growth or propagation leading to secondary cracks which finally resulted in spalling. The position of the crack in the rolling contact had a huge influence on fatigue life of test specimens. Further, residual stress relating to stress cycles and specimen defects were detailed. An inverse relationship of compressive residual stresses

to the number of stress cycles during rolling contact fatigue was proposed to use a measure to estimate residual fatigue life. Sub-surface crack initiation and propagation was reported as the mechanism for material failure due to spalling. However, no erosive wear was reported in their study.

1.3.3.4 Cryogenic Fluids:

Hybrid bearing tests in cryogenic fluids are limited as only a very few reports have been published so far. (Nosaka et al 1999) from the Japanese National Aerospace Laboratory published their findings on wear characteristics of all-steel and hybrid bearings tested in cryogenic environments. Bearing test equipment was built to achieve high speeds of up to a maximum of 35,000 rpm with thrust loads to 2840N. They tested all-steel and hybrid bearings in liquid hydrogen, oxygen and nitrogen. Test materials were self lubricated by a thick layer of PTFE (polytetrafluoroethylene) which was generated from a glass cloth-reinforced PTFE retainer. The bearing tester allowed a test bearing to be installed in the bearing housing which was completely immersed in cryogenic fluids.

Results obtained from tests at various speeds, loads and durations were reported. A comparative study on all-steel and hybrid bearing performance was done in these three cryogenic fluids. All-steel bearings showed good performance in liquid hydrogen and oxygen, but severe wear was noticed when tested in liquid nitrogen. Surprisingly, poor performance of hybrid bearings in liquid oxygen was reported even at a low speed of 10,000 rpm with a relatively lower thrust load. Microscopic examination of this test specimen showed little evidence of spalling or stress cracks. But, a severe adhesion between steel races and ceramic balls were reported. The reason for this poor performance in liquid oxygen was attributed to the weak adhesion of PTFE transfer film. Nothing about river mark type wear was mentioned in their work.

The very first report on the development of a new testing facility for tribological tests in cryogenic environments was by Subramonian (Subramonian et al 2006). The so called cryogenic tribometer provide similar testing facilities to a normal tribometer. Two

notable features of their tribometer is the roller-on-disk and the ball bearing tester submerged in cryogenic fluids. This cryogenic tribometer can only be used to study friction and wear characteristics in sliding contacts and not rolling contacts. Also, their published results did not include ceramic materials but only steel. Tribological testing under these conditions is an important background for this project and hence it is worth reviewing their work. Figure 1.11 below show the design description of this tribometer.

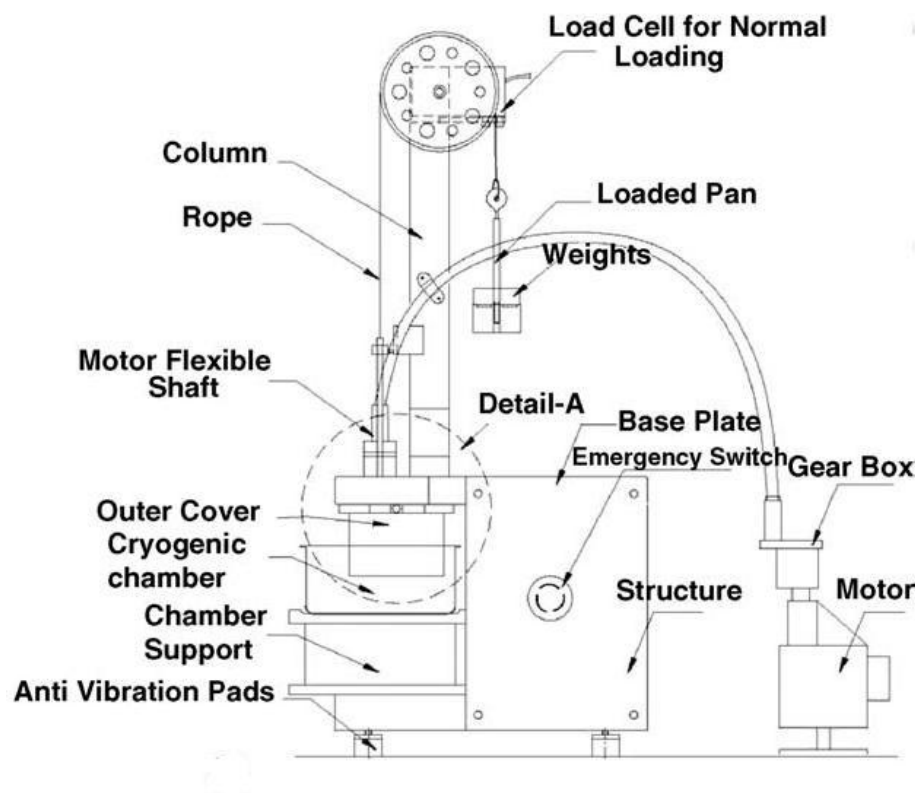


Fig: 1.11 A detailed description of ball-on-disk high speed cryo-tribometer.

(Subramonian et al 2006).

This tribometer consists of main modules of a spindle assembly coupled with a motor and a gear box to transfer motion with 14 speeds in steps from 850 to 36,000 rpm. A bearing housing unit holds the test specimens in cryogenic fluids and a constant level was maintained by an external supply. Test materials were smoothly polished SS304 stainless steel and 440C grade martensitic stainless steel with cages made of glass fiber reinforced PTFE composite material. Surface analysis after testing showed highly uneven worn

surface with cracks originating from the central region of the wear track and propagating perpendicularly to the sliding direction as shown in Figure 1.12. This wear was noted only at high sliding speeds of 22.4 m/s; at low speed of 0.89 m/s no signs of wear were reported. This clearly signifies that high speed plays a leading role in the wear process. They concluded that wear formation was mainly due to repeated abrasion of asperities resulting to fracture. However, nothing about ceramic materials, erosion or river marks was reported.

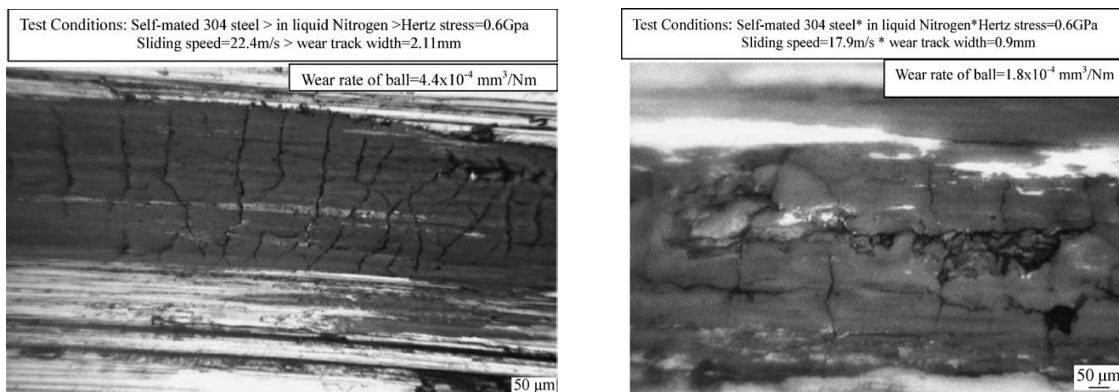


Fig: 1.12 Cracks on wear track of test materials in liquid nitrogen. (Subramonian et al 2006).

1.4. Aims and Objectives:

The principal aim of this project is to investigate the cavitation erosion wear mechanism of silicon nitride and the effect of erosion in rolling contact fatigue life of hybrid bearings. With the increased demand and widespread applications of hybrid bearings, a wear mechanism which clearly describes the process of cavitation erosion namely initiation and progression and its effect on rolling contact is required. This aim can be divided into individual objectives as follows:

- Acquire knowledge on cavitation erosion concept and experiments to install cavitation erosion testing facility in the laboratory.

- Experimentally study the erosive wear mechanism on silicon nitride using advanced surface analysis techniques.
- Perform a comparative study on silicon nitride with different microstructure and physical properties to identify the parameters which provide resistance to erosion.
- Examine the effect of lubricant and surface defects on cavitation erosion.
- Identify the effect of cavitation flow conditions on the rate of erosive wear.
- Find the correlation between cavitation erosion and river mark type wear as seen in application bearings.
- Computational fluid dynamics modeling of bubble dynamics generated by acoustic cavitation test bench to understand the strength of impact forces on test materials
- Perform a coupled-field analysis to simulate the fluid-structural interaction (FSI) of collapsing bubbles on silicon nitride rolling elements
- Design and manufacture a test rig to couple controlled erosion and rolling contact fatigue testing, termed here as “Mechano-Erosion”
- Inspect the effect of liquid/gas phase transition in the lubricant on the life of rolling elements.
- Investigate wear mechanisms of hybrid and ceramic contacts due to both erosion and rolling contact in the novel mechano-erosion testing.
- Study the effect of lubricants on the material degradation in Mechano-Erosion testing.
- Examine the effect of contact stress, rolling speed and cavitation intensity on the material wear rate.

1.5 Overview of Thesis:

Importance and the role of hybrid bearings in engineering advancements were discussed in this Chapter. A detailed review on the background work and supporting literature was also covered along with aims and objectives of this work to address the problems encountered by hybrid bearings in oil-free lubrication applications.

Chapter two contains all the details of experimental work carried out in the laboratory. This includes the testing approach, cavitation erosion and rolling wear testing setup, specimens tested and visual inspection techniques for surface analysis such as light microscope, scanning electron microscope (SEM) and optical interferometry methods.

Chapter three covers the erosion mechanism of silicon nitride, documenting the process of wear due to cavitation from wear initiation to the final material failure. The effect of material properties, microstructure and fluid flow conditions on the progression of erosion is also discussed in this Chapter.

Chapter four describes a new testing methodology to combine laboratory erosion and rolling contact testing. All experimental studies carried out using this testing method is detailed in this Chapter.

Chapter five contains a brief summary of this work and overall conclusions reached. It also discusses the recommendations to continue this work in future.

Appendix A contains a concise data on silicon nitride: namely, manufacturing and processing routes, types and its applications

Appendix B details the different experimental methods to perform cavitation erosion testing discussing the advantages and disadvantages of each method.

Appendix C contains all the supporting pictures and data of laboratory experiments performed for this project.

Appendix D contains the numerical study of cavitation using Rayleigh-Plesset equation. This contains modeling of fluid flow conditions due to acoustically generated cavitation using advanced finite element and computational fluid dynamics.

Chapter 2

EXPERIMENTAL METHODOLOGY

Several sets of laboratory experiments were conducted to study the erosive and rolling wear mechanism of silicon nitride. Many parameters influence the cavitation and rolling wear testing and a careful attention must be paid to successfully perform these experiments. Hence, all testing performed for this project underwent a systematic procedure such that every crucial test parameter was controlled and monitored individually. All these experimental data: equipments employed, procedures followed, result observation are briefly described in this Chapter. Section 2.1 presents the test materials used for this study followed by section 2.2 which discuss the testing approach: mainly the test procedure and details of test setups, and finally section 2.3 presents the post-processing of experimental data.

2.1. Test Materials:

Silicon nitride manufactured into bearing rolling elements was used as test materials for most of the testing in addition to bearing steel for a comparative study. As mentioned early, the primary objective of this project is to understand the erosion characteristics of ceramic rolling elements. Hence, it was decided to use the rolling elements itself as test materials rather using any other form of silicon nitride. This allowed us to have the materials which are typically employed in bearing applications. Wear or any other form of material degradation of these application samples enabled us to compare the results obtained in the laboratory. These rolling elements are spherical balls of 12.47 mm diameter and were precisely polished to a surface roughness of submicron accuracy. Manufacturing rolling elements to such a level of polished surface follows a series of steps from blank silicon nitride powder to polishing with diamond paste, and is a time consuming and very expensive process. Manufacturing of these test materials is out of the

scope of this project; however test materials of different manufacturing methods resulting in different microstructure and sintering additives are important factors for this erosion study. The processing details are described in appendix A. Hence, rolling elements from different commercial manufactures with varying properties were utilized for this study.

2.1.1 Silicon Nitride:

Silicon Nitride is prepared by sintering or direct reaction between silicon and nitrogen at high temperatures. Three crystallographic structures of Si_3N_4 exist, of which α and β phases are common and can be produced at normal pressure conditions. These phases have trigonal and hexagonal structures respectively which are formed by corner-sharing SiN_4 tetrahedra (Wikipedia, 2007). Further details of this material including crystallographic structures, different manufacturing methods are provided in appendix A. Compared with other ceramics, silicon nitride has higher fracture toughness due to the presence of β grains which is well known to deflect the crack (Huang et al 1996). Fracture toughness values of $10 \text{ MPa m}^{1/2}$ of silicon nitride has been reported (Wang 2001). This makes this material widely used in several engineering applications. In particular, hot isostatically pressed silicon nitride is well suited for bearing applications. Silicon Nitride is broadly classified into two types based on the processing types as follows:

- Sintered silicon nitride (SSN)
- Reaction Bonded Silicon Nitride (RBSN)

Apart from the processing types, silicon nitride is further classified into three types based on the manufacturing methods:

- Hot Pressed Silicon Nitride (HPSN)
- Gas Pressure Silicon Nitride (GPSN)
- Hot Iso-statically Pressed Silicon Nitride (HIPSN)

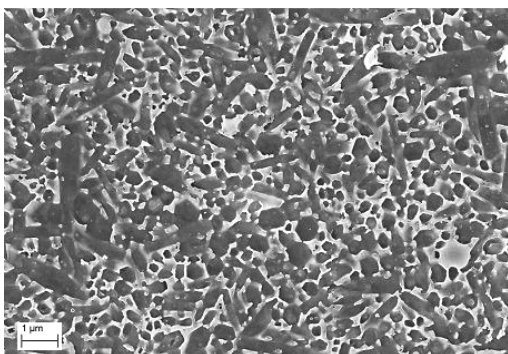
Test materials used for this project were produced by hot isostatically pressed. This way of manufactured silicon nitride has shown better bearing performance and offer several characteristics like zero porosity, high fracture toughness, hardness, strength, fine microstructure and minimum dopant level. Extremely pure starting powders are required to develop such a high quality silicon nitride ceramics. This initial stage determines the characteristics of sintering and the subsequent microstructure formation. Blank silicon nitride ball is produced by traditional machining processes such as blending, milling and agglomeration. This is further densified by liquid phase sintering at pressures of 200 to 300 MPa and at temperatures of 1750 to 1900 °C. This can only be achieved using indirect methods by adding chemical additions called as sintering additives. The most common sintering additives are Magnesium oxide (MgO), Yttrium oxide (Y₂O₃) Aluminium oxide (Al₂O₃). The factors which determine the percentage of additives largely depend on the application of the final silicon nitride ceramic and sintering conditions. Commercial manufactures of silicon nitride balls do not provide the exact values of the sintering aids used, but approximate values can be deduced from energy dispersive X-ray spectrum.

Densified material undergoes several stages of polishing to achieve very fine polished surface free from any pores. Several screening techniques are employed at the final stages of this manufacturing to screen for any surface defects such as pores or cracks. This ensures good quality of the final product. Silicon nitride materials used for this project are from different ceramic manufactures. These are widely used in several engineering applications. These three materials named here as A, B and C are very successful in the present bearing industry and hence the reason for selection. Moreover, the variations in their properties, microstructure and sintering additives are essential for a comparative study on the mechanism of cavitation erosion. Mechanical properties of these materials are presented in Table 2.1. Plasma etching and high magnification microscopy techniques are described in the final sections of this Chapter. These methods were used to image the microstructure of these three test materials and are shown in Figure 2.1. As shown in the below Table and Figure, these three materials have a huge variation in the microstructure,

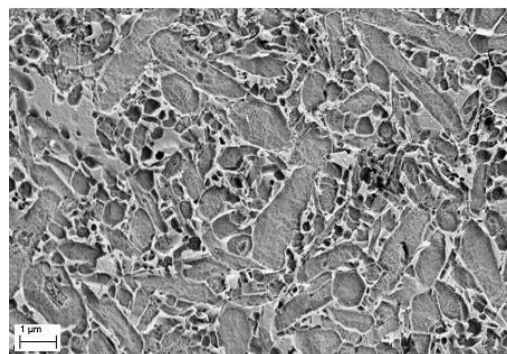
properties. These key factors were considered for the erosion study to assess their influence on wear resistance and are described in Chapter 3 of this thesis.

Material	Hardness (HV 10 kg/mm ²)	Indentation Fracture Toughness (MPa√m)	Avg. Grain size (μm)	Young's Modulus (GPa)	Surface Effective strength (kJ/m ²)
A	1600-1700	6.4-7	0.3	290	15.8
B	1630-1750	6.3-6.5	0.7	310	12.9
C	1520-1560	5.8-6.1	0.6	320	12.55

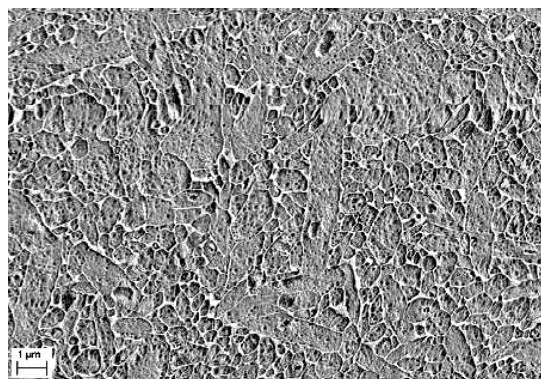
Table: 2.1. Mechanical properties of test samples (SKF)



(a)



(b)



(c)

Fig: 2.1 Plasma etched images of test samples A, B and C in order (SKF).

2.1.2. Bearing Steel:

All-steel bearing balls were also used for erosion testing along with Silicon Nitride balls. Moreover to study the effect of erosion in hybrid contacts steel balls are necessary and were used appropriately with silicon nitride. This steel ball is carbon chromium steel and the dimensions are same as the silicon nitride balls which is 12.7mm in diameter. This has an average roughness of 0.02 μm R_a . Mechanical properties of this material are presented in the below Table 2.2

Density g/cm^3 kg/mm^2)	Hardness (HV 10	Fracture Toughness ($\text{MPa}\sqrt{\text{m}}$)	Poisson's ratio	Young's Modulus (GPa)	Bending strength (MPa)	Yield Strength (MPa)
7.85	700	25	0.3	270	2400	2030

Table: 2.2 Properties of Bearing steel (Wang 2001)

2.1.3. Test specimen preparation:

Fresh samples from manufactures were used for most of the tests which did not require any further sample preparation for testing. But despite sophisticated screening techniques deployed during manufacturing process, silicon nitride balls manufactured are not always free from surface defects. Mainly surface cracks, star defects, tiny pits result during the final stage of the material preparation. This final preparation stage comprises polishing using diamond paste. This motivated us to also test specimens with pre-existing defects. These defects were created in the laboratory as part of experimental preparation and are detailed in this section.

2.1.3.1. Indentation and Crack Generation:

Star defects and tiny pits are similar to indents. Vickers Hardness indent were made on some samples to study the erosion behaviour of surface defects. This uses a square shaped pyramid diamond tip to create indent as shown in Figure 2.2. Steps followed were:

- Silicon nitride ball was placed in a chuck and the indenter was pressed on the specimen with the required load.
- Duration of load application varied from 10 to 20 seconds
- Indent was carefully marked using the microscope eyepiece
- Specimen was removed and dimensions of the indent were measured using an optical microscope and 3D surface measurement system.

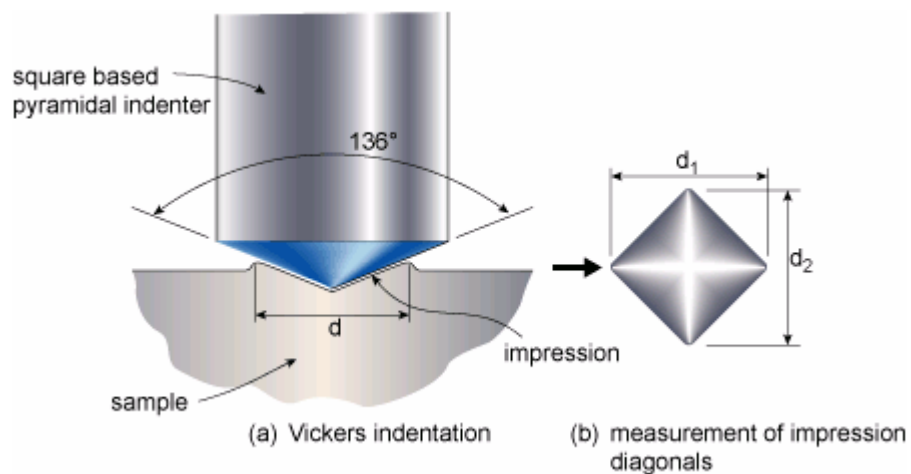


Fig 2.2 Indent generation and resulting indent (TWI).

Artificial surface ring cracks were produced on silicon nitride balls. An available crack generating device (CGD) in the laboratory was used for this purpose which is shown in Figure 2.3. The working principle of this device is similar to impact tests. This consists of a base and a pendulum hammer. A high force is applied for a very short period of time which is achieved by the impact of the pendulum hammer. The swing angle of the pendulum is directly proportional to the applied force. Test specimens were fixed in the

appropriate places – one at the base stand and the other in the pendulum. The pendulum hammer was lifted to the required angle of impact and allowed to drop under gravity to generate the crack. The angle of impact and impact force are displayed in the device. The area of impact was marked and the crack geometry was measured in a similar way as was followed for indents.



Fig: 2.3 Crack generation using a Plint impact pendulum

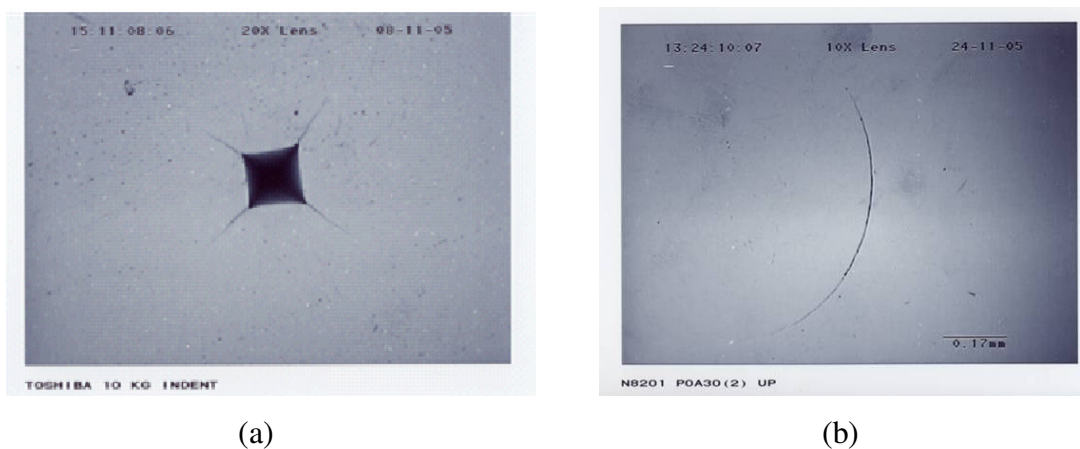


Fig: 2.4 (a) Vickers Indent and (b) Surface crack on test samples

Apart from fresh and surface defect specimens, some silicon nitride specimens were cut and polished to understand the cavitation behaviour in flat polished surfaces. A rotating diamond cutting wheel lubricated with water was used for sectioning silicon nitride balls. Low cutting speed and pressure was used to carefully section the specimen without damaging both the specimen and the cutting wheel. For a 12.7mm diameter silicon nitride ball this process usually last for 30 minutes.

2.2. Cavitation Erosion:

Cavitation is defined as the repeated nucleation, growth, and violent collapse of cavities or bubbles in a liquid. This is possible only when a liquid is subjected to sufficiently high tensile stresses. The theoretical tensile strength of water at room temperature is 1000 atm (Young 1999). But cavitation is observed with pressure amplitudes of 1 atm, which implies presence of minute pre-existing bubbles within the liquid, called as nuclei. Thus Bubble formation means both creation of new bubbles or expansion of pre-existing nuclei. Cavitation can be initiated by any of the following three ways when pressure is reduced to a negative value:

- Presence of large number of minute spherical gas bubbles.
- Solid impurities or particles with gas trapped in.
- Trapped gas in the tiny cracks or splits of the vessel containing the liquid.

This initiation process can be accomplished by either creating tension or by depositing energy into the liquid. Applying tension is broadly classified into hydrodynamic and acoustic cavitation. The first one is the low frequency process and the later is a high frequency phenomena. Figure 2.5 shows the classification of different types of cavitation. The highlighted one in the Figure was used for this project.

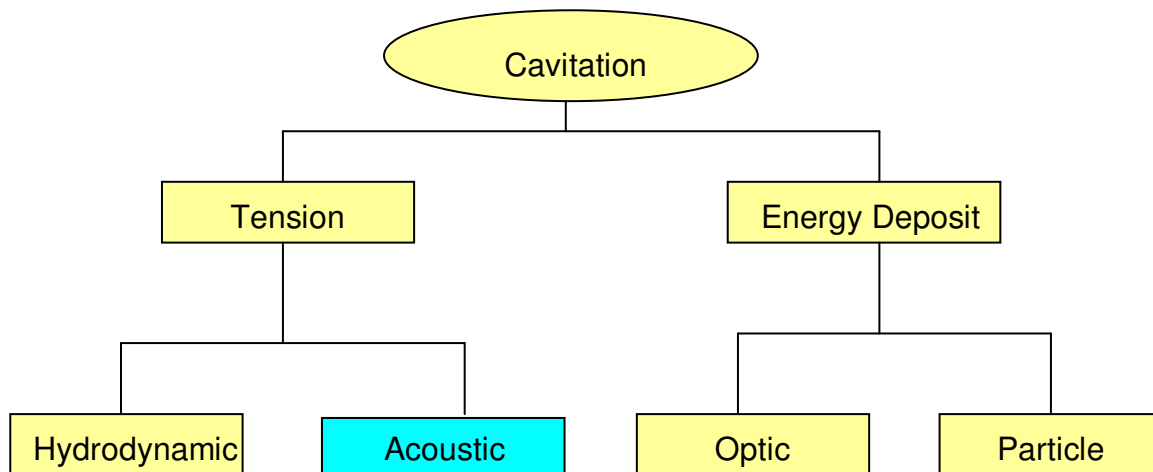


Fig: 2.5 Different Types of Cavitation - Redrawn from Reference (Gong 1999).

- Hydrodynamic cavitation is the one which is produced due to the geometry of hydraulic structures. Geometry of the system creates pressure variations in the flowing liquid. Examples are Ship propellers, Turbines.
- Acoustic cavitation is a high frequency process, which creates cavitation by applying acoustic waves to a liquid. Example: Ultrasound in a liquid.
- Optic cavitation is a type of producing cavitation by rupturing the liquid with photons of high intensity light. Example: LASER.
- Particle cavitation is produced by elementary particles in the liquid. A charged particle sent to a liquid can produce rapid local heating resulting in cavitation. Example: Bubble chamber.

Out of the above four different methods of producing cavitation, hydrodynamic and acoustic cavitation are widely used in laboratories. Acoustic method of producing cavitation was selected over the other due to the following advantages:

- Higher erosion rate in a short duration of time. Six hours of testing is typically enough for an experiment.
- Smaller rig size – simple, easy control and maintenance.
- Low power consumption.

Disadvantages of this method are that this is a poor reproduction of cavitation in actual hydraulic machines and it's noisy. The main objective of this erosion testing is to study the erosive wear mechanism of silicon nitride. Also the material damage resulting from this type of cavitation is believed to be similar to other methods. An acoustic enclosure was made to cut down the level of noise to avoid any health hazard.

2.2.1. Vibratory Cavitation:

The principle of this method is applying high intensity ultrasound to liquid to create cavitation. This test method generally utilizes a magnetostrictive transducer submerged in the liquid which vibrates at high frequency. This method of generating cavitation was first developed by Gaines in 1932 using a length wise resonant nickel tube. Advancements in this technique came following the use of piezoelectric crystals for vibration. A first standard vibratory cavitation apparatus was developed at the National Engineering Laboratory, UK in 1963. Since then several adoptions to this standard were followed. For engineers and researchers, a systematic approach of performing cavitation experiments is described in ASTM international standard (ASTM 2006). The testing methodology used for this project follows this standard and is described in the following sections.

In a stagnant liquid, pressure is varied by applying sound waves. When the pressure difference is high enough to reach or go below the vapour pressure of the liquid, available nuclei in the liquid will grow into cavities and thus creating cavitation. These cavities are set in motion due to varying flow field, the intensity of growth and collapse of these cavities is directly proportional to the applied pressure changes to the liquid. If the pressure difference is high in a short duration of time by a sinusoidal motion, very high compressibility is achieved. This motion sends in huge potential energy in the negative cycle which then transfers into kinetic energy during collapse. Any substance - solid, liquid or gas present near this collapsing region undergo very high pressure and temperature cycles eventually causing erosion. Main components of a typical vibratory

cavitation are listed below. One commercially available ultrasonic system was used for this project (sonic systems 2005). The main components of the test rig are:

- Ultrasonic generator
- Piezoelectric Transducer
- Titanium alloy Horn
- Cavitation medium
- Cooling system.

2.2.1.1 Apparatus:

The piezoelectric transducer is excited by an ultrasonic generator. The vibration generated by the transducer is sufficient to cause cavitation in the liquid, but is not enough to create sufficient power density in the liquid to cause erosion. Hence a resonant element in the compressor mode, called Horn is fastened to the transducer in order to magnify this vibration. This horn is made of Titanium alloy to achieve the following characteristics:

- High dynamic fatigue strength
- Low acoustic loss
- Resistance to cavitation erosion
- Chemical inertness.

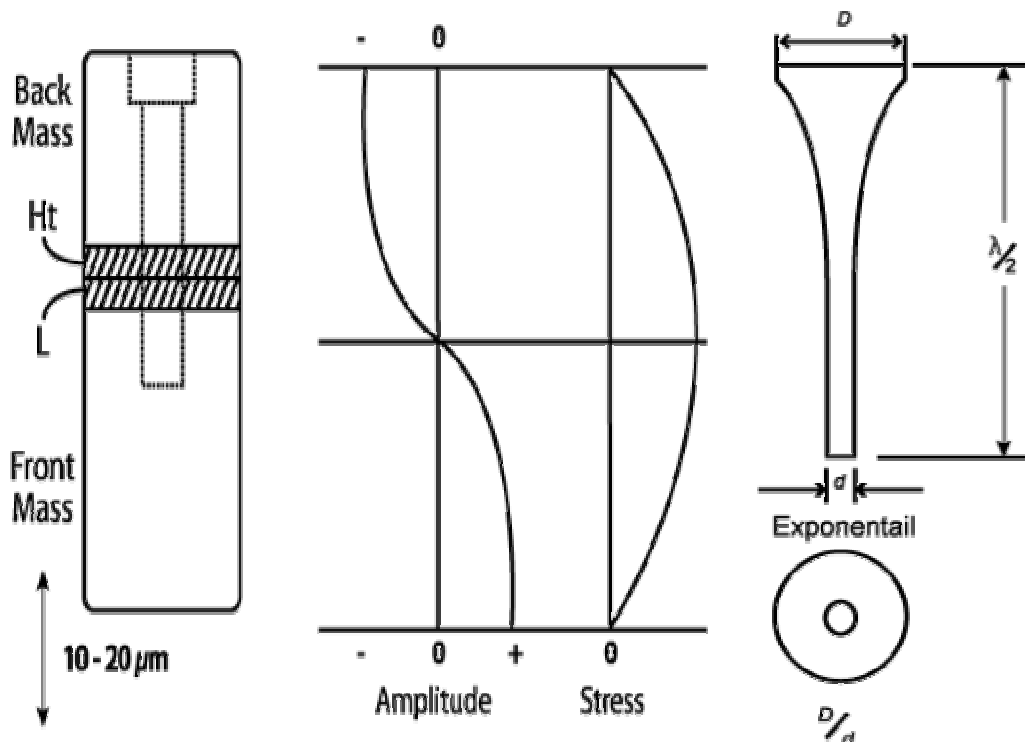


Fig: 2.6. Pre-stressed sandwich transducer - picture reproduced from Equipment supplier for this project (sonic systems, 2005).

This ultrasonic system is constructed to generate high power density in the liquid load. Polarised PZT (Lead Zirconate Titanate) ceramics are sandwiched normally to low acoustic loss materials such as titanium and aluminium as shown in Figure 2.6. Upon electrically exciting the PZT ceramics, an alternating sinusoidal motion is achieved. The key factor which determines the efficiency of vibration is resonance. So the rod, which is a metal sandwiched with PZT ceramics must be designed in such a way that the required mode shape is achieved upon electrical load. Any frequency deviation in the input load to the transducer will result in useless motion. An ultrasonic generator gives output electrical signals of 20 KHz fixed frequency. Another important component as previously mentioned is the horn. This is same as the transducer but the main difference is the shape. This can be made as a cylinder, exponential or linear. Horn is designed to have a half wavelength $\lambda/2$ of the whole transducer assembly as shown in Figure 2.6. Dimensions of this assembly are totally determined by the operating frequency requirements.

All the test parameters were continuously monitored whilst testing. Two different transducer-horn assemblies were used for this project mainly to have low and high power densities in the liquid load. The magnitudes of vibration of low and high power transducer are 0 to 16 and 0 to 60 microns peak to peak respectively. This vibration of the horn while testing can also be observed with a help of a microscope. Both amplitude of vibration and electric power are digitally displayed in the equipment and hence providing the user to control these as required. The level of power density to the load is determined by a term called acoustic power which varies with the type of liquid and the depth of transducer immersion. This can be calculated using the relation:

$$P_{ac} = \frac{1}{2} \rho c a^2$$

Where,

P_{ac} - Acoustic power

ρ - Density of load

c - Sound velocity in the load

a - Amplitude of transducer/Horn vibration.

2.2.1.2. Experimental Setup

The ultrasonic system used in the project was fully calibrated before used for experiments. A 5 litre cylindrical glass container with the test liquid was used as the cavitating medium. For vibratory cavitation erosion testing, a known mass of specimen is usually made in a form of button, which then can be threaded into the horn, or as a disc which can be cemented. When transducer is excited, the threaded or cemented specimen vibrates with the horn and is subjected to cavitation attack which results in erosion. But here, due to difficulties in machining silicon nitride, it was decided to keep it stationary rather coupling it with the horn. The experimental setup is shown in Figure 2.7. A stainless steel cylinder was manufactured to hold the specimen in the test liquid from a distance beneath the transducer. A sketch of this specimen holder is provided in appendix C. Stainless steel was selected as material mainly because of its superior resistance to

cavitation erosion (Chen 2002). Use of balls instead of flat specimens offer advantages like commercially available with good quality, the geometry allow investigating different stages of erosion in a single test step due to the variation in the fluid thickness.

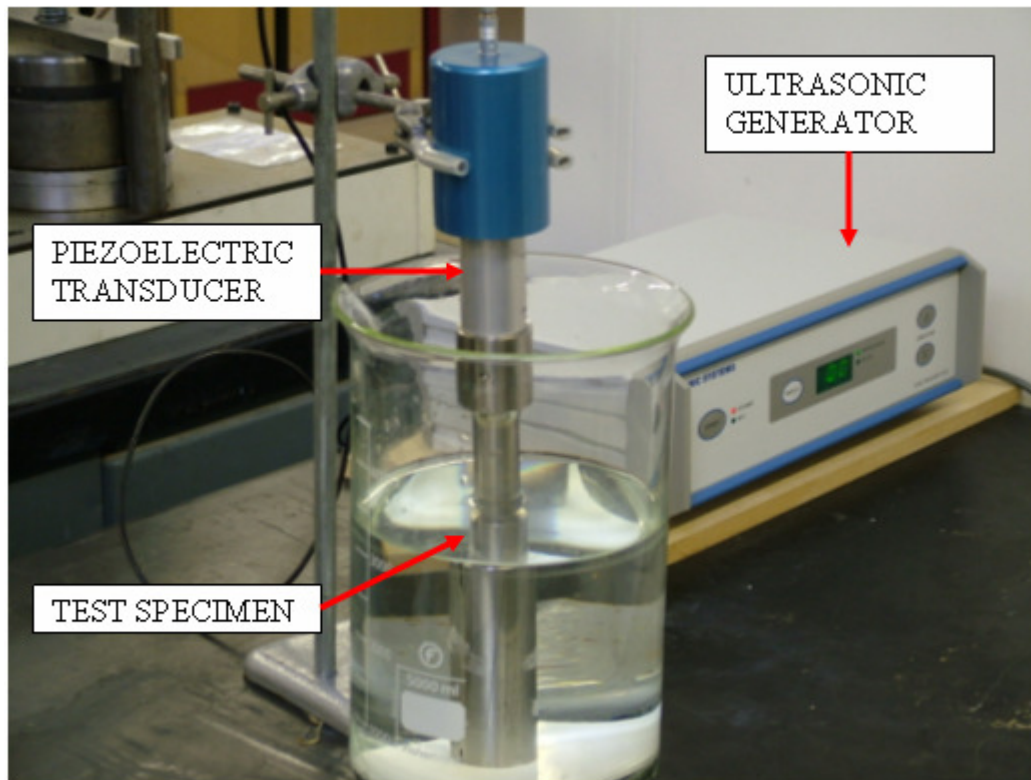


Fig: 2.7 Cavitation Erosion experiment setup

Locking and unlocking of the specimen were made easy by providing a couple of slots on either side of the holder. Two holes of diameter $\text{\O} 12.6$ and $\text{\O} 25.4$ mm were made on both ends to have a flexibility to hold specimens of these two diameters. The test specimen fixed in the holder was immersed in the liquid. The level of liquid in the container was filled to have sufficient liquid for cavitation. The depth of specimen immersion was varied as per the acoustic power requirement depending on the liquid load. This was 15 mm for distilled water to full rated power of the ultrasonic system. The deeper the transducer was immersed the higher the load and hence less power was supplied to the transducer which resulted in low intensity of cavitation. The transducer was firmly held by a laboratory stand just above the specimen. The distance between the horn tip and the specimen is critical as it influence the rate of erosion. This distance was

set using a feeler gauge and was kept constant for all tests. This distance influence on the erosion rate was also studied in this project and the results are produced in section 3.7.3.

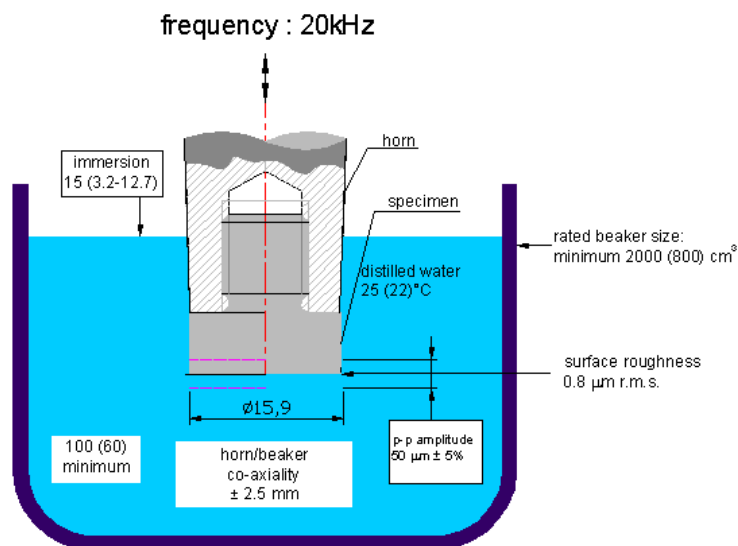


Fig 2.8 Schematic of test set up as described in ASTM (ASTM G-32-06)

The piezoelectric transducer was connected to the ultrasonic generator after setting up the required distance from the test specimen. Temperature has an influence on cavitation erosion (Auref 1993) and was kept constant. This was achieved by circulating water around the test setup. A large tank was kept above the test bench to supply water by gravity. A pump was connected to the water bath to pump back the water to the tank. A thermocouple connected to the test liquid helped to monitor the temperature continuously. An acoustic enclosure was built to cut-down the noise generated by testing. All tests were timed and were run for the required time interval. This was achieved by a timer connected to the ultrasonic generator which automatically turns on and off the power supply to the transducer according to the timing program.

2.2.1.3. Test Procedure:

Several factors can affect the rate of cavitation erosion. For example, presence of any debris or gas content largely affects the formation and collapse of cavities. Hence, a strict procedure was followed for this testing and is described as follows:

- The cylindrical liquid container was cleaned and dried before and after each test intervals to avoid presence of any impurities.
- Clean distilled water was poured in to the container to have sufficient level for generating cavitation.
- The transducer-horn setup was fixed in a stand to have 15 mm immersed in the test liquid.
- Ultrasonic generator was connected to this setup and then to corresponding power connections.
- The magnitude of vibration was gradually increased from 0 to the maximum and this initial run was carried on for approximately 20 minutes to clear away any gas content in the test liquid.
- Test specimens, mostly silicon nitride balls were visually inspected under the optical microscope for any defects. Specimens with pre-existing defects were not considered for testing
- Specimens were fixed in the cleaned and dried specimen holder and were then moved to the liquid container.
- The piezoelectric transducer-horn set up was fixed to the required distance from the specimen using a feeler gauge.
- Circulating water for cooling was turned on and a thermocouple was connected to the test liquid.
- Required test interval was set using the timer and the ultrasonic generator was turned on. Acoustic power and the magnitude of vibration were adjusted to the requirement.
- Once the test was over, the system was turned off and the test specimens were carefully removed from the holder

- Test samples were cleaned in an ultrasonic bath with acetone for 15 minutes, and dried with a blower before set for surface analysis.
- Test liquid was replaced after every 2 to 4 hrs to clean away any debris, if left unchanged, the debris resulted in the previous test interval will cause abrasive wear which would mislead the result interpretation.

2.3. Rolling Contact Fatigue Experiments:

Rolling contact bearings with balls or rollers undergo surface damage due to repeated loading, termed as rolling contact fatigue. This application of stresses initiates cracks, which eventually grow resulting in bearing failure. There are several factors which influence the rolling contact life such as loading conditions, lubrication, surface contacts, materials, and surface defects. Therefore, rolling contact testing becomes necessary to estimate the actual performance of rolling elements. There are different types of rolling contact fatigue testing available as discussed in section 1.3.2. An available four-ball machine was modified to allow testing hybrid rolling elements was used for this project (Wang 2000, 2002, Zhao 2006, 2007, Khan 2006).

2.3.1. Rotary Tribometer:

The four-ball machine used for this project is a TE92 Microprocessor Controlled Rotary Tribometer and shown in Figure 2.9 Main components of the Tribometer are the test chamber, the loading piston, the drive spindle and related bearings which are lubricated with grease for life. Advanced control and instrumentation in this machine makes it possible to conduct tests in a wide range of speeds and loads. The microcontroller interface of the machine is connected via a serial port to a computer. The test chamber consists of a steel cup, oil bath, lower balls, and an upper ball for applying load and transferring motion effectively as shown in Figure 2.9. The cup, lower three balls and the upper ball represents the outer, rolling elements and inner race of a bearing respectively. This test chamber simulates an angular contact ball bearing configuration. This test

machine is very useful for rolling contact fatigue study of materials under different conditions (Wang 2000).



Fig: 2.9. Rolling contact fatigue test facility.

The upper ball is fixed to a drive spindle and its accurate positing is achieved by two rigid vertical columns of the machine. Load is applied by a pneumatic actuator; this actuator assembly includes an in-line force transducer to get the direct feedback control. Direct friction and torque measurements are also possible by a strain gauge transducer attached to the test adapters, which are mounted on a cross beam, guided by linear bearings on the machine columns. Tests can be conducted at high temperatures up to 200 °C which is continuously monitored by a thermocouple attached to the test chamber. Also a sensor is employed to monitor and stop the machine if the vibration exceeds the testing limit. A computer connected to the machine, provides a graphical user interface to run,

control and record tests. This allow user to run tests for the required number of stress cycles, speed and load. A test is a set of series of steps, each with load, speed and temperature, data recording and alarm information.

2.3.1.1. Contact stress calculations:

Figure 2.10 below shows the loading configuration in the test chamber. The load applied to the shaft is related to the contact stress of the rolling elements and can be deducted from Hertz elastic contact stress formulae as below:

$$\text{Contact load } P = \frac{L}{3 \cos \theta}$$

Where,

P = Contact load

L = Applied shaft load

θ = Contact angle, which is 35.3 degrees

$$\text{Mean radius } R = \left[\frac{1}{R_1} + \frac{1}{R_2} \right]^{-1}$$

Where, R_1 and R_2 is the radius of ceramic and steel balls.

$$\text{Young's Modulus } E^* = \left[\frac{1-\nu_1^2}{E_1} + \frac{1-\nu_2^2}{E_2} \right]^{-1}$$

Where, $E_{1,2}$ and $\nu_{1,2}$ are the young's modulus and Poisson's ratio of ceramic and steel balls.

$$\text{Radius of the contact path } a = \left[\frac{3PR}{4E^*} \right]^{\frac{1}{3}}$$

From the above relation, maximum contact pressure P_o can be obtained as follows:

$$P_o = \left[\frac{3P}{2\pi a^2} \right]$$

$$= \left[\frac{6PE^{*2}}{\pi^3 R^2} \right]^{\frac{1}{3}}$$

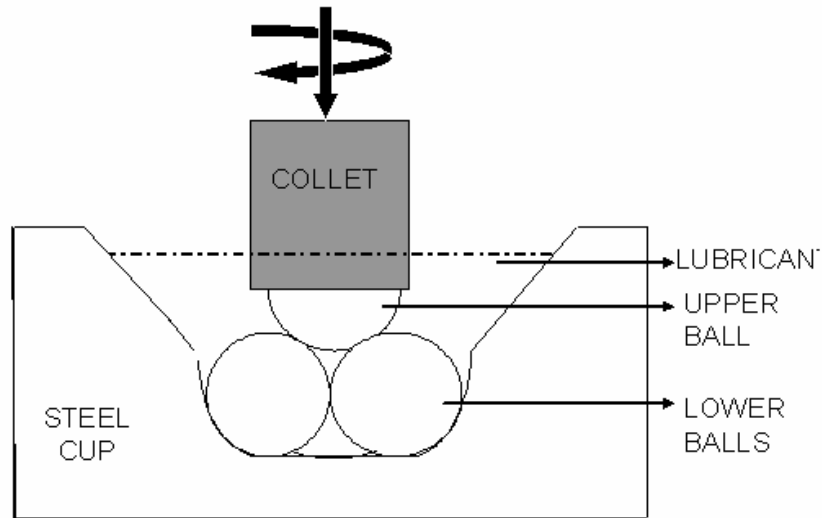


Fig: 2.10. Loading configuration of the rotary Tribometer.

A spreadsheet with the above calculations was created to conduct tests for the required contact stress. These detailed calculated values of different contacts are given in appendix C.

2.3.1.2 Defect Positing:

Smooth specimens could run for months without any failure and it becomes advantageous to shorten the tests by creating surface defects like indents and cracks. Accurate positioning of the specimens is critical and necessary to achieve this task. Also, the location and orientation of the defect play a vital role in the failure mechanism. When

specimens are inserted in the test chamber, the probability for a defect to be in contact can be determined by

$$p = \frac{A}{A_0}$$

Where, p is the probability of the contact, and A is the area of the contact path which is given by

$$A = 4\pi a R_1 \sin \theta$$

Here, a is the contact radius, R_1 is the radius of the ceramic ball, θ is the contact angle 35.5° . Area of the ball surface is given by

$$A_0 = 4\pi R_1^2$$

Substituting the values for $R_1 = 6.35$ mm, $a = 0.21$ mm, and $\theta = 35.3^\circ$, we get the probability of the defect to be in contact p to be 0.02, which is merely 2%. The test specimen can be fixed at the right distance x by using the below relation.

$$x = R_1 - (R_1 - \cos \theta)$$

This gives us the value for $x = 1.17$ mm to the centre of the contact path from the tip of the specimen as held in the collet. A novel method was developed by Ying Wang (Wang 1999) to position surface defects on the contact path. This method was used for the testing performed as part of this project.

2.3.1.3. Test Procedure:

The following procedure was followed for rolling contact fatigue testing:

- Test specimens were visually inspected using an optical microscope to locate the surface defect.

- Surface defect was positioned using the above mentioned method and the collet was fixed to the Tribometer.
- The test chamber - steel cup and the holder were cleaned with acetone before fixing it to the machine.
- Lower balls, either ceramic or steel were placed in the steel cup. Lubricant was then poured until these lower balls were completely immersed.
- Vibration sensitivity was adjusted and set for the relevant readings.
- A safety cover was used to cover the machine.
- Test program software installed in the computer was used to create the required test parameters such as speed and load.
- Tests varied from few hours to few days depending on the testing conditions. Failure observations were performed in between tests by removing the collet and performing surface analysis using an optical microscope.
- Once the test was completed, the specimen was removed from the collet and set for surface analysis.
- Test results were stored in the computer. The test chamber was removed and the lubricant was disposed as per the safety disposals.
- The steel cup was once again visually inspected for any damage, and was replaced for future testing, if necessary.

2.4. Surface Analysis:

Test specimens were investigated for failure mechanisms by comprehensive examination on specimen surfaces. Advanced surface analysis techniques like scanning electron microscopy and 3-dimensional non contact profiling was used for this purpose. Energy dispersive X-ray analysis coupled with Scanning electron microscope is a powerful for element and chemical analysis which was also utilized for this work. Unlike metals, ceramics are strongly dependent on the composition and microstructure for providing high performance. This microstructure examination is mandatory to conclude any relation between materials and its performance. The microstructure influence of silicon nitride on cavitation erosion resistance was investigated by imaging the eroded microstructure. A

high magnification microscopy alone is not necessary for this task. Initial sample preparation is required to visualize the grain structure and the damage at grain level. This was achieved by etching the eroded sample using plasma etcher. All the surface analysis tools and methods followed for this project is briefly described in the following sections.

2.4.1. Optical Microscopy:

For a quick and preliminary study of test samples an optical microscope was used. This is a simple microscope employed for material study in the laboratory, which uses visible light and a collection of interacting lens to magnify samples. A commercially available system was utilized for this project shown in Figure 2.11. Apart from the traditional system of eyepiece, specimen stand and lens, this microscopy is equipped with a CCD camera which makes it possible to visualize the specimen surface live on a computer screen.

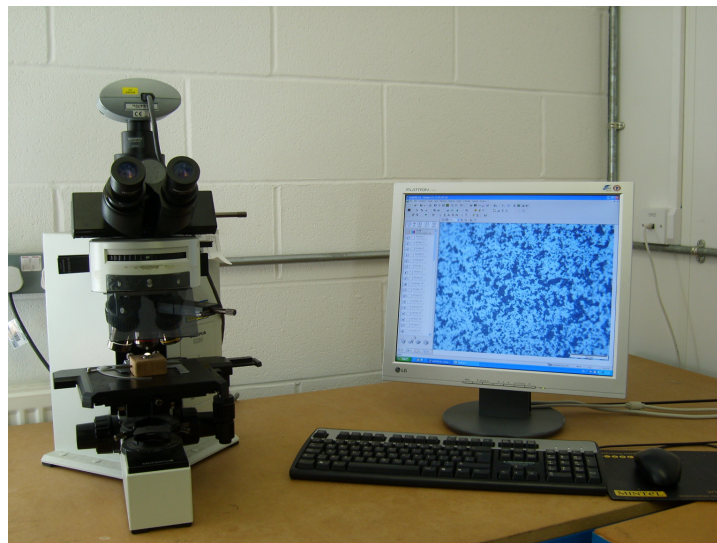


Fig 2.11 Optical Microscopy

The purpose of the specimen stage in the microscope is to support specimens, but it's impossible to support rolling elements in this stage. A manipulator to support and rotate the specimen for easy visualization of the full ball surface was required. A wooden

manipulator was manufactured in the workshop, pictures of this manipulator are provided in appendix C. Magnifications in the order of 5X, 10X, 20X, 50X and 100X are possible in this system. Operating procedure to obtain images of material surface includes the following:

- Turn on power and secure the manipulator with the clamp in the specimen stage.
- Choose the required light field from the available options bright field, dark field or Ultraviolet field.
- Adjust the phase contrast and light intensity as required. Align the manipulator to position the location of interest within specimen.
- Material surface visualized in the computer screen can be used to identify and locate any material defect of user interest by shifting in between various magnifications.
- A built-in software of this microscope help to analyze the surface details like length, area and angle measurements.

Images of the material surface can then be stored in the computer or printed off using the printer connected to the system. Below Figure 2.12 shows an example of images obtained using this microscopy.

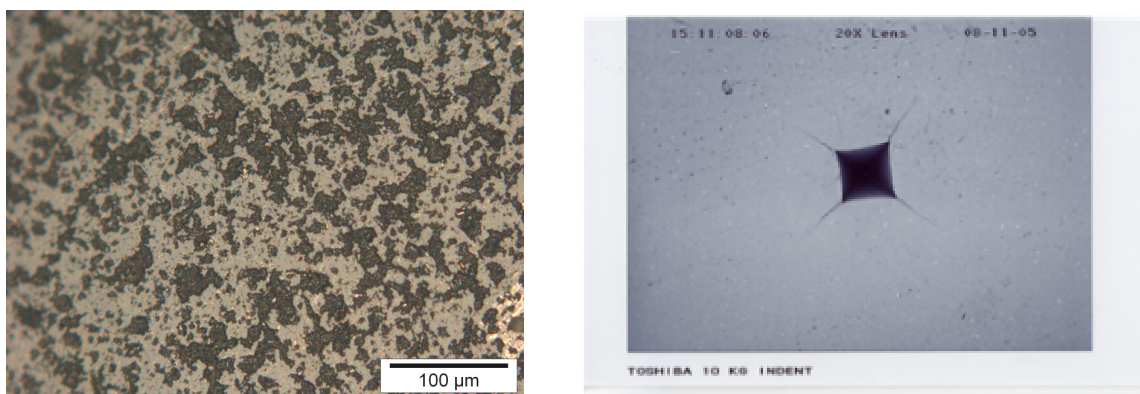


Fig. 2.12 Magnified surface Images using Optical Microscope.

2.4.2. Scanning Electron Microscopy:

An optical microscopy is not sufficient to prevail with high quality microstructure images and to obtain chemical composition of sample materials. Scanning electron microscope is widely used for this task and is one of the most versatile instruments for these investigations. The major difference in the operating principle of a SEM and OM is that the SEM uses electron instead of light to form an image. Fundamental systems of a typical scanning electron microscope are: an electrical optical column, signal detection and display equipment, and a vacuum system. Electrons are generated in the electron gun, which consists of a tungsten filament which when electrically excited produces heat, light and electrons. This high energy beam of electrons passes through series of deflecting plates in the optical column to hit the sample. Upon collision, low energy secondary electrons are emitted by the sample which then can be easily collected using an electron detector. These collected electrons are then used to generate the image. Thus the quality of surface image largely depends on these low energy secondary electrons.

Silicon Nitride is a poor conductor of electricity. If a sample of this material is used in SEM, it would result in charge build up in the sample, which will affect both the primary and secondary electrons and thus resulting in a very poor and distorted image. In order to avoid this, non-conductive samples set for SEM study are recommended to coat it with a conductive material. These silicon nitride balls were coated with a thin layer of gold in a sputter coater. Silicon nitride balls were fixed in a metal stud with a conductive adhesive, a silver paint was applied to the top of the ball connecting the metal stud to increase conductivity. This is then placed in the vacuum chamber of sputter coater beneath gold. Vacuum in the order of 0.1 millibar is achieved for a good coating. Argon is introduced into the chamber after 20 seconds along with voltage across gold and silicon nitride. This applied voltage produces argon ions which bombard and remove atoms of gold which then stick to the silicon nitride ball placed beneath it. The time of deposition was selected by experience and found that excellent film thickness is achieved for 5 minutes coating. Figure 2.13 (a) and (b) show images obtained in SEM.

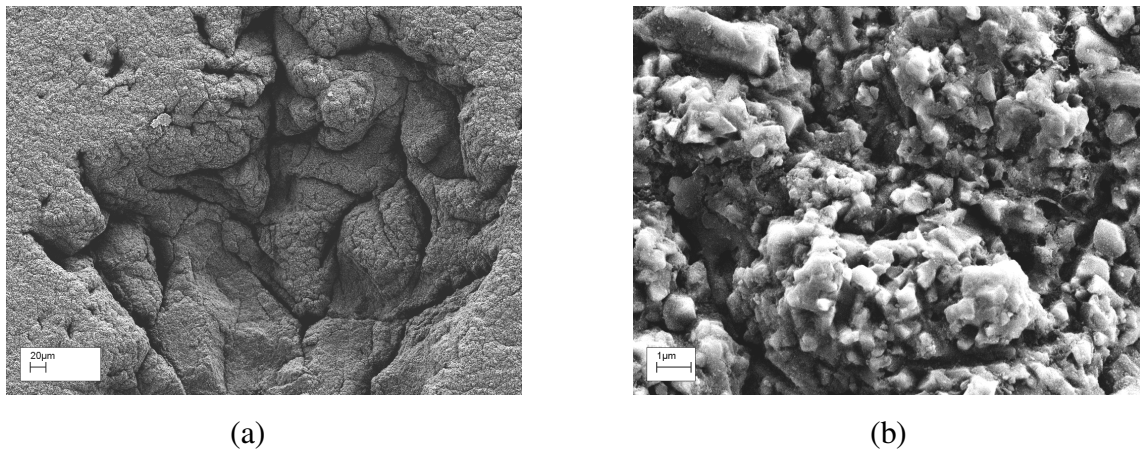


Fig: 2.13 (a) and (b) Scanning Electron Images of silicon nitride balls

The other main requirements of sample preparation are - it should be dry, free from water, any solvents and dirt to maintain a good vacuum level in the specimen chamber. The stud used to fix silicon nitride balls showed excellent mechanical stability which is another requirement to avoid any specimen movement whilst imaging. Before investigating samples in SEM, they were analyzed in optical microscope and were marked on the areas of interest. The SEM user chooses the operating conditions that suit his/her specimen. For this silicon nitride specimen, we found the following conditions resulted in good imaging. For specimens with and without plasma coating (1) a working distance (WD) of 5 to 10mm and 15 to 20 mm - that is the distance between the specimen and the sample (2) accelerated voltage in between 1 to 4 Kv and 10 to 20 Kv.

Apart from imaging, SEM was also used for EDX (Energy Dispersive X-ray) analysis. This is normally done for element analysis. A chemical composition study on erosion samples were conducted to understand how different sintering additives or any other elements used in final preparation of silicon nitride balls influence erosion. A point analysis was performed for this task, this is an analysis type which selects the point of interest in the image and proceeds for EDX analysis. Figure 2.14 shows an energy dispersive spectrum taken on two points of an eroded sample.

Label A: dark pits

Label B: turned out area next to pit

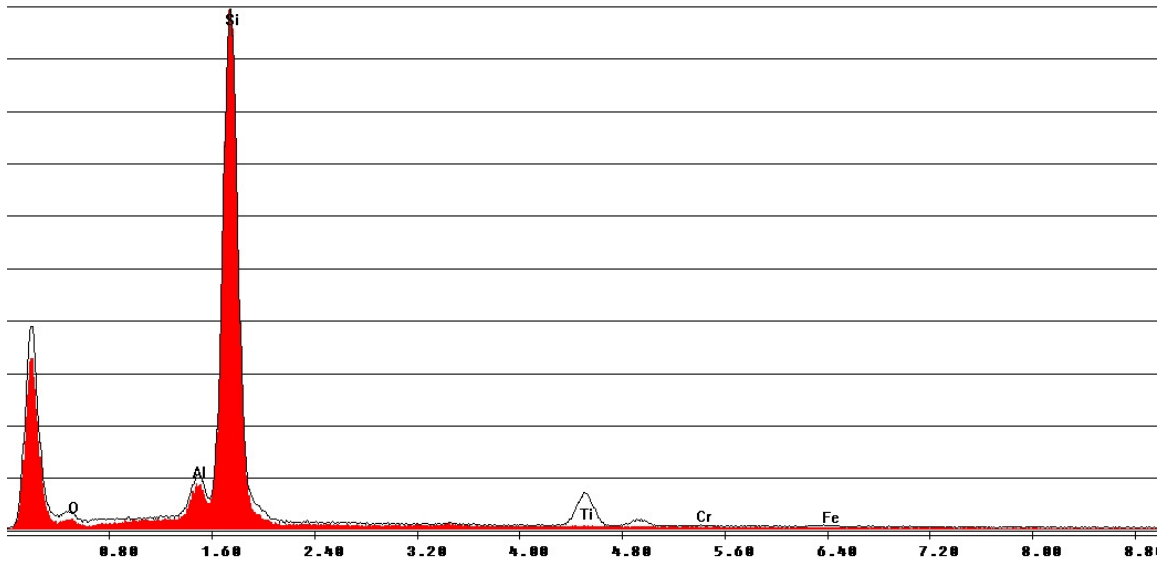


Fig 2.14 EDX Spectrum of point analysis

2.4.3. 3D Surface Optical Profiling and Measurement System:

Erosion results in severe mechanical degradation of materials. Understanding the surface changes for each test intervals is necessary. A 3-D surface mapping non-contact optical profiler was used to accurately measure the surface roughness, depth of cavitation pits, step heights, angle measurements, and volume loss. This system is based on the principle of white light scanning interferometry, and is capable of mapping ten millimetres wide area in a single measurement with sub-nanometre resolution, providing instantaneous information about surface roughness, shape and waviness. When larger areas need to be measured, a stitching procedure can be employed, in which a number of partially overlapping measurements are combined into one surface profile. This device splits a beam of light into two separate beams and then recombines them to create bright and dark bands called fringes that make up the interferogram. This interferogram carries a wealth of information about the profile of an object under test and its material characteristics. A CCD detector registers this information and forwards it to the computer. A picture of this system is shown in Figure 2.15

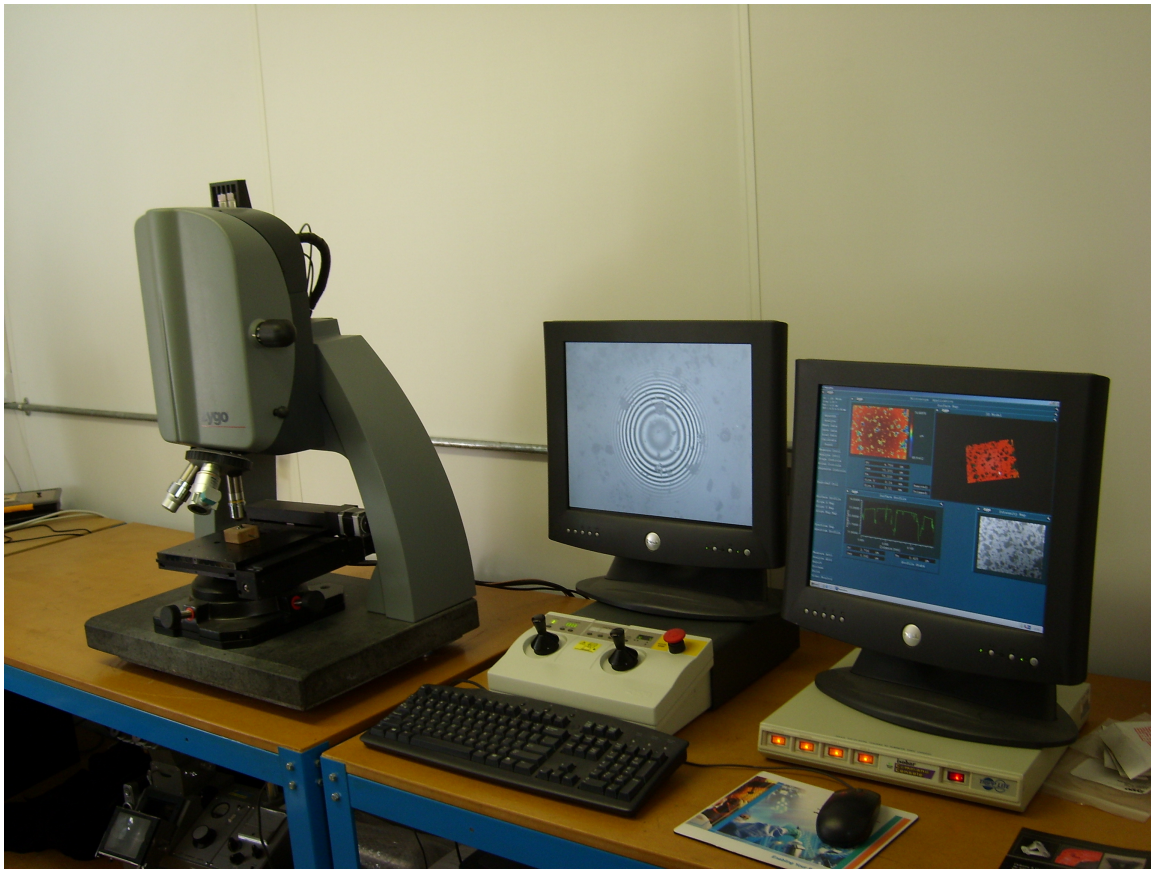


Fig: 2.15 3D Optical Profilometer

For taking measurements, sample is set in the manipulator as followed for optical microscope. Light focus is adjusted from coarse focus to fine focus by adjusting the instrument head to bring the sample into focus. At the best focus level fringes appear at their clearest and sharpest contrast. Light intensity is another important parameter and must be selected to the maximum brightness. The specimen stand can be tilted as per the specimen requirements. Sphere specimens like the silicon nitride balls are difficult to measure compared to flat specimens, so much care was taken during these measurements. Huge depth variations or higher peak to depth value specimens are impossible to obtain precise surface data in a single measurement. In this case, the area of interest was divided into several sections and measurements were carried out on those sections which were then stitched together. This option provides complete surface

of these type of damage. Below Figure 2.16 show a typical result obtained using this measurement system.

Surface Stats:

Ra: 671.25 nm

Rq: 843.38 nm

Rt: 7.37 μm **Measurement Info:**

Magnification: 1.00

Measurement Mode: PS

Sampling: 454.87 nm

Array Size: 640 X 480

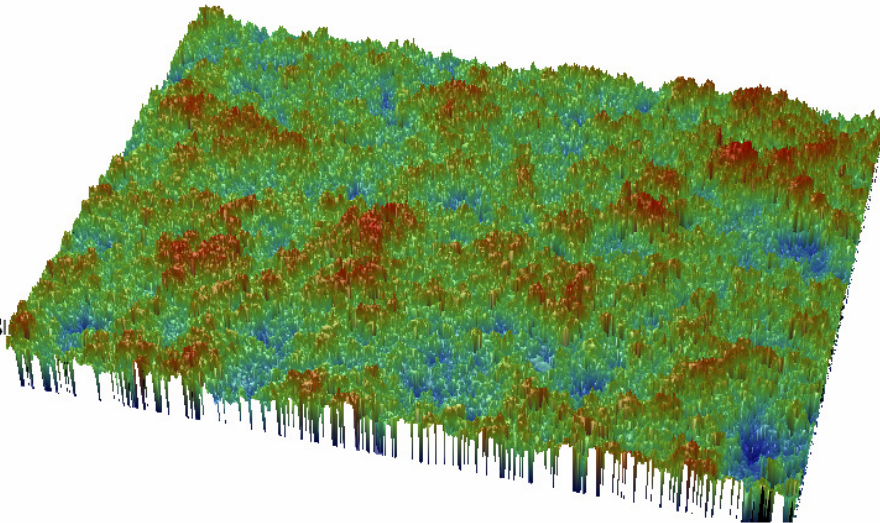


Fig: 2.16 3D Interactive surface display

Chapter 3

EROSIVE WEAR: THE MECHANISM OF MECHANICAL DEGRADATION

All Erosion results obtained in the laboratory using vibratory cavitation method are presented in this chapter. Cavitation erosion is a complex material failure mechanism and is often difficult to assess the material resistance. This is mainly due to different testing methods and approaches followed to evaluate materials. Cavitation erosion phenomenon is two fold: one deals with the fluid mechanics and the other with material science. Two phase flow involving bubble nucleation, growth and collapse constitutes the fluid mechanics part as presented in chapter 4. The material response to this cyclic pressure loading is presented in this chapter. Evaluation of different materials to cavitation is out of scope of this work as this work is aimed to understand the mechanism of cavitation erosion in silicon nitride. Test parameters were kept constant for all experiments and where necessary their influence was examined. Mechanical properties, microstructure, and sintering additives are the key factors which determine the material resistance to cavitation and are detailed in this chapter. Section 3.1 explain how erosion initiates in silicon nitride through an advanced micro structural and metallographic analysis, followed by the advancement of erosion due to continued cavitation exposure as presented in sections 3.2, 3.3 and 3.4. The effect of material surface and the testing conditions were also investigated and are detailed in sections 3.6 and 3.7. Finally, erosive nature in bearing steel is presented as a comparison to silicon nitride.

3.1. Erosion Initiation:

During the initial stages of this work, the response of silicon nitride to cavitation was unclear. Several trials were made to understand the vibratory cavitation testing equipment and methodology, and frequent microscopic examination on test samples helped acquire a first hand understanding on this process. Erosion investigators often point out the stage where notable material mass loss can be measured as erosion

initiation. But, this work addresses the initial microstructure changes in the test sample as the beginning stage of erosion. In order to understand this microstructure changes a ceramographic etching, precisely a plasma etching technique was used to achieve the surface quality required to study under scanning electron microscope. This method allowed monitoring erosion damage at micro structural level on grains and grain boundaries.

As mentioned early, test materials used for this study are commercial bearing rolling elements named here as A, B & C and their properties are listed in Table 2.1. These test samples are polished to submicron accuracy. Generally, any free surface is rough at atomic level which acts as local stress raisers causing bond rupture (Suresh 1998). This atomic scale study is out of the scope of this work and was not investigated. Whereas, pores and similar surface defects at microscopic level was considered. All test samples went through a surface analysis to ensure that they were free from any surface defects prior to testing. No signs of erosion were noted during very initial stages of testing. Also, the cavitation intensity has a major influence on the rate of erosion process. Under certain level of cavitation intensity in the test liquid, a stable cavitation was observed. This type of cavitation is defined by a permanent oscillation of bubbles or cavities without collapsing. This part is detailed in section 3.7.1. Erosion initiated just after this threshold cavitation intensity.

During the very initial stages, the impact energy released during cavity collapse on the surface is absorbed without any deformation. This characteristic of energy absorption without material removal or damage is directly related to the resistance of materials to cavitation. Determining the exact period of this stage largely depend on the investigator and should not be considered for ranking materials unless a similar approach and testing conditions are followed. Brittle materials with strong covalent bond such as silicon nitride are characterized with less point defect mobility and dislocation as opposed in the case of metals. This is the reason why brittle materials could not withstand cavitation as compared to metals. The initiation of erosion varied with the low and high powered ultrasonic transducer. The erosion initiation in silicon nitride was found to be a combination of two damage mechanisms. Formation of inter and transgranular fractures which are detailed in the following sections.

3.1.1. Transgranular Fracture

This type of fracture is defined by crack formation and progression through grains. Material B and C showed clear signs of transgranular fracture as part of the erosion initiation, whereas there were no signs of this type of fracture in material A during this initial stage. Material B after testing with high powered transducer for just three minutes showed grain fracture as shown in Figure 3.1. Several numbers of grains were fractured at this stage. These grains were approximately twice or three times larger than the average grain size. Smaller grains were not affected at this stage and remained same as in the fresh samples. Initiated fracture micro crack propagated by cutting through the large grains. These fractured grains also showed their boundaries were ruptured in later stages.

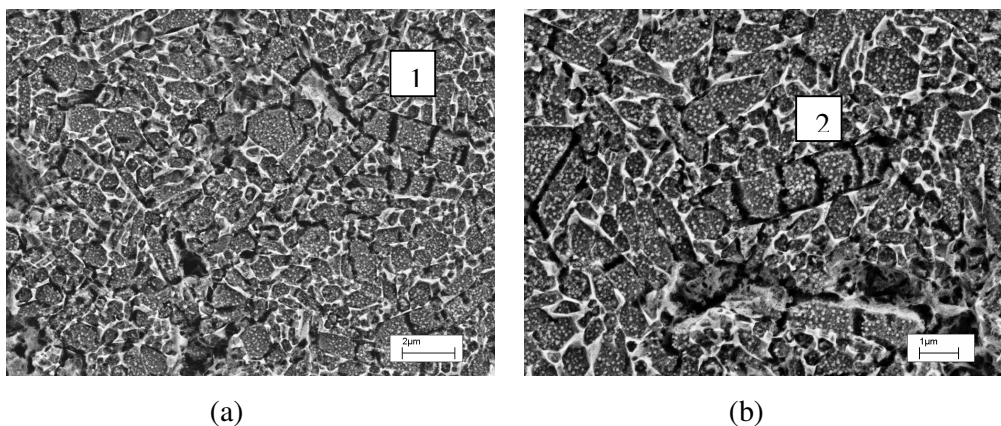


Fig: 3.1 (a) and (b) Material B showing Transgranular fracture after 3 minutes of erosion testing

Silicon nitride being a strong covalent bonded material undergoes very little plastic deformation. The only way to relieve the imposed stress due to cyclic cavity collapse is by nucleating cracks which is responsible for this irreversible microscopic deformation. The intensity of the cavity collapse must be very high to crack a grain, but at this stage it did not seem to be enough to fracture smaller grains. In material C as shown in Figure 3.2 coarse and elongated grains are the ones which fracture during this stage. The finer grains showed excellent resistance. As marked as 1 and 2 in the Figure 3.2 show an elongated grain been sliced off, clearly showing transgranular fracture.

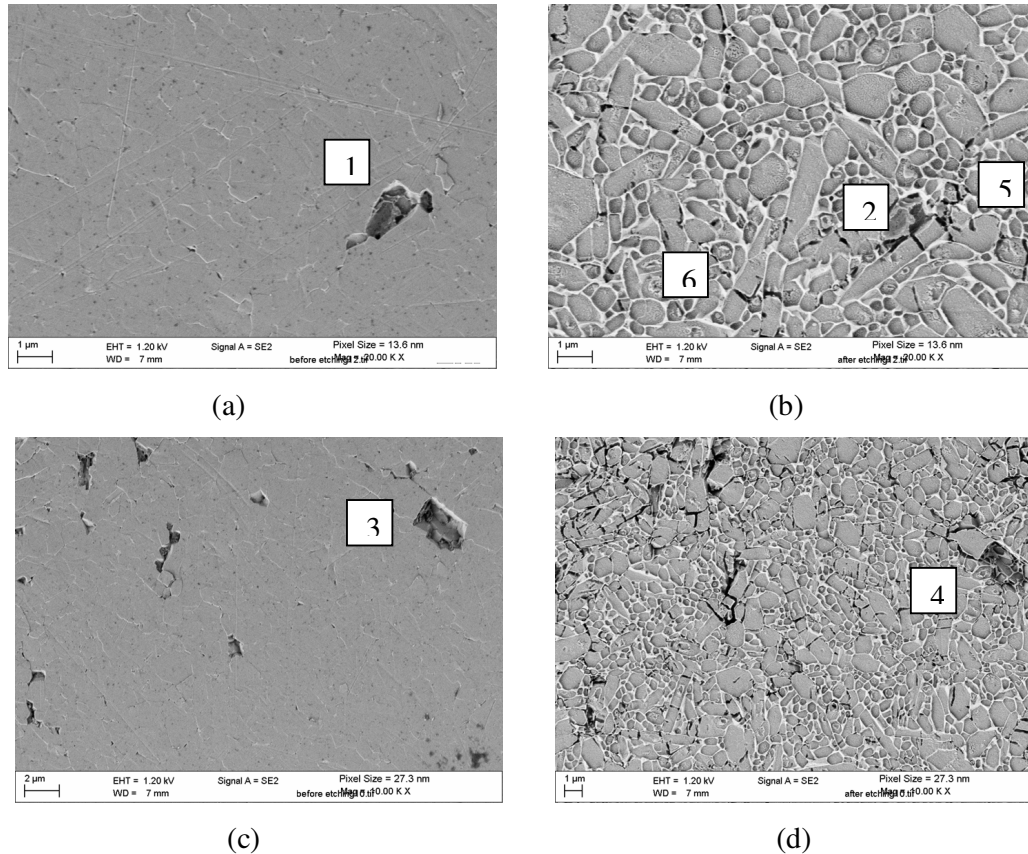


Fig: 3.2 (a) Before etched SEM image of material C showing Transgranular fracture after 10 minutes and (b) after etching (c) Before etched SEM image of material C showing fractured grain after 10 minutes and (d) after etching

Figures 3.2 (c) and (d) show half of coarse grain displaced which constitutes that the transgranular fracture did not propagate further in to the grain boundary or to the adjacent grain. This displacement of half grain can be justified by the presence of very fine surrounding grains as marked as number 4 in Figure 3.2 (d). This clarifies that very fine microstructure in silicon nitride can provide high resistance to cavitation especially to grain fracture compared to the microstructure with coarse and elongated grains. The marked areas near numbers 5 and 6 show fracture crack propagating to the adjacent grains. At number 5, two large elongated grains share a common boundary and the fracture initiated and propagated through to the other. Whereas, near the marked number 6 a fine non-elongated grain between the two large elongated grains resist fracturing.

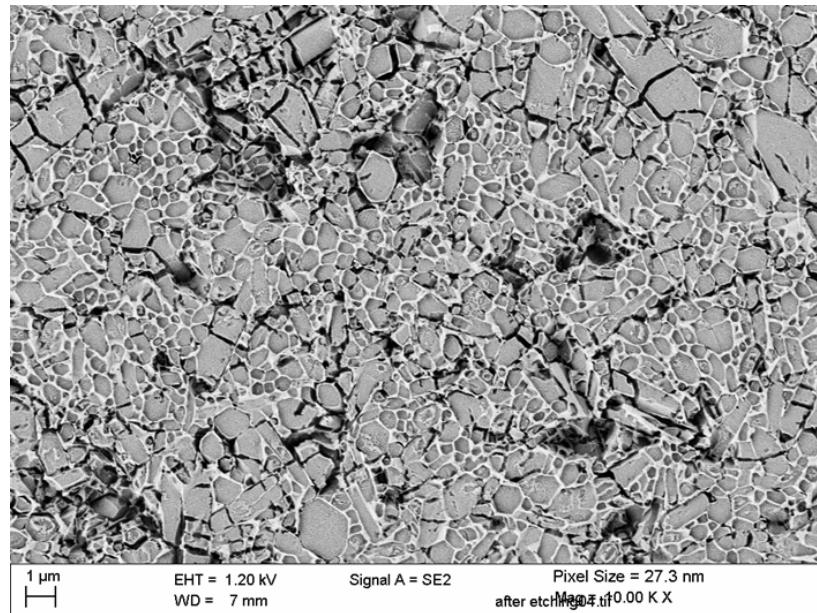


Fig: 3.3 Material B showing advanced stages of Transgranular fracture after 10 minutes of testing

Due to the spherical shape of the test materials, several stages of erosion can be seen after each test interval. The above scanning electron microscope image in Figure 3.3 shows the advanced stage of transgranular fracture. As shown in the Figure only larger grains were fractured and the area with group of smaller grains did not show much damage. Displacement of grains can also be noted which is responsible for cavitation pit formation and also pores which is detailed in the following sections.

3.1.2. Intergranular Fracture

Materials B and C showed enormous transgranular fracture during the initial stages of erosion. But material A with very fine needle like grains act as reinforcement preventing grain fracture. However, formation of fracture at the grain boundaries is unavoidable in all materials. These fracture occurred at the grain boundaries as shown in Figure 3.4. The areas marked by an arrow show few pores or tiny holes. Fracture at the grain boundaries disrupt the grain bonding strength and thus leave grains loosened created a gap between the adjacent grains. Pore or fracture at the grain boundary junction is a micro void formation could be due to diffusion, which is driven by stress

gradient developed due to the variation in the thermal expansion coefficient at the boundary.

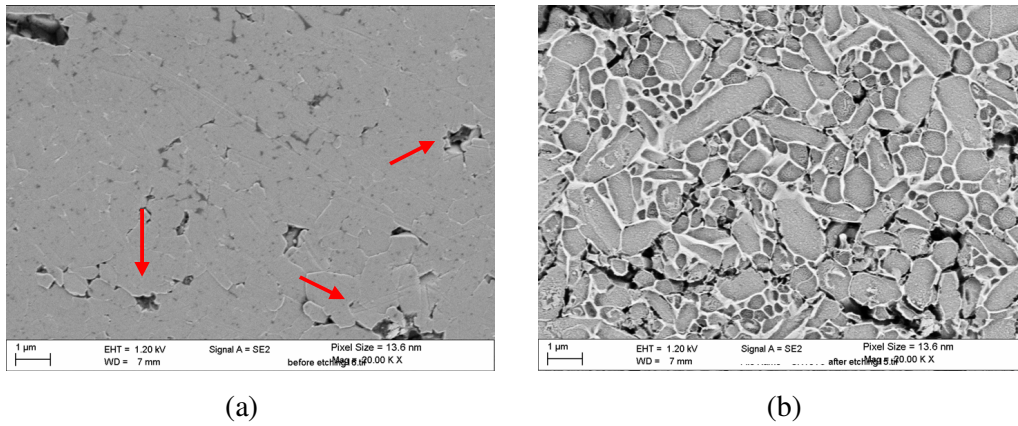
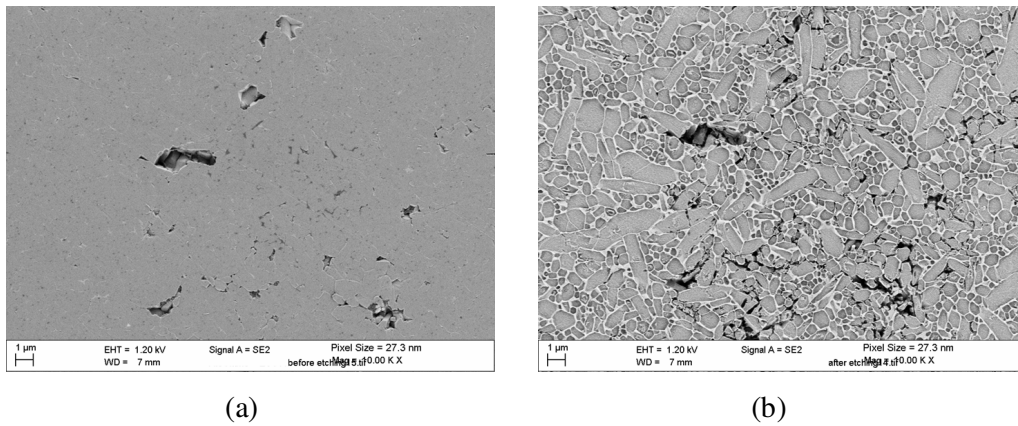


Fig: 3.4 (a) and (b) Fracture at grain boundaries in material C

Pores in material B and C are shown in the Figure 3.5 below. The common feature in the pore formation of these two materials is that they hardly displace any grains. As the grain size is larger compared to material A, the initial pores are clearly visible at the grain boundaries.



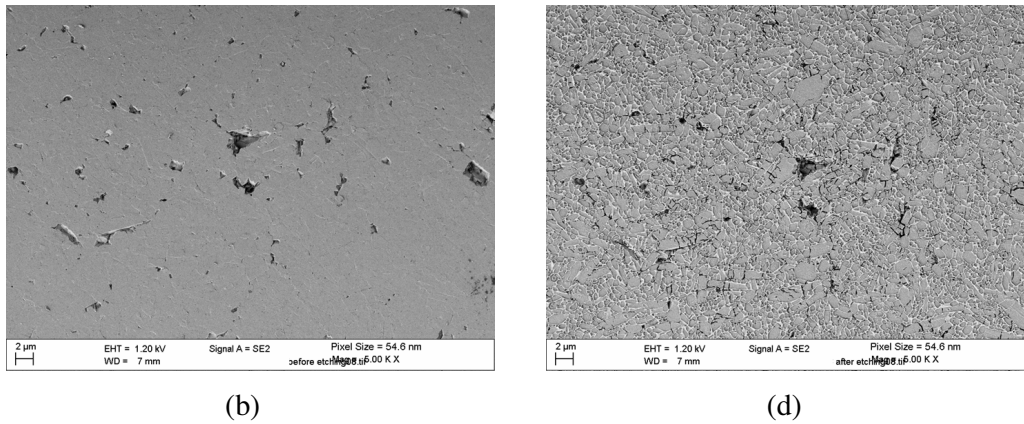
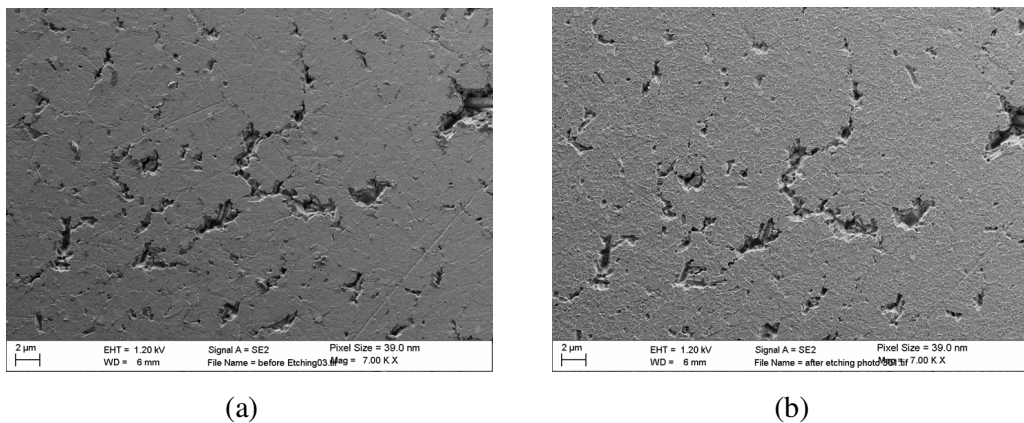


Fig: 3.5 (a) and (b) pores in material C and (c) and (d) in material B

Apart from these three materials, several other silicon nitride materials were also tested as part of this project. All these materials showed this formation of intergranular fracture, and are clear that this is inevitable by all materials. As mentioned in the early section, that grain cracking can be avoided by refining them to a very fine needle like grains and a good example is material A. The mechanism behind this intergranular fracture is very complex mainly due to the scale of loading, damage and the material composition involved. Material A did not show any grain fracture, but showed extensive intergranular fracture and huge loss material through this. As shown in Figure 3.6 fracture occurs at the grain junction and then grows to large scale by the process of linking up across the grain boundaries.



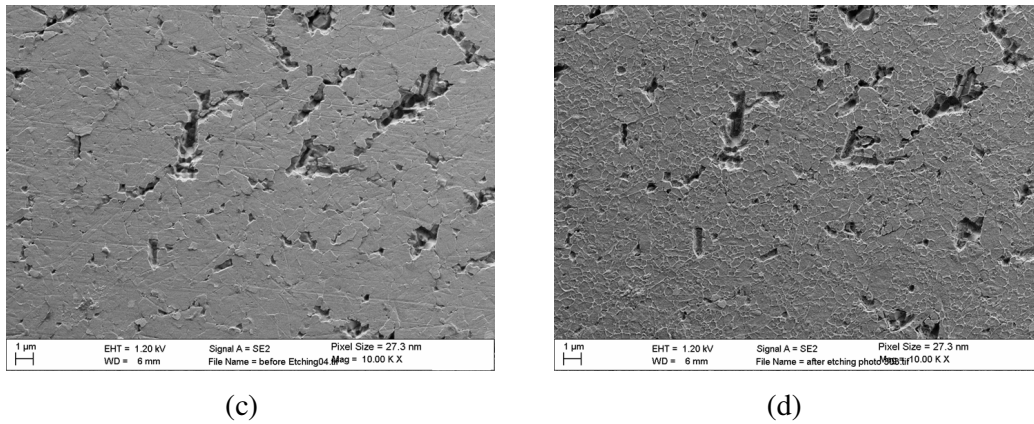


Fig: 3.6. Pore formation material A after 10 minutes of testing without any grain fracture.

The intergranular fracture might happen by two processes. Despite the sophisticated manufacturing techniques employed by commercial manufactures, certain amount of flaws is unavoidable. These flaws act as stress raisers and upon any loading such as cavitation can increase localized stresses at these locations. This increase in stress at these flaws develops into fracture zones due to cyclic pressure loading. The second factor is the addition of oxides and sintering additives in order to manufacture densified silicon nitride ceramics. Common sintering additives are Aluminum, Calcium, Iron, Tungsten and Magnesium e.t.c. These additives favour the Intergranular glass formation. This glassy phase is quite high in material A often called as triple points as shown in Figure 3.7 below.

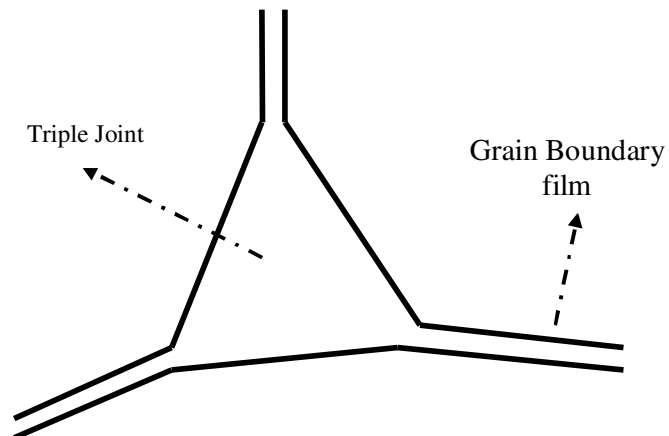


Fig: 3.7 Schematic of a triple junction grain boundary in silicon nitride - Redrawn from (Hoffmann 1995).

This densification process is a liquid phase sintering and depending on the sintering additives the final liquid phase can be amorphous or crystalline boundary phase (Hoffmann, 1995). The composition of this grain boundary phase determines the strength of the material and thus directly influences their resistance to the formation of pores due to cavitation. This grain boundary phase is engineered to withstand high temperatures such as in material A in which a single phase called as SiAlON is achieved without an amorphous boundary phase.

The oxygen content in these materials has a huge influence on the glass formation along with sintering and solid solution. There is a possibility that the residual stress release at the grain boundaries may be one of the reasons for intergranular fracture. This material A which is SiALON is well known to provide thermal shock resistance. But cavitation can provide very high temperatures to several thousand degrees centigrade (Flint 1991). This temperature could be sufficient to liquefy this grain boundary phase to degrade the material by forming pores, however, no evidence is observed to support this statement. Figure 3.8 shows material B at the pore forming stage during cavitation testing.

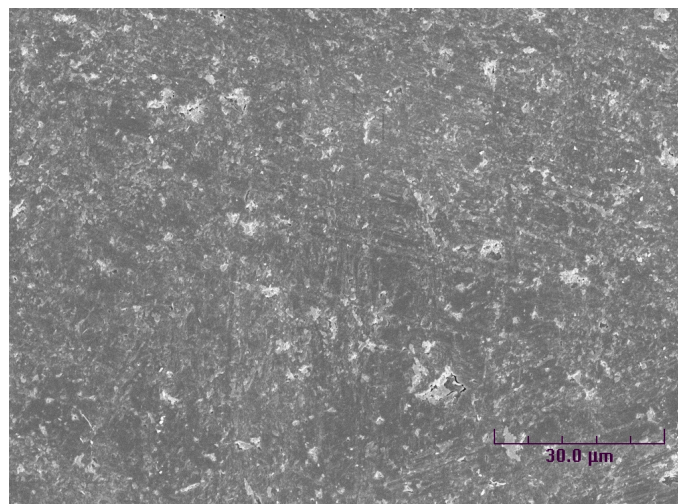


Fig: 3.8 Material B showing intergranular fracture after 45 minutes of testing with low powered transducer.

The intergranular fracture in material B was found predominately near the coarser grains. Grain boundary region adjacent very fine regions showed no damage at this stage as shown in Figure 3.9. As seen in these Figures, the fracture formations are only at the regions where the volume of coarse grains is high. These initially formed fracture zones propagate by linking up and provide home for bubble nuclei, which encourage continued erosion in the formation permanent strain. In many cases, the test samples showed both Trans and intergranular fracture as the beginning stages of erosion. This can be seen in Figure 3.9 (b) where no grain fracture is seen but only fracture at the grain boundaries.

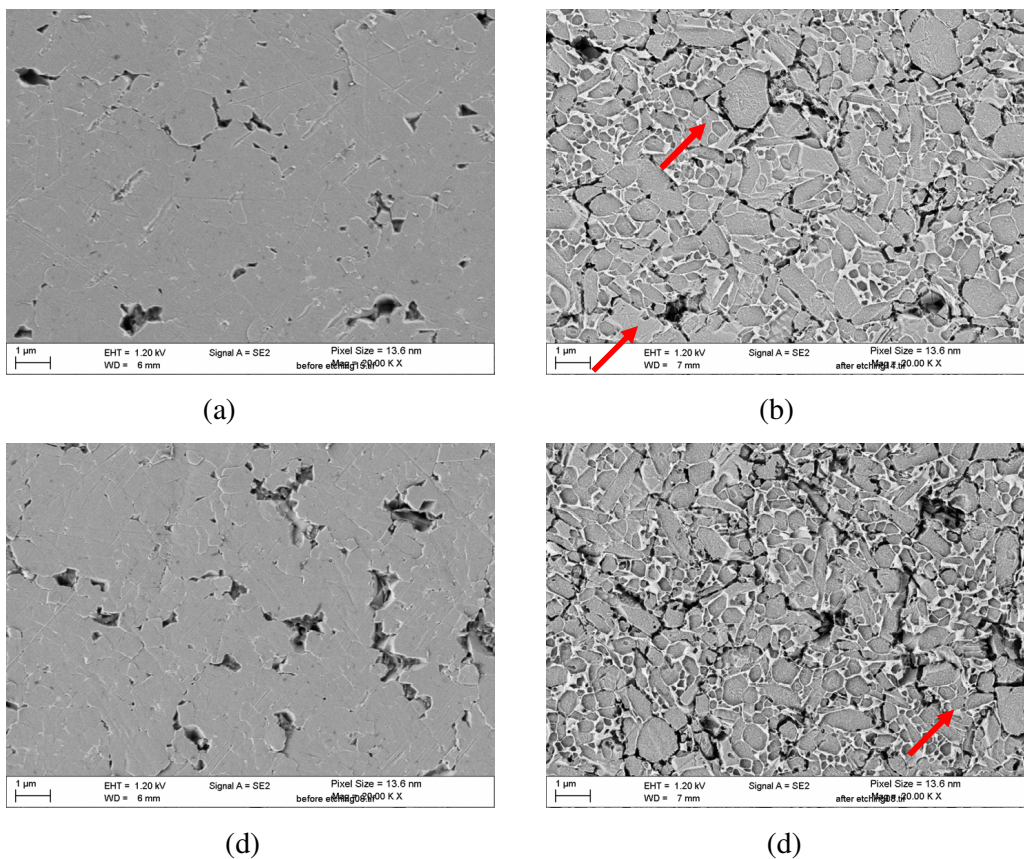


Fig: 3.9 SEM and plasma etched Material B with initial pores next to coarser grains

In both cases, coarser or large grains are the first to get affected by cavitation as shown in the below Figure 3.10

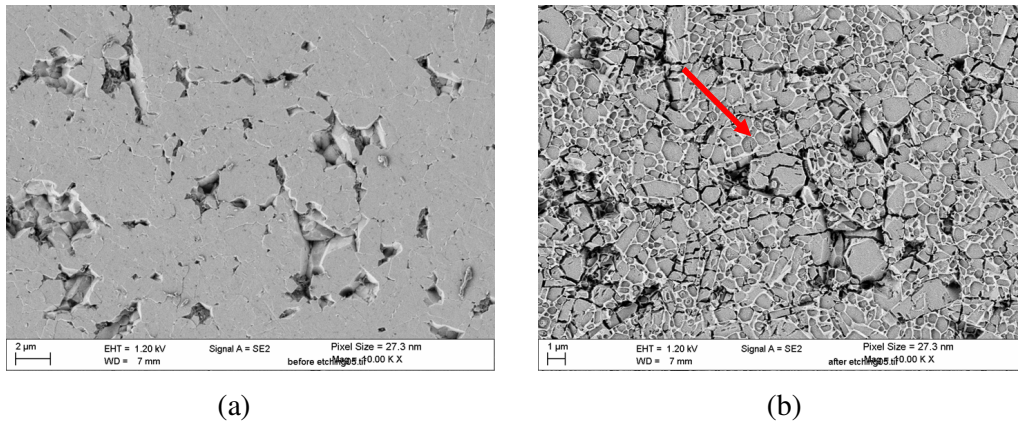


Fig: 3.10 (a) and (b) SEM and plasma etched image of material B showing both grain and grain boundary fracture

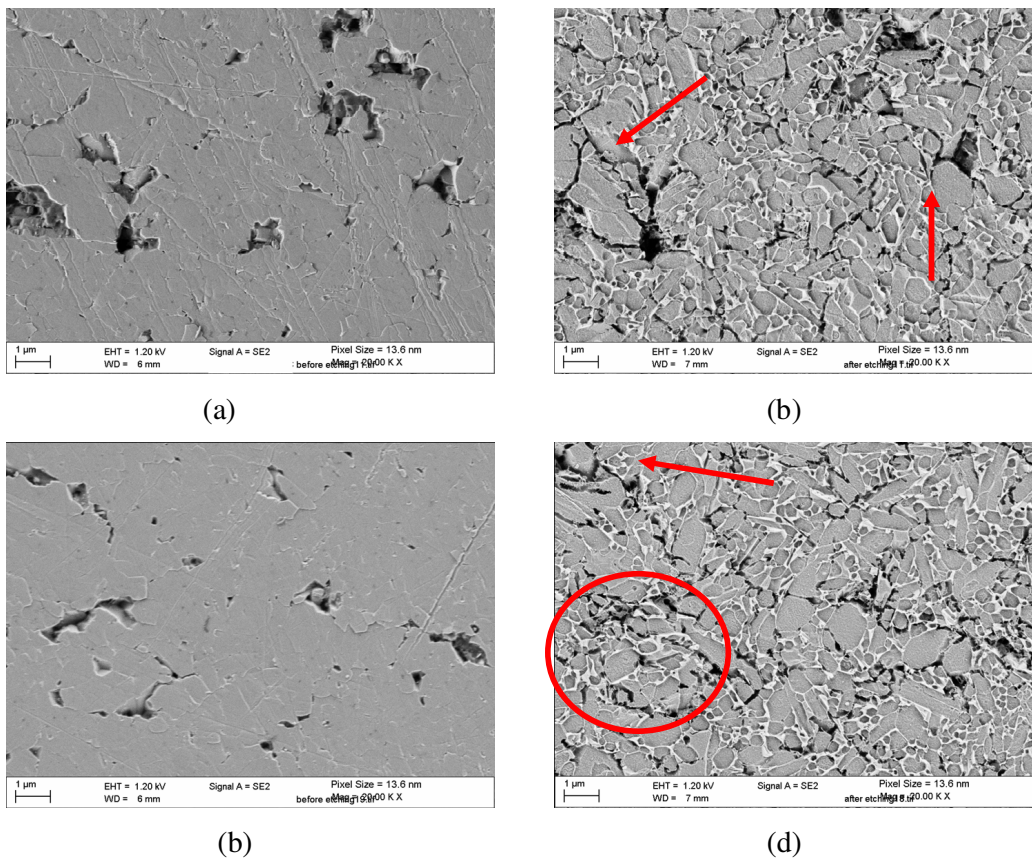


Fig: 3.11 (a) and (b) show SEM an etched image of intergranular fracture surrounding a large grain. (c) and (d) show pore formation circling a bunch of small grains.

The boundary fracture formation as shown in Figure 3.11 (a) and (b) clearly illustrates the coarser grains being lifted off as similar to the process of surface plowing. This is due to linking up of pores which formed around this grain by fracture. Thus initial grain boundary fracture grows in the form of linking up, and their enlargement is a time and history dependent process. The influence of iron oxide in this material B on the grain boundary fracture is not clearly understood. It is very clear that in all materials the interface strength is very crucial for the formation of pores. If this interface strength is increased it will certainly provide increased resistance for this stage and thus for cavitation. It should also be noted that not only the coarser grains are vulnerable to intergranular fracture, but also the linking up process initiate the displacement of bunch of smaller grains as marked as a circle in Figure 3.11 c and (d). Intergranular fracture can be concluded as due to grain boundary diffusion and grain boundary sliding due to very high cavitation temperatures and pressure cycles.

3.1.3. Micro Cracks

The immediate stage which follows trans and intergranular fracture is the formation of micro cracks with lengths ranging in the order of sub microns to few microns. The main reason for the formation of these micro cracks is linking up pores at the grain boundary region. Cracks opened up along the grain boundary region as a sign of intergranular fracture. It is clear from the pores, that the micro void nucleation due to grain diffusion is the major reason for intergranular fracture. The initial and progression of these micro cracks can only be studied at the microstructure level. Hence it is important to etch the test sample to reveal their microstructure after relevant test intervals. The difficulty in monitoring the propagation or the growth of these cracks is that once the test sample is etched cavitation tests cannot be continued on the sample. Some light polishing techniques must be employed to clear away the coated surface but this will also damage the erosion marks. Due to this difficulty, micro cracks on different samples after different test intervals were considered to understand this mechanism.

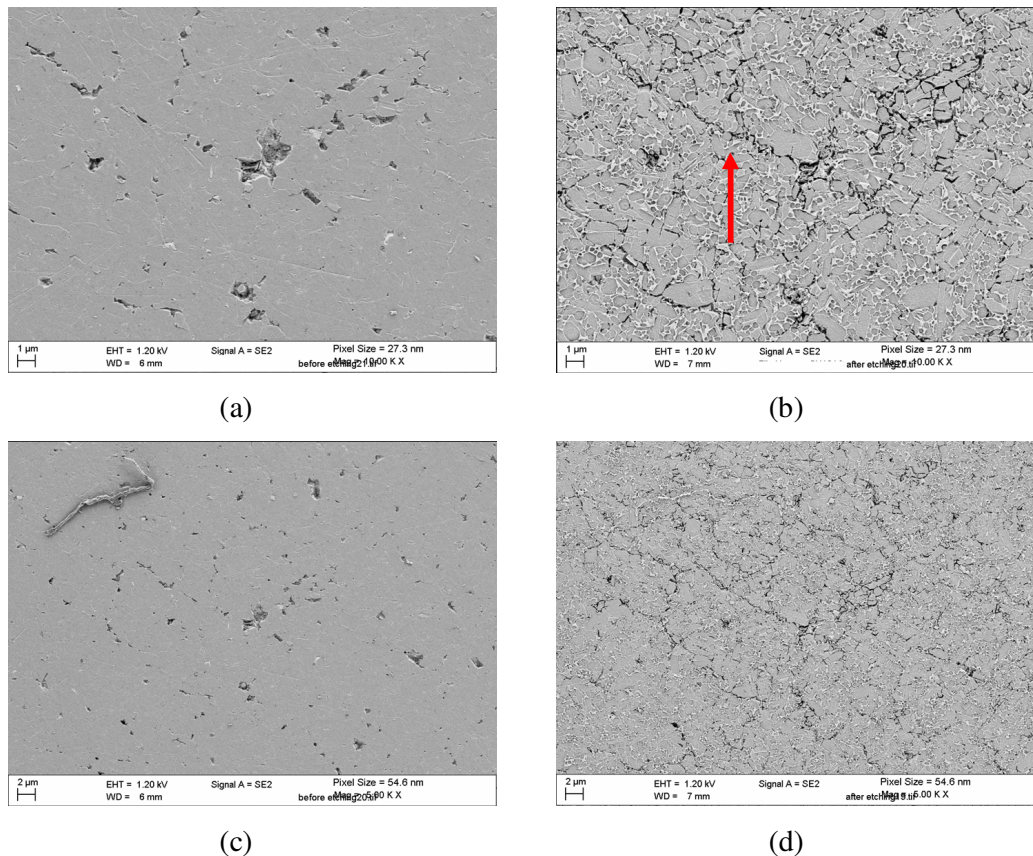


Fig: 3.12 Micro crack formations at microstructure on material B at different scales.

Micro cracks which appeared in all these three materials tested were not similar. This is mainly due to their variation in micro structure and boundary phase composition. Material B shown in the above Figure 3.12 show thin elongated cracks whereas in material A these cracks were also very short but they were broader which is shown in Figure 3.13. Surface investigations on these micro cracks clearly showed that they were not initiated at a single location, but initiated at multiple locations. This is due to the linking of pores. Once a micro void or pore is formed, and upon further exposure to cavitation these pores enlarge and extend to the adjacent pore to link up. Removal of a grain or grains retards the growth of these cracks as shown in Figure 3.13 (a) and (b).

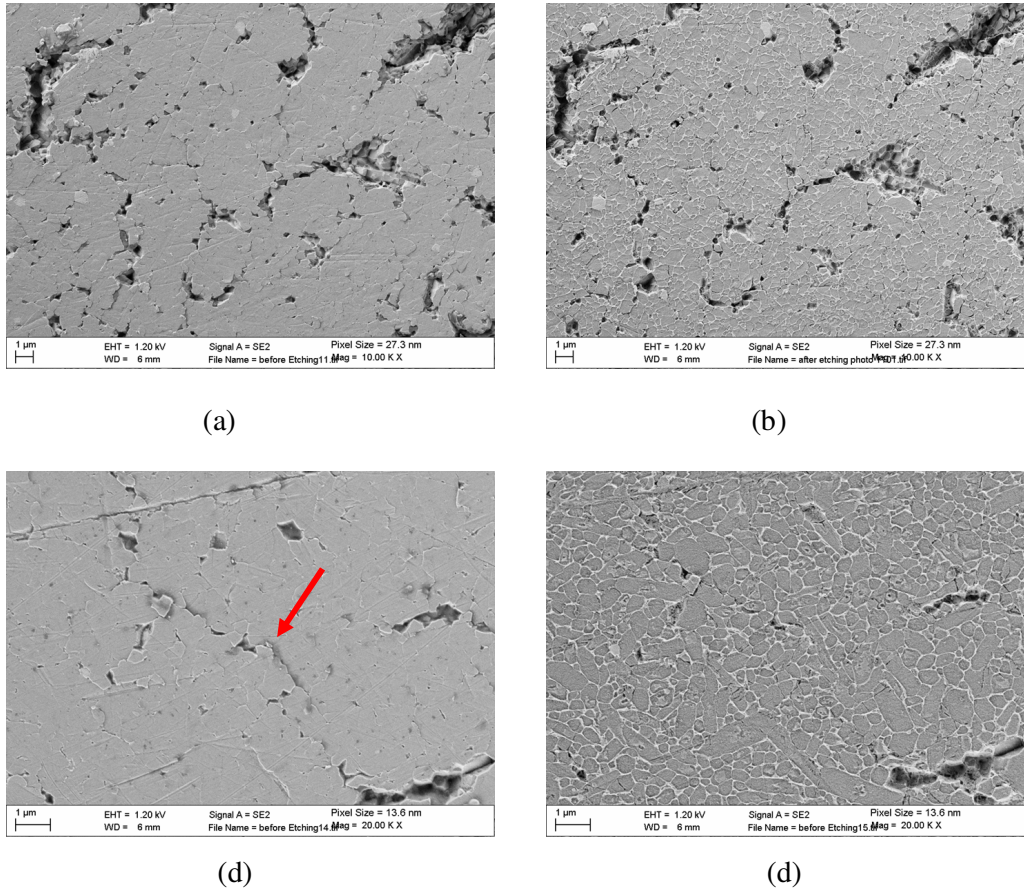


Fig: 3.13 (a) and (b) Broader cracks in material A. (c) and (d) micro cracks propagating in material A

These cracks are not visible at macroscopic level and can only be observed under a scanning electron microscope. The pattern of crack propagation is hard to quantify but they are short lived until the nearby material is displaced. In material C, it was clearly observed that once a crack initiated it did not prolong further in length but grew broader. An elongated grain on the crack path show severe fracture as shown in Figure 3.14.

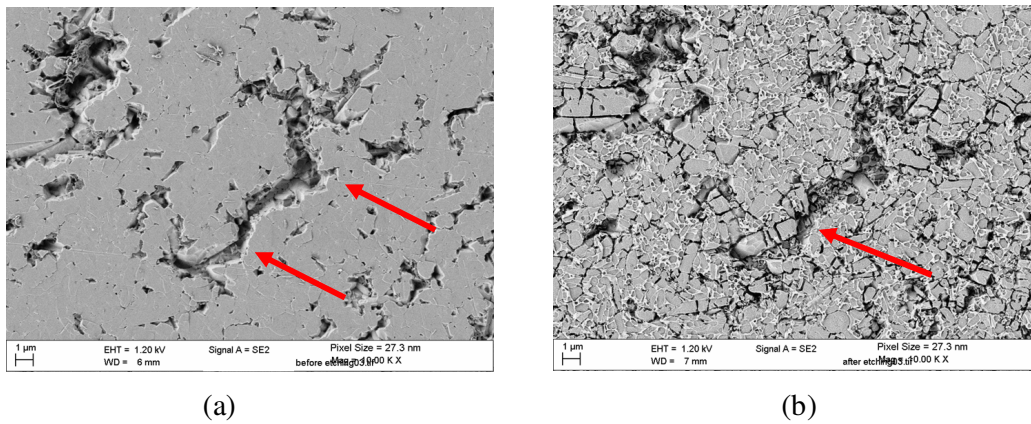


Fig: 3.14 Micro thin cracks transformed to broader cracks by displacing nearby material as observed in material C

These cracks were also deflected by long elongated grains which act as reinforcement with increased fracture strength. This can be seen in the above Figure 3.14 (b). This elongated needle like grains in material A showed a similar resistance to crack by deflecting them. This forced only these elongated grains to be displaced and is shown in the below Figure 3.15.

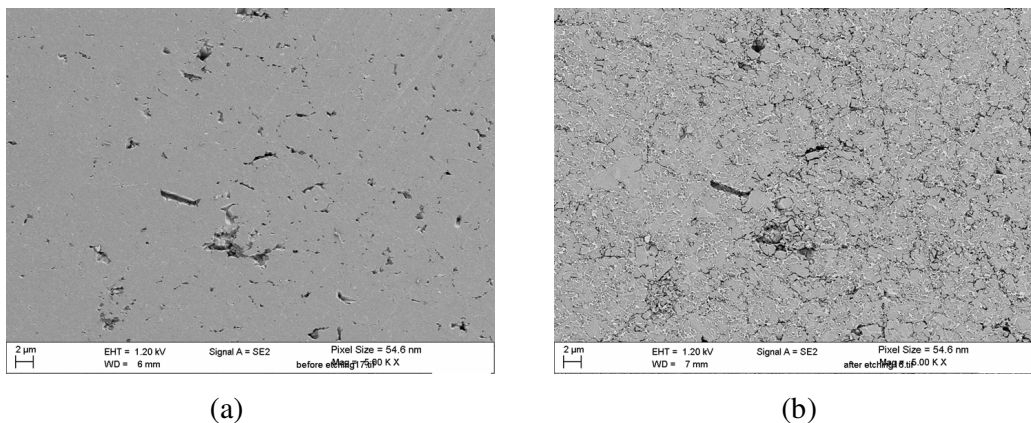


Fig: 3.15 Micro crack growth retardation as seen in material A

3.2. Erosion Pitting

Pitting is the process in cavitation erosion which is largely responsible for material loss. During the continued cavitation testing, pitting immediately followed erosion initiation and accelerated the rate of erosion. That is, once the micro pores, cracks develop they get broadened allowing the cavitation test liquid to squeeze in. A well

understood nature of cavitation erosion is that the rate of erosion is directly proportional to the surface roughness. The rough surface formed during the initial stages of erosion thus helped accelerate erosion by pitting. The influence of surface roughness on erosion rate was experimentally studied and the results are presented in section 3.6 of this chapter. The grain boundary regions which became much weaker during the initial stages of erosion resulted in grain pull out in this pitting stage. Also, the micro cracks resulted in surface layer peeling off at small layers contributes to the formation of cavitation pits. This section details this process of cavitation pit initiation and growth.

3.2.1. Pit Inception:

The concept of a cavitation pit formation can be described as the displacement of material due to weakening of its surroundings by cracks and pores. Real time observation of material displacement is impossible due to the complexity in monitoring the cavitation erosion process at microscopic level. But, results obtained at different test intervals help understand this process.

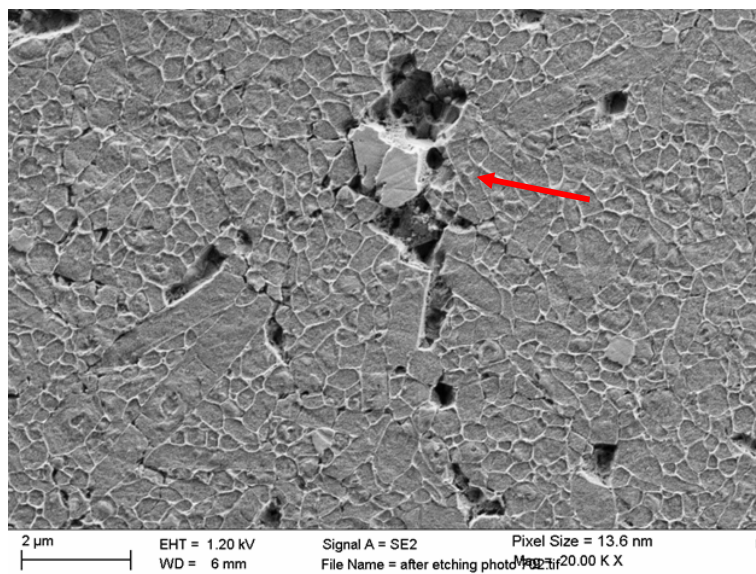


Fig: 3.16 Pit formations in Material A

Figure 3.16 above clearly shows the nature of cavitation pit formation. A bunch of few grains are about to be detached from the test material in the subsequent cavitation loading. This leaves behind an erosion pit. From this image it is also clear that erosion pit in silicon nitride is not a result of just one grain displacement, but it can also be

due to displacement of bunch of few grains at a time. The nature of the pit geometry is not related to the shape of bubbles which impact on them. This was observed in these three different test materials where the shape and size of the pits were not identical. This concludes that pit shape is determined by the microstructure and material strength rather than by the shape of the imposing bubbles. Figure 3.17 shows erosion pits on material A which are sharp and narrowed due to their needle like sharp grains.

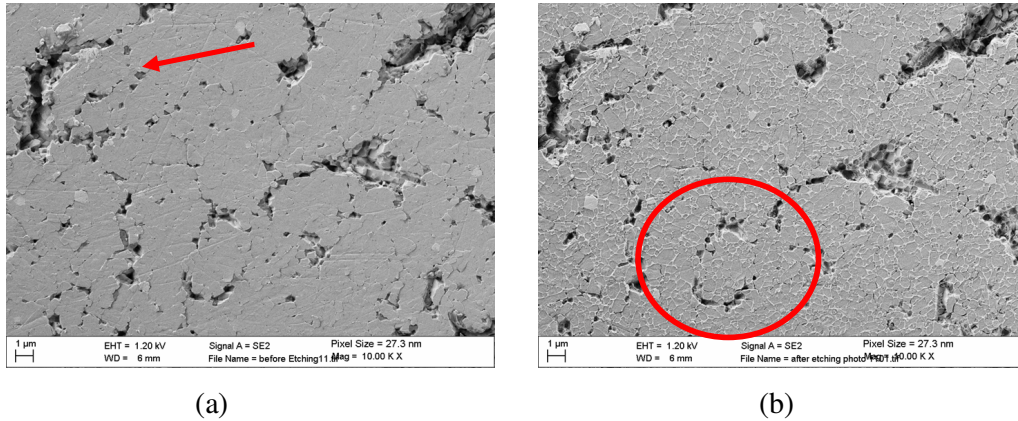


Fig: 3.17 Sharp and narrow pits in material A

The marked area in Figure 3.17 (a) with an arrow shows a deep micro crack on one side and extended to a thin one to encapsulate a large area. Upon further excitation to cavitation this area will be displaced leaving out a pit. Also, the circled area in Figure 3.17 (b) shows linking up of pores encapsulating a small region and furthermore a nearby micro crack propagates towards this area. All these clearly explain the inception of a cavitation erosion pit. The time taken to form erosion pits largely depend on the cavitation test conditions and the material. The images shown in this section are pits formed after 10 minutes of cavitation testing with the high powered transducer. Identifying different stages of erosion damage against test duration is explained in section 3.4 only the mechanism is detailed this section.

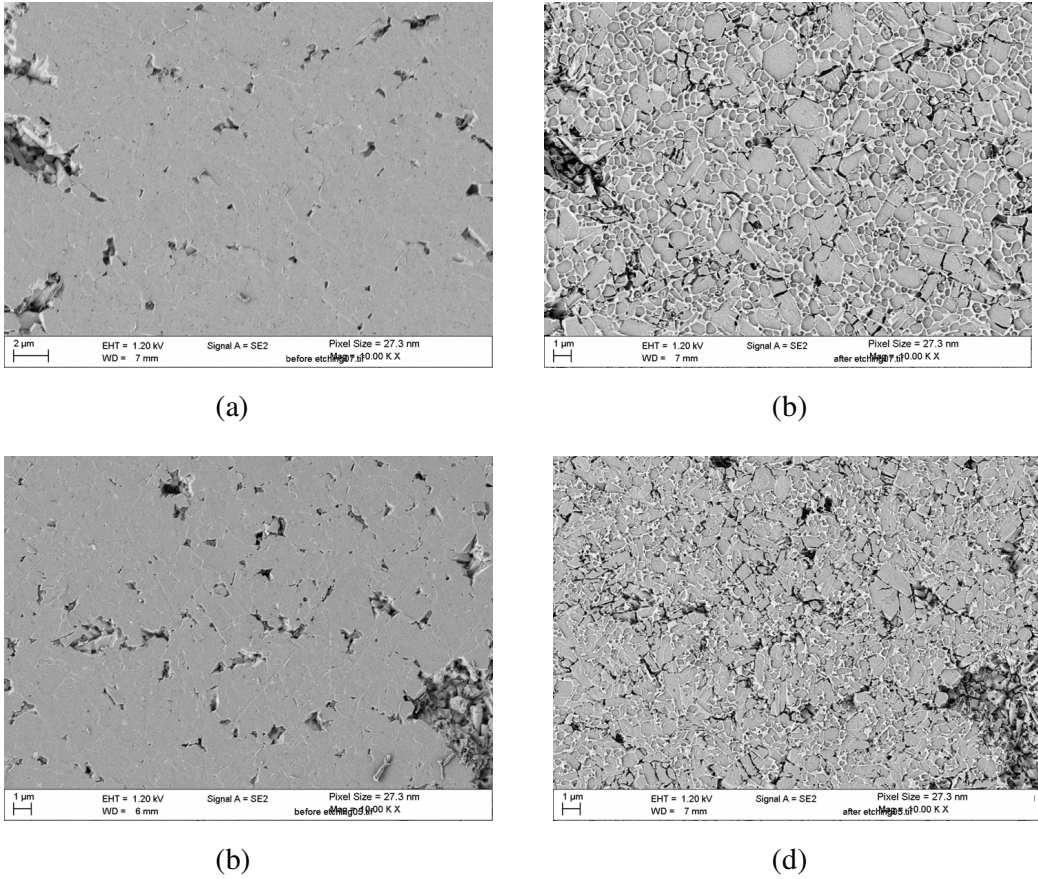


Fig: 3.18 Erosion pit inception in material B

As mentioned early in this section, pit shapes were different in different test materials. Pit initiation as observed in material B is shown in Figure 3.18 and material C in Figure 3.19

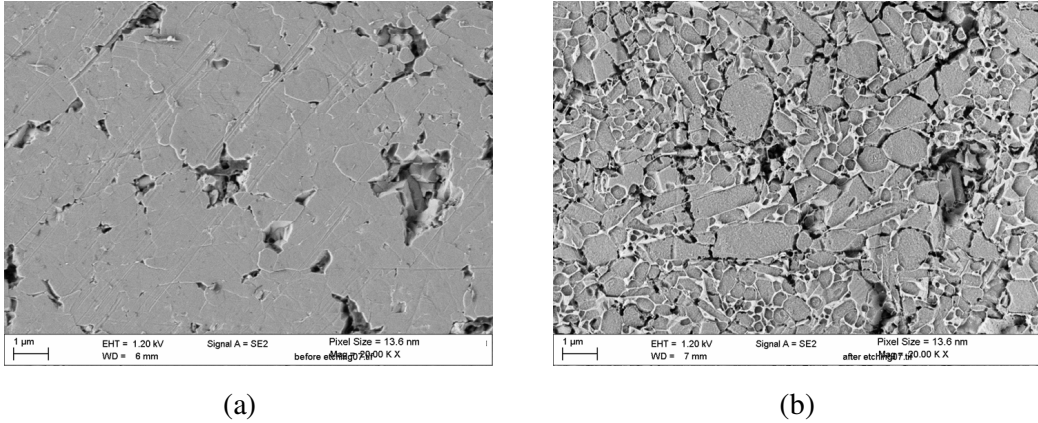


Fig: 3.19 (a) and (b) SEM and plasma etched image of Material C with cavitation pits.

The reason why erosion pits do not form in spherical shape could also be due to the following two reasons. Bubbles are not always spherical in shape, due to the pressure of other bubbles, particles and boundary gradients, and asymmetries in the flow field can be generated. This leads to non-spherical bubble behaviour (Blake et al 1999, Brujan et al 2004). Also, counter jet developed after bubble collapse on the solid surface could play role in erosion (Lindau et al, 2001). Surface analysis on all these test samples showed that there is no difference in the shape, size or even the location of the pits at different areas of the test specimen. But, clearly the initiation of pit occurred at the centre of the test samples where the fluid thickness between the transducer horn and the specimen was set at 0.5mm. The area away from the centre was exposed to low intensity compared to the centre due to the fluid thickness. So it is clear why pits on these specimens initiated at the centre. The Figure 3.20 below shows the start of erosion pits at the centre of the test specimen tested for about an hour using low powered transducer.

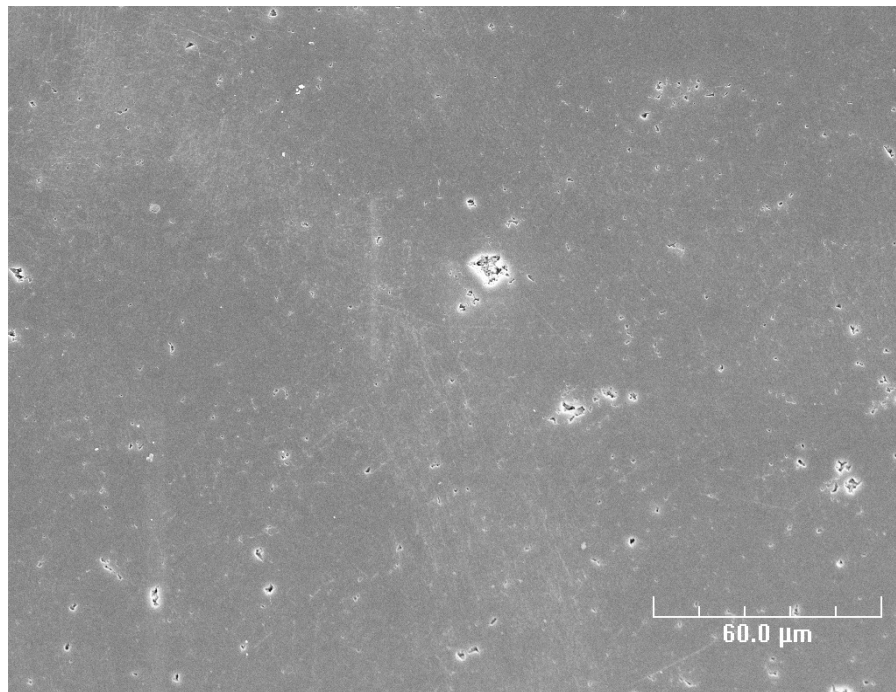


Fig: 3.20 Very few Erosion pits after one hour testing with low powered transducer.

3.2.1. Pit Growth:

The growth of cavitation pits is largely by linking up nearby pits. The pits which were developed during the initial stages of erosion increased the surface roughness which accelerated the rate of material removal. Most of the pits grew by a process called bridging; two cavitation pits join together by creating a bridge between them by a micro crack or even through another pit. Figure 3.21 (a) below show pit bridging process and (b) show enlargement of a pit by additional material removal. Most cavitation pits show micro crack extensions at their boundaries. These micro cracks grow and linkup up an area which upon further cavitation excitation remove the material leaving out another pit, which then link up the old pit. This process of pit enlargement is shown in Figure 3.21 (b).

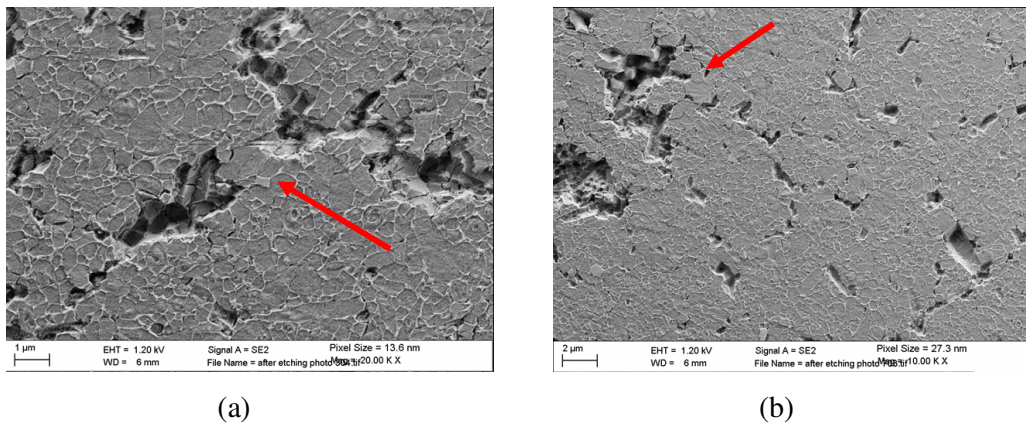


Fig: 3.21 (a) Pit bridging and (b) pit enlargement

The process of pit bridging was also noted for large pits of few microns wide. These pits were grown into large ones by enlargement, deeper but not wider as shown in Figure 3.22 below.

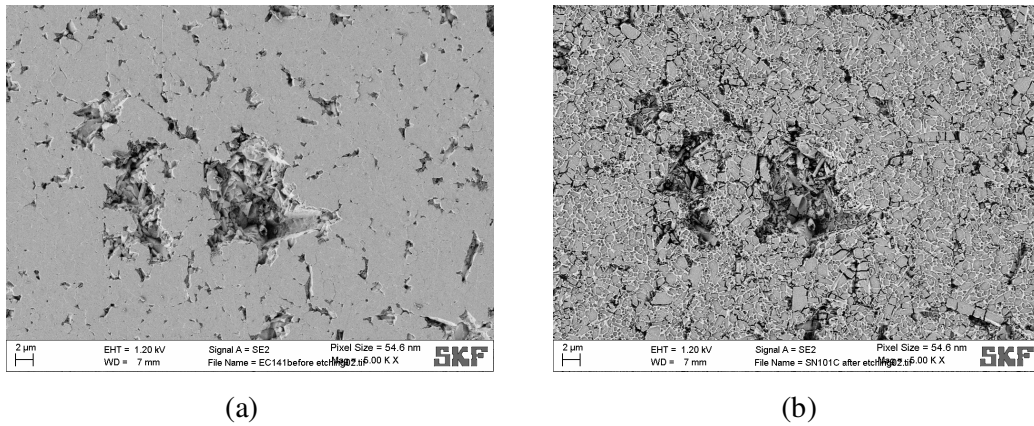
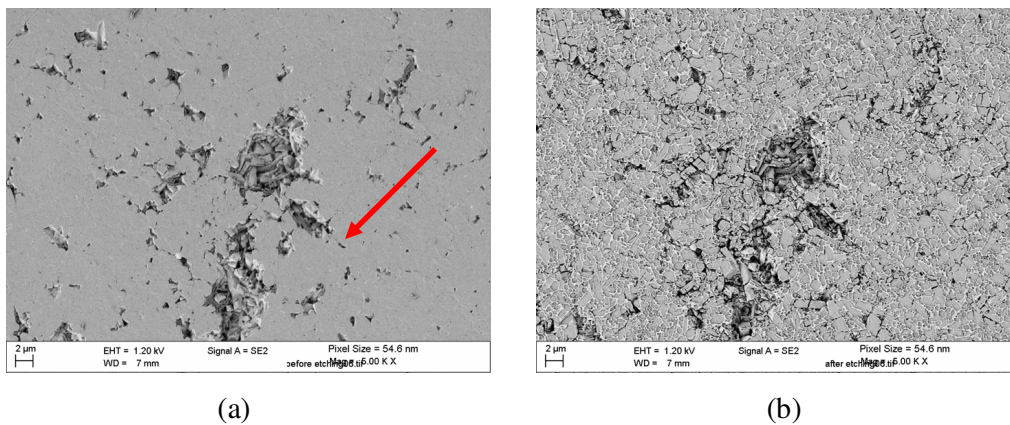


Fig: 3.22 Pit bridging of two large pits

The mechanism of pit growth in all materials was identical. Below Figure 3.23 show cavitation pit growth in material A. In Figure 3.23 (a) Shows two adjacent pits were about to join together. There is no process of bridging or enlargement as early mentioned, but rather a new erosion pit area is being formed by linking up micro cracks. This development leads to a third erosion pit adjacent to the present erosion pits. In the subsequent testing these three will join together and thus removing lot of material, which then further extend wider. In Figure 3.23 (c) and (d) bridging of smaller and larger pits can be seen in the marked areas. Near the marked area with number 1 shows an enlargement of a pit by linking up micro cracks and simultaneously bridging with the adjacent pit. This leads to a two way growth of this pitting region, by enlargement and by pit bridging.



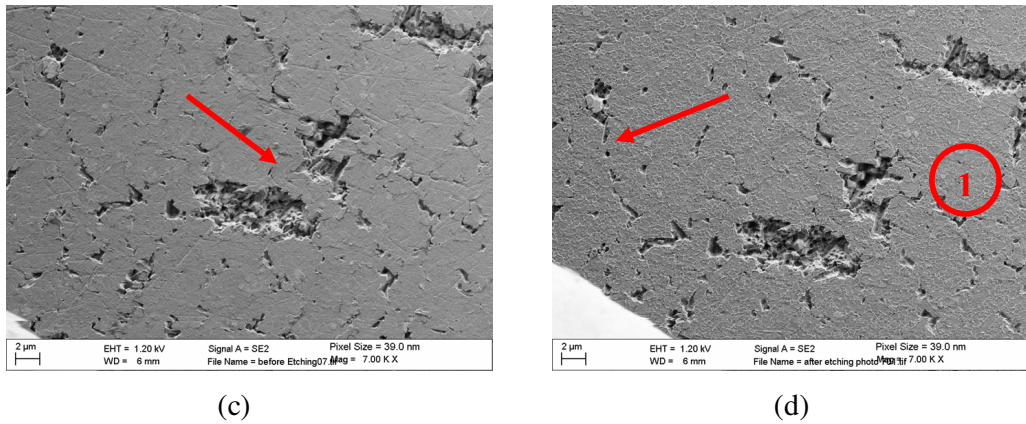


Fig: 3.23 SEM images showing pit growth by linking up pits

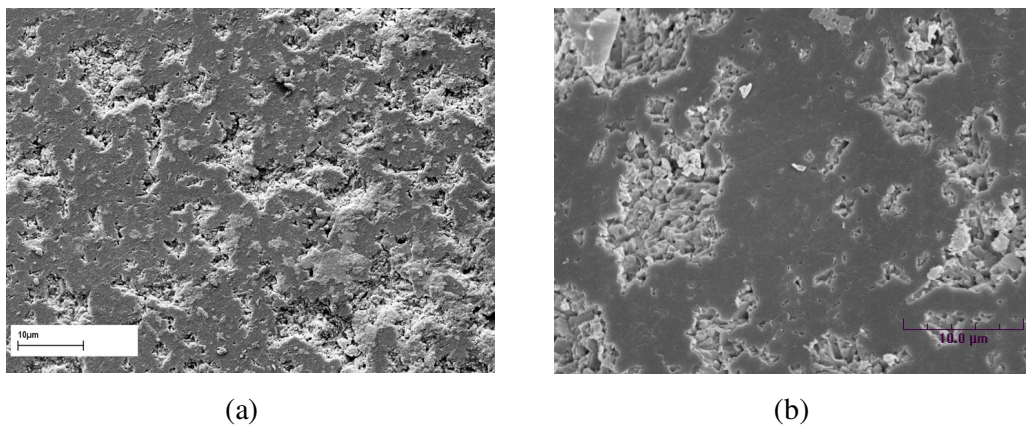
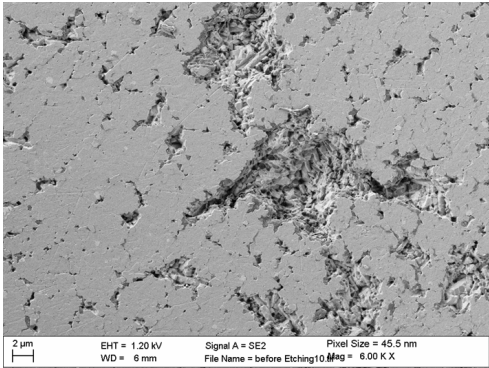
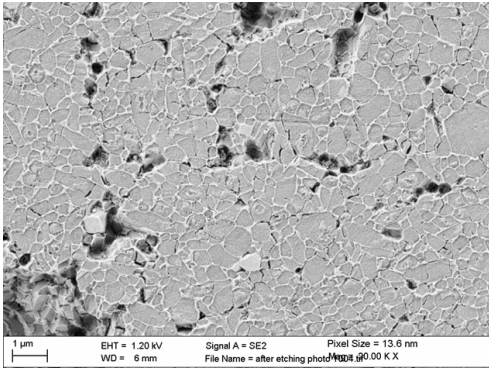


Fig: 3.24 Cavitation pits of different shapes in two materials.

The shape of large pits in material B is shown in the Figure 3.24 (b). The end pits do resemble closer to the grain shape or its microstructure. This image was taken after 5 hours of erosion testing using low powered transducer. A new material apart from these A, B and C was tested and is described in the later sections of this chapter. The pit geometry of this material is shown in Figure 3.24 (a) which is completely different from other materials. Material A with sharp needle like grains always developed into sharp pits. The change in the geometry of these sharp pits occurred when they bridge to the near by sharp pit to form a wide enlarged pit. This is marked in Figure 3.25 (b) Material C with wide and elongated grains had both type of erosion pits and a typical geometry of its pit is shown in Figure 3.25 (a). Measurements were carried out to monitor the depth and width of these pits and are discussed in section 3.3. It must be noted that erosion pits grew deeper only to maximum of 7 microns.



(a)



(b)

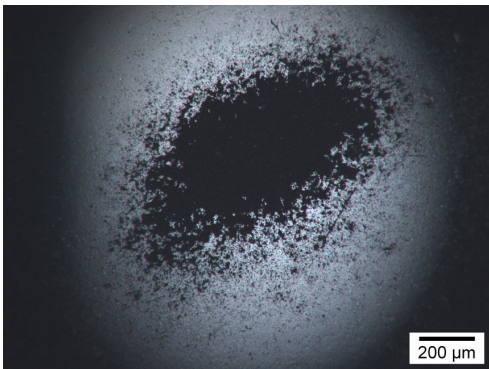
Fig: 3.25 (a) and (b) Cavitation pits in material A and C



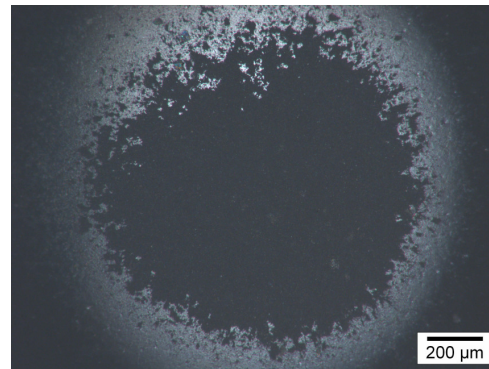
(a)



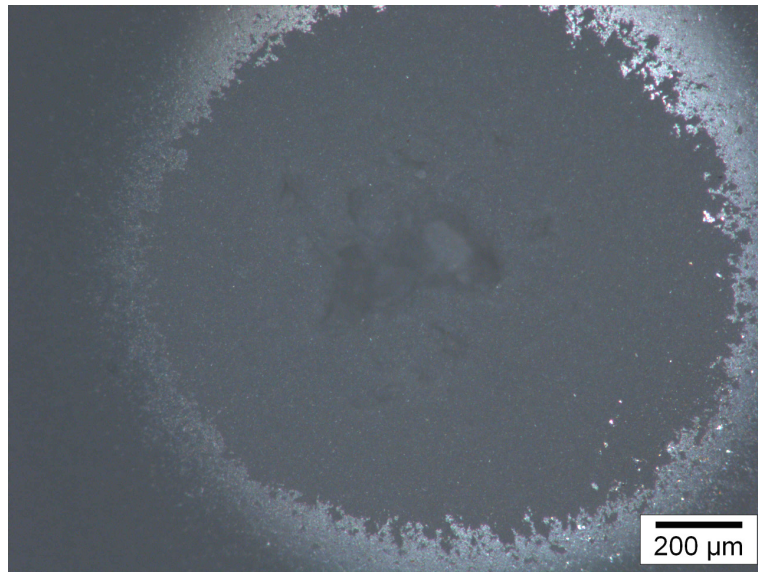
(b)



(c)



(d)



(e)

Fig: 3.26 Light microscope images of erosion pits at different stages.

A series of light microscope images were taken at different test intervals to get an overview of the pit formation and growth in these materials. One such result on material B is shown in Figure 3.26 this material was tested with high powered transducer. The first image shows the initial stage of erosion pit formation as observed just after 3 minutes of testing. It should be noted that initial pits only appear at the centre of the testing area. This is because of the curvature of the test specimens which vary the fluid thickness between the transducer and the test specimen. The next stage as shown in Figure 3.26 (b) is after 5 minutes of testing. This stage shows pit initiation at the edge of the centre area and the previous pits were grown denser by the process of pit enlargement and bridging. After 10 minutes of continued testing on this material, the centre area was severely eroded forming a centre wear scar with a few erosion pits at the edges as shown in Figure 3.26 (c). Further testing for 20 and 30 minutes resulted in severe erosion on the surface and is shown in Figure 3.26 (d) and (e).

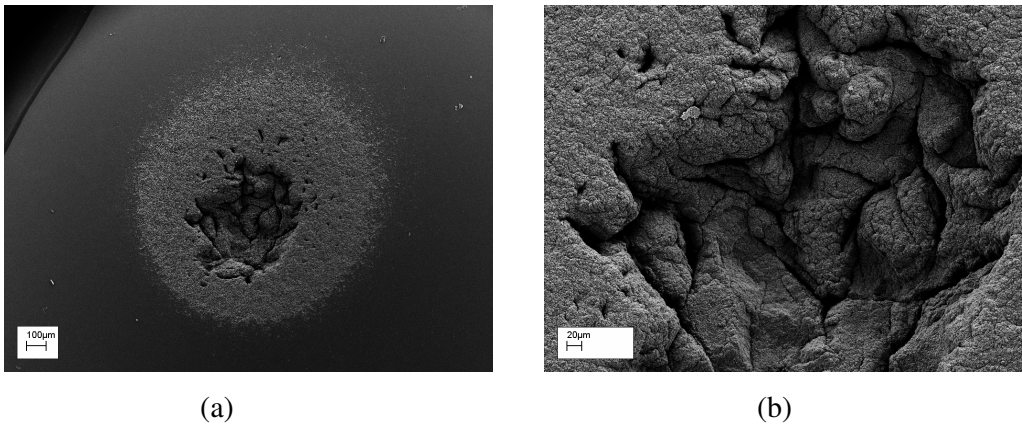


Fig: 3.27 (a) and (b) Erosion pits developed into large crater

The eroded area normally remained at a near constant wear depth of about 7 microns. The cavitation testing transducer is made of titanium alloy in order to have superior erosion resistance. Regular surface inspection of this transducer was carried out to ensure optimal performance. An eroded transducer was once used for testing to observe its impact on the test results. Testing was carried out on material B and after 20 minutes of continued testing the erosive wear region was narrowed as shown in Figure 3.27. The white area in Figure 3.27 (a) is the initial wear region and in later stages more material was removed only at the centre due to the transducer defect. This resulted in a large crater; a close up SEM image of this crater is shown in Figure 3.27 (b).

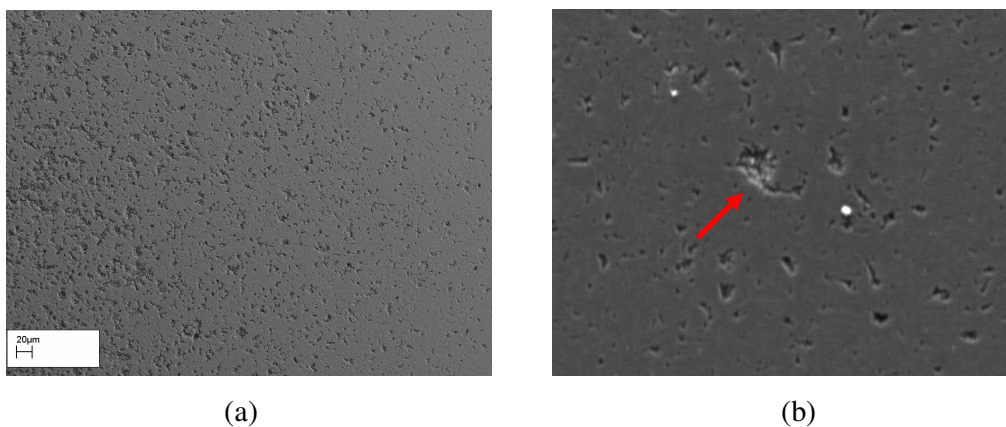


Fig: 3.28 (a) Erosion pits at the edge of the centre wear scar and (b) pit growth at the edges.

The area away from the centre wear showed less density of erosion pits due to the curvature of the test specimen. This variation in the pit density is shown in Figure 3.28 (a). The interesting point about the growth of these less dense pits is shown in Figure 3.28 (b). It was noted that no pit bridging was possible at these areas due to the distance between pits and all pits showed a tail like structure and appeared as “tadpole”. This suggests that the only way for the growth of an isolated pit is to develop a micro crack and thereby enlarge them to reach the adjacent pit. Also, the intensity of cavitation in this region is very less which means the rate of pit growth is also very slow.

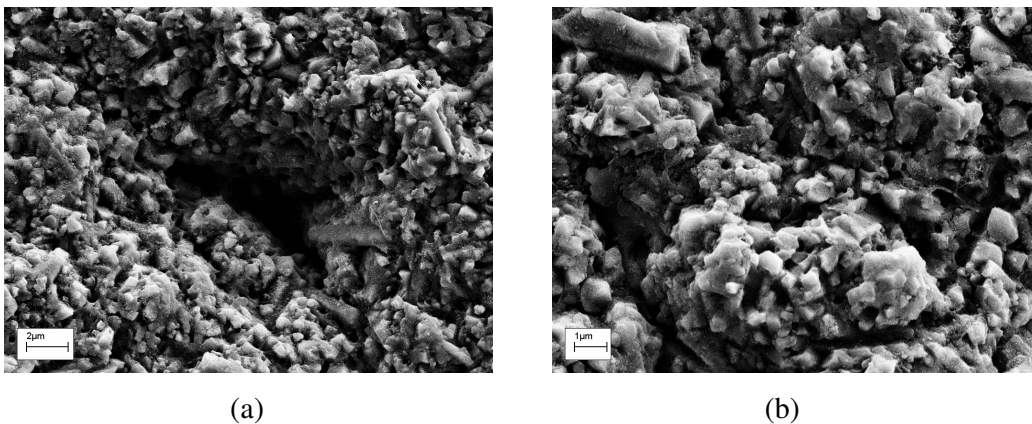


Fig: 3.29 SEM images on severely eroded areas.

Further stages of erosion pit growth showed almost all pits at the centre region of the test specimen were joined together. This showed the severity of the wear and huge material loss was observed until this stage. High magnifications of this advanced stages of erosion pit growth is shown in Figure 3.29 above. As seen in these Figures, it becomes very hard to differentiate the pit from the other wear region. Almost all pits were transformed to a very rough surface. Microscope images during this stage are shown in Figure 3.30. As shown in Figure 3.30 (a) only a rough surface is visible without any notable erosion pits. Further exposure to cavitation resulted in accumulation of surface layers without any pit formation. This stage showed that no more erosion pitting was possible and the material removal was only by means of displacing surface layers from this area. As marked in Figure 3.30 (b) and (c) the surface layer remained at few areas. Some pits were transformed to large craters as shown in Figure 3.30 (d).

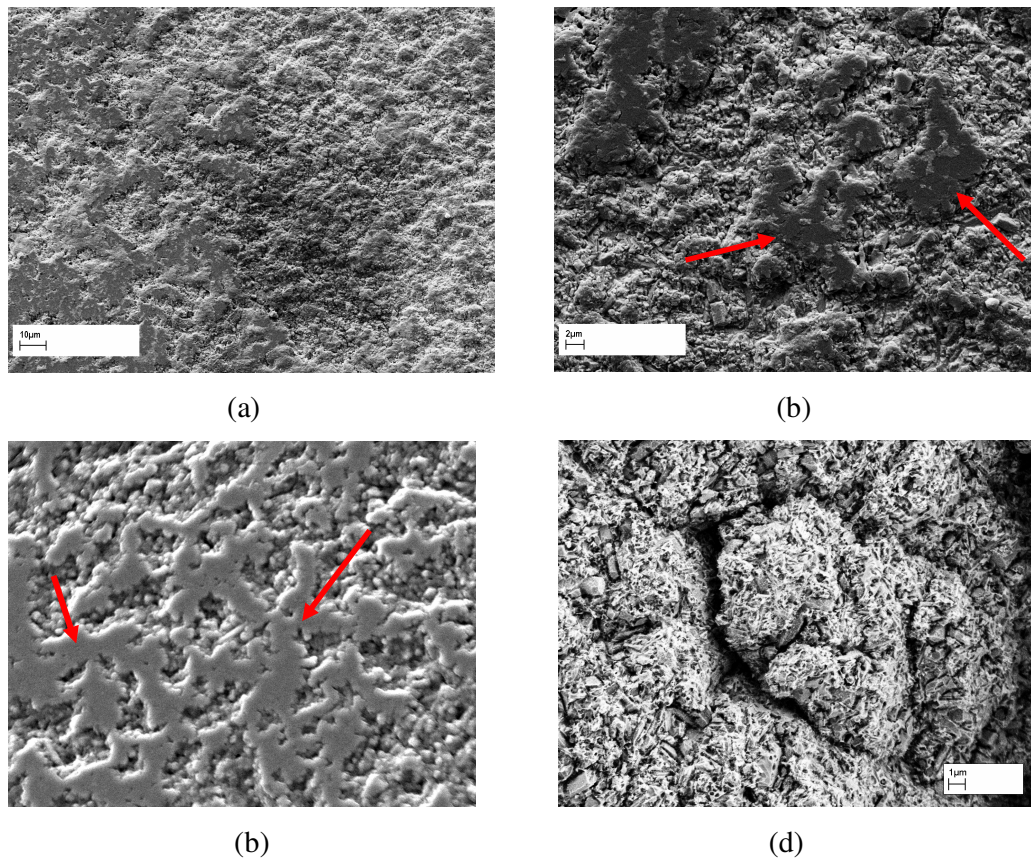


Fig: 3.30 SEM images of final stages of erosion pit growth

It is clear that the primary mechanism involved in the growth of pit is bridging. The process of pit bridging was also investigated by testing the same specimen at nearby different locations. Test material B was tested initially at one area for 25 minutes using high powered transducer. The eroded area was marked under the microscope. The specimen was placed in the specimen holder by carefully locating the nearby area of the eroded part. After 15 minutes of erosion testing, a new centre wear was found at the preferred area as marked in Figure 3.31 (b) as number 2. The edge of these two wear areas clearly showed bridging of erosion pits which can be seen in Figure 3.31 (b). A typical erosion pit bridging is shown in Figure 3.31 (a) for comparison.

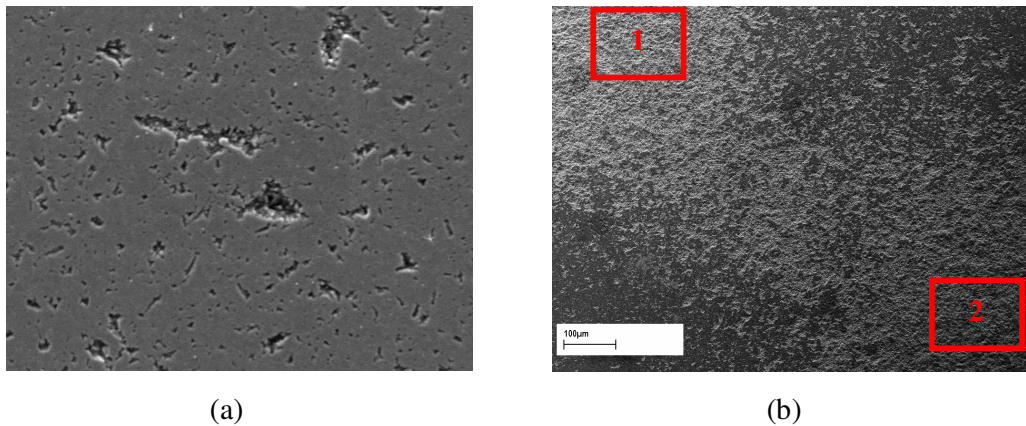


Fig: 3.31. (a) pit bridge and (b) erosion wear bridging between two test areas.

3.2.2. Wear Sheet

Apart from the formation of cracks and pits, wear sheet formation was also noted. This type of material damage is characterized by peeling off the surface layer similar to plowing. This wear sheet formation is very common in abrasive machining – where material is removed by abrasion using hard particles. Solid particle erosion can also cause a similar damage. Change of test liquid was regularly carried out during all tests in order to ensure no chances for third body abrasion or solid particle erosion. Hence these wear sheets are part of cavitation erosion. Wear sheet formation was found on materials B and C, but not on material A. These wear sheets were noted only at the edge of the centre wear scar and were not extensive. A large area of wear sheet removal is shown in Figure 3.32. This wear sheet formation occurred after 5 hrs of erosion testing using the low power transducer. A huge area of sheet was thrown away, exposing the material subsurface to cavitation. Cracks can be seen on this exposed area as shown in the Figure 3.32. Linking up pores is the reason for crack like appearance. These formed an enclosed region which on further exposure to cavitation peeled off the surface layer.

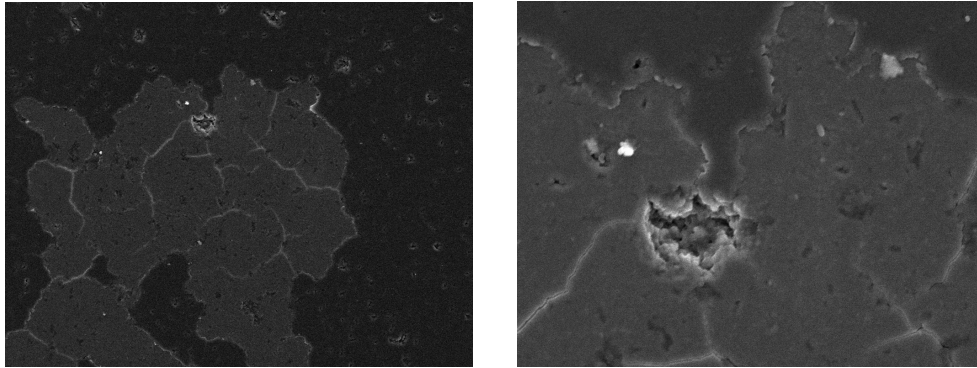


Fig: 3.32 Wear sheet formation in material B after 5 hours of testing using low powered transducer.

Wear sheets lead to a major material loss. EDAX chemical analysis to determine the composition on this wear sheet area was carried out. The result is shown in Figure 3.33. The red area shows the composition inside the wear sheet or the peeled off area and the black line show the composition on the surface outside this wear sheet. Loss of Aluminum and Iron can be seen which are used as sintering additives for this material as Alumina and Iron oxide. This composition change however does not explain the process of wear sheet formation.

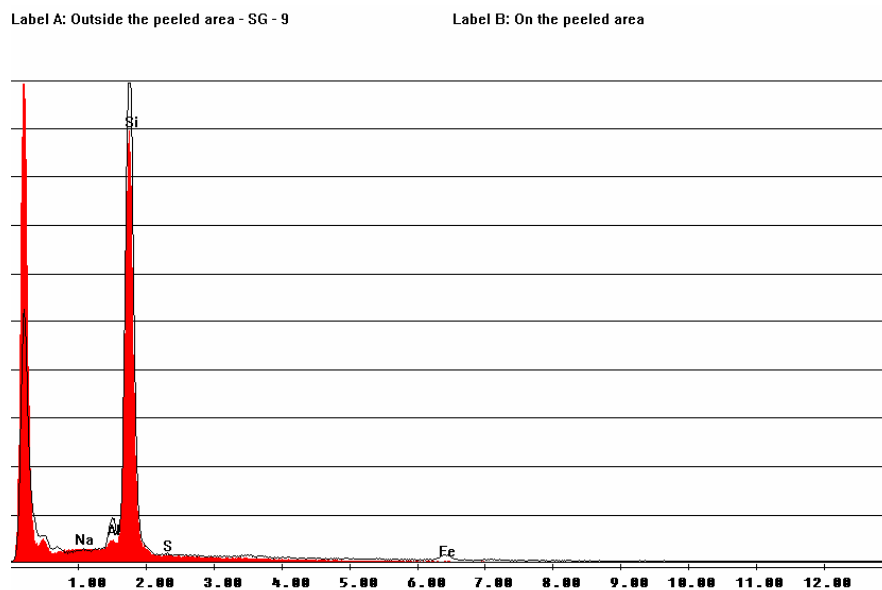


Fig: 3.33 EDAX spectra of wear sheet on material B

Material C showed smaller size of wear sheet formation like in material B. There were many wear sheet areas in this material compared to material B. But, the wear formed in this material was not thicker as in the other. In material A, there were no signs of wear sheet formation.

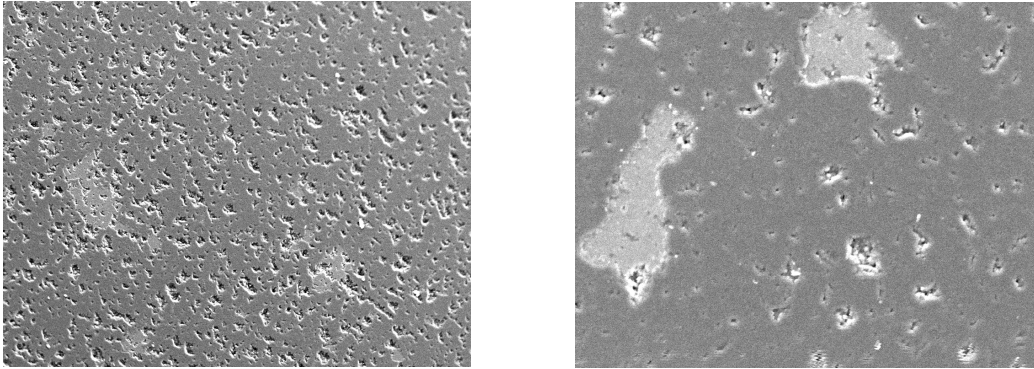
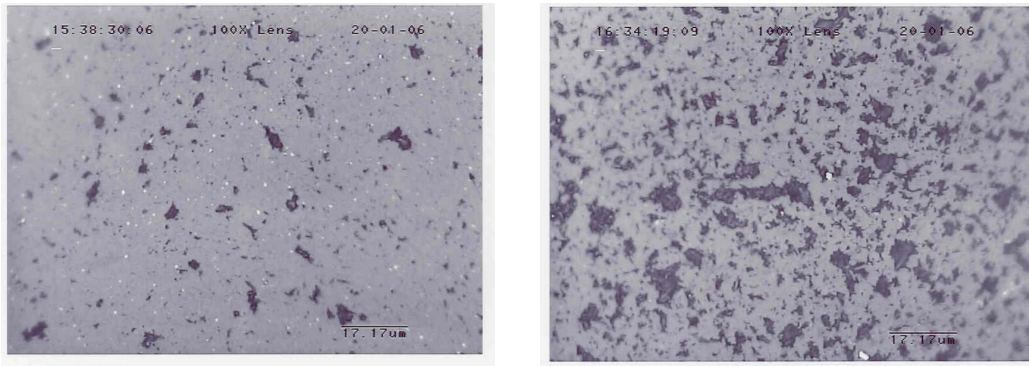


Fig: 3.34 Wear sheet formations in material C

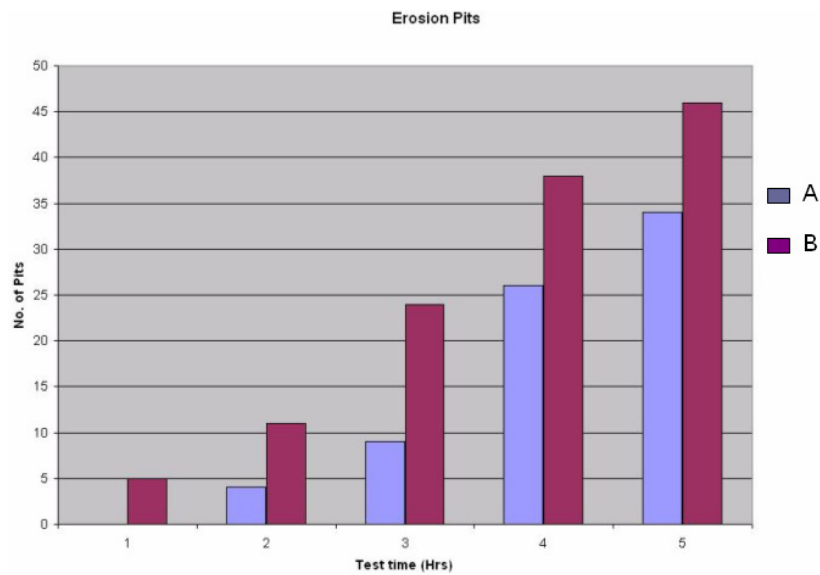
3.3. Surface Analysis

Cavitation erosion damage is very difficult to measure but recent advancements in meteorology overcome this problem. One such advanced 3D scanning laser profilometry technique was utilized for these erosion measurements. Surface changes due to cavitation was continuously measured at relevant test intervals to monitor the formation and growth of cavitation pits, measure surface roughness and volume loss to evaluate the material for ranking their resistance. A simple method to compare two materials to evaluate their performance against cavitation is to count the number of pits after certain time of testing. An example is shown in Figure 3.35.



(a)

(b)



(c)

Fig: 3.35 (a) Pits in material A and (b) pits in material B after 5 hours of testing. (c) A plot of pit count

On the other hand, surface scanning measurement techniques give precise details on the erosion parameters such as pit depth, pit shape and volume of material removed during each test intervals. Figure 3.36 show surface scan after 3 and 5 hours of erosion testing. The pits formed after 3 hours were joined together and a huge material loss was observed after 5 hours as shown in Figure 3.36 (b).

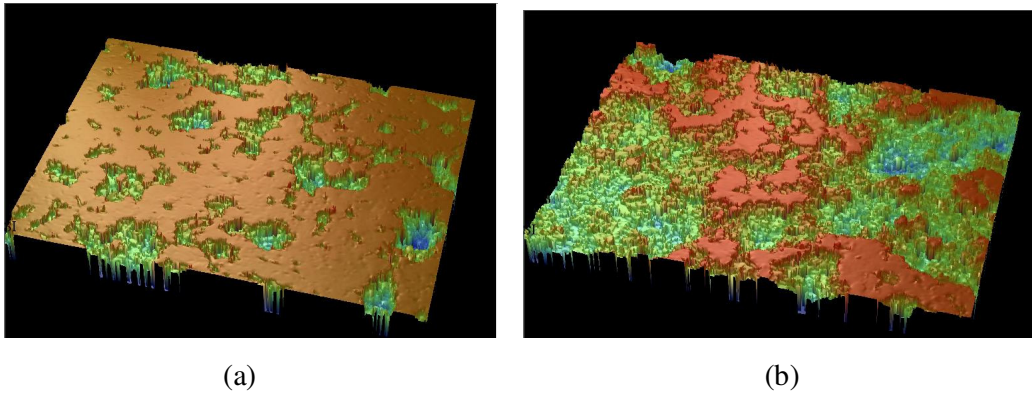


Fig: 3.36 (a) Eroded surface after 3 hours of testing and (b) after 5 hours

3.3.1 Average Roughness

During the course of erosion, it was detailed in the early sections that the wear process initiates by roughening the surface by forming micro cracks and pores. These pores and micro cracks then develop into cavitation pits. Any sort of surface changes or loss of material is directly related to the material loss due to wear. Test materials were tested for up to 5 hours using the low powered transducer in order to measure their roughness at equal test intervals for comparison to evaluate the material against cavitation erosion. Measurements were carried out and the results are plotted as in Figure 3.37. Material B showed poor resistance compared to material A and C with increased surface roughness values over time. It was evident from the surface analysis performed using light microscope and scanning electron microscope that material B had many number of erosion pits compared to the other two. Also, during the initial stages material B showed severe grain fracture and huge loss of material due to the nature of its microstructure.

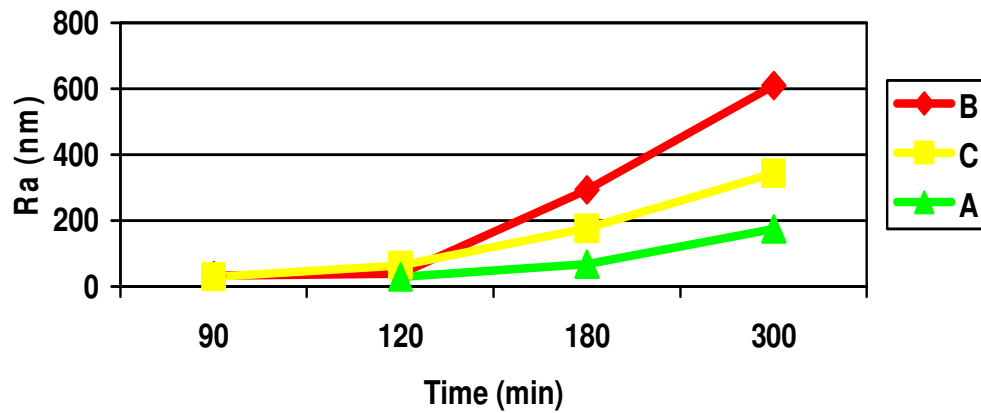


Fig: 3.37. Average roughness plot of test materials over time

3.3.2. Volume Loss

The rate of erosion is normally calculated by measuring the mass loss after each test interval. Silicon nitride being a low dense material, a very precise measuring balance with microgram accuracy is required to get accurate mass loss measurements. Another way of calculating the rate of erosion is using volume loss measurements. This was done with the same 3D interferometry technique by calculating the net missing volume, the method which was reported by Miyoshi and Patella (Miyoshi 2003, Patella 2000) and the results are shown in Figure 3.38 which confirms the test material rankings against cavitation.

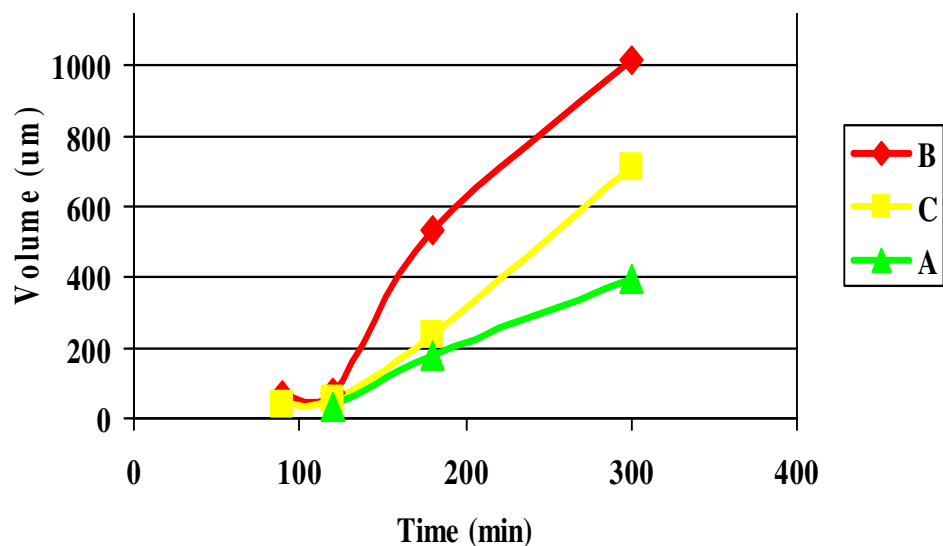


Fig: 3.38 Volume loss measurements over time

Table: 3.1 Incubation periods (minutes)

Material	Low powered transducer	High powered transducer
A	40	5
B	25	3
C	30	4

Also, the incubation time which determines the onset of material loss is listed in the above Table 3.1. These values confirm the material rankings as seen in the wear images. Material A was strongest of all with better resistance to cavitation followed by material C and B. The material properties for material A such as hardness and fracture toughness are high compared to the other two. This provide an explanation why this material is high resistant to cavitation. But on the other hand, hardness and fracture toughness values of material C is less than material B, only the average grain size value is smaller than the other.

3.4 Erosion Attenuation

There was decrease in the rate of material removal after a certain period of testing. This stage is normally called as attenuation stage. The start of this stage varied highly with the low and high powered probe and slightly with the test materials. A light microscope image of the severely eroded area is shown in Figure 3.39 (a). This surface became very rough with presence of large number of deep craters of up to a maximum of 12 microns. This stage was reached after 2 hours of cavitation testing using high powered transducer. A scanning electron microscope image of this severely eroded area clearly shows the rough surface in Figure 3.39 (b).

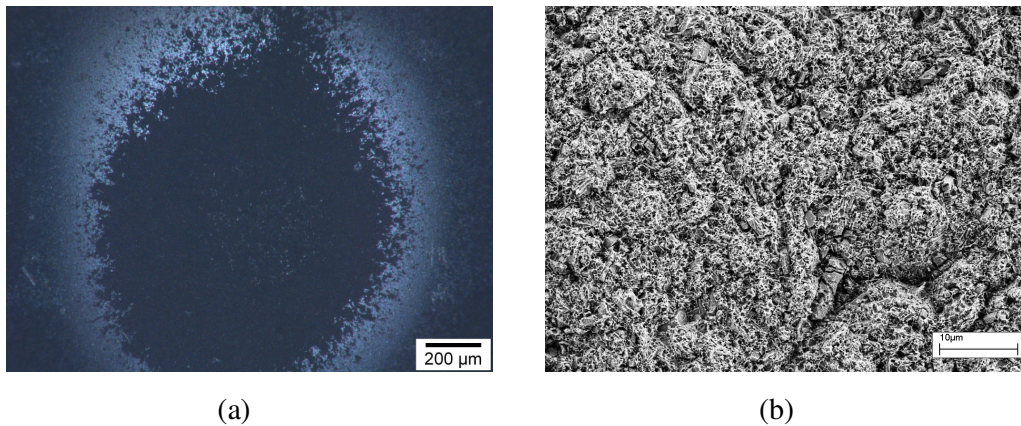


Fig: 3.39 (a) Light microscope image of severely eroded surface and (b) SEM image of the same area.

Material C was tested for a long time of 45 hours to investigate the crater formation. Most of the pits were joined together in the early stages and appeared as a large crater. One such crater is shown in Figure 3.40 (a) and (b). As seen in the below image, due to the presence large number of pores, the probability of liquid squeezing is high. This lets the bubbles to be trapped inside these pores. This during further testing act as dampers, providing a cushioning effect often called as bubble cushion effect. Also, residual gas air in these craters can absorb a part of the impact energy during cavity collapse and thus retarding the rate of erosion. An EDAX analysis was carried out on this crater to understand the chemical composition which is shown in Figure 3.41 inside and outside the crater showing loss of aluminum and silicon.

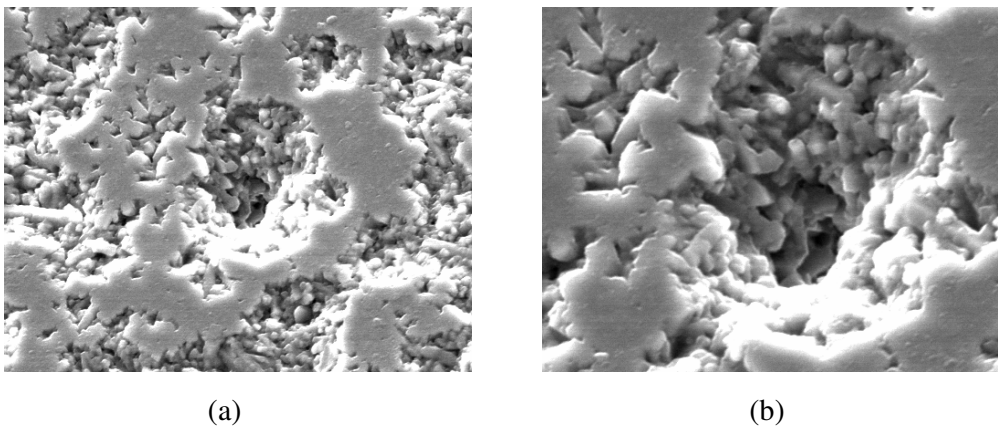


Fig: 3.40 (a) Observed crater in material C after 45 hours of cavitation testing and (b) close up

Label A: Inside the pit

Label B: Outside the pit (Ball surface)

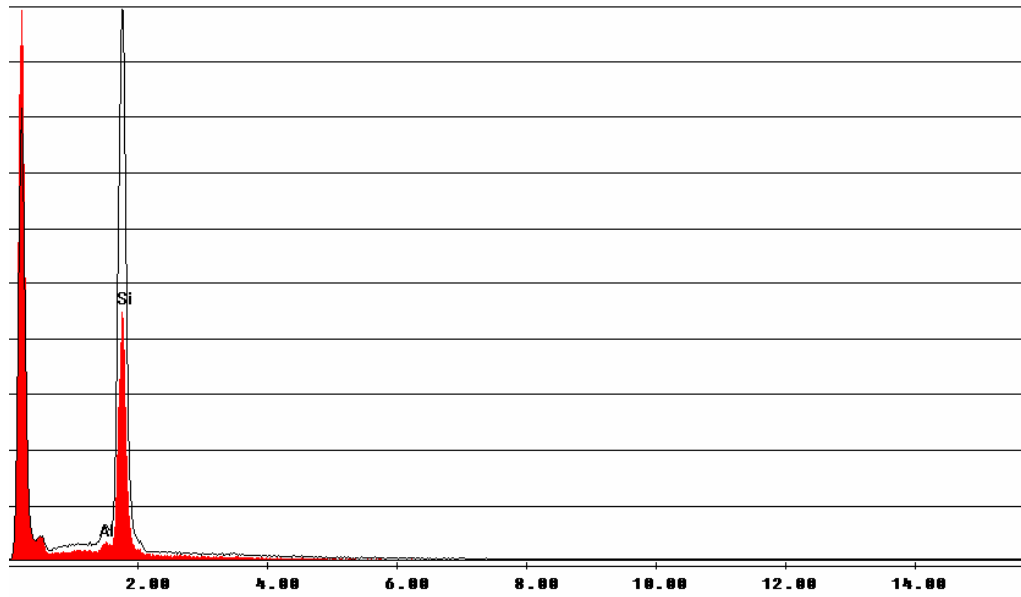


Fig: 3.41. EDAX spectra comparison inside and outside of the crater.

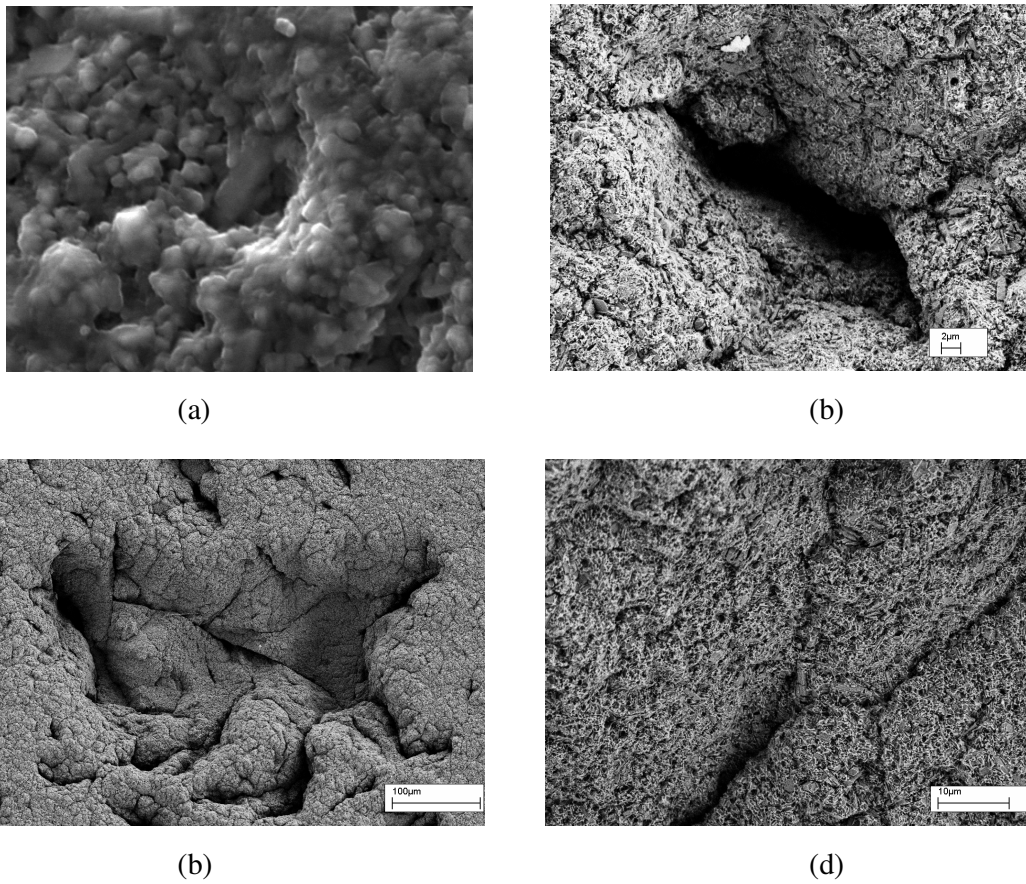


Fig: 3.42. Attenuation stage images on material A and B show deep craters.

3.5 Stages of Erosion

Despite differences in cavitation conditions and material properties, the process of material damage which undergoes a certain progression is common in all materials exposed to cavitation. The whole process of cavitation erosion can be divided into five major stages as shown in the Table 3.2 below: The very beginning period of cavitation erosion where no detectable loss of material is observed corresponds to this incubation stage. The time duration of this stage varies with different materials and also with varying test conditions like test liquids, magnitude of erosion, operating frequency. Hence comparing incubation period of materials should only be made with similar testing conditions. Material behaviour during this stage is very difficult to understand as no visible modifications are made to the material surface.

No:	Stage	Description
1	Incubation	No detectable material loss
2	Acceleration	Increase in the rate of erosion
3	Steady-rate	Material loss remains constant
4	Attenuation	Decrease in the rate of erosion
5	Terminal	Material loss remains constant at a very low level

Table: 3.2. Description of stages in cavitation erosion

There are several factors responsible for this incubation stage. First and foremost is the nature of load applied on the material surface. Experiments carried out on the test samples for a very short period of time showed no material loss or even any visible damage under scanning electron microscopy. Test period was extended for 15 minutes with a very high powered transducer and found severe erosion on the material. The same testing conditions were repeated on a test specimen, which was allowed to rotate freely rather being stationary. This rotated specimen showed only a very few number of pits with no severity of erosion which clearly proves that cavitation erosion is fatigue process and several thousands of stress or load cycles are required to cause failure.

Surface investigations on eroded samples revealed the nature of failure to be brittle fracture in silicon nitride as discussed in section 3.1. It was shown that micro cracks generated and propagated during the early stages of erosion. It is well known that brittle fracture requires crack initiation and propagation and thus consumes some time before failure. Also the energy released during cavity collapse is observed by the material. This impact energy absorbing capability of the material is another reason for incubation period during erosion. The testing conditions are one of the primary reasons which vary this incubation period by varying the impact cyclic pressure. This scenario was investigated and is presented in section 3.7.1. Using the high powered transducer with amplitude of vibration 60 microns peak to peak had a very short incubation period of 3 minutes compared to 40 minutes by low powered transducer which operates at amplitude of 16 microns peak to peak. Different stages of erosion as tested with high powered transducer with reduced amplitude of 25 micron peak-peak amplitude are shown in Figure 3.43 below. This power reduction was used for these long run tests mainly to avoid damaging the transducer by cavitation.

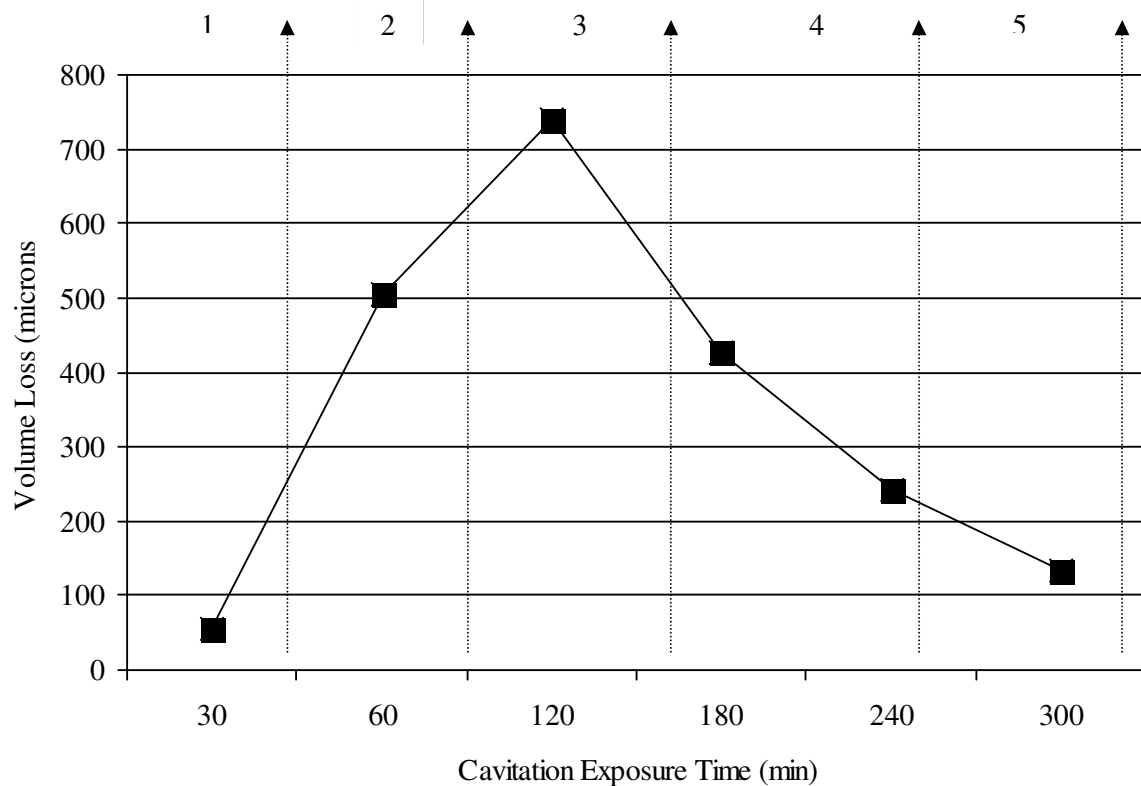


Fig: 3.43. Different stages of cavitation erosion in silicon nitride

This incubation stage was followed by huge loss of material by pitting as marked as number 2 in the Figure 3.43. This stage corresponds to the increased rate of erosion, where new cavitation pits formed from linking up pores and micro cracks. Pit growth is the next stage where constant level of material was removed. Once severe pitting was observed, a decrease in the rate of erosion was observed corresponds to the stage 4 as in the Figure 3.43. Finally, large pits were formed which developed into craters permitting bubble cushion effect as discussed in section 3.4 where a low level of material loss was constantly observed. This stage is not common in all materials but was found in many materials (Chen 2002).

3.6. Heterogeneous Surface

It was found that microstructure and porosity plays a vital role in providing cavitation erosion resistance. This was systematically investigated by experimenting different material surfaces of silicon nitride. Rough surface with surface defects such as indents

and surface cracks were generated for this purpose. Three silicon nitride ceramics from different manufactures were chosen for this purpose. A diamond cutting tool was used to section the specimens into a flat surface as explained in section 2.13. This was then polished to sub micron finish to attain a very smooth surface for testing. These specimens were tested for cavitation erosion and results are presented in the following sub sections.

3.6.1. Polished flat specimens

Three silicon nitride materials named S₁, S₂ and S₃ of varying properties as shown in Table 3.3 were tested for certain duration of time. These are materials with high nitrogen content and have almost no glass phase as in conventional silicon nitride. Tests were carried out at maximum transducer power for durations of 15, 30 and 60 minutes. Instead of distilled water a cutting fluid of viscosity of 2.4 cSt at temperature of 40⁰C was mainly used because of industrial interest. Effect of viscosity on the rate of erosion is presented in section 3.7.2. All these materials did not show any signs below 10 minutes of test duration. Notable material loss was noted from 15 minutes. Surface parameters like roughness, volume loss, maximum height and peak-to-peak were measured at equal intervals and are presented in the following Figures 3.44 to 3.47.

Material	Primary Matrix	HV 10 GPa	Fracture Toughness MPa(m) ^(1/2)
S ₁	$\alpha + \beta$ Sialons	17	7.3
S ₂	α Sialons	20	4.8
S ₃	α Sialons	18	5.5

Table: 3.3. Properties of flat and polished silicon nitride test specimens.

As shown in Figure 3.44, test material S2 has a very high roughness at the initial stages of 15 minutes compared to the other two. This material has a low fracture toughness of $4.8 \text{ MPa } \sqrt{\text{m}}$. It was shown in the previous sections that erosion in silicon nitride initiated by fracture. With low fracture toughness this material showed poor resistance at the initial stages, but the interesting thing to be noted is in the subsequent stages where the roughness remained lower compared to the other two.

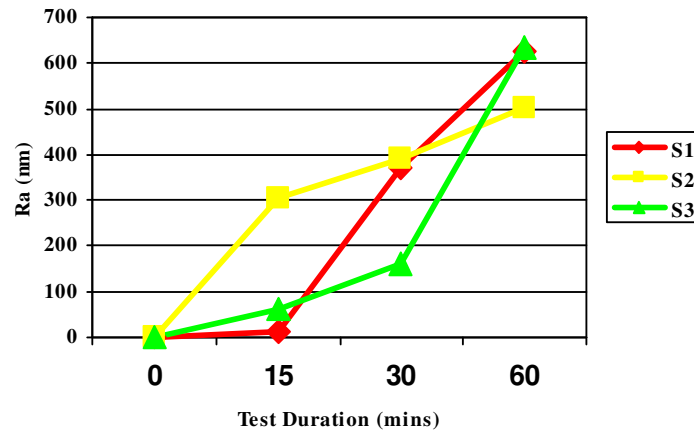


Fig: 3.44. Surface Average roughness over cavitation exposed time

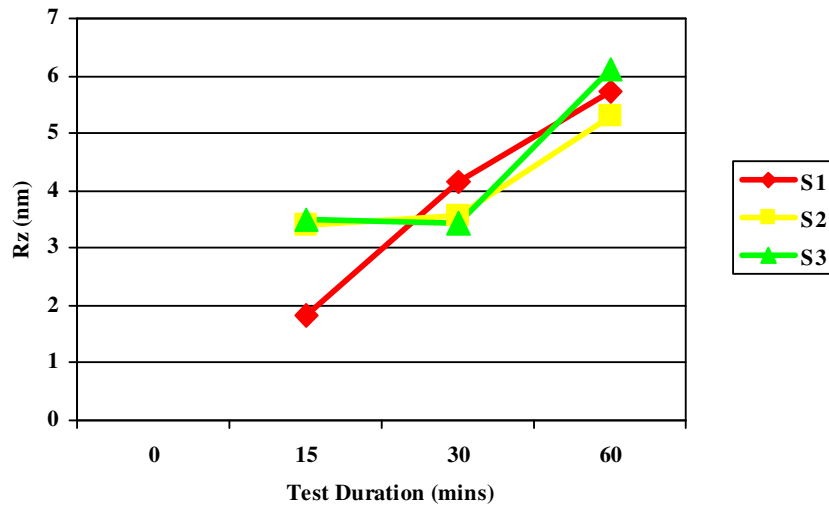


Fig: 3.45. Average Maximum Height over cavitation exposed time

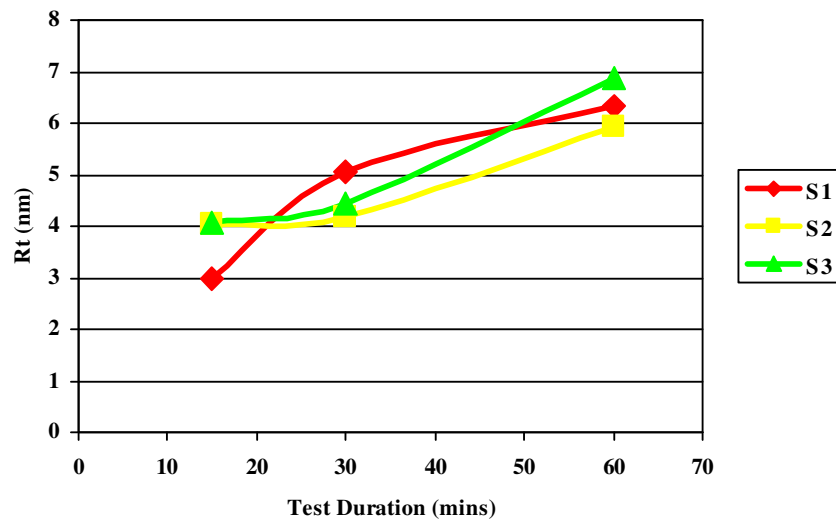


Fig: 3.46. Peak-to-Peak value over cavitation exposed time

Material S1 has a primary matrix of both alpha and beta sialons, beta matrix is mainly attributed to long elongated grains which increase the fracture toughness of the material. This property plays a vital role in deflecting the crack and also provides resistance for crack bridging. If trans-granular fracture occurs at the initial stages, this breaks up the grains and thereby increasing the porosity in the material. This porous surface encourages cavitation nucleation and accelerates the rate of erosion. From Figures 3.44 to 3.47 shows that this material S1 has a strong resistance remaining at a very low level of material degradation compared to the other two. With the test continued after 15 minutes shows that the material S1 is no longer capable of providing good resistance. This is due to the displacement of a whole grain or bunch of grains by two possible mechanisms. One is the grain cracking which lifts up the grain and the other is the grain boundary phase weakening due to inter-granular fracture. Microscopic investigations on these materials showed that the damage initiation and progression was similar to the conventional materials. There was no difference identified in the mechanism of wear despite the variation in erosion rate.

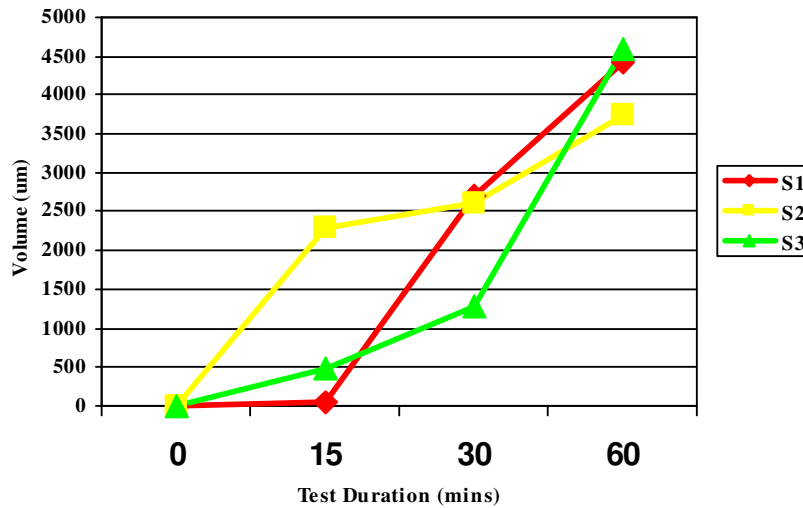


Fig: 3.47. Volume loss over cavitation exposed time

3.6.2. Surface Defects

The quality of surface finish largely contributes to the life of silicon nitride balls in applications. Surface defects such as surface cracks, radial and lateral cracks are common on finished balls due to manufacturing pressing faults or impact cracking. These defects are the primary cause for fatigue spalling which reduces the RCF life compared to bearing steels (Wang 2000). Advanced manufacturing and surface finishing methods have nearly eliminated these defects and thus have an improved RCF life. Extensive research work has been carried out to examine the rolling contact life with such defects (Wang 2000, 2002, Zhao 2004). But, cavitation erosion studies on these defects were not reported and are presented in the following sections.

3.6.2.1 Indents

A 10 kg Vickers's hardness indent was created on the surface of the silicon nitride ball as explained in section 2.1.3. The geometry of the indent is shown in the Figure 3.48. Light microscopy was used to measure the diagonals, which are $d_1 = 0.06$ and $d_2 = 0.08$ mm respectively. This area was carefully marked and positioned in the erosion test specimen holder. The area of cavitation exposure is approximately 20 mm

which also covers the smooth area adjacent to this indent. This helps to compare the response of both surfaces at same time. Cavitation erosion experiments were carried out on the indent for few hours until the indent was severely eroded, with test intervals monitoring the wear progression.

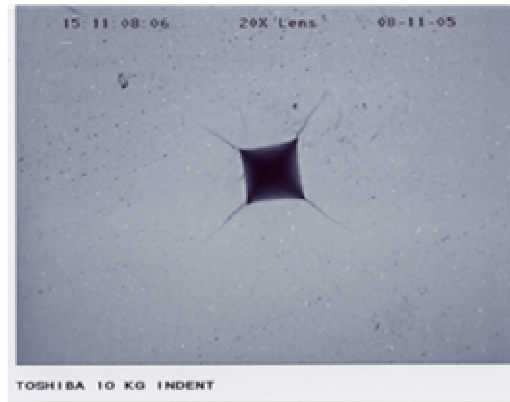
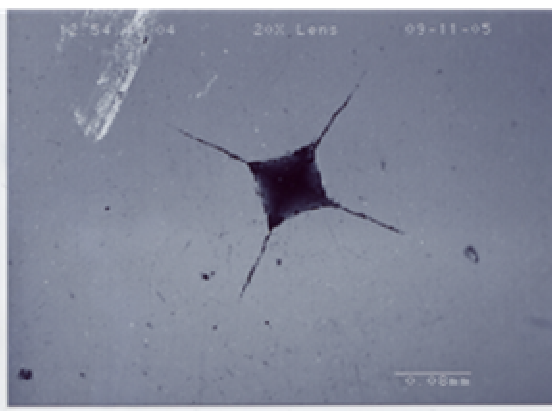
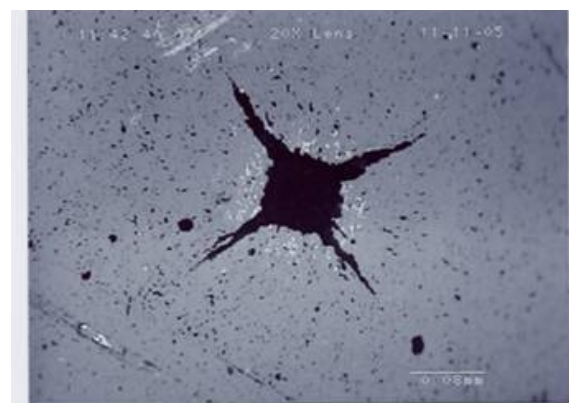


Fig: 3.48. 10 Kg Vickers's Hardness Indent

These experiments used the low power probe which vibrates at amplitude of 16 microns peak-to-peak. The indent was examined under light microscope after equal intervals of exposure to cavitation and is shown in Figure 3.49. Figure 3.49 (a) Shows the eroded indent after 30 minutes. The indent is quite moderately eroded, whereas the surrounding areas show no sign of erosion. This clearly proves that porosity is the important factor for erosion. Any small defects or rough surface encourages cavitation by providing a favourable condition for bubble nuclei.



(a)



(b)

Fig: 3.49 (a) & (b) Eroded Indent after 30 and 60 minutes.

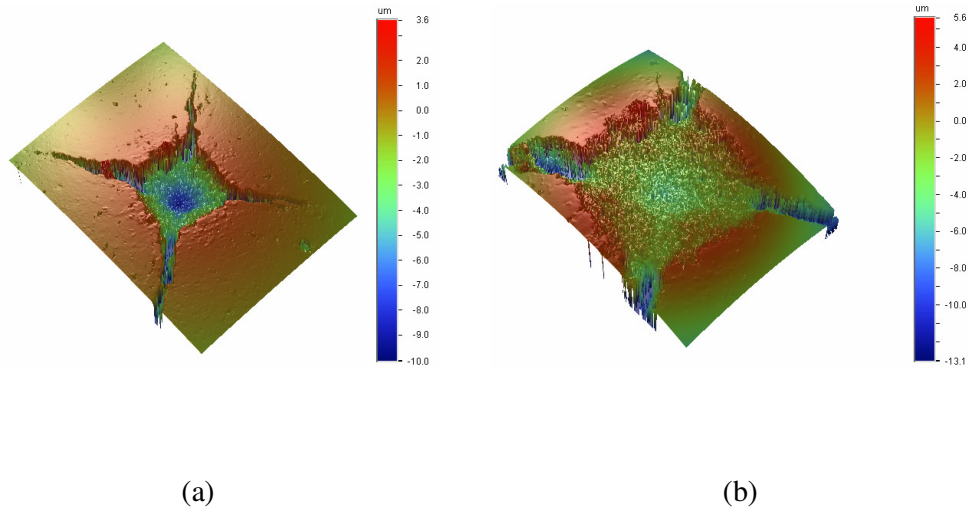


Fig: 3.50. (a) and (b) Eroded Indent after 240 minutes.

Further exposure to cavitation for the next 30 minutes results in a severely eroded indent and erosion initiation in the surrounding areas was noted which is shown in Figure 3.50 (b)

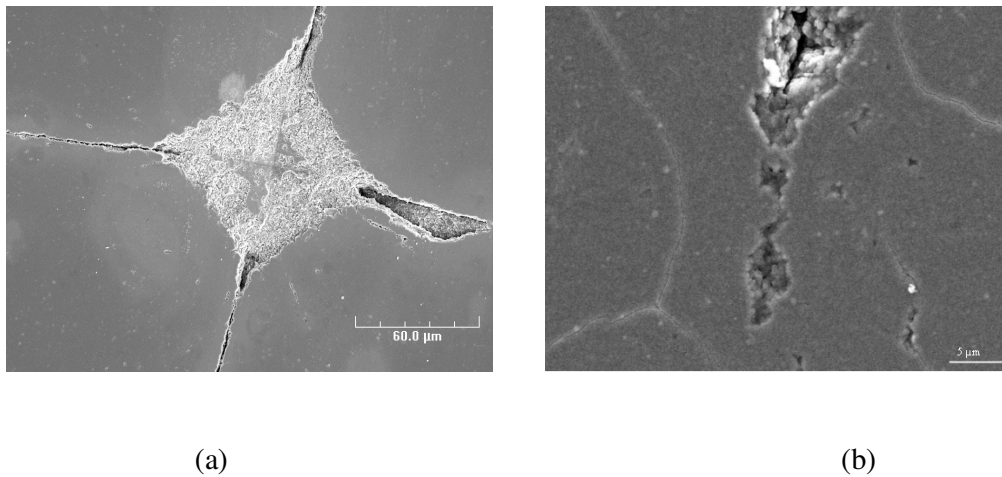


Fig: 3.51 (a) SEM images of Indent eroded after 60 minutes and (b) visible cracks

3D surface scanning microscopy, described in section 2.4.3 was used to measure the surface changes encountered during erosion tests. Indent and the edges were severely eroded, whereas the surrounding surface shows no damage. The indent edges serve as a home for bubble nuclei. This helps cavities to grow and violently collapse under transducer excitation. Also the process indentation applies high load to cause damage or indent on the surface which locally disturbs the microstructure of the material. This weakened area was no longer able to withstand any further loading and hence eroded much faster than the smooth and fresh adjacent surface. This clearly proves that cavitation erosion is a material degradation process resulting from highly localized forces and damage occurs at microscopic level.

Erosion on Indent after 2hrs show that the edges were widened and further exposure to cavitation showed erosion initiation on the fresh surfaces. These erosion marks were typical erosion pits as shown in the previous sections. But, the interesting feature to be noted is the visibility of cracks surrounding the indent as shown in Figure 3.52 (b) Scanning electron microscopy studies showed this formation of cracks which are very long than the cracks observed in tests carried on samples without indents. Surface away from indents showed similar cracks and few of them on specimens tested without any surface defects. Tests on this material A showed the cracks and were only observed originating from the white ball like feature as shown in Figure 3.52 (b) EDAX analyses on these white coloured features showed that they are titanium. The presence of these micro cracks signifies that erosion initiates in the smooth surface adjacent to defects. This is specially related to material A and no such failure feature was observed in other materials. Figure 3.53 shows the EDAX spectrum taken on inside and outside the indent. The red colour is the reading taken inside the indent and the black coloured spectra overlying it is the one taken outside the indent. This shows loss of Titanium, the crucial material which provides superior resistance to cavitation.

3.6.2.2 Cracks

Like indent, surface cracks were tested for erosion response. As expected, the damage process was quite similar to that of indent. Figure 3.54 shows the surface crack and

the subsequent erosion damages. Same testing conditions were followed for this. Erosion initiated on the crack during the beginning stages of erosion testing. No sign of damage was observed in the surrounding areas during this stage. In later stages erosion pits formed all over the exposed area while the crack was widened and severely eroded.

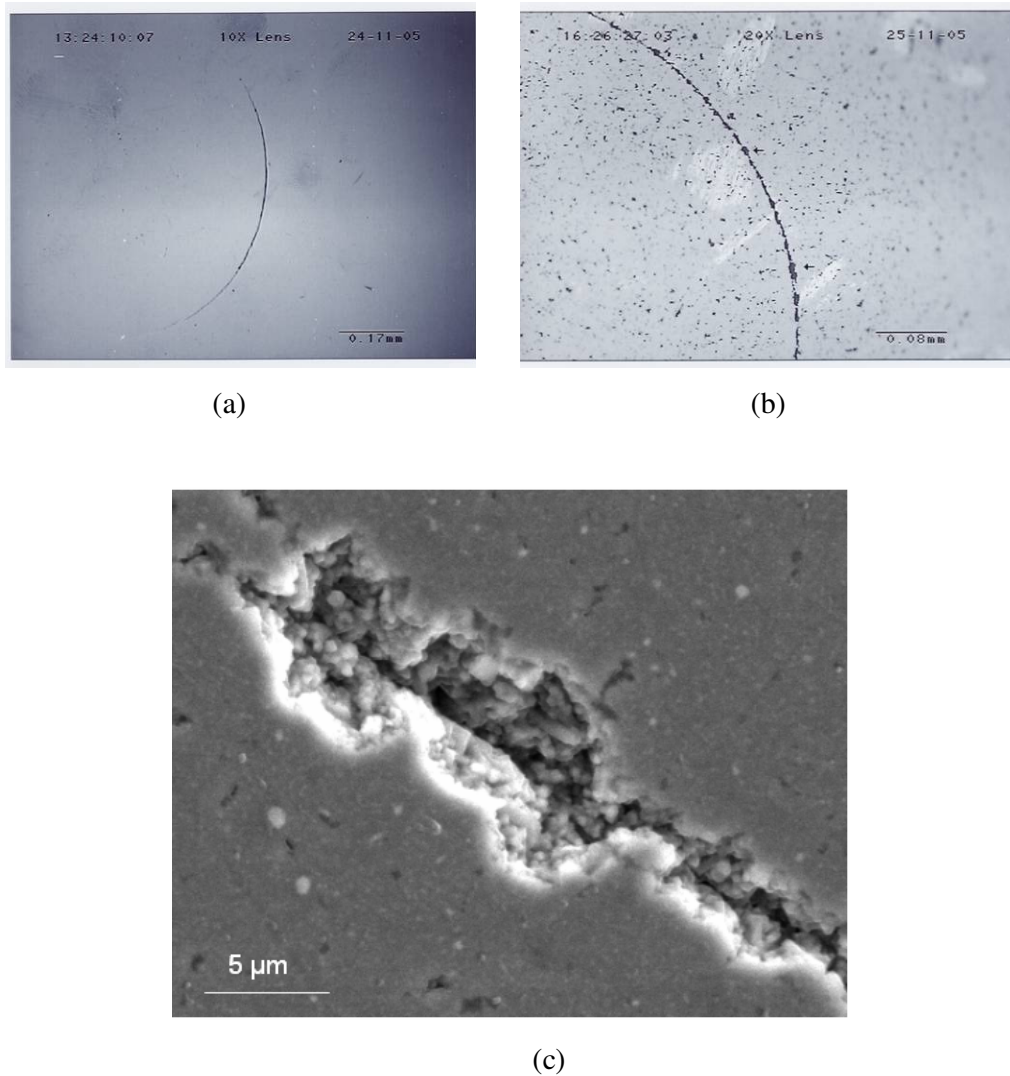


Fig: 3.54 Surface crack (a) Light Microscope image of crack before testing, (b) after 2 hrs of erosion testing and (c) SEM image of eroded crack.

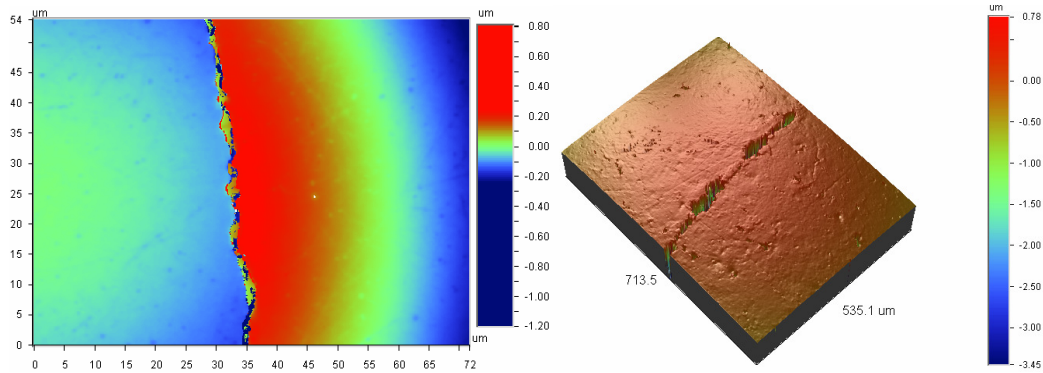


Fig: 3.55. Surface microscopy images (a) Surface crack and (b) eroded crack and surrounded by pit inception.

3.6.2.3. Star Defect

Another surface defect was accidentally found while testing fresh silicon nitride balls. This defect appears in a star shaped form and hence called as star defect. This defect is not very common, but can sometimes be found in finished bearing balls. Formation of this type of defect is caused due to diamond particles during the final stages of polishing.

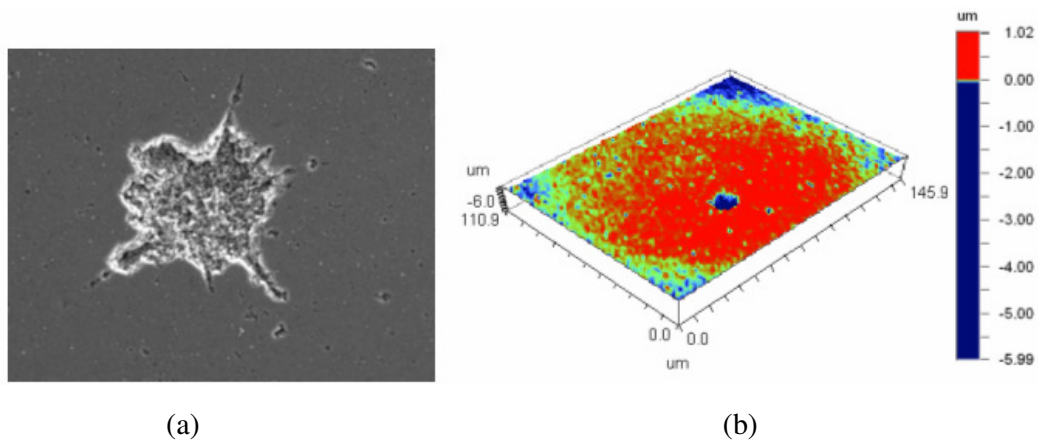


Fig: 3.56 SEM image of eroded star pattern and (b) Surface parameters

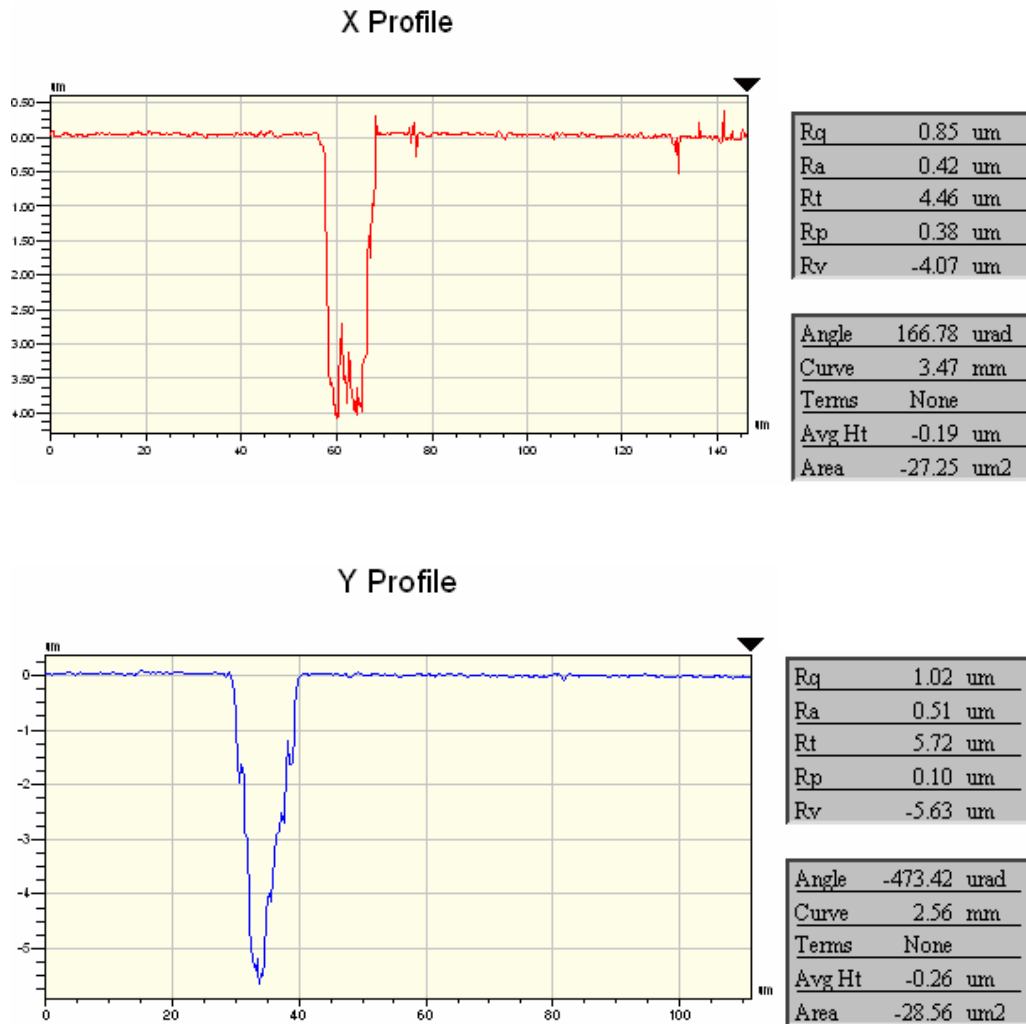


Fig: 3.57. Surface profilometer measurements on the STAR defect.

Scanning electron microscope image showed in the Figure 3.56 clearly shows severe erosion on the star defect and only a very few pits is seen on the surrounding areas. This is another solid proof that erosion is largely influenced by surface porosity. Light interferometry measurements shown in Figure 3.56 and 3.57 that the star defect is deep as 6 micron with half a micron of average roughness. This increase in roughness due to erosion would encourage further failure mechanisms in rolling contact such as, subsurface cracking, delamination and spalling. Silicon nitride ball manufactures have developed their own sophisticated screening techniques to identify and remove the balls with such defects.

3.7. Cavitation Conditions

The level of cavitation and the rate of wear produced largely depend on the cavitation conditions and extensive research was carried out to examine this dependence. Pressure, temperature, flow velocity, liquid properties and gas content in the test liquid were among the parameters included for these studies. Effect of pressure and temperature showed that erosion rate increased to a certain level and decreased as any further increase in both (Tao 1971, Young 1999, Chen 2002). Fluid velocity was found to be directly proportional to the erosion rate with experiments conducted in cavitation tunnels and rotating test rigs (Steller 1999). Influence of gas content is same as with pressure and temperature, small amount of increase in gas content in the test liquid helps generate more nuclei for bubble generation and thus increasing cavitation. Further increase in gas content creates a cushioning effect during bubble collapse and thus reducing the wear rate (Young 1999). Parameters which are interested to this project like the effect of vibration amplitude, viscosity and fluid thickness between the horn tip and the test specimen were studied and are presented in the following sections. The remaining test parameters were kept constant for all experiments.

3.7.1. Effect of Magnitude of vibration

It is generally believed that vibration amplitude of the transducer is directly proportional to the rate of erosion. This was initially experimented to find out the incubation period of silicon nitride in order to understand the ultrasonic power system performance for further experiments. As mentioned early, two high and low powered piezoelectric transducers of vibration amplitude 16 and 60 μm respectively was utilized for this project. The amplitude of vibration is directly proportional to the acoustic power and hence investigating the effect of one is sufficient to understand the other. At very low amplitudes of until 3 microns peak-to-peak no signs of damage were noted. This is because for less than 3 microns of vibration amplitude, the bubbles generated are stable which continue oscillating for several cycles without collision with the solid surface. Erosion started to appear just over this amplitude and the test duration was very long which made to discontinue tests under the amplitude

of 10 microns. Above this amplitude, erosion rate sharply increased against increase in vibration amplitude and peaks up at the maximum available amplitude of 60 microns where a notable material loss was observed in 3 minutes. These observations were shown in the graph in Figure 3.58 where the erosion starts in a short time of testing as the vibration amplitude was increased. The increase in amplitude increases the acoustic streaming which help generate transient bubbles causing disruptive effects on the solid surface.

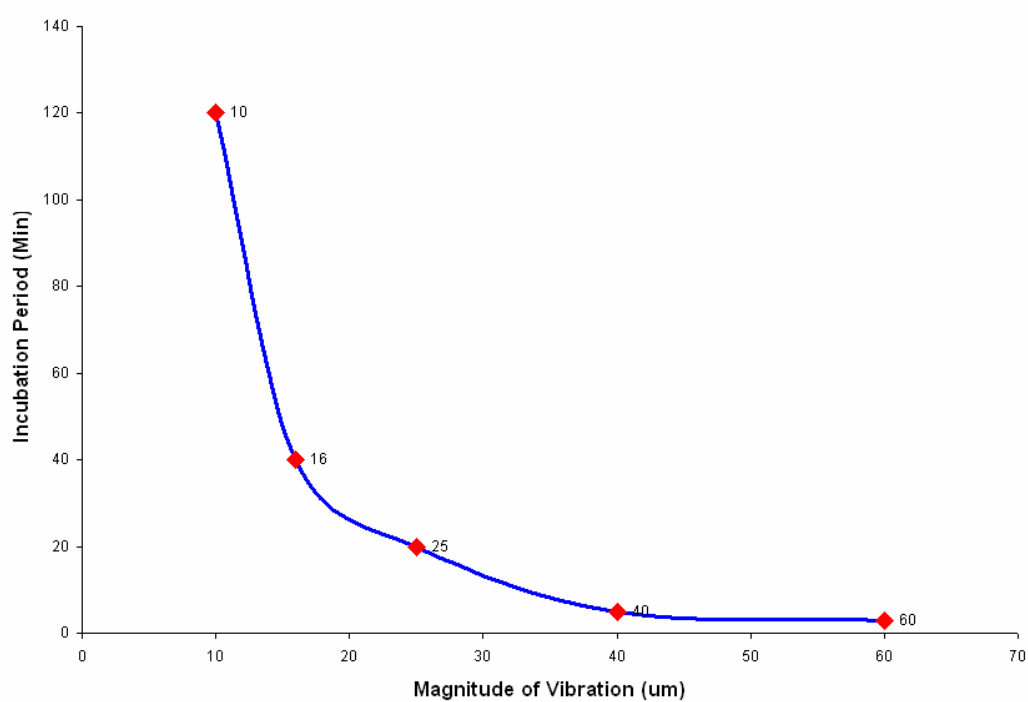


Fig: 3.58. Influence of Vibration amplitude on erosive wear

3.7.2. Effect of Viscosity:

Most of the cavitation experiments carried out for this project used distilled water as test liquid. Apart from this, some lubrication oils used in industrial applications were also tested to understand their influence on the rate and mechanism of erosion. All test parameters like magnitude of vibration, operating frequency were kept constant for these tests. This systematic investigation helped understand the effect of fluid properties on cavitation damage. Different test liquids as shown in Table 3.4 below

were chosen mainly because of varying viscosity values. As seen from the Table, highest rate of erosion was noted in water and the lowest was in cylinder oil which has a viscosity value of 1040 cent-strokes. A high viscous fluid subjected to cavitation must produce a high intensity pressure pulse upon collision, and therefore the rate of erosion must increase. But results show that there is a decrease in the rate of erosion as viscosity increases.

Liquid	Viscosity at 40 ⁰ C (cSt)	Notable Material Loss
Distilled water	0.658	20 minutes
Shell Macron 110	2.4	60 minutes
Gargoyle oil	32	90 minutes
Shell Talpa 20	94.6	4 hours
Cylinder oil	1040	Test discontinued after 12 hours

Table: 3.4 Viscosity influence on the rate of erosion

This is attributed to the overall level of cavitation intensity produced by the ultrasonic transducer. Test liquid with an increase in viscosity directly increases the load for the ultrasonic power system. This results in the creation of less cavitation for the same magnitude of vibration and power. Also, the bubbles generated by the horn form a cluster which oscillates until it becomes unstable and violently collapse on the surface. This bubble cluster is directed to the solid surface by the steady forces generated by the acoustic field. Increase in viscosity also affects this translational motion and thus decreasing the rate of erosion. On the other hand, the mechanism of

erosion was found to be similar in all test liquids. There is no difference in the nature of cavitation damage formation. To conclude, liquid properties affect the rate of cavitation erosion but not the wear mechanism.

3.7.3. Effect of Fluid Thickness

The fluid thickness between specimen and the transducer horn is crucial and plays an important role in the rate of cavitation erosion. This effect was studied by performing experiments by varying the distance of test specimens away from the transducer end and these results are presented in Figure 3.59. As mentioned early, very high pressures are generated in the liquid upon exciting the transducer. In order to produce an effective transformation of this high pressure pulses to the specimen, any loss in the magnitude of this acoustic signals must be avoided and this can only be achieved by placing the test specimen as close as possible to the transducer. On the other hand, time duration in the order of few micro seconds is required for the generated bubbles to grow up to resonance or transient size before colliding the solid boundary. This time duration could be only be permitted by allowing some distance for the acoustic waves to travel. Experimental results show that a distance of 0.5mm between the specimen and the transducer tip provides the maximum rate of erosion. This is in good agreement with the previous findings (Chen 2002, Cheng 2003)

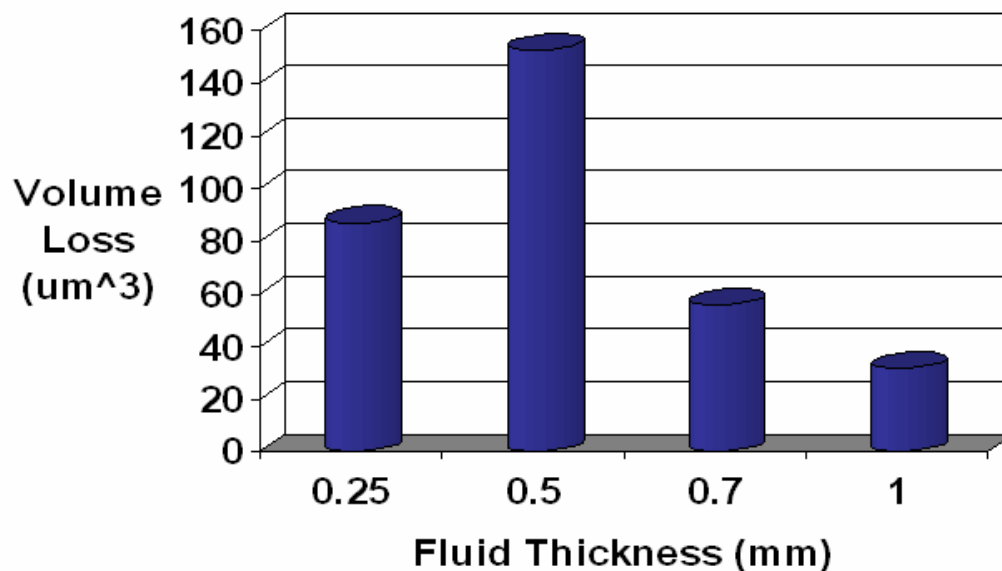


Fig: 3.59. Erosion rate dependence on film thickness

3.8 Erosion in Steel

Cavitation erosion tests were also conducted on bearing steel in order to get an idea about its resistance compared to silicon nitride. Many reports on cavitation erosion of steel can be found in the literature (Vyas 1990, Feller 1984, Fu 1998, Lin 2005). Test material used for this purpose was a bearing rolling material made of carbon chromium steel with same dimensions to the silicon nitride rolling elements. Material properties of this material are given in Table 2.2. Ductile materials are well known to provide good resistance to cavitation and in particular, steel is ranked one of the superior materials (Young 1999, Chen 2002). Erosion testing was carried out using both low and high powered transducer. It was found that erosion initiation time in steel was found to be 5 times longer compared to silicon nitride. Figure 3.60 below show the erosion initiation process with very few numbers of pits. This was observed after 30 minutes of testing with the high powered probe. It took 5 minutes to attain the same level of damage in silicon nitride. It was same for the low powered transducer; this initiation time is in good agreement with the literature (Chen 2002)

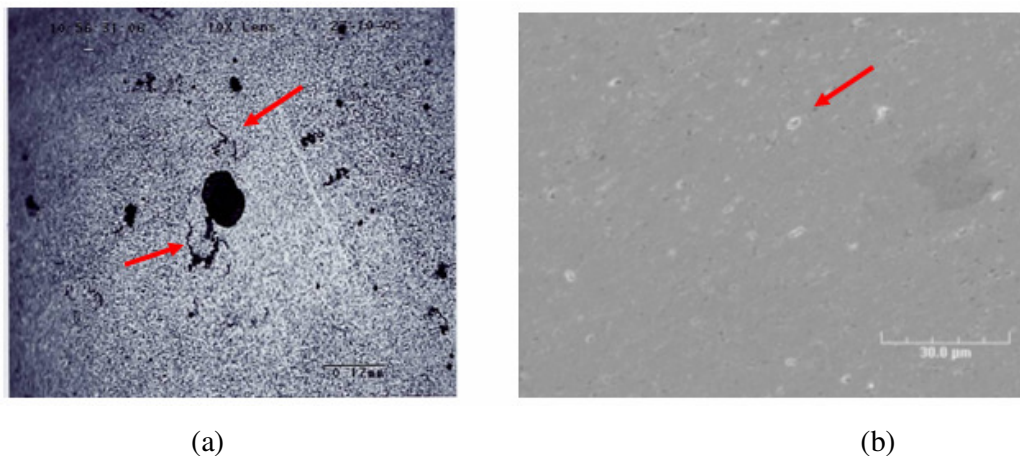


Fig: 3.60 (a) and (b) Light and scanning electron microscope images of erosion initiation in bearing steel.

The main damage mechanism in ductile materials is by plastic deformation or ductile rupture. The initial stages of erosion shows some minor surface changes without any notable material loss. This can be seen in the above Figure 3.60 where marked areas show development of micro cracks. These cracks are developed from the pores or micro pits which act as stress concentrated areas. These cracks are very large

compared to silicon nitride. This stage is also related to the surface work hardening effect, which then removes the surface layer as shown in Figure 3.61. Further exposure to cavitation results in pitting, process similar to in silicon nitride.

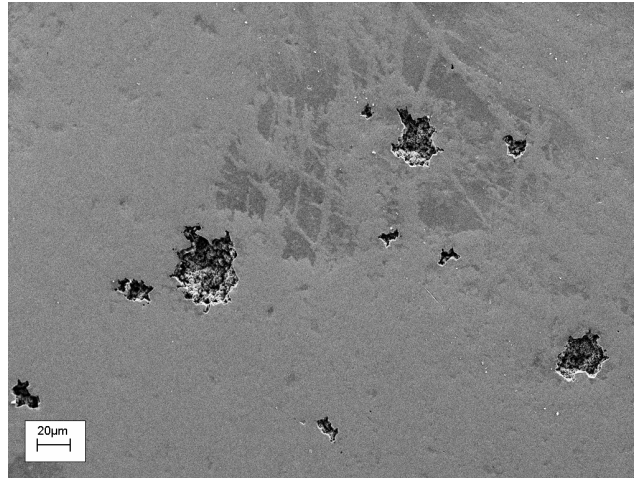
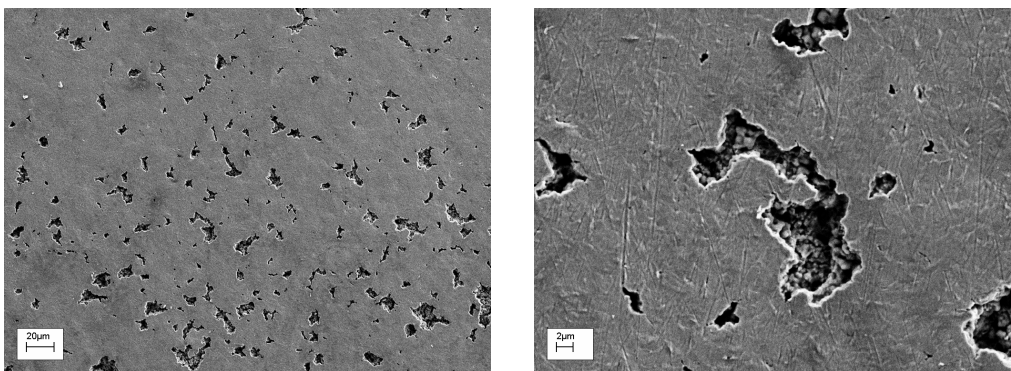


Fig: 3.61 Surface layer damage in steel due to erosion

Erosion pits in steel are different from the geometry of pits observed in silicon nitride as shown in Figure 3.62. The mechanism of failure is ductile fracture. Not different steel test materials were tested to find out the mechanical properties and micro structure correlation to its resistance for cavitation. This is already detailed in previous findings (Bregliozzi et al 2005), and is out of scope of this work. However, this comparative study clearly shows that steel is much superior to cavitation compared to silicon nitride.



(a)

(b)

Fig: 3.62 SEM images of erosion pits in bearing steel.

Chapter 4

MECHANO-EROSION

This chapter provides the experimental methods and results of combined erosion and rolling contact wear testing. Cavitation erosion and rolling contact fatigue were mostly seen as different wear mechanisms and there were few attempts to find the correlation between these two. Cavitation in bearings has been studied for over a century, a controlled approach to study this phenomenon is very limited. Beginning sections of this chapter discuss about the correlation of cavitation erosion and contact fatigue of ball bearings. Section 4.2 presents an attempt made to study erosion on rotating specimens which required few alterations in the erosion testing approach leading to an external drive motor setup. Section 4.3 presents rolling contact fatigue experiments performed on eroded specimens from conventional testing. This is followed by a novel test methodology which was designed to accelerate and study erosion in rolling contact. This test method made it possible to achieve controlled cavitation in rolling contact fatigue experiments. This section 4.4 discusses the design and modifications made to the rotary tribometer, and the following sections describe the testing conditions and subsequent results obtained from this method leading to the delivery of a new testing methodology.

4.1 Cavitation Erosion and Rolling contact Fatigue

The first notable publication in an effort to find the correlation between cavitation erosion and rolling contact fatigue resistance was by Tichler and Scott (J W Tichler et al, 1970). They reported on the resistance of materials to both rolling contact fatigue and cavitation erosion. Their test materials were ball bearing steels, a rolling four-ball test similar to the one used for this project was used. A magnetostrictive transducer vibratory test method for cavitation erosion was utilized. They concluded that both tests on the test materials showed that they quite corresponds each other in their time to failure. For cavitation testing, materials showed severe pitting after 17,000 and 9,000 minutes and 121 and 69 minutes for rolling contact testing.

Further few questions they raised were:

1. Under conditions of lubricated high-stress rolling contact is cavitation erosion a contributory factor in the initiation of surface fatigue?
2. Is there a fatigue process interpretation of cavitation erosion?

The answer to the second question was detailed in chapter 4 by showing the fatigue damage process involved in cavitation erosion. Cavitation certainly occurs in the lubricating oil at the trailing edge of the rolling contact. But how cavitation affects the material damage in rolling contact is unclear. In a later publication, Scott et al presented results on the formation of spherical particles in rolling contact fatigue (Scott et al, 1973). The presence of these particles is as shown in Figure 4.1 they argued that it could be a result of cavitation due to the application and release of extreme pressure in the contact.

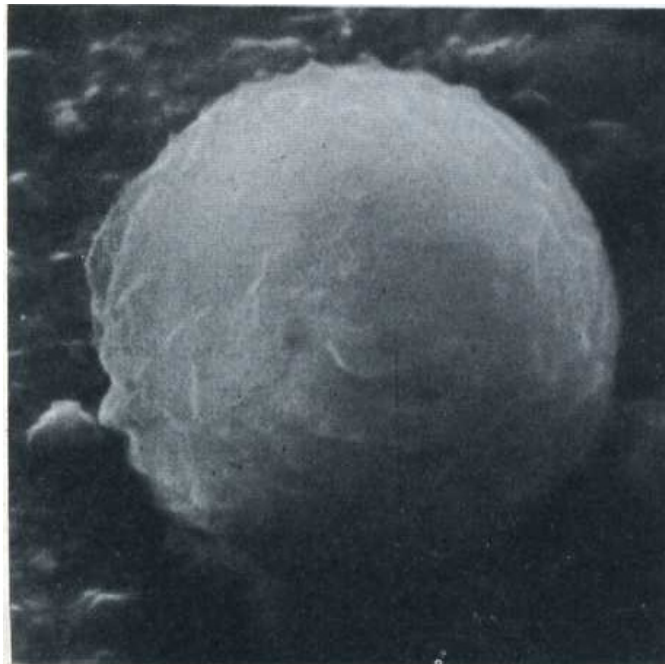


Fig: 4.1 Typical spherical particle debris reported in rolling contact (Scott et al, 1973)

4.2 Rotating Specimen

Erosion tests on stationary specimen were presented in chapter 3 of this report. Thorough surface investigations did reveal close relation between erosion wear damage and river mark type wear found in applications. As shown in Figure 4.2 the nature of pit formation growth is similar in both application and laboratory testing. However, the geometry of the river mark which runs all over the rolling element with tributaries in the shape of a river was not observed in the laboratory. The major difference between erosion damage in laboratory testing and application rolling element is the scale of erosion damage, mainly the pit formation which is very dense in case of materials tested in laboratories. Although the number of pits in application balls is very less they clearly show the pit growth is same as in erosion i.e. by the process of linking up or pit bridging as described in section 3.2

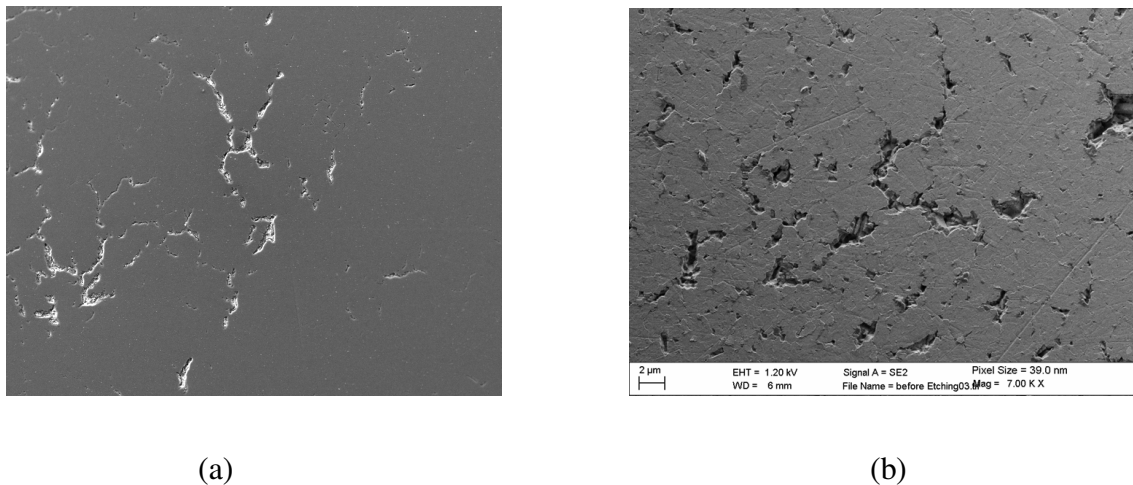


Fig: 4.2 (a) River marks in application balls (SKF Unpublished) and (b) Erosion marks obtained in laboratory.

One major reason for this difference is the dynamics of the rolling elements in real applications. As mentioned early, the cavitation erosion produced by vibratory cavitation method is a poor reproduction of real cavitation conditions. In applications, rolling

elements can exhibit varying state of material removal in the form of wear due to variations in the running conditions which is not the case in the laboratory testing, where the loading type is characterized by steady-state. Moreover, the specimen is kept stationary in cavitation erosion experiments which expose the same area of the test material to cavitation. The high intense and dense cloud of cavities generated in the vibratory testing can also be the reason for this difference. In order to vary this laboratory testing conditions, a rotating specimen approach was tested to investigate any significant variation in the erosion wear process.

4.2.1 Testing Methodology

An external drive set up had to be designed to set the test sample in rotation whilst testing. In stationary specimen testing, the specimen was held in a specimen holder which was placed at the bottom of the test beaker. To realize motion in the test rolling element, a drive set up should be placed beneath the specimen to transmit motion effectively. This is very difficult as the drive set up should be immersed in the liquid which raise design complications. One way to solve this was to keep the drive motor externally out of the test beaker but transmit motion through a shaft drive. Further complications rose to hold the silicon nitride ball vertically in the beaker as this required to keep the test specimen close to the piezoelectric transducer. This way of holding the specimen needs the motion to be transmitted in many directions from the motor to the specimen. Also, as mentioned early the diameter of the test specimen is 12.7 mm which provide a small tolerance to fasten it in a specimen holder.

To overcome these challenges, it was decided to test a specimen of different shape that would allow solve these problems. A cylinder silicon nitride test sample of 50 mm in length and 15 mm in diameter was provided by the project sponsor. This longer axis of 50 mm can be placed under the transducer. To set the required rotation in the test specimen an external motor gearbox as shown in the Figure 4.3 was used. This is a small gear box made of steel and brass with brass gears and is mounted on a 1 mm thick steel bracket. It has a 3 pole motor with sleeved bearings, which provide a controlled rotational

speed in the range of 200 to 1120 rpm through an output shaft of 4 mm diameter. To transfer this motion to the specimen a bevel gear setup was used, which has steel gears and shafts running in ball braces and is made of nylon, offering high strength. A long steel shaft was manufactured in the workshop along with the required couplings. These were then mounted as shown in the Figure 4.3 using the pre-drilled mounting holes. A wooden block was made to mount the gearbox setup. This was achieved by fastening the steel bracket of the gearbox by screwing it to the wooden block. A laboratory stand was used to hold the wooden block firmly and the required power was supplied by an electrical source. An aluminum stand was manufactured to fix the bevel gear setup as shown in the Figure to hold the specimen at the desired position.

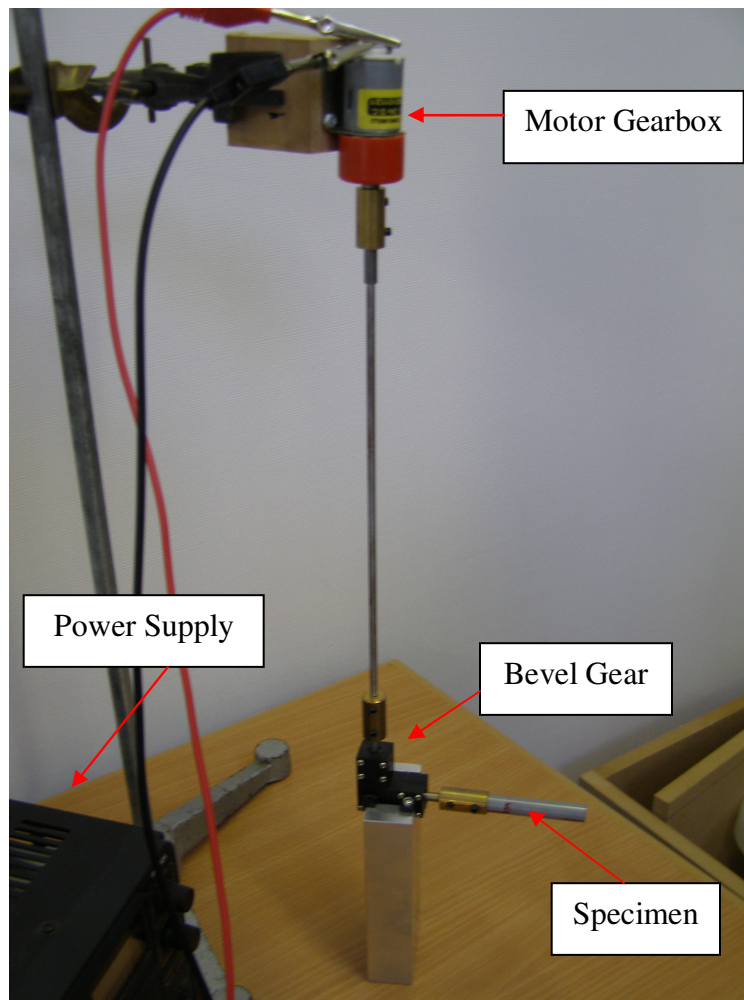


Fig: 4.3. Rotating test specimen set up.

4.2.2 Results and Discussion

With reasonable high speeds of 600 rpm specimen rotation, the incubation period was found to be longer compared to the stationary specimen by at least a factor of 2. The variation in the erosion rate or material loss was not measured as the main objective of this test was to find if there is any change in the nature of erosion damage compared to stationary specimen. After 90 minutes of testing with the low powered transducer, erosion pits were formed on the test material. The usual damage variation observed in the stationary test specimen such as centre wear was not observed on this specimen due to same level of cavitation intensity on all parts of the material which was exposed to cavitation. The interesting part of the observation was that there was an uniformity in the presence of erosion pits. The light microscope images of this result are shown in Figure 4.4. The initial erosion pits formed in a straight line across the cylinder. Further testing on this specimen showed similar pit bridging process as part of the erosion growth. The distance between the initial pits were reduced by formation of new erosion pits in between them. This is due to the concentrated load nature of vibratory cavitation. This load concentration encouraged further erosion in the form of new pits. As marked in Figure 4.5 the nearby pits were joined together. The material damage geometry was not similar to river marks as found in application balls.

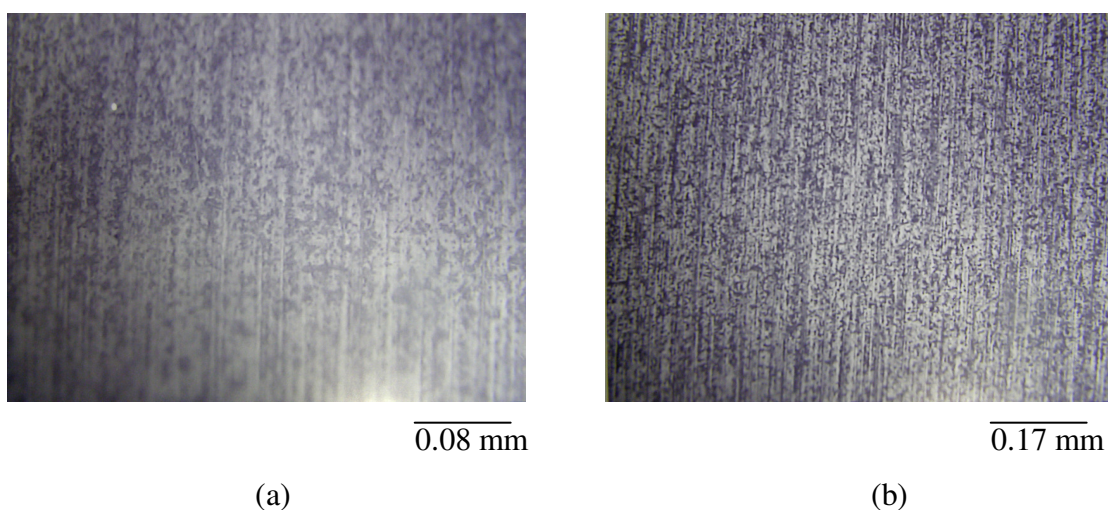


Fig: 4.4 Eroded rotating specimen at various magnifications

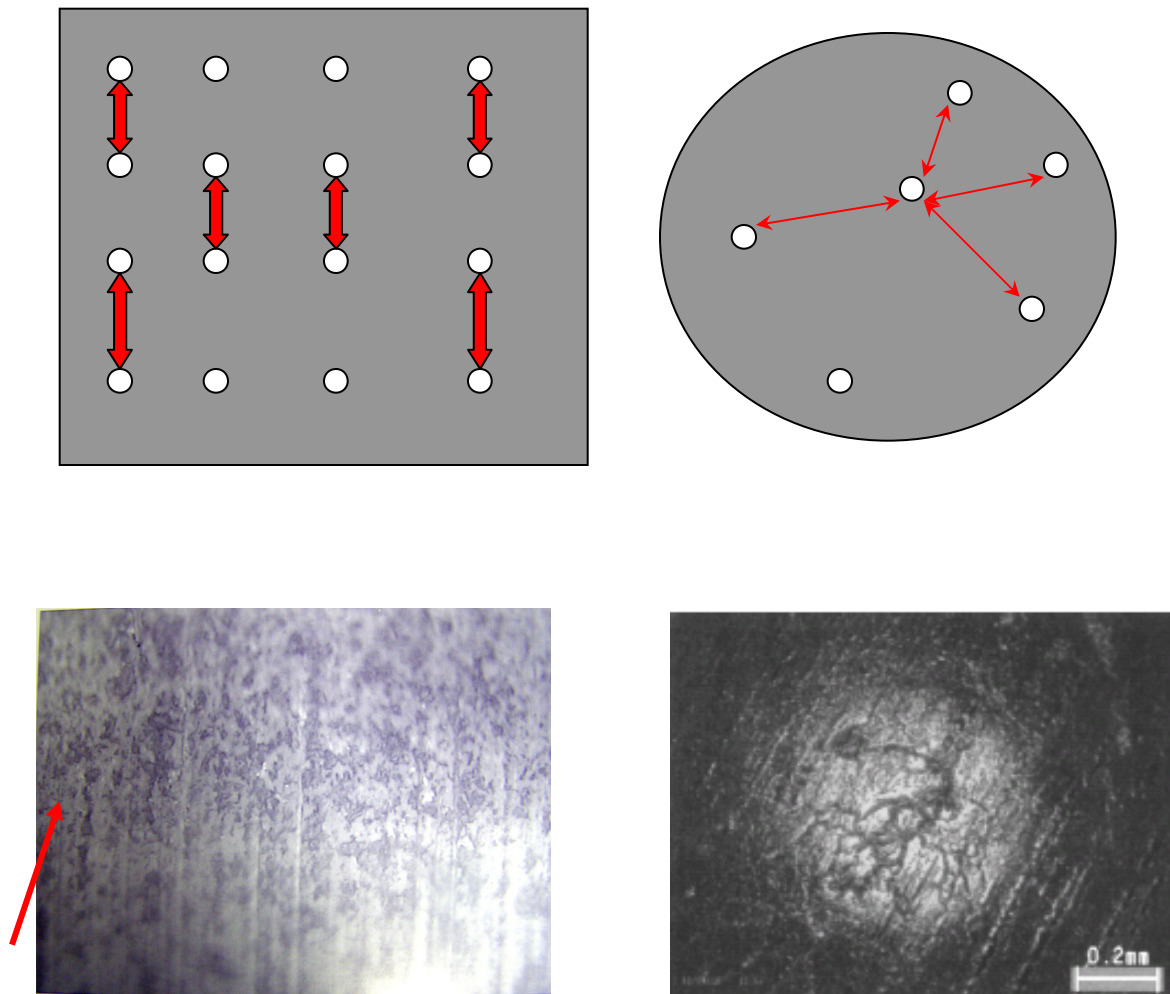


Fig: 4.5. Erosion mark comparison with application rolling elements.

The above Figure 4.5 show the type of wear obtained in the rotating specimen test and one that was formed in the application. As shown in the schematic, the erosion initiation zones in laboratory testing form almost straight line due to the rotation and nature of loading. The initially formed erosion pits tend to grow by enlargement and bridging. This growth leads to a narrow line of wear mark in this testing. The formation of erosion initiation largely depends on the cavitation zones in applications and also the surface roughness changes due to contact which accelerate the wear. As shown in the above Figure, erosion initiation at various locations on the rolling elements might grow and form a river mark like appearance as in application balls.

4.3 RCF Experiments on Eroded specimens

Rolling contact fatigue experiments were carried out on the eroded test specimens to understand the nature of material wear progression in rolling contact. In rotating specimen experiments it was clearly shown that pit formation and growth was continuous as testing continued. In river marks as observed in applications balls, pits form initially and grew wider and in length rather growing deeper. This is because of the cavitation intensity generated in bearing running conditions which is much less compared to the high intensity laboratory testing. Also, loading in the form of rolling contact is also applied in applications balls. This combination of rolling contact and cavitation has a combined material degradation process and thus result in different wear form. Erosion pits can initiate the material damage in the form of pits which could then grow further as seen in river marks. To investigate this hypothesis, test samples were initially tested with the vibratory cavitation equipment to generate reasonable erosion pits on the sample. This sample was then tested for rolling contact fatigue experiments with eroded area placed in the contact track.

4.3.1 Testing Approach

One test material B was tested using low powered transducer for 5 hours which created enough erosion pits to be used for rolling contact experiments. Details of rolling contact experiments are described in section 2.3. Rotary tribometer was used for this purpose. A schematic of the test chamber which consists of a steel cup filled with test lubricant and three lower balls and an upper ball as shown in Figure 2.10. The upper ball, here in this case is the eroded test specimen, which was fixed in the collet and was driven by a spindle which simultaneously applied load.

Test Specimen	Material B eroded after 5 hours of exposure to cavitation
Lubricant	Macron 110
Contact stress (GPa)	5.
Rotational speed (rpm)	2500
Stress Cycle	9.17×10^5

Table: 4.1 Test conditions for eroded specimen

As mentioned early in section 2.3 positioning the surface defect in the contact track is very crucial and a successful method was developed to place the surface defect on the track (Wang 2001). Testing conditions are presented in the Table 4.1. Lubricant Macron 110 was used for this testing mainly because of its low viscosity of $2.4 \text{ mm}^2/\text{s}$ at 40°C and of industrial interest. Shaft speed of 2500 rpm and a contact stress of 5 GPa was used. The specimen was cleaned in an ultrasonic bath with acetone to clear away material debris left over from erosion testing in case if any present. The steel cup in the RCF test chamber was filled with the test lubricant Macron 110. The eroded part was carefully positioned in the collect to allow the eroded area to stay in the contact path. The collect was then fastened to the tribometer and the testing was done for about 5 hours at this low speed. Frequent surface analysis on the test sample was carried out and the lubrication level was kept constant by refilling the test chamber regularly.

4.3.2 Wear Results

Surface analysis after 2 hours of testing in rotary tribometer is shown in Figure 4.6. The thin white layer in the contact track is due to the adhesion of lubricant. The contact track can be clearly seen with no notable changes in the erosion pits.

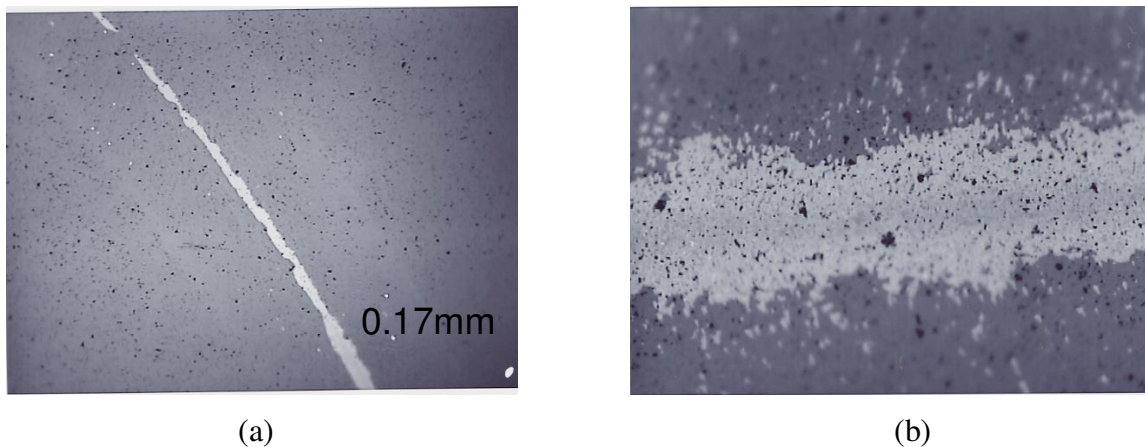


Fig: 4.6 (a) Test specimen after 2 hrs of RCF testing and (b) close up of the contact track

Continued testing on the same area showed erosion pit growth as shown in Figure 4.7. This growth was mainly in the form of linking up and bridging as observed in cavitation testing. The pits which were away from the contact track showed no sign of alteration as no load was applied to this part. As seen in the Figure 4.7 severe pitting continued at the contact track but no spalling was observed, a typical failure mechanism in rolling contact fatigue testing. This clearly signifies that no subsurface cracks are generated in cavitation erosion. This was also observed in application balls with river marks that the depths of those wear marks were to a maximum of 7 microns similar to what was seen in erosion testing.

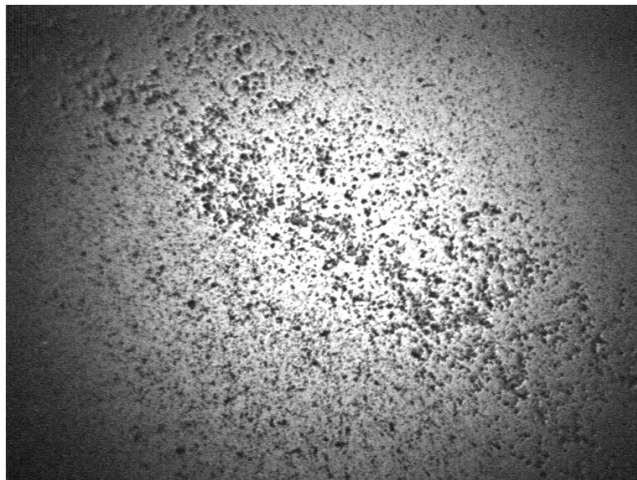


Fig: 4.7 Erosion progressions in rolling contact after 4 hours of testing.

Light interferometry technique was used to measure the surface parameters on this test sample which is shown in Figure 4.8 the maximum depth as shown in this measurement is 5.12 microns. The pit progression in the contact path was very same as the process in cavitation testing and did not lead to a river mark type of material wear. This is due to the multiple origins generated in eroded specimen; origins here refer to erosion pits. A minimum number of origins with reasonable distance between them can develop cracks due to fatigue leading to river mark type of wear because of variations in loading conditions, which is not the case in these experiments.

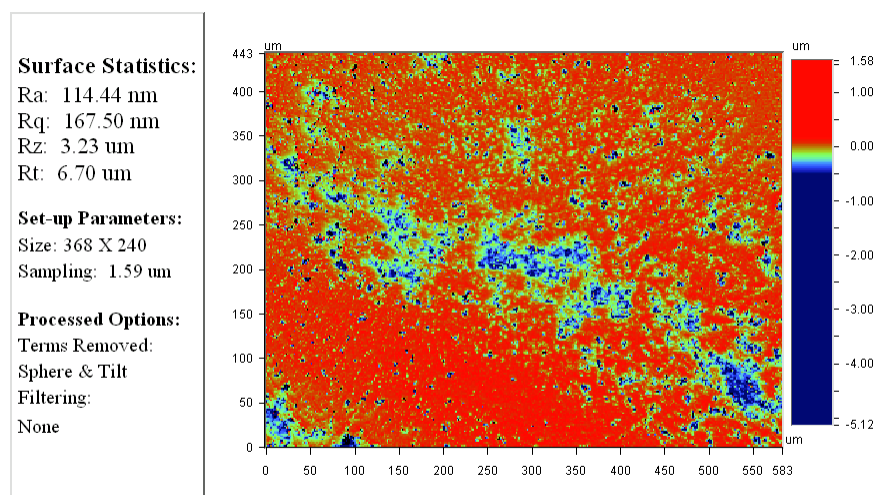


Fig: 4.8 Surface scan of the contact path.

4.4 Mechano-Erosion Experiments

Rolling contact fatigue testing of bearing elements is typically in the form of applying contact stress between rolling elements under lubricated conditions. This method precisely includes the effect of load, stress cycles and lubrication properties in order to evaluate the rolling contact life of bearings. Present bearing technology is capable to have bearings run for infinite number of cycles, provided a proper lubrication is ensured and operated under the fatigue limit stress. In reality, cavitation and contamination in lubricants play a role in the life of bearings. There are several publications on the effect of contaminated lubricant on their fatigue life (Sayles et al 1982 & 1988, Williams et al 1992, Nixon et al 1995 and Mitchell et al 2000). To reduce the testing time, a surface defect is often introduced in the rolling element such as hardness indents and surface cracks. For contamination tests, debris is introduced in the test lubricant to study their effect and for abrasive wear effect on rolling contact. Bearings operated under low saturation temperature lubricant are vulnerable to cavitation erosion. Thus, to evaluate bearing running under this condition a test method which include the effects of cavitation in rolling contact fatigue testing is required. This has been a major challenge to study the effect of cavitation along with rolling contact fatigue testing, with such limited work been reported on the study in this particular field. This also encouraged designing a test setup to couple two phenomena cavitation and rolling contact fatigue. A novel test methodology was designed for this purpose and is detailed in the following sections (Karunamurthy 2007).

4.4.1 Test Rig Design

The rotary tribometer used for this testing is described in section 2.3.1. This rotary tribometer can simulate the running conditions of an angular contact ball bearing configuration under different conditions of contact stress and lubrication. As shown in Figure 2.10 the loading configuration of this rotary tribometer consists of a steel cup of 50 mm outer diameter supported by a steel cylinder to allow fix the steel cup to the

machine. Three lower balls representing a planetary motion are placed inside the cup which is then filled with lubricant. Load is applied through a rotating shaft from the top which at the end has a collet to fix the test rolling element. All test rolling elements are of 12.7 mm in diameter. Any specimen with higher or lower diameter cannot be tested using this tribometer. It is not possible to produce cavitation in this test chamber with hydrodynamic methods. That is to generate cavitation using high speed liquids passing through geometry restrictions thereby producing cavitation. Other options which are left to produce cavitation in this conditions is either by vibratory method or by rupturing the liquid using high intensity light such as LASER.

Designing and manufacturing another test method is not only time consuming but also expensive to go for LASER cavitation method. The available vibratory cavitation method has a piezoelectric transducer with a diameter of 20 mm. This cannot be adapted to implement it into the test chamber of the tribometer. To account for the space requirements, new piezoelectric transducer geometry was designed with a diameter of 5 mm. This design was manufactured by the cavitation equipment supplier to allow vibrating the transducer with a resonance frequency of 20 KHz which is generated by the available ultrasonic generator in the laboratory. This newly designed transducer must be implemented on to the test chamber such that a reasonable level of cavitation can be produced in the test lubricant and also, the intensity of cavitation must be high enough to cause erosion in the rolling contact region. As shown in the test configuration in the Figure 2.10, the only way to insert the transducer is from the side of the test cup. This way it ensures that the end of the transducer horn which generates cavitation stay close to the rolling contact track.

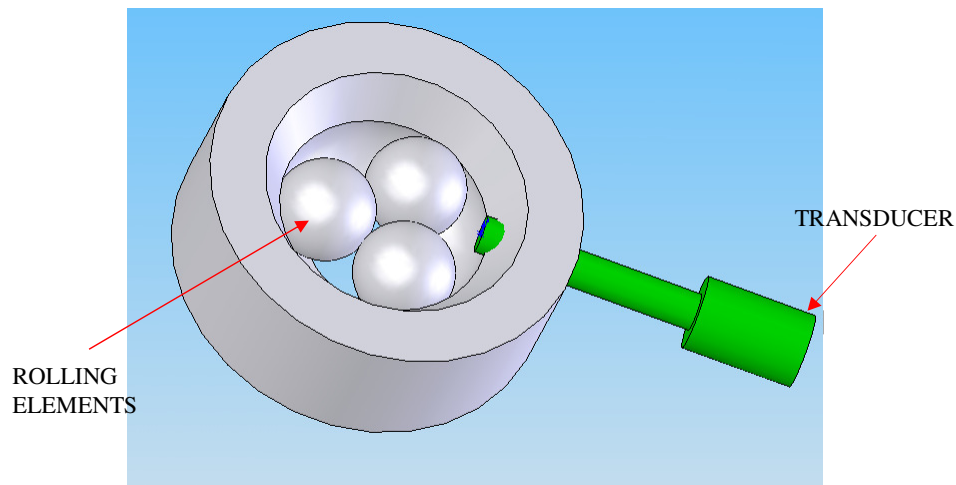


Fig: 4.9. Ultrasonic transducer in RCF test chamber

Another important design consideration was the lower balls. Implementation of the transducer horn into the test chamber should not disturb the dynamics of these lower balls. Any mild contact with these lower balls will result in abrasive wear of test materials due to sliding and a strong contact will damage the transducer as well as the test materials. The tolerance between the transducer horn and the lower balls were accurately calculated to determine the correct position of the transducer during testing. The curvature of the rolling elements offers advantage to position the transducer end slightly above the centre of the lower rolling elements. The Figure 4.9 above shows this designed position of the transducer in the steel cup with the lower balls.

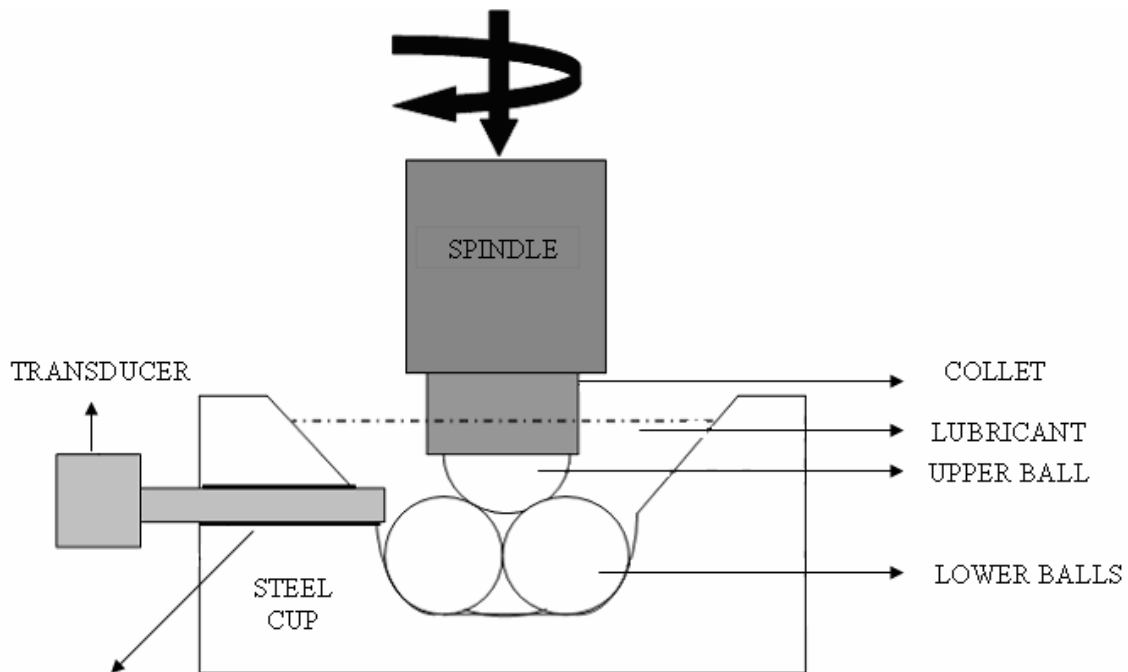


Fig: 4.10 Schematic of Test configuration.

Once the accurate position of the transducer was determined, it was decided to create a port in the steel cup which is the only way to ensure placing the transducer at this location. A new stainless steel cup of the same design as shown in Figure 4.9 and 4.10 was manufactured in the workshop for this purpose. A high carbide drill bit was used for creating the port of required dimension. This port was designed to a diameter of 5.5 mm in such a way that it accommodates the transducer horn which is of 5 mm in diameter with good tolerance. Major challenge rose when a proper sealant had to be found to seal the transducer in the port. The vibratory cavitation equipment must freely vibrate without constraining as it is essential to generate cavitation in the liquid. Any prevention to this vibration will not result in a good intensity level of cavitation in the liquid and would also damage the transducer horn due to abrasion.

The purpose of the sealant is as follows:

1. To position the piezoelectric transducer in the test chamber
2. To seal off the port to avoid any lubrication leakage without vibration.
3. To allow the transducer horn to effectively vibrate without any constraints, and thereby eliminating any heat generation due to sliding contact and abrasion of materials.

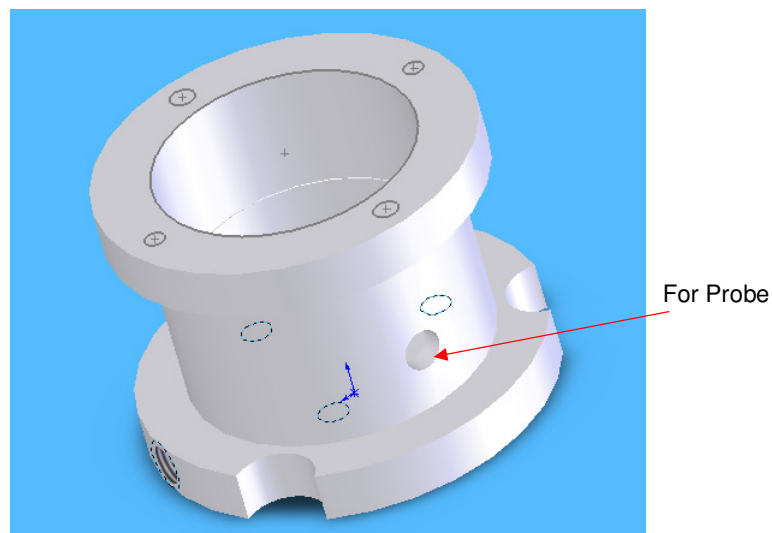
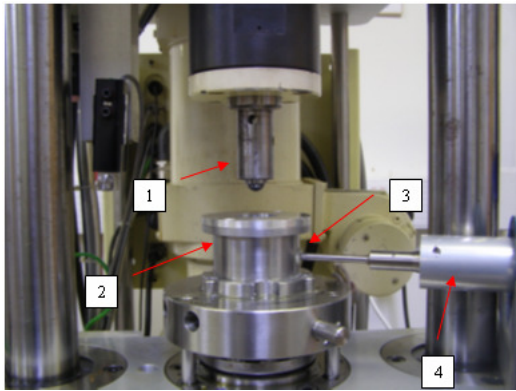


Fig: 4.11 Stainless steel test chamber to accommodate test steel cup in the tribometer.

These requirements eliminate the possibility of using any mechanical sealants. The only option is to use a sealant of adhesive type and hence a high temperature adhesive sealant was selected. This adhesive sealant is also chemically inert and thus advantageous when applied in oil environment. The steel cup is fixed to the rotary tribometer with the help of a steel cylinder as shown in Figure 4.11 above. Another port had to be created on this cylinder to align the port with the steel cup to allow inserting the transducer. To position the transducer to the test chamber, the sealant was applied to both ports such that it fills them completely. This was achieved using a sealant gun.



(a)



(b)



(c)

Fig: 4.12 Mechano-Erosion Test setup (a) Before loading (b) After loading and (c) Complete set up.

Once the sealant was applied to the ports it was allowed for a setting time of 24 hours. After curing, the centre of the port was carefully marked using a marker. This area was then drilled with a drill bit with less pressure to a diameter of 4 mm. This diameter was found sufficient enough to insert the transducer of 5 mm diameter with a small force. The positioning of the whole transducer horn setup on to the tribometer was difficult due to the reason that the two rigid vertical columns of the tribometer guide the test chamber to move vertically upwards to apply load and rotation by the drive spindle. Also, when the specimen fails during the testing, the machine is configured to move the test chamber downwards automatically. Thus the cavitation equipment attachment must therefore be designed in such a way that it moves along with the test chamber. An aluminum holder was manufactured to firmly hold the transducer set up and as well to move along with the motion generated by the tribometer during the start and end of the test. The dimensions of this holder are shown in appendix C. The whole test set up is shown in Figure 4.12. The marked areas in Figure 4.12(a) show 1. The drive spindle with the collect attached at the end, 2. Test chamber with lower balls and lubricant, 3. Port sealed with the high temperature resistance adhesive sealant and 4. Transducer horn set up constrained to the holder.

4.4.2 Experimental Procedure

The following describe the step by step procedure for testing bearing rolling elements with the new Mechano-Erosion method:

- The test chamber which consists of the steel cup and cylinder was cleaned with acetone to ensure no presence of debris and dried using a blower.
- High temperature adhesive sealant was injected to the port using the sealant gun to shut the port completely with the sealant
- The sealant was allowed to a minimum time of 24 hours for curing.
- After sealant curing, the centre of the port was carefully marked with a marker
- A driller was used to drill a hole of 4 mm at the marked point.

- The piezoelectric horn assembly detached from the ultrasonic generator was forced through the generated port gently.
- Test chamber was then fixed on the rotary tribometer. The transducer assembly was supported by the aluminum holder as shown in Figure 4.12. This aluminum block was manufactured with a conical cut at the middle to firmly hold the transducer. This block was clamped with the tribometer test chamber beam.
- Lower balls were added to the steel cup in the test chamber. Materials of these lower balls were both bearing steel and silicon nitride depending on the contact requirement for the tests
- Lubricant was then supplied to the chamber and ensured the level of lubricant was sufficient during the whole test, when required the test chamber was refilled. Different type of lubricants were tested and is mentioned in appropriate sections where necessary
- Test material was fixed in the collect simply by applying force
- Collect was fastened to the drive spindle of the tribometer
- The position of the transducer horn tip was adjusted back to the desired position to ensure no metal to metal contact.
- Piezoelectric transducer horn assembly was connected to the ultrasonic generator and then to a power supply
- Required rotational speed, contact stress and test duration was set using the computer which controls the rotary tribometer
- All tests were conducted at room temperature, and vibration safety limit was specified in the computer program to allow the machine to stop automatically if the vibration exceeds the specified limit
- A new test is defined using the graphical user friendly program to define the series of steps, load for each step, temperature and required stress cycles. This program records the whole test.
- The vibratory cavitation equipment was turned on to create cavitation in the test liquid and simultaneously the rotary tribometer was started for rolling contact fatigue experiments.

- The maximum power that can be generated by this new piezoelectric transducer is about 700 watts with a maximum vibration amplitude peak-to-peak of 60 microns. The amplitude and the output power of the system is directly proportional to each other
- The vibration amplitude of the transducer was gradually increased from zero to the maximum at the start of the test. This is achieved in about 30 seconds.
- This maximum vibration amplitude was used for all tests, but the effect of this vibration on the test results was also studied.
- A forced air cooling was used to keep the transducer from heating up as the recommended operating temperature of the transducer is 50 degree centigrade
- Visual inspection of the test chamber and the transducer and its position was followed every 30 minutes
- The lubricant was evacuated every 2 hours and disposed following the safety disposal methods
- Tests were paused at required intervals for test specimen inspection which was typically every hour of testing
- The collet was removed from the tribometer; the test specimen was cleaned with acetone without removing it from the collet. This ensured the contact track to be at the same position for any continued tests
- Test specimens were examined under the microscope using a specially designed holder which allows the collect-test sample set up to be studied under the microscope.
- After surface analysis the collet was placed back to the tribometer to continue the test
- Surface examination of the transducer horn tip was regularly followed to remove the worn material if any present.
- Once the test was finished, the specimen was removed from the collet, cleaned using an ultrasonic cleaner using acetone and set for surface analysis.
- The above procedure was repeated for all tests.

Specimen Id	Lubricant	Contact Pressure (Gpa)	Shaft Speed (Rpm)	Test Time (Min)	Stress Cycles	Cavitation Intensity In Vibration P-To-P(μM)
S-1	Macron 110	0.2	2000	240	2.53×10^5	60
S-2	Macron 110	3	3000	120	3.57×10^5	60
S-3	Macron 110	5	3000	360	1.08×10^6	60
S-4	Macron 110	5	7000	180	1.26×10^6	60
S-5	Macron 110	5	5000	180	9.3×10^5	60
S-6	Macron 110	3	3000	240	7.63×10^5	60
S-7	Macron 110	5.1	2000	40	8.2×10^4	60
S-8	Macron 110	5	3000	120	3.6×10^5	60
S-9	Macron 110	5	3000	240	7.1×10^5	60
S-10	Macron 110	5.1	3000	180	5.25×10^5	60
S-11	Macron 110	5	5000	240	1.2×10^6	60
S-12	Macron 110	5.2	7000	180	1.26×10^6	60
S-13	Macron 110	5.2	7000	300	2.1×10^6	0

S-14	Macron 110	3	5000	240	1.26×10^6	60
S-15	Macron 110	5.2	5000	240	1.26×10^6	60
S-16	Macron 110	3	2000	180	3.6×10^5	60
S-17	Macron 110	3	3000	180	5.4×10^5	60
S-18	Distilled water	5.2	5000	40	2×10^5	60
S-19	Macron 110	5.2	5000	60	3×10^5	60
S-20	Refrigeration oil	5.2	5000	480	2.4×10^6	60
S-21	Base oil	5.2	5000	Test discontinued	Test Discontinued	60
S-22	Cylinder oil	5.2	5000	Test Discontinued	Test discontinued	60
S-23	Macron 110	5.2	5000	Test Discontinued	Test discontinued	10
S-24	Macron 110	5.2	5000	Test Discontinued	Test discontinued	20
S-25	Macron 110	5.2	5000	420	2.1×10^6	30

Table: 4.2 Mechnao-Erosion test programme

4.5 Erosion in rolling elements

Some preliminary tests were conducted to test the function of the new testing methodology. This was done by running the tests at varying speeds but without applying heavy load through the machine spindle i.e. with a minimal load just to ensure that the upper ball is contact with the lower balls to transfer the motion from the spindle. The cavitation testing methods were kept the same as the conventional vibratory cavitation testing. The only difference is the distance between the specimen and the transducer tip. In bench testing, it was found a distance of 0.5 mm showed high erosion rate. This distance of fluid gap is not possible here in this case of mechano-erosion testing. However, the intensity of cavitation generated in the test lubricant is high enough to cause erosion in the test material. The rate of erosion is slower compared to the bench testing due to this reason. Figure 4.13 below shows the result of one of these preliminary tests. This is the result of specimen S-1 which was run for a stress cycles of 2.53×10^5 at a speed of 2000 rpm. As seen in the light microscope images, erosion marks was observed all over the lower balls. This is a clear indication that cavitation erosion can be produced on the rolling elements using this new test method.

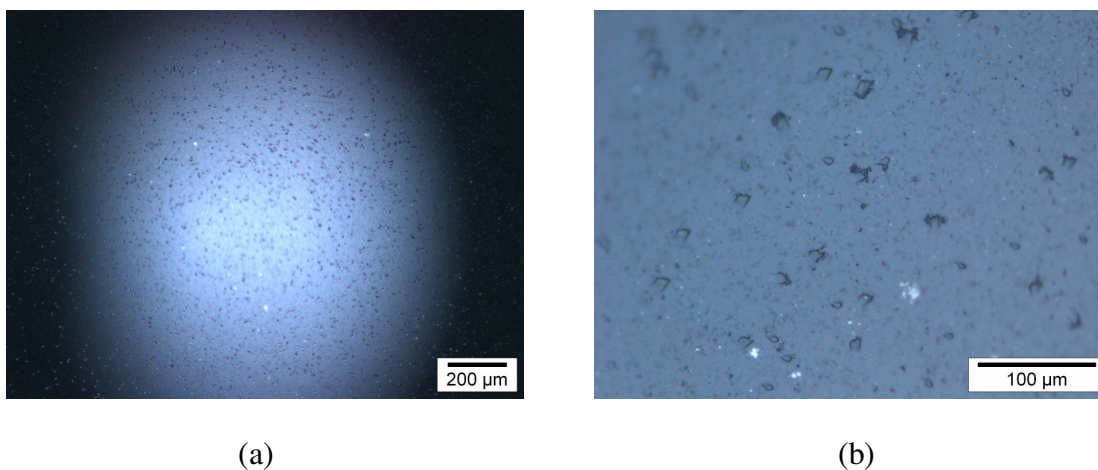


Fig: 4.13 Erosion marks on lower balls of S-1.

The close up of these erosion marks is shown in Figure 4.13 (b). These marks showed signs of directionality due to rolling. Rotation of test specimens during rolling contact is the reason for this C-shaped marks or pits. Also, the concentration of these pits was not as observed in bench testing. The distance between these pits show that erosion can cause fatigue zones to begin at various locations on the rolling element not necessarily very close as in the case of bench testing. This is also encouraging as river marks on application balls showed similar distant fatigue zones. A light microscope image with high magnification on one of these erosion marks is shown in below Figure 4.14. This is clearly an erosion pit as no other loading was applied during this test. As seen in the below Figure 4.14 the surrounding area of the pit does not show any signs of surface changes. This was not the case in conventional erosion testing, where to get to this same stage of pitting as shown here would result in a very rough surface and presence of several pits nearby. This strongly proves that cavitation on rolling elements result in very less density of erosion pits all over the surface.

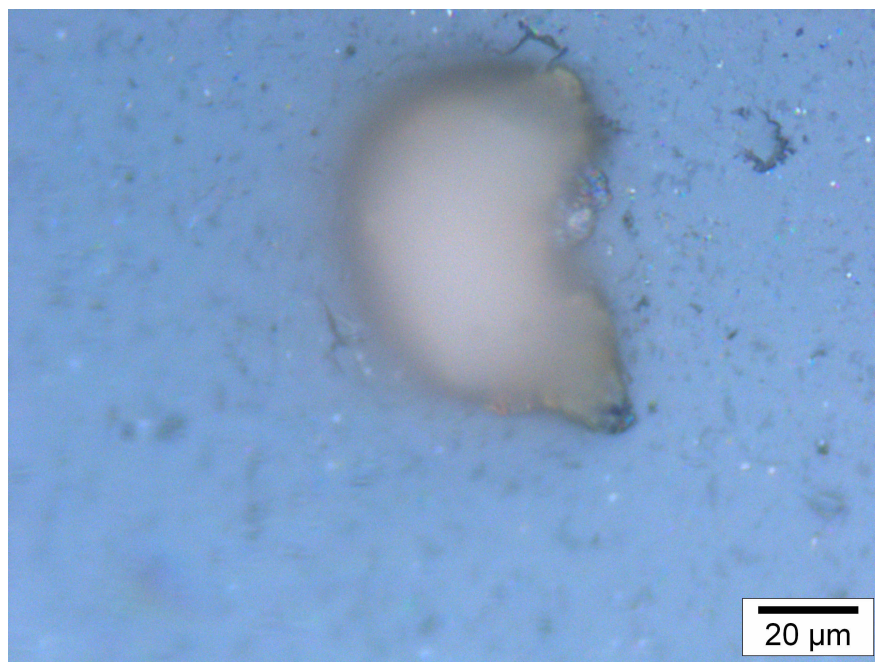


Fig: 4.14 Microscope image of Erosion mark on rolling element.

4.5.1. Erosion on contact track

Another set of preliminary tests were also conducted with load applied by the tribometer along with cavitation. Result of one of these tests is shown in Figure 4.15 below. This was a hybrid contact test of specimen S-2 i.e. upper ball was silicon nitride and lower balls were bearing steel. Surface investigation after a couple of hours showed formation of erosion pits on the contact track. As shown in the Figure 4.15 after 3.5×10^5 stress cycles erosion marks are only seen on the contact track not any where else on the upper ball and lower balls showed no surface change. This proves that these marks are not only due to cavitation or contact stress loading, but a combination of these two.

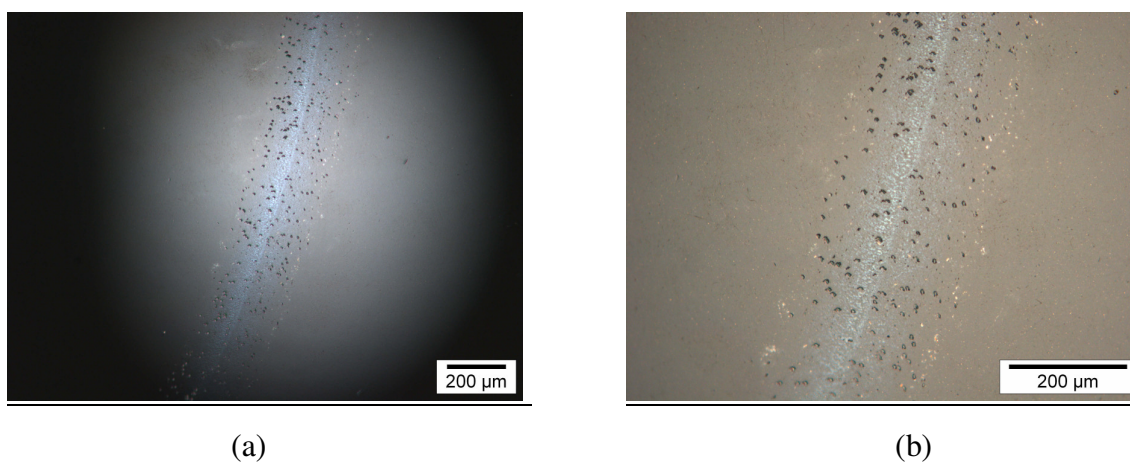


Fig: 4.15 Erosion pits on contact track of S-2.

The reason for formation of erosion marks only on the contact track is due to the surface changes due to contact stress coupled with rotation. Due to increase in the number of stress cycles the surface gets rougher and no longer remains smooth as the rest of the test specimen. As previously described in section 3.6 highly polished materials provide good resistance to erosion compared to rough surface. A low viscosity lubricating oil was used for this test and the contact stress was 3 GPa at a maximum shaft speed of 3000 rpm.

Tests were also conducted without cavitation in this test set up. These tests showed no signs of surface changes and remained smooth. In test S-2, erosion pit density was high on the contact track. A scanning electron Microscope image of the edge of this contact track is shown in Figure 4.16 below. It is clearly seen that the population of erosion pits gradually reduce as from the centre of the contact track towards the outer region. Also the erosion pits show a direction in their geometry due to rolling.

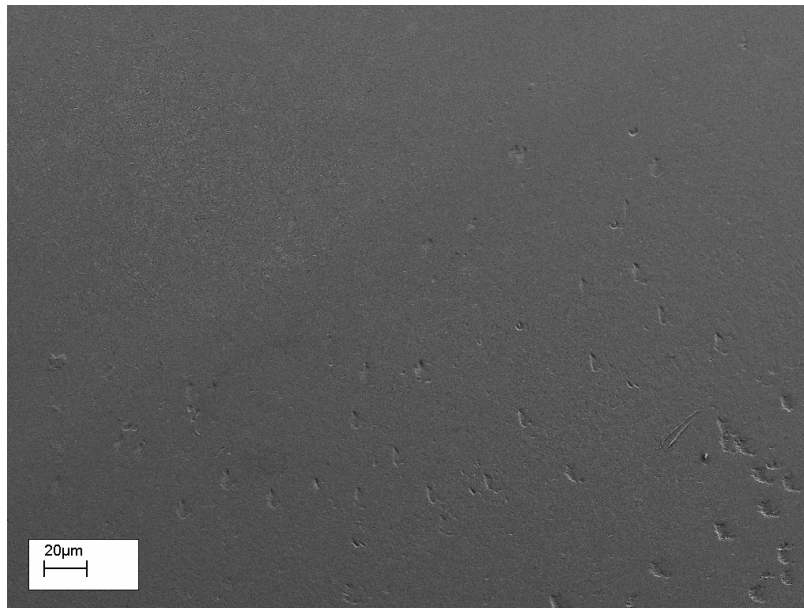


Fig: 4.16 Edge of contact track

4.5.1.1 Ceramic contact

Once erosion marks were observed on the contact track using this test method, different rolling contacts were investigated preliminary to understand the difference. Hybrid contact i.e. ceramic rolling elements with steel races are widely used in industry applications. Ceramic to ceramic contact is also used in applications and was tested to understand the difference in the nature of erosion progression in these two contacts. As silicon nitride provides less resistant to cavitation compared to bearing steel and hence the severity of material damage was found to be high in this contact.

The below Figure 4.17 shows results obtained from test specimen S-3. This is material B with same material for lower rolling elements. Erosion marks were observed just over an hour with very less number of micro erosion pit formation. With high contact stress of 5GPa applied the contact track was clearly visible. The micro pits formed during the initial hours of testing were appeared as small indents due to the increased load. But as the time continued over time, some micro pits were grown to major pits which appear big as same as in conventional erosion testing. These erosion pits on the contact track is shown in Figure 4.17 below. Also, micro pits can be seen at the edge of this track suggesting less contact stress region give rise to small number of erosion pit formation compared to the centre of the track where the applied load was high.

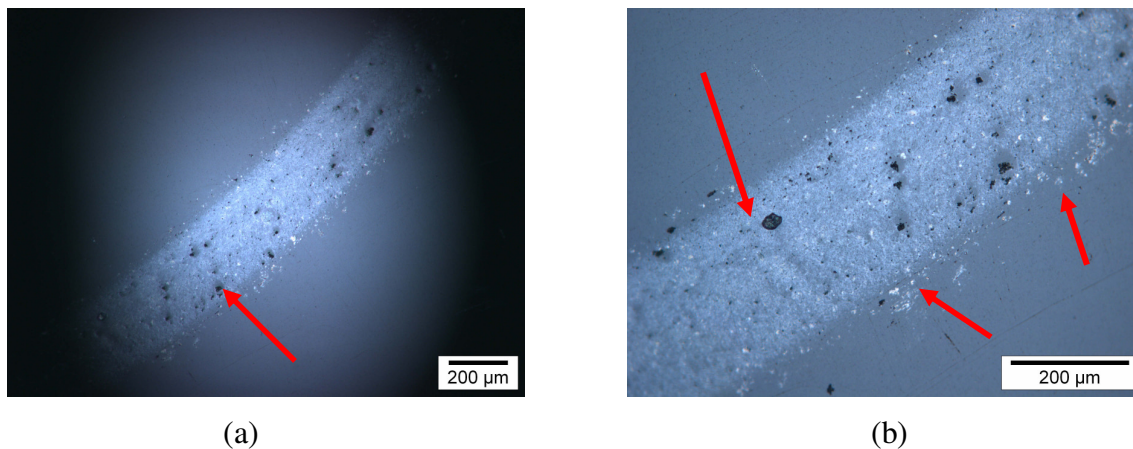


Fig: 4.17 Erosion pits in ceramic to ceramic contact

Another important feature to note in this test is the distance between larger pits was large. Micro pits show extensive pit bridging and growth whereas large pits were mostly isolated from other large erosion pits. Also the shape of these erosion pits is nearly spherical as marked in the Figure 4.17 (b). The edge area marked by arrows in the Figure 4.17 (b) show erosion pit formation which are not large as the one seen on the track. These edge pits clearly show the mechanism of pit bridging and can be justified that loading has an effect on this process. All pits did not show any growth in depth over the testing time.

Tests on the same ceramic to ceramic contact was conducted on material C. This is test specimen S-4 with very high speed of 7000 rpm. The increase in rotational speed increases the number of stress cycles there by reducing the test time. This material was failed in just 3 hours of testing at a contact stress of 5GPa. The contact region was severely eroded as shown in Figure 4.18 below. The contact region was deeper due to high load with numerous erosion pits as shown in Figure 4.18 (b). The lower balls were also damaged severely by major material loss in the form of delamination wear. This material was tested again without erosion test coupling and found that it withstood such high pressure and speed without failure concluding that erosion has accelerated the material failure.

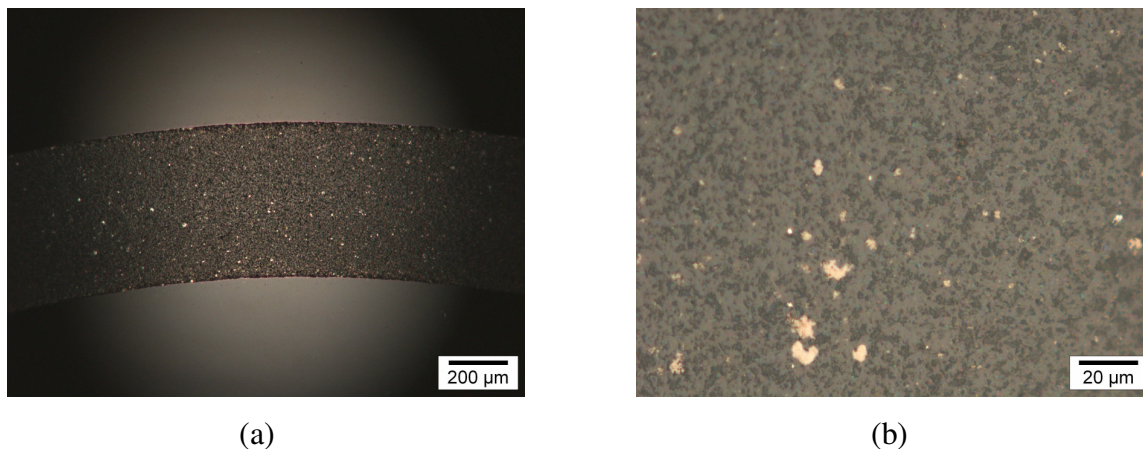


Fig: 4.18 Light microscope images of material C eroded contact track (a) full view of the eroded track and (b) High magnification of the contact track.

The region away from the contact track remained unchanged. They were smooth even after the test was completed. A Scanning electron microscope image on this region is shown in Figure 4.19. These erosion pits in the contact region were not big as observed in the bench erosion testing. Also, due to high contact pressure these erosion pits were rubbed strongly during contact and the roughness of this region was very less as compared to the same level of erosion observed in static erosion testing. Light interferometry method was used to measure the surface parameters and is shown in Figure 4.20.

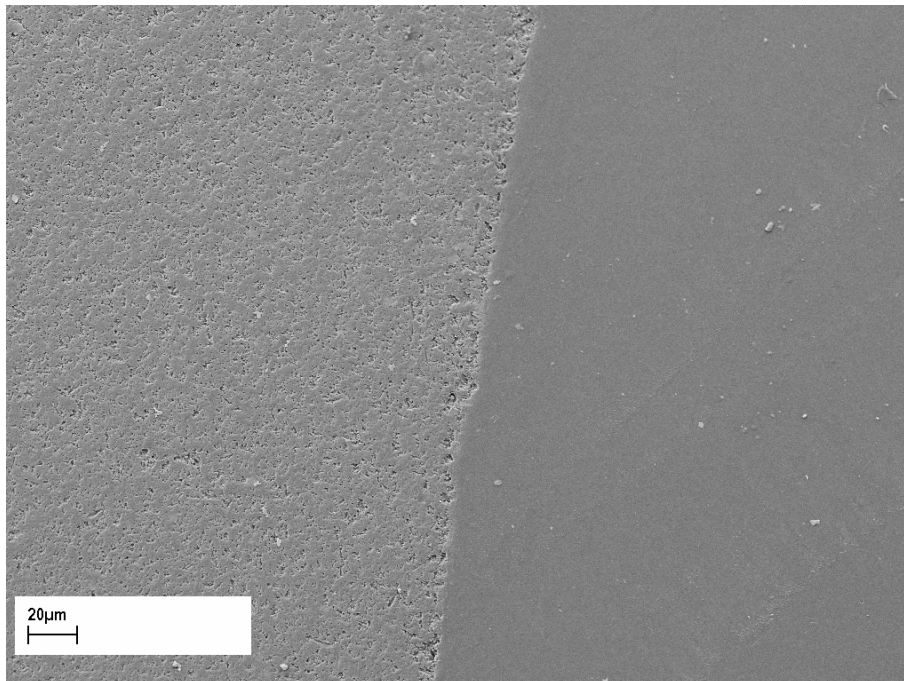


Fig: 4.19.Contact track and adjacent area

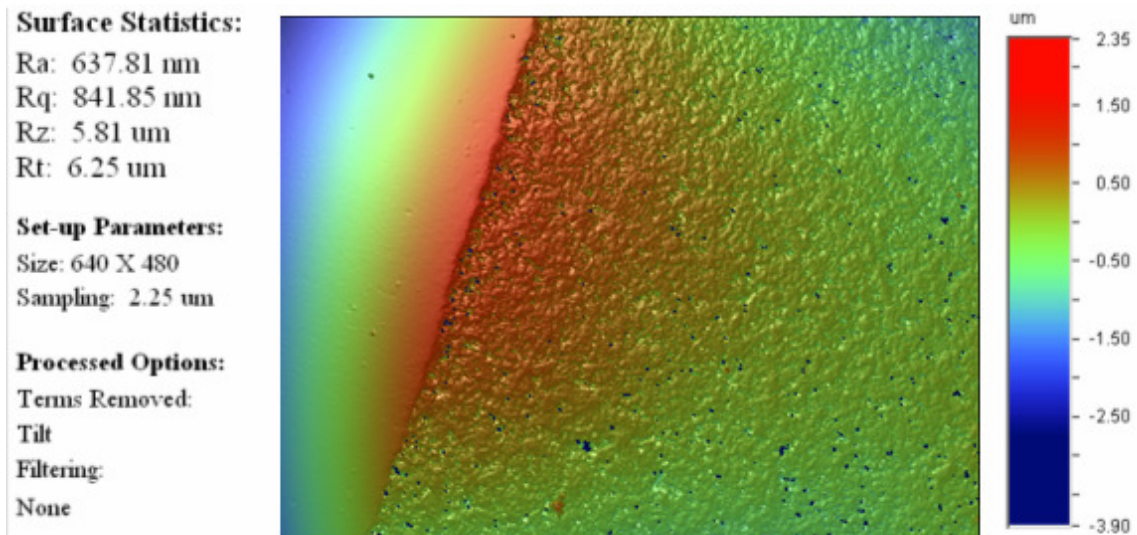


Fig: 4.20 Surface measurements on the contact track region

The maximum depth of these erosion pits measured to 3.9 microns compared to a maximum of 6 microns measured in static erosion testing of this same material C. Accumulation of material due to formation of pores and pits is usually noted in static testing, but here in this case, this accumulated material was either removed away or prevented due to high contact pressure. This part is shown in Figure 4.21 (a), where the contact region is fairly smooth with deep pits. Also, as marked in this Figure, the process of pit bridging is also shown. The geometry of the pits in this material C was observed to be wider as shown in Figure 4.21 (b). In this S-4 testing, erosion pits on the contact region are sharper and tiny showing no displacement of grains or bunch of grains were noted. However, this tiny erosion pits certainly correspond to displacement of broken grains due to transgranular fracture. Comparison of static and rolling contact erosion pits is shown in Figure 4.21 below:

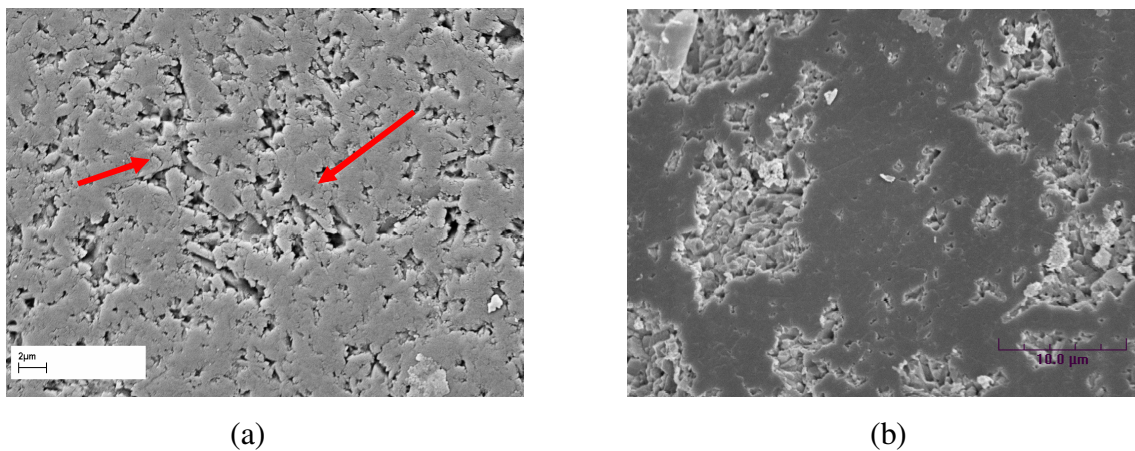


Fig: 4.21 Comparison of erosion pits in rolling contact and bench testing (a) Eroded contact track and (b) erosion pits on stationary specimen.

4.5.1.2 Hybrid Contact

This section describes the wear mechanism on hybrid contact – with silicon nitride as upper ball and bearing steel were lower rolling elements. This is test specimen S-5 which was run at the same contact pressure used for ceramic to ceramic contact but with a less

rotation speed of 5000 rpm. The microscope images shown in Figure 4.22 are after testing for 3 hours. The formation of erosion was similar to ceramic to ceramic contact as erosion marks were formed only on the contact region. The erosion marks formed on this contact track were very different in shapes compared to the ceramic to ceramic contact. These erosion marks showed directionality to rotation and contact stress and they are in identical shape as English alphabet “C” and hence therefore referred here as C marks.

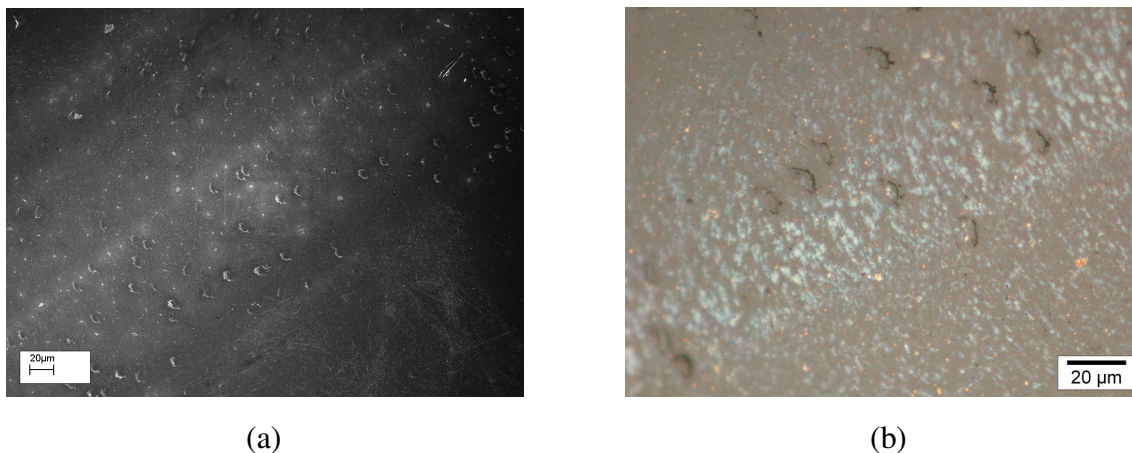


Fig: 4.22 Erosion marks on ceramic rolling element with hybrid contact

These C marks were not closely packed and showed a reasonable distance between them. They were also thinner compared to results obtained in static erosion tests. This formation of different shape of erosion marks clearly signify that erosion pits or marks need not supposed to be spherical or in the shape of microstructure of the material or bubble shape. Rather this is largely influenced by the contact materials and test conditions play a huge role in determining the shape of erosion pits. Bearing steel which was used as lower balls in this test showed sharper erosion pits in their contact track. This is shown in Figure 4.23 below. The difference in the shape of erosion marks in the contact track of lower steel balls shown in Figure 4.23 (b) can also be due to abrasion despite change of lubricant frequently was followed. Also typical erosion damage of bearing steel is shown in Figure 4.23 (a) which is similar to erosion observed in static erosion tests.

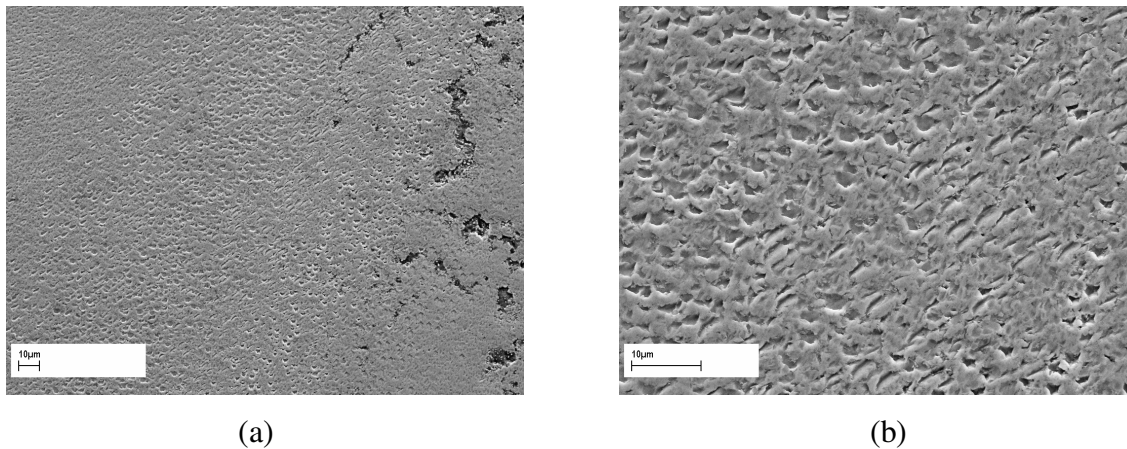


Fig: 4.23 (a) Contact track eroded on steel lower balls and (b) close up

High magnification images of these erosion pits on bearing steel is shown in Figure 4.24 below. As shown in these Figures, erosion pits are very sharp as well as broad in Figure 4.24 (a) and (b). These entire sharp and broad pits clearly show directionality in the formation which is due to effect of rolling contact. There is also the process of pit bridging can be seen in the marked area in Figure 4.24 (a). The sharper pits are similar to surface indents which is also a characteristic of erosion damage and the broad pits shown in the next image is as similar to what was observed in static erosion tests on bearing steel.

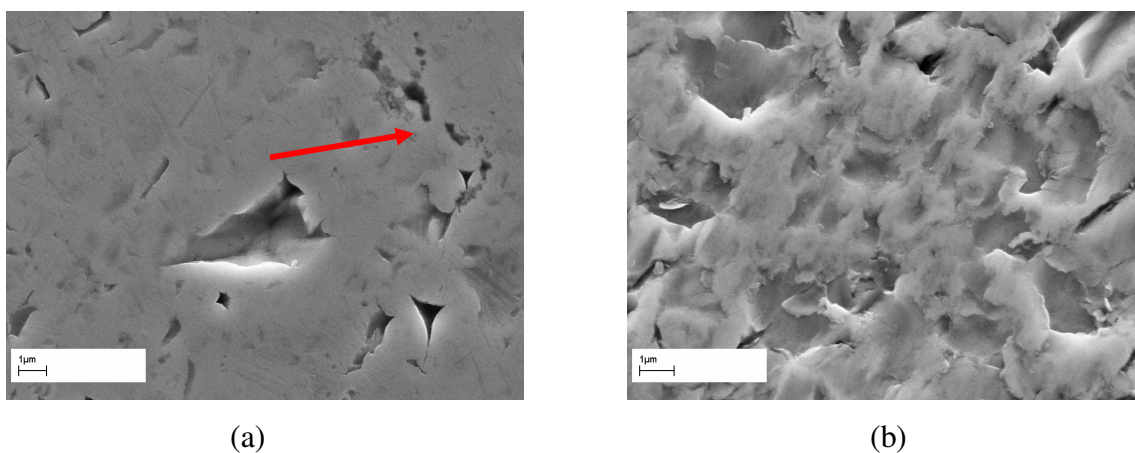


Fig: 4.24 High magnification of steel ball contact track (a) showing sharp erosion pits and (b) high density of erosion marks

Apart from these sharp and close packed broad pits, a bunch of erosion pits was observed on and near the contact region. This is shown in Figure 4.25 (a) and (b). As shown in Figure 4.25 (a) erosion pits are seen very far away from the eroded contact track on the left. This suggests that lower balls are also subjected to cavitation in the test chamber. However, the rate of erosion on this region is very low due to pure cavitation loading, whereas in contact regions rolling contact add up to the load and thus accelerating the rate of erosion. A closer look on this bunch of erosion pits as shown in Figure 4.25 (b) is very similar to cavitation erosion observed in the bench erosion testing on this material.

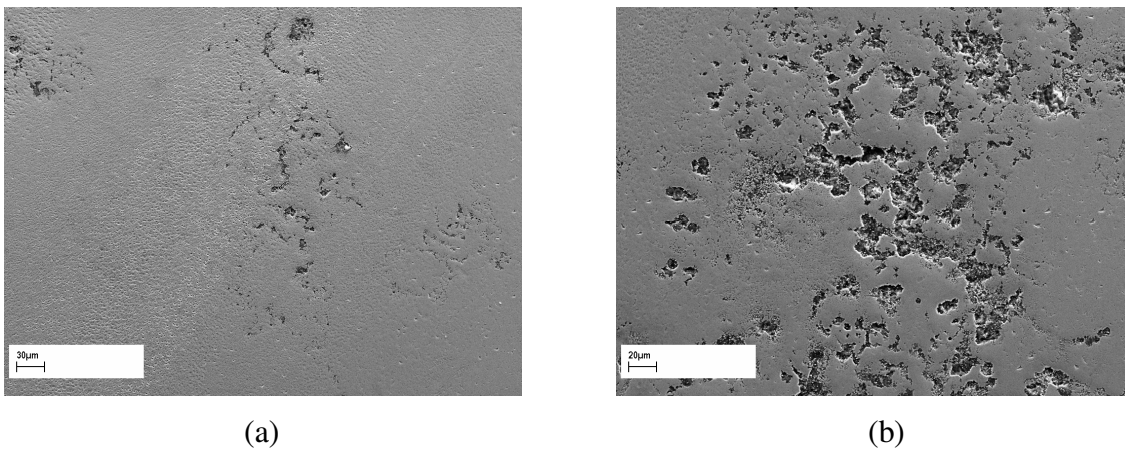


Fig: 4.25 (a) Bird's eye view of contact track of steel lower ball and (b) Area with bunch of erosion pits.

The lower steel balls showed signs of material removal in the form of ring shaped surface layer peeling. This deformation of surface layer was not observed in static erosion tests. The edge of these ring shaped damage showed lifting of material surface as show in Figure 4.26. Erosion marks were also seen close to these edge areas, which are of both sharp and broad shaped. Upon further testing, this edge area would eventually loose the material by flaking of surface layer contributing to huge material loss.

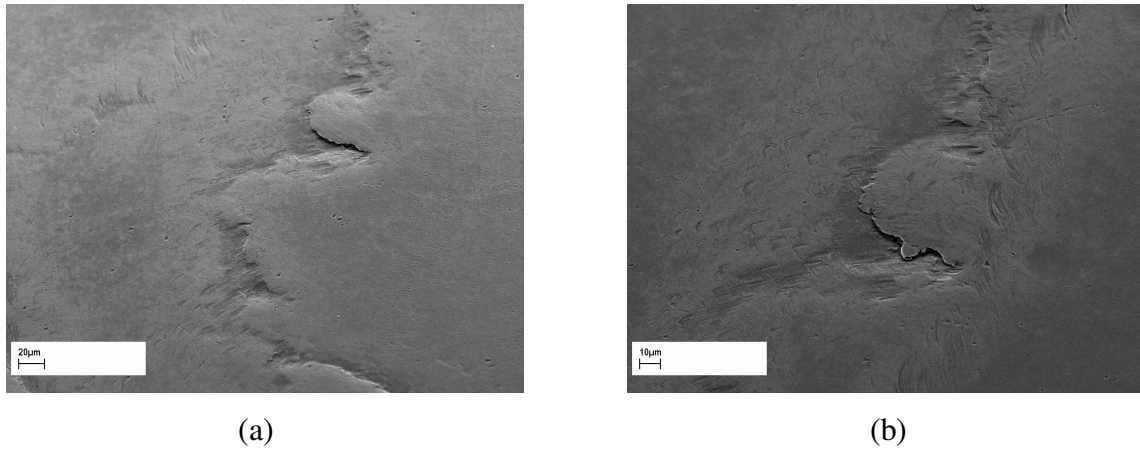


Fig: 4.26 (a) Ring edge of lower steel ball and (b) ring mouth

This process of material flaking is shown in Figure 4.27 below. Cracking of material surface layer can also be seen in this Figure. This flaking process is normally due to adhesion failure and is caused by induced crack. This type of crack formation and flaking was only observed in this type of testing.

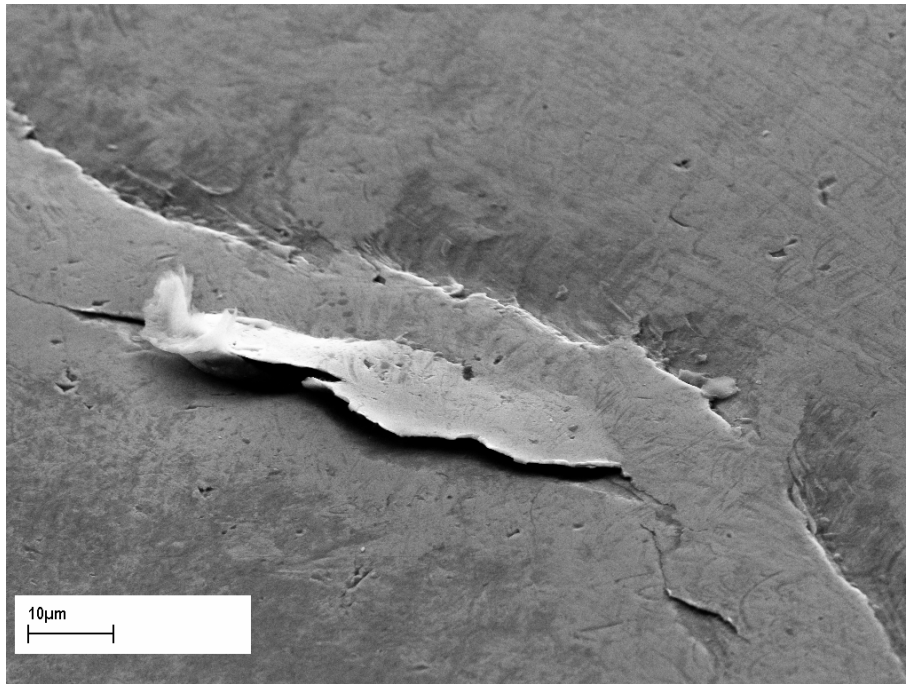


Fig: 4.27 Material flaking at the edge of the ring in bearing steel

4.5.2 Wear mechanism in rolling contact

The erosive wear mechanism due to cavitation consists of formation of multiple trans and intergranular fracture which then followed by formation of pit and growth developing into craters leading to a heavy loss of material. Here in mechano erosion testing, the wear process is very complicated to assess the mechanism due to the nature of loading conditions and material failure. Few tests were carried out at different conditions to find out erosive wear initiation and progression in rolling contact. Frequent surface analysis on the test specimen was carried to find out the precise erosion initiation stage of material damage. The beginning stage of wear does not show any signs of micro crack formation rather only micro pits. These micro pits were characterized by bubbling out of the surface layer which then undergoes cracking allowing the lubricant to squeeze in due to rolling contact. This in later stages of testing grows into pits and continued testing resulted in formation of numerous pits of high concentration in the track and mild wear at the edges in the formation erosion pits. This mechanism of wear is detailed in the following parts of this section.

4.5.2.1 Formation of micro pits

The result of test specimen S-6 is shown in Figure 4.28. As shown in the Figure the contact track of the silicon nitride test specimen became rough at the initial stages of testing. This rough surface then showed signs of micro pit formation. The “bubbling out” process was found to be the main part of micro pit formation. As both cavitation and rolling contact stress loading was applied, the squeezing in of lubricant in the contact region allow formation of this bubbling out phenomena of the surface layer due to cavity collapse. This process of bubbling out of the surface layer is much localized due to the nature of loading conditions. Once this bubble like bursting occurs, they form micro cracks at this region which show signs of fracture. These minute cracks allow the lubricant to get in to surface thereby changing the mechanism of lubrication.

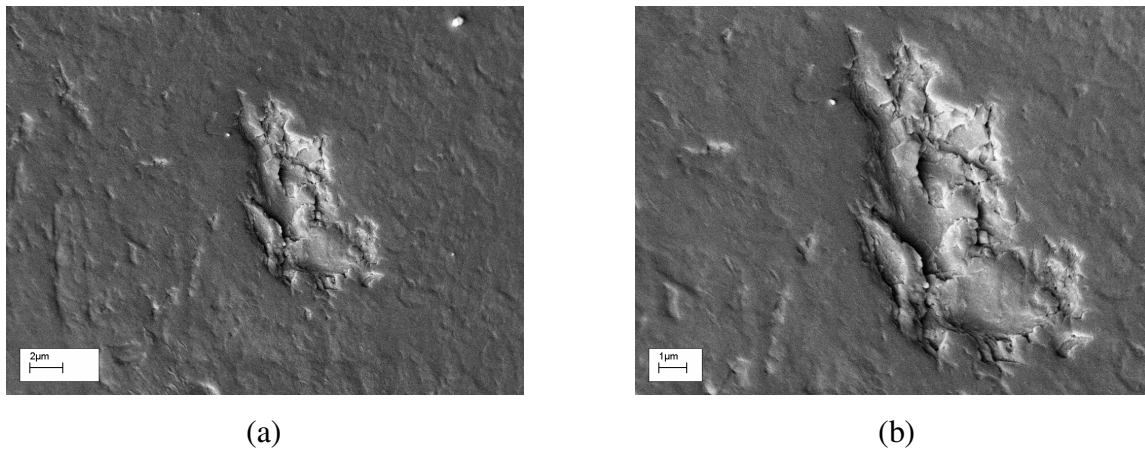


Fig: 4.28. Bubbling out of surface layer in rolling contact

The passage of lubricant into this bubbling out feature accelerates erosion locally due to the presence of bubble nuclei. The growth of bubble in this area allows sufficient cavitation formation which encourages material removal. This material removal leads to the formation of micro pits. As shown in Figure 4.29 below, these bubbling out features were found just after 8.2×10^4 of mechano-erosion testing. This is test specimen S-7 which as marked in the Figure 4.29 (b) show clearly the formation of micro pit from these bubbling out features.

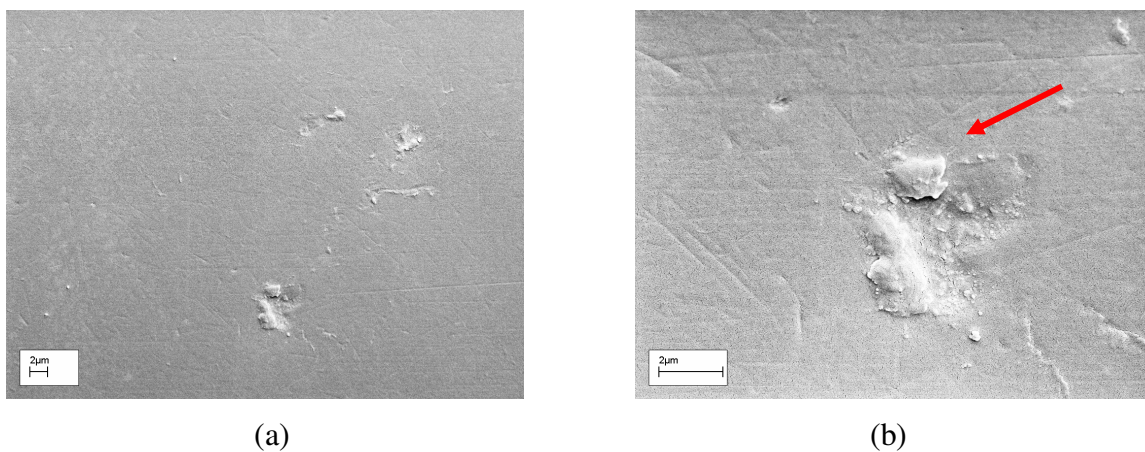


Fig: 4.29 Wear initiations in rolling contact after 40 minutes

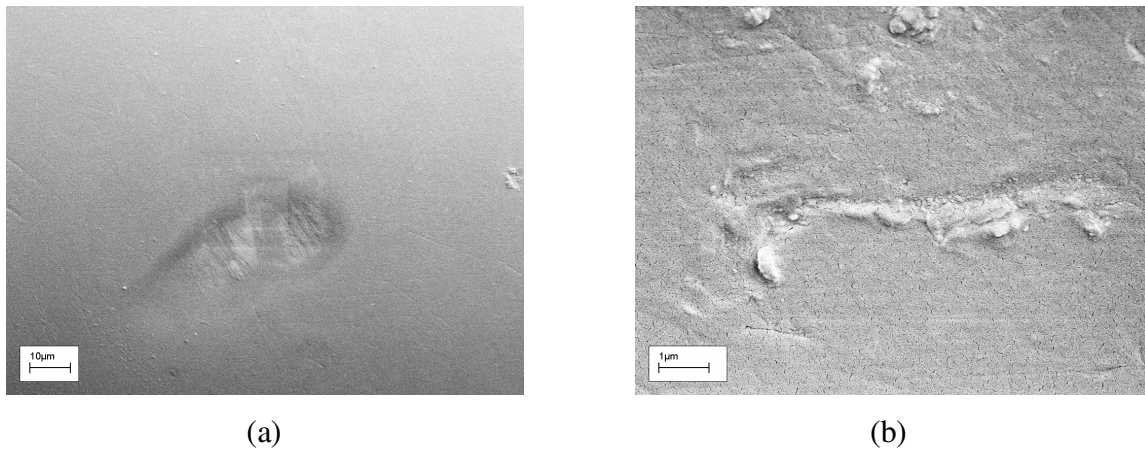


Fig: 4.30 (a) Micro pit formation and (b) C-shaped damage initiation

This process of micro pit formation was found to be same for C-mark formation. As shown in Figure 4.30 (a) above of test specimen S-7, the bubbling out feature upon further excitation to cavitation and rolling contact leaves behind this type of pit marks. On the Figure shown in 4.30 (b), the C- shaped marks show accumulation of material on the edges which during continued testing allow displacing this material causing the formation of C- shaped marks. This clearly suggests that material removal process at the initial stages takes place at small scale as observed in static erosion testing.

4.5.2.2 Erosion pits and material failure

The formation of erosion pits accelerated after this stage of micro pit formation. Different stages of pit formation are shown in Figure 4.31 below. These are test materials S-8 and S-9 which is material A silicon nitride with bearing steel as lower balls. As shown in Figure 4.31 (a) the test material exhibit very less concentration of erosion pits which was observed after 3.6×10^5 stress cycles of testing. The white colour layer as seen on the contact track is the lubricant layer which is a typical behaviour of this low viscosity lubricant Macron 110. For test specimen S-9 which was tested at same conditions but for more number of stress cycles for 7.1×10^5 shows extensive pit formation in Figure 4.31 (b).

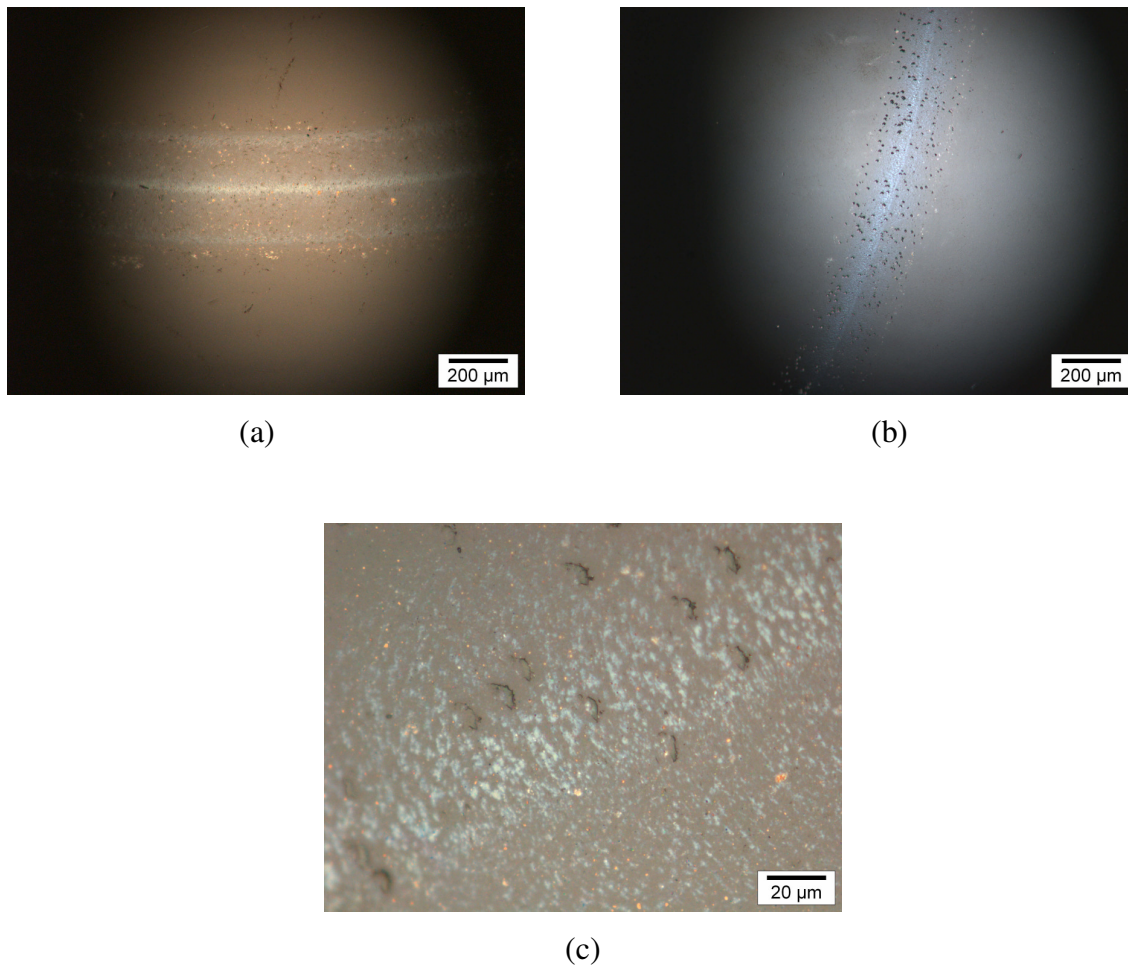


Fig: 4.31 Material A erosion marks (a) after 2 hours (b) after 4 hours and (c) close up of erosion marks

The close up of this erosion marks are shown in Figure 4.32 (c) above. These C- shaped marks clearly show directionality due to rolling contact with lower balls. This type of marks is unique for specimens tested under hybrid contact as mentioned in section 4.5.1.2. Further similar tests with hybrid contacts showed this C-shaped marks and are shown in Figure 4.33 below. As shown in Figure 4.33 (a) the process of pit bridging can be seen as part of pit growth. Also, the edge of these C-marks open up during rolling in the opposite direction and gets broader as marked in Figure 4.33 (b). This is test

specimen S-10 which was tested for 5.25×10^5 stress cycles at a contact pressure of 5 GPa.

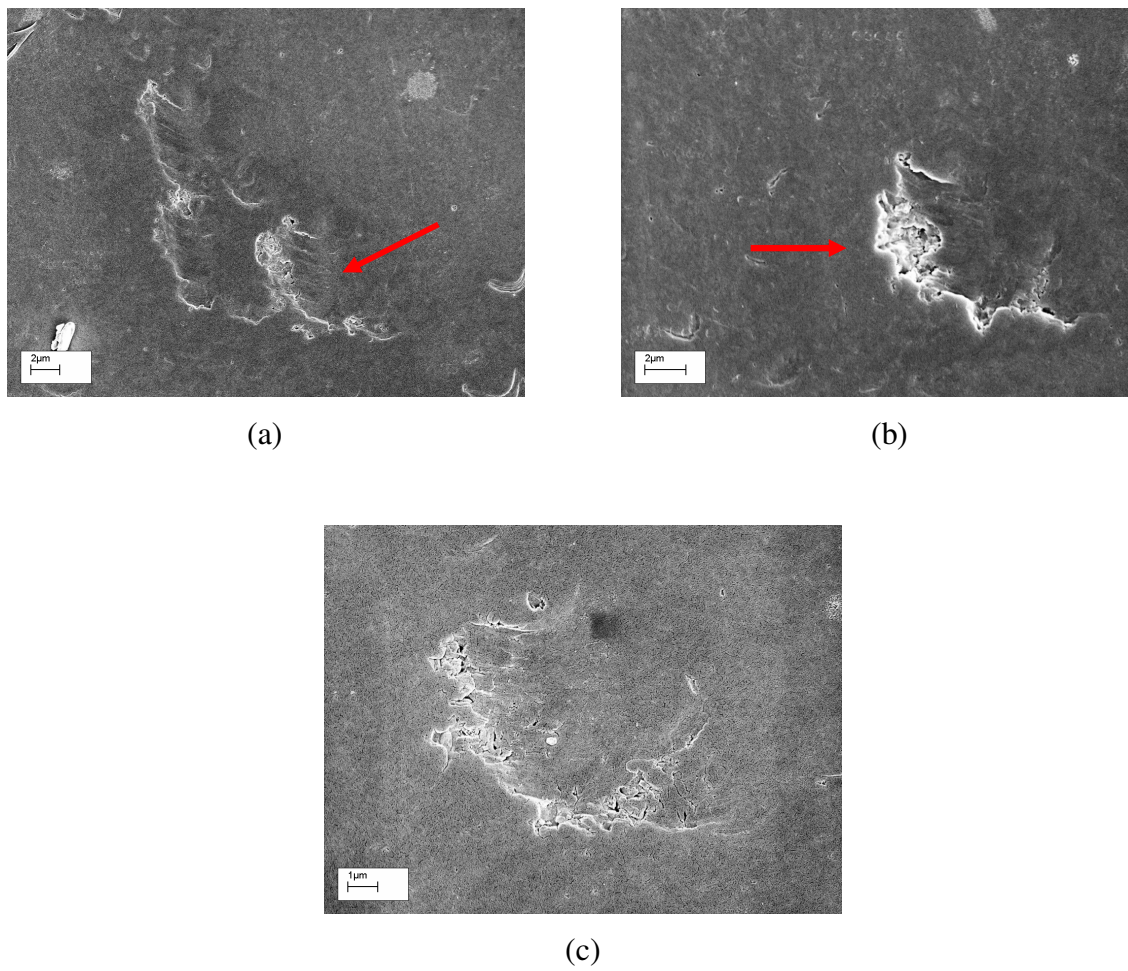


Fig: 4.33 Formation of C-shaped erosion marks on contact track

The high magnification image of this C-mark is shown in 4.33 (c). The edge of this C-mark gets wider during the course of testing which leads to the formation of micro pits. These micro pits then grow during continued exposure to mechano erosion testing. This leads to erosion severity eventually causing the test material to fail. Results of test specimen S-11 is shown in Figure 4.34. As marked in the Figure 4.34 (a) the smooth area is due to rolling contact and a large pit corresponding to the displacement of grain or bunch of grains and the adjacent areas show pit enlargement. The surface also becomes

very rough. High magnification scanning electron microscope of the failed area show clear eroded surface as observed in static erosion testing which proves the material failure in this mechano erosion testing is predominately due to erosion.

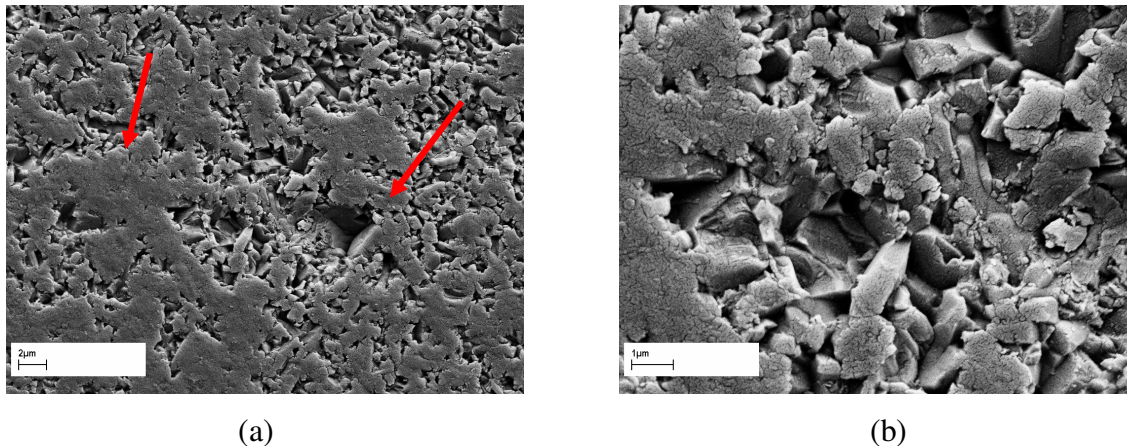


Fig: 4.34 Final stages of material failure showing severe erosion

4.5.2.3 Delamination wear

Delamination wear was also observed as part of this mechano erosion testing. This was observed only on the lower balls not on the upper balls. Scanning electron microscope images of this failure is shown in Figure 4.35. This is the result of test S-12 which ceramic to ceramic contact of material C. This test was run at high contact pressure and speeds of 7000 rpm. The material failed after 1.26×10^6 stress cycles of testing and surface investigation on the lower balls showed severe delamination wear with erosion signs on the delaminated areas. This delamination wear was not observed when the same material was tested without cavitation; test number S-13 i.e. only rolling contact fatigue at this high load and speed. The contact track of the upper ball was severely eroded as well. The explanation of this delamination wear is due to formation of many numbers of micro pits due to bubbling out process. The concentration of these micro pits upon further exposure to cavitation and rolling contact allowed displacing a large area resulting in this

failure. There is no subsurface crack formation which is typical for spall and delamination type of failure.

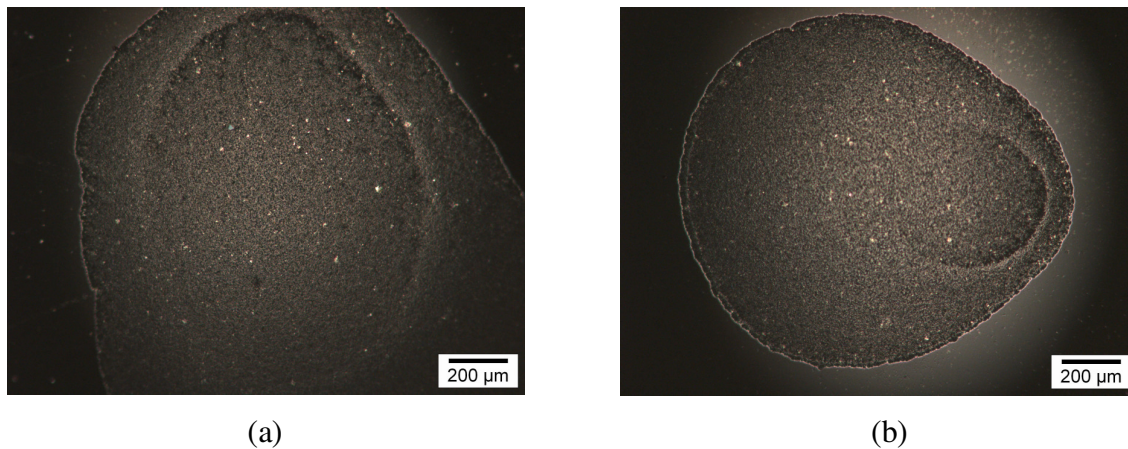


Fig: 4.35 Delamination wear on material C on lower balls

4.6 Wear conditions

The effect of these mechano erosion testing conditions were also studied to understand the test parameter influence on material failure. For this, several tests were carried out by varying each parameter in a test thereby allowing arriving at a conclusion on the parametric effect. Effect of magnitude of vibration, lubricant was studied in the static erosion testing which was repeated in this testing. Also for the rolling contact testing, contact pressure and rotational speed are the two key test parameters. The effect of these two was also investigated and is detailed in this section.

4.6.1 Effect of contact stress

The effect of contact stress largely influences the nature of erosion pit formation. At low loads, the erosion pits formed on the contact track were not deeper compared to the test results obtained from high loads. Figure 4.36 (b) shows results of test specimen S-14 which was run at low load of 3 GPa at the speed of 5000 rpm. As seen in this Figure the

number of pit formation is quite high but is not deep. But the results of test specimen S-15 as shown in Figure 4.36 (a) show deep and elongated erosion pits.

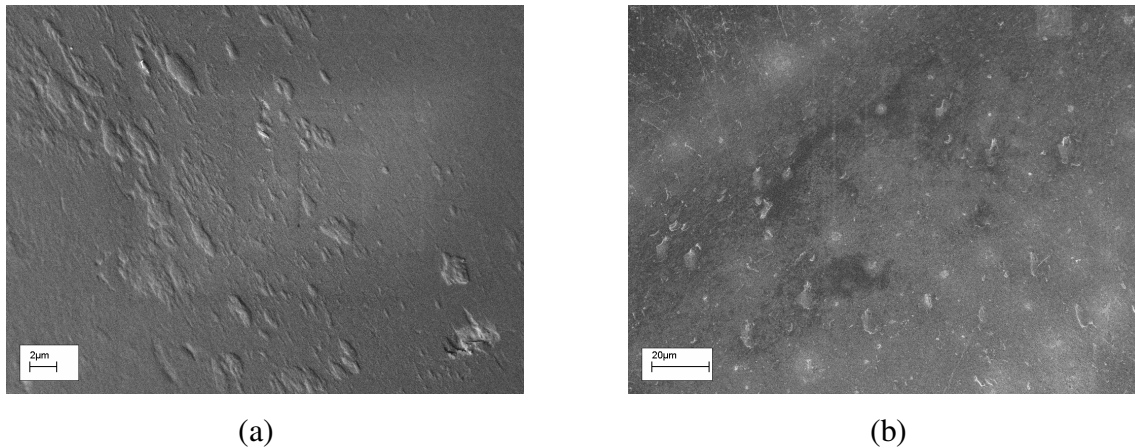


Fig: 4.36 Effect of contact stress (a) contact track at high load of 5.2 GPa and (b) Contact track at low load of 3.5 GPa

This is clearly due to the effect of high load which increases the contact pressure between the rolling elements causing deep and broad erosion marks. One example erosion pit is shown in Figure 4.37 below. This is from the same test S-15 which was tested at high loads. As seen in these Figures, the erosion pits formed are large which was not observed in tests with low loads.

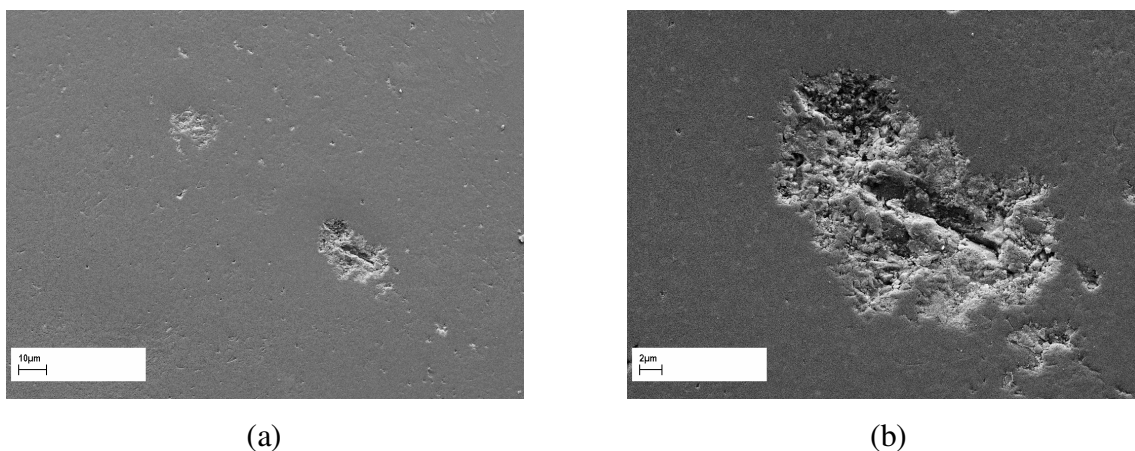


Fig: 4.37 (a) Large pit formation due to high load and (b) Close up of erosion pit

4.6.2 Effect of rotational speed

The effect of rotational speed is very clear as the increase in speed increases the number of stress cycles. This is shown in Figure 4.38 result obtained from specimens S-16 and S-17 which was tested at a speed of 2000 and 3000 rpm. The less number of stress cycles in the test S-16 shows very less number of erosion pits, whereas in S-17 with an increase in the stress cycles show increased wear with more concentrated erosion marks. High speeds also induce certain level of cavitation in the test chamber which could also play a role in material wear.

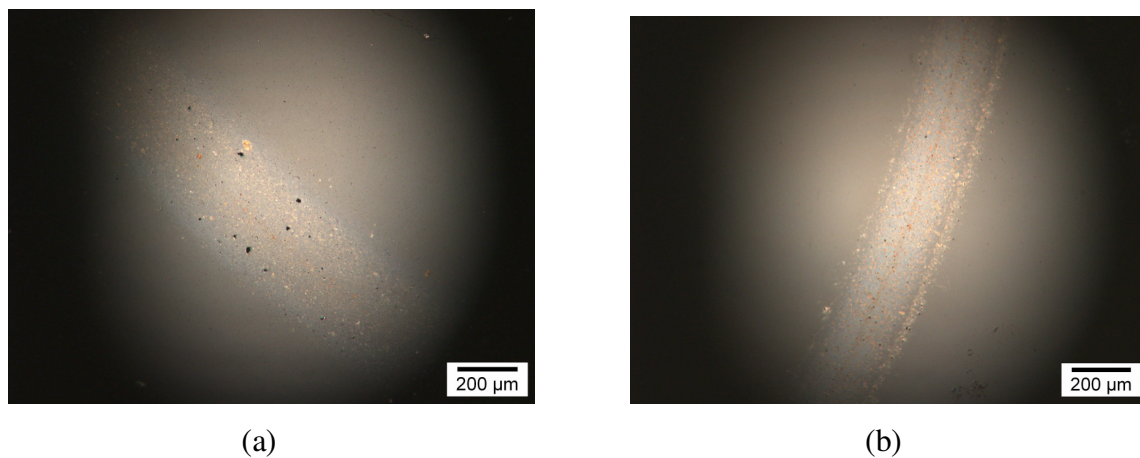


Fig: 4.38 Contact track after 3 hours of testing at speed of (a) 2000 rpm and (b) 3000 rpm

4.6.3 Effect of Lubricant

Most of the tests conducted using this new testing methodology was with Macron 110 lubricant due to industry interest. The influence of test lubricant was also investigated as part of this study. Different lubricants used are given in Table 4.3. As previously investigated in the static erosion testing for viscosity influence resembles the effect of

viscosity on this mechano-erosion testing. The test lubricant with a very low viscosity showed a rapid formation of erosion marks on the contact track compared to high viscous lubricant. Distilled water, which is lowest of all test lubricants showed erosion marks within 40 minutes of testing. Tests on Macron 110 lubricant showed almost similar time as distilled water to form erosion pits in one hour of exposure to mechano-erosion. A refrigeration oil with a Kinematic viscosity of 32 cSt showed formation of very less number of erosion marks on the contact track after 5 hours of testing. This is test specimen S- 20. Tests on other high viscous lubricants such as base oil and cylinder oil did not show any signs of erosion for a long time and hence these tests were discontinued. This clearly suggests that viscosity has a strong influence on the rate of erosion. Any increase in the viscosity of the test liquid decreases the rate of erosion and therefore the subsequent material damage in this condition.

Lubricant	Viscosity at 40 C (cSt)	Erosion Initiation period (minutes)
<i>Distilled Water</i>	0.658	40
<i>Macron 110</i>	2.4	60
<i>Gargoyle Arctic Refrigeration oil</i>	32	480
<i>Base Oil</i>	94.6	Test discontinued
<i>Cylinder oil</i>	1040	Test discontinued

Table: 4.3 Effect of test lubricant

4.6.4 Effect cavitation conditions

The effect of cavitation intensity in the test liquid obviously plays a major role in this wear process. This can be easily understood by turning off the piezoelectric transducer or set it to zero amplitude of vibration. As the vibration amplitude of the transducer was gradually increased the rate of erosion increased accordingly. The cavitation intensity in the test liquid is determined by the acoustic power generated by the transducer which is directly proportional to its vibration amplitude. Below the vibration of 30 microns peak-to-peak no erosion signs were observed on the test sample for a long time. In static erosion testing, the erosion process begins when the amplitude of vibration reached 10 microns peak-to-peak. But, in mechano erosion testing this was found to be higher due to the distance between the tip of the transducer horn and test materials is higher compared to static erosion testing.

Chapter 5

CONCLUSIONS

5.1. Conclusions:

With the major advancement of hybrid bearings, particularly operating in low saturation temperature lubricants, studies on the wear mechanism of silicon nitride due to cavitation is limited. The outcome of the research work presented in this thesis provides a clear picture on this. This helped to conclude that erosive wear initiation in silicon nitride is due to multiple trans and inter-granular fracture. Also the comparative study on different silicon nitride materials showed that microstructure plays a major role. An effort to combine cavitation erosion and rolling contact wear testing resulted in delivering a new material testing methodology. This has shown promising results in creating controlled erosion on rolling elements in rolling contact experiments. This testing methodology can also be adapted for situations where erosion is a concern in moving bodies. Conclusions of this research finding for the aims and objectives mentioned in chapter 1 are as follows:

1. The cavitation wear initiation in silicon nitride is due to fracture of grains and grain boundaries depending on the material microstructure. This wear initiation caused extrication and detachment of material particles completing the incubation period of this wear process leading to the next stage of large scale material removal, which is the formation of erosion pits. The formation of complete grain or Intergranular boundary phase pockets dislodging was not due to single cavity impact but rather formed after several cycles of cavity collapse. Also crack initiation and propagation was noted which concludes cavitation erosion is a surface fatigue process. Cracks which were formed during the initial and wear acceleration stages are short and propagate only to a maximum distance of few microns due to the nature of erosion loading. Also their growth was retarded by adjacent erosion pit or fractured region.

2. Hardness and fracture indentation toughness values were similar for material A and B, and was smaller for material C. Hardness and fracture indentation toughness have limited influence on the cavitation erosion as opposed to micro structural aspects and strength. It is expected that conventional fracture indentation toughness determined from fairly long cracks which are opposed to the grain scale of cracks as observed here are strongly influenced by grain bridging, frictional pull-out mechanisms. Hence this could not be a representative parameter for assessing the erosion initial cracking damage. A grain scale crack initiation and propagation property for these materials is critical. Overall strength and effective surface strength does not have a dominating effect on erosion resistance from the materials tested here. Microscopic-scale aspects of the material microstructure other than grain size may also have more impacts on the erosion damage initiation and propagation.
3. Amount, thickness and presence of larger pockets of the intergranular boundary phase may influence the local damping and energy absorption or stress transmission to the surrounding matrix during cavity collapse. Also the amorphous or crystalline character of the intergranular boundary phase or the eventual secondary crystalline phase presence from reaction of the sintering additives during sintering may be a contributing factor for resistance.
4. Formation of erosion pit clearly shows that it is not displacement of a single grain, but it could also be due to displacing bunch of grains. This pit formation is the reason for accelerating the wear by huge material loss. Local residual micro-stresses and binding strength or energy between the different microstructure constituents would certainly affect the initial morphology of the cracking, erosion pit development and the progression rate of the material damage.
5. Tests carried out on rotating cylinder specimens did not show any major change in the erosive wear formation compared to the stationary specimen mainly due to

the nature of cavitation loading applied in the laboratory. The formation of fracture zones were very close and almost appeared in a straight line because of the way the specimen was exposed to cavitation.

6. Design exploration on the rotary tribometer and acoustic cavitation techniques resulted in developing new mechano-erosion testing facility. This made it possible to study the effect of liquid/gas phase transition in the lubricant in rolling contact testing. Desired level of cavitation in the test lubricant can be achieved thereby paving a way to perform studies on the effect of lubricant phase changes on rolling contact life.
7. Material wear observed in the mechano-erosion testing is very difficult to assess the mechanism due to the complexity in loading conditions. But frequent surface analysis revealed that “bubbling out” feature is the reason for material damage at initiation stages followed by pit formation and growth. Development of several fatigue zones on the contact track lead to concentrated formation of erosion pits as opposed to the actual bearing running conditions.
8. Tests on different contacts, hybrid and ceramic showed varying rate in the wear process. This is because silicon nitride is less resistant to cavitation compared to steel. The difference in the noted wear morphology suggests that the contact materials also play a role. Testing conditions such as cavitation intensity, contact stress has a strong effect on the rate of the material wear process, but no change in the mechanism was identified.

5.2 Recommendations for future work

First, an in-depth material characterization is necessary to measure the material properties at micro level. This would enable the investigator to identify the critical material property which is responsible to resist or accelerate cavitation erosion. So far it has been concluded that only the grain size of the material can be used as a parameter to assess erosion resistance. Investigation on the contact lubrication in the new mechano-erosion testing is required to understand the process of lubrication changes due to the introduction of cavitation. This change in the lubrication is critical as it not only affects the rolling contact fatigue life but also would change the wear mechanism and hence must be explored. Also, the primary wear mechanism produced in these experiments were found to be dominated by cavitation. The secondary mechanisms such as redistribution of stresses caused by erosion pit and the lubricant pressure intensity at these locations are also critical.

Rolling contact fatigue experiments with pure refrigeration lubrication are possible and the results did not show any river mark type wear. A tribometer which would let test materials under cryogenic conditions would certainly be valuable, this can be adapted from the cryo-tribometer reported in the literature and as reviewed in the beginning of this thesis. This will allow perform RCF experiments at these conditions and will provide a platform to perform a comparative study between cavitation erosive wear and wear due to rolling contact. This will enable to understand more about the correlation between river marks and erosive wear. A model which describes the cumulative damage accumulation of material wear due to cavitation and rolling contact will help predict the life of rolling elements and plan preventive measures, but is a long way forward.

Appendix A

Silicon Nitride - Material Data

A brief summary of silicon nitride is presented here. This includes the different processing methods to manufacture this material, properties and its common applications. Ceramics are a class of materials characterized as brittle, low density, chemically inert, very high melting point, and high young's modulus. This made them find their application in several engineering disciplines and has now grown in to a multi-billion dollar a year industry.

A1.1 Overview:

The development of silicon nitride was a result of investigation of materials to replace metals for turbine engine applications in the 1950s. Materials employed in these turbine engine applications should withstand high temperatures of 1100°C . This initial goal was not yet achieved, but silicon nitride is now used in several industrial applications. Silicon nitride is a covalent bond material with a Si atom surrounded by 4 N to form SiN_4 tetrahedra. The high melting point and strong covalent bond make them difficult to sinter. Three crystallographic phases exist, out of which α and β phases are common and can be produced at normal pressure conditions.

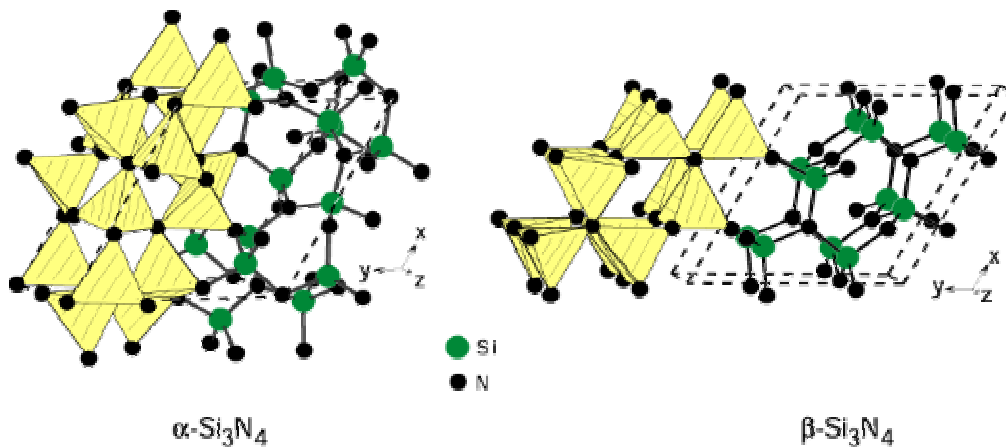


Fig: A1.1 Crystal structure of α and β Silicon nitride (Reidal 2000)

The other method to process silicon nitride is by reaction-bonding. The reaction bonding method uses an endothermic reaction to react Si and N gas resulting in a pure silicon nitride without any glass phase at the grain boundaries. Iron is used as a catalyst to achieve this reaction between the temperatures of 1200⁰ to 1400⁰ C; this leaves the formation of iron silicates as marked in figure A1.2. This method forms a porous silicon nitride to ensure nitrogen transport.

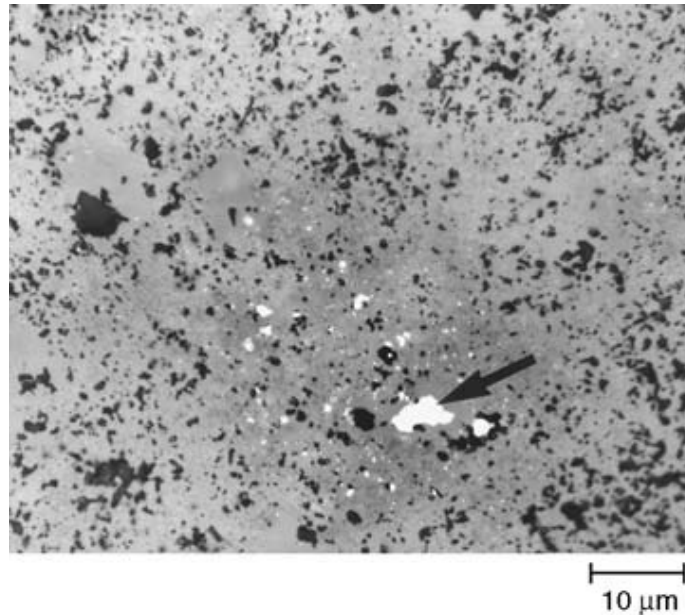
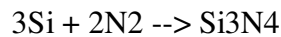


Fig: A1.3 Reaction bonded silicon nitride (RBSN) (Taeffner 2004).

Sintering is further based on the manufacturing methods as: gas-pressure sintered (GPSN), hot-pressed (HPSN) and hot isostatically pressed silicon nitride (HIPSN). The most common sintering additives used are Alumina, Magnesia, Yttrium, Titanium oxide. These additives leave a glassy intergranular phase affecting the properties of the material. The selection of sintering additives determines the method to be manufactured as HPSN,

HIPSN or GPSN. Microstructure of materials obtained using these different methods are shown in figure A1.4.

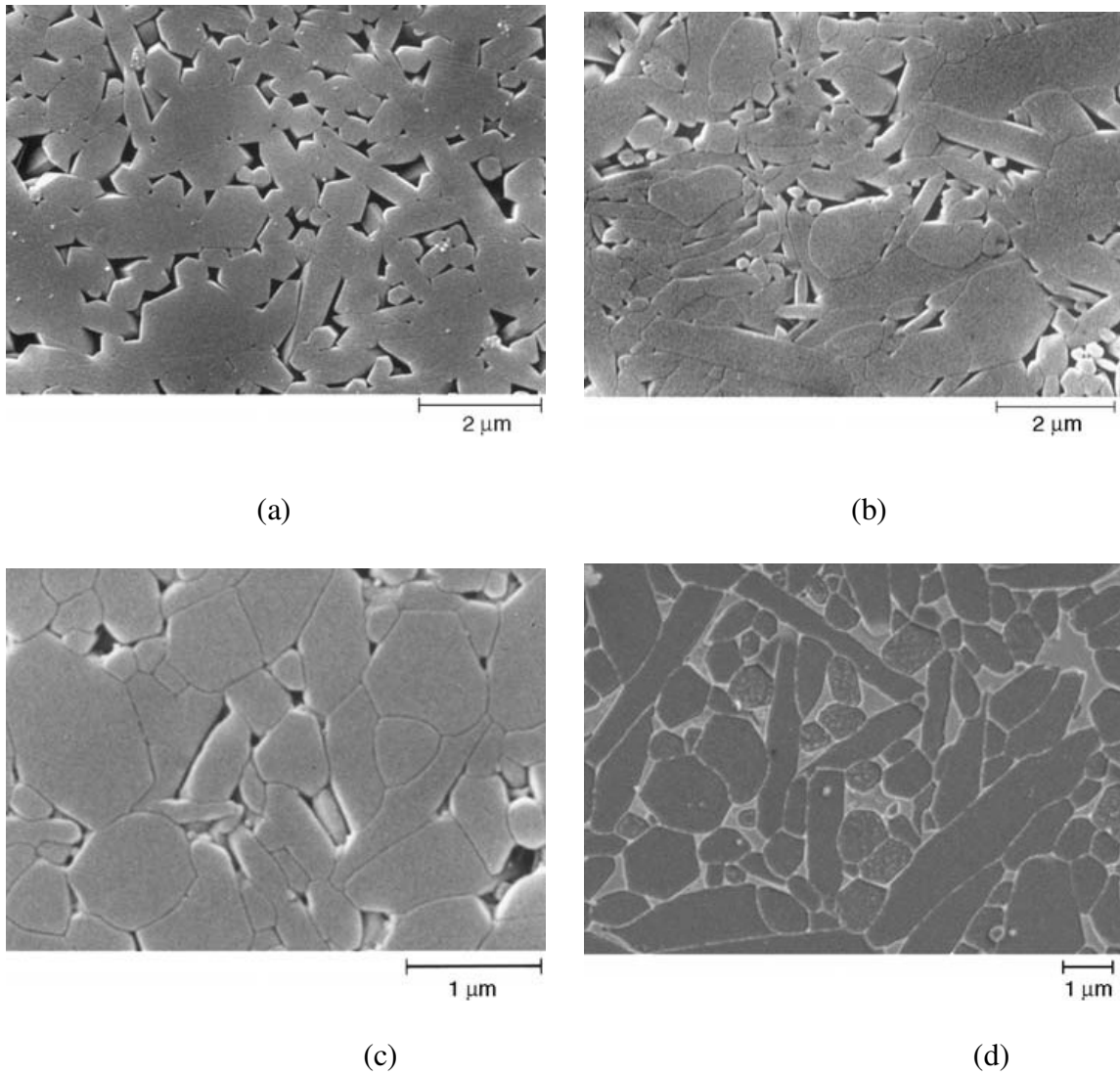


Fig: A1.4. Etched surfaces of different silicon nitride (a) sintered (SSN), (b) Hot pressed (HPSN), (c) Hot isotatically pressed (HIPSN) and (d) Gas pressure sintered (GPSN) (Taeffner 2004).

A1.3 Physical Properties:

Key Properties of silicon nitride from (CERAM 2005):

- Low density
- High temperature strength
- Superior thermal shock resistance
- Excellent wear resistance
- Good fracture toughness
- Mechanical fatigue and creep resistance
- Good oxidation resistance

Processing Method	Density (g/cm ³)	Elastic Modulus (GPa)	Fracture Toughness (MPa m ^{1/2})	Flexural Strength (MPa)	Hardness (GPa)	Poisson's Ratio
Sintered	3.2	276	4.5	600	14	0.24
Hot-pressed	3.2	317	5	800	20	0.28
Reaction-bound	2.5	165	3.6	210	10	0.22
Sintered reaction bound	3.3	297	NA	825	19	0.28
Hot Isostatic pressing	3.2	310	6	1000	20	0.28

Table A1.1 Mechanical properties of silicon nitride with different processing (Ying 2001)

Material	Density (g/cm³)	Elastic Modulus (GPa)	Hardness (GPa)	Fracture Toughness (MPa m^{1/2})	Flexural Strength (MPa)
Silicon Nitride (Si ₃ N ₄)	3.2	315	14-18	4-7	600-1000
Silicon Carbide (SiC)	3.1	420	20-24	2-4	
Alumina (Al ₂ O ₃)	3.9	390	18-20	3-5	200-300
Zirconia (ZrO ₂)	5.8	210	11-14	8-12	440-720
Bearing Steel	7.8	200	10	> 16	

Table A1.2 Typical properties of Engineering ceramics and bearing steel

A1.4 Applications:

Some example applications of silicon nitride are (Morgen 2005)

- Bearing balls and rollers
- Cutting tools
- Valves, turbocharger rotors for engines
- Turbine blades
- Glow plugs
- Molten metal handling
- Thermocouple sheaths
- Welding jigs and fixtures
- Welding nozzles

Appendix B

Cavitation Erosion Experiments

This appendix provides a brief summary of the different types of cavitation erosion methods used in laboratories to assess the material against cavitation erosion.

A2.1 Cavitation Laboratory Testing Methods

This can be broadly classified into hydrodynamic and acoustic cavitation. Summary of these methods as described in ICET (International Cavitation Erosion Test) is given in this section. Hydrodynamic method of cavitation is generated due to flow conditions by varying velocity. At high velocities, low pressures and cavities are formed. As shown in figure A2.1 a cavitating jet is supplied at a constant pressure through a long nozzle. A circular or cylindrical test specimen is kept at the desired location. Upon cavity collapse on the specimen, the test specimen erodes and the rate of erosion varies with the intensity of the cavitation generated. The flow rate in the nozzle depends on the up stream pressure and a cavitation number C_v , a ratio of downstream and upstream pressure is used to determine the flow rate.

High intensity of cavitation can be achieved using rotating disk compared to cavitation tunnel. This method uses a rotating disk and resembles a pump impeller and therefore considered as a well-suited method to replicate the cavitation conditions observed in hydraulic machines. This contains a rotating disk with circular or cylindrical holes which create cavitation due to low pressures at the holes. Test specimens are fixed on the disc at the downstream side allowing to get exposed to cavitation as shown in figure A2.2. The major drawback of this method is that it requires extensive cooling system to control the heat generation. Acoustic method of generating cavitation is described in the text and hence is not included in this appendix.

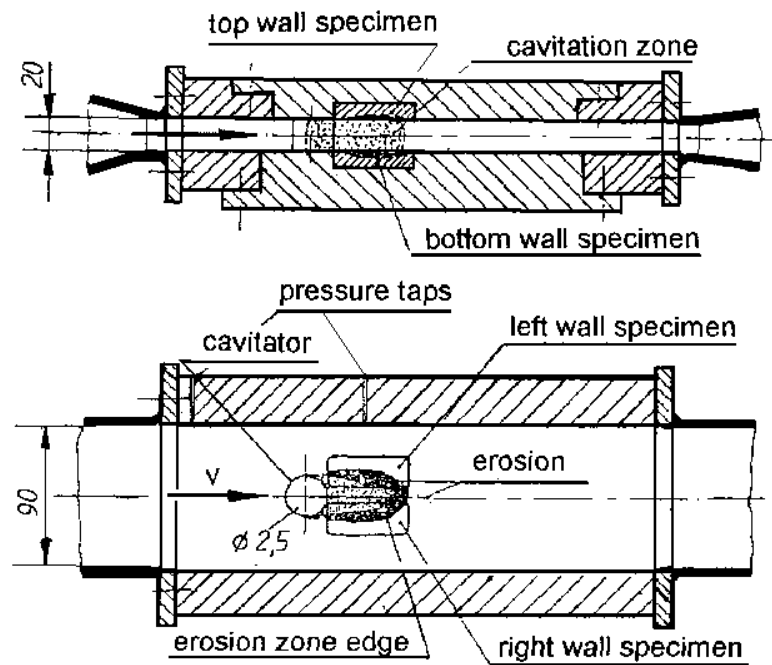


Fig: A2.1. Cavitation tunnel in the Hohenwarte II Pumped-Storage Power Plant in Germany (ICET 1998)

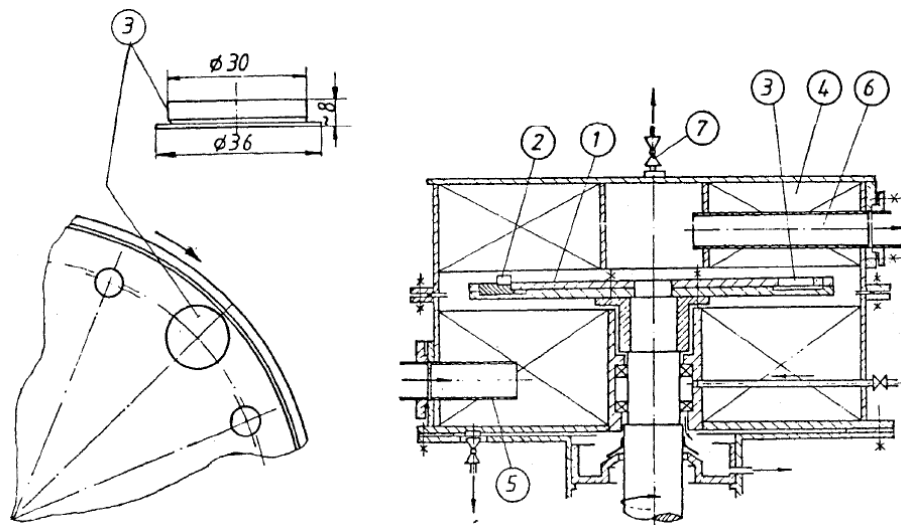


Fig.A2.2. Rotating disk facility in the IMP PAN lab in Gdansk, Poland (ICET 1998)
 1 - disk, 2 -cavitator, 3 - specimen, 4 - stagnator vane, 5,6 - working liquid inlet and outlet, respectively, 7 de-aerating valve

Appendix C

Experimental preparation and surface analysis

Equipments used to test samples for experiments and surface analyses are presented in this appendix.



Fig: A3.1 Buehler Vickers Indent generating device

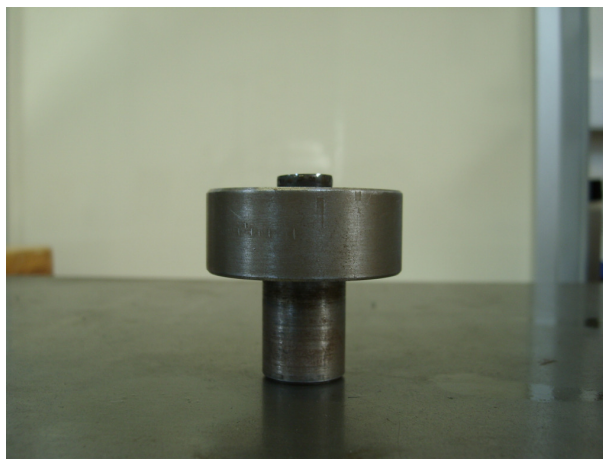


Fig: A3.2 Specimen Holder for Indentation

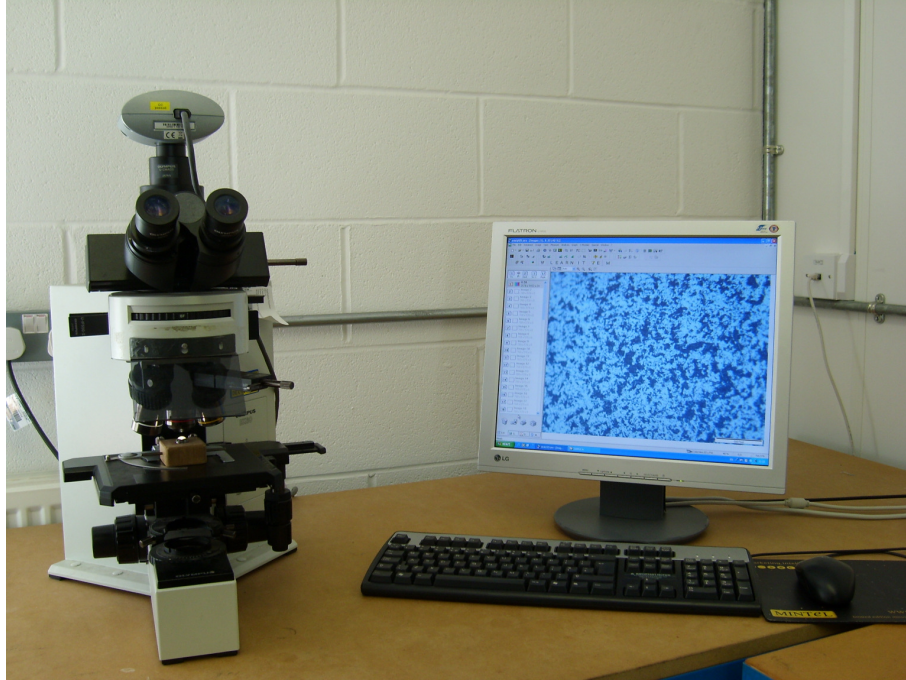
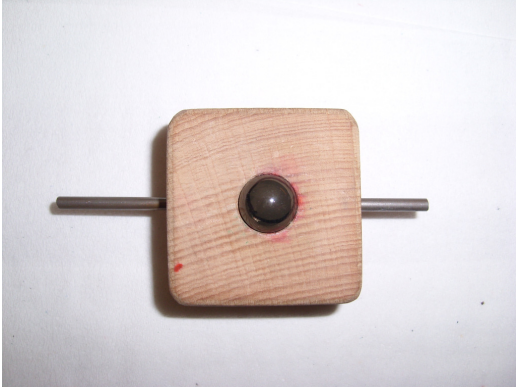


Fig: A3.3 Digital Light Microscope used for preliminary surface analysis and imaging



Fig: A3.4 ZYGO Surface scanning microscopy



(a)



(b)

Fig: A3.5 (a) Hand free ball rotating manipulator and (b) Manipulator in Light microscope

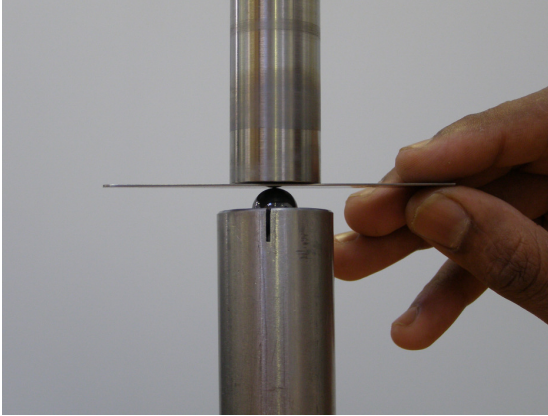


(a)



(b)

Fig: A3.6 (a) Ultrasonic bath for specimen cleaning and (b) Specimen dryer



(a)

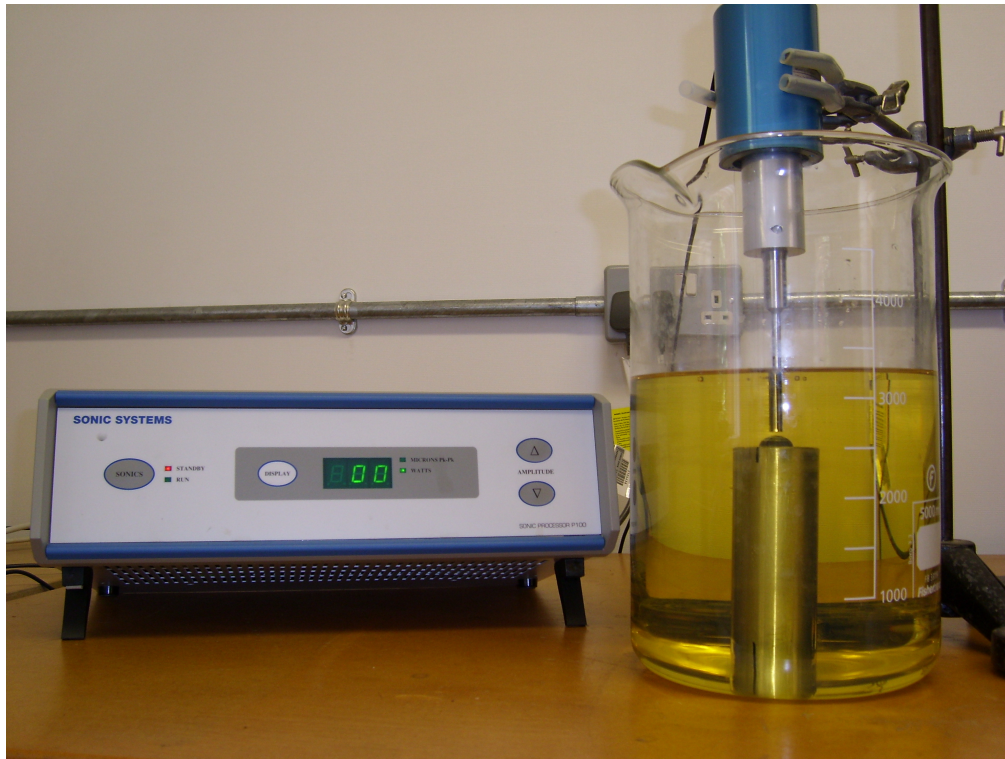


(b)

A3.7. Specimen setup for cavitation experiments (a) using feeler gauge and (b) transducer horn and specimen



Fig: A3.8. Cavitation erosion test setup.



A3.9. Cavitation test in lubricating oil.



Fig: A3.10. Low and High powered piezoelectric transducer.



Fig: A3.11. Specimen holders' for cavitation experiments.



Fig: A3.12. Cutting machine for specimen dicing.



Fig: 3A.13. Crack generating equipment.



Fig: A3.14. Crack positioning for RCF experiments.

Input parameters

va	0.2798	Poisson's Ratio of Silicon Nitride
vb	0.2798	Poisson's Ratio of Steel
Ea	306.96	Young's Modulus of Silicon Nitride (GPa)
Eb	306.96	Young's Modulus of Steel ball (GPa)
Ra	6.35	Silicon Nitride ball radius (mm)
Rb	6.35	Steel ball radius (mm)

Intermediate Calculation Result

Effective Elasticity (GPa)	166.5162292
Effective Radius (m)	0.003175

Calculation

Plint Machine Load (KN)	Contact Load (N)	Max. Compressive Stress (GPa)	Radius of contact circle (m)	Max. shear stress (Gpa)	Max. tensile stress (Gpa)
0.195873022	80	3.491982296	0.000104587	1.082514512	0.535437285
0.391746043	160	4.399622001	0.000131772	1.36388282	0.674608707
0.587619065	240	5.036309966	0.000150841	1.56125609	0.772234195
0.783492086	320	5.543176371	0.000166022	1.718384675	0.84995371
0.979365108	400	5.971205733	0.000178842	1.851073777	0.915584879
1.17523813	480	6.34535294	0.000190048	1.967059411	0.972954118
1.371111151	560	6.679921824	0.000200069	2.070775765	1.02425468
1.566984173	640	6.983964592	0.000209175	2.165029024	1.070874571
1.762857195	720	7.263615885	0.000217551	2.251720924	1.113754436
1.958730216	800	7.523247796	0.000225327	2.332206817	1.153564662
2.154603238	880	7.766099103	0.0002326	2.407490722	1.190801863
2.350476259	960	7.994643739	0.000239446	2.478339559	1.225845373
2.546349281	1040	8.210819102	0.00024592	2.545353922	1.258992262
2.742222303	1120	8.416174118	0.000252071	2.609013977	1.290480031
2.938095324	1200	8.611968902	0.000257935	2.66971036	1.320501898
3.133968346	1280	8.799244002	0.000263544	2.727765641	1.349217414
3.329841368	1360	8.978869793	0.000268924	2.783449636	1.376760035
3.525714389	1440	9.151582552	0.000274097	2.836990591	1.403242658
3.721587411	1520	9.318011317	0.000279081	2.888583508	1.428761735
3.917460432	1600	9.478698262	0.000283894	2.938396461	1.4534004
4.113333454	1680	9.634114381	0.000288549	2.986575458	1.477230872

Table: A3.1 Contact stress calculations

Appendix D

CAVITATING FLOW MODELLING

This appendix contains the numerical study on cavitating fluid flow of vibratory cavitation in order to assess the pressure loads imposed on test specimen. A computational fluid dynamic CFD model was developed to assess these variables and is described in section A.D.2. Multiphase flow analysis forms the basis of cavitation model development with water and vapour as fluid pairs and is detailed in section A.D 1. The bubble growth and collapse near the solid surface is modelled using Rayleigh-Plesset model as presented in section A.D 2. To calculate the resulting stresses on test materials due to cavitation requires a coupling of two different fields namely fluid dynamics and structural modelling is required. A multi-field simulation called as fluid-structural interaction was performed and is described in section A.D 3.

A.D 1 Multi Phase Flow:

Multiphase flow is a flow in which more than one fluid is present. The fluids in the multiphase flow are assumed to be mixed at macroscopic scale, much larger than molecular. Examples are gas bubbles in a liquid, liquid droplet in a gas or in another immiscible liquid etc. In these cases, it is necessary to solve for different velocity and temperature fields etc. for each fluid. These may interact with each other by means of interfacial forces, heat and mass transfer across the phase interfaces. Commercially available CFD software was utilized for modelling purposes. This software includes a variety of multiphase models to allow the simulation of processes which transport and bring into direct contact multiple fluid streams to effect mixing, reaction, and separation (CFX 2007). Eulerian–Eulerian multiphase model is commonly used in most situations. The Eulerian multiphase method, sometimes also called the multi-fluid model, is characterized by the solution of an individual set of momentum equations for each phase,

liquid and vapour. Two different sub-models are available for Eulerian-Eulerian multiphase flow:

- The Homogeneous Model: This is the simplest model, in which all fluids share the same flow field. This model was used for cavitation modelling since the water vapour is finely dispersed in the continuous fluid, which is water. During vibratory cavitation, it is clear that bubbles are very well mixed and are sufficiently small to eliminate any relative motion between phases. Many bubbly flow come close to the limit of negligible relative motion and hence can be assumed as homogeneous (Brennen 1995)
- The Inter-fluid Transfer or Inhomogeneous Model: Each fluid possesses its own flow field and the fluids interact via inter phase transfer terms. Flow field definition such as separate velocity and temperature are required for both phases to model this behaviour.

A.D.1.1 Cavitation Models

Numerical modelling and prediction of cavitation is achieved by several methods. Dupont (Dupont 2003) summarizes the following methods introduced with three-dimensional Reynolds-averaged Navier-Stokes codes. They are:

1. Single fluid model with empirical state law that defines the density variation of a liquid-vapour mixture (Rebound et.al 1998)
2. A volume-of-fluid method based on a two-phase approach where the convection of one phase in a second phase is calculated with a possible mass exchange between the two phases based on a law of the state (Dieval et al., 1998)
3. A cavity-interface tracking method, which iteratively adapts the cavity shape in order to reach a given condition (velocity or pressure) at its interface (Hirschi 1998)

4. A bubbly two-phase flow model solving a Rayleigh-Plesset equation in order to calculate the density of a mixture of water and bubbles (Tamura 2001)

Dupont (Dupont et al, 2003) performed a bench-mark study on various commercially available CFD codes to evaluate them for cavitation modelling. A double-volute centrifugal pump was tested for this purpose and compared with experiments. The results obtained from various CFD codes showed that ‘CFX’ – a commercially available CFD code was more appropriate for predicting cavitation performance regarding accuracy, and is used for this project. CFX uses finite volume method, which means the governing equations are integrated around the mesh elements (CFX 2007). The main advantage of this method is that the spatial discretisation is carried out directly in the physical space. Also it is very flexible and can be easily implemented on a structured or unstructured mesh, which means complex geometries can be easily handled (Blazek 2006)

A.D.1.2 Rayleigh-Plesset Model

The growth of cavities or bubbles is two fold: Upon excitation, bubble nuclei can grow into stable bubbles which oscillate for a while until it becomes unstable for a collapse which is called stable cavitation or by growing rapidly into much larger one which collapses violently called transient cavitation. Young (Young 1999) explains the possible causes which prevents a bubble to be in equilibrium. For a perfect gas bubble in equilibrium in a liquid,

$$P_v = P_o + \frac{2\sigma}{R_o} \quad (1)$$

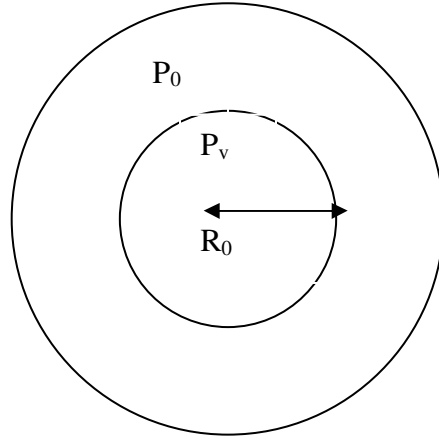


Fig: A.D.1 Gas bubble in a liquid

Where

P_v - is the gas pressure,

P_o - The ambient liquid pressure,

σ - The surface tension of the liquid and R_o the radius of the bubble.

Thus

$$R_o = \frac{2\sigma}{P_v - P_o} \quad (2)$$

For stability, critical radius

$$R_c = \frac{2\sigma}{P_v - P_o} \quad (3)$$

The above equation is an unstable condition. For if R is less than R_c , the surface tension $\frac{2\sigma}{R_o}$ predominates and bubble contracts, and if $R > R_c$, the gas pressure P_v dominates and the bubble expands indefinitely.

There are four possible ways which prevent the bubble to be stable:

- Rise due to buoyancy

- Dissolve due to diffusion of gas out of the bubble
- Contract due to surface tension
- Grow due to gas pressure.

Stable bubbles can grow by a second-order effect called rectified diffusion. The rate of bubble growth or contraction is provided by Rayleigh-Pesset equation which describes the bubble growth in a liquid as follows:

$$R_o \frac{d^2 R_o}{dt^2} + \frac{3}{2} \left(\frac{d R_o}{dt} \right)^2 + \frac{2\sigma}{R_o} = \frac{p_v - p}{\rho_f} \quad (4)$$

Where, p is the pressure in the liquid surrounding the bubble. This equation is derived from a mechanical balance, assuming no thermal barriers to bubble growth.

Neglecting the second order terms and the surface tension, equation (4) reduces to:

$$\frac{d R_o}{dt} = \sqrt{\frac{2}{3} \frac{p_v - p}{\rho_f}} \quad (5)$$

The rate of change of bubble volume follows as:

$$\begin{aligned} \frac{d V_o}{dt} &= \frac{d}{dt} \left(\frac{4}{3} \pi R_o^3 \right) \\ &= 4\pi R_o^2 \sqrt{\frac{2}{3} \frac{p_v - p}{\rho_f}} \end{aligned} \quad (6)$$

The rate of change of bubble mass is:

$$\begin{aligned} \frac{d m_o}{dt} &= \rho_g \frac{d V_o}{dt} \\ &= 4\pi R_o^2 \rho_g \sqrt{\frac{2}{3} \frac{p_v - p}{\rho_f}} \end{aligned} \quad (7)$$

If there are N numbers of bubbles per unit volume, then the volume fraction r may be expressed as:

$$\begin{aligned} r &= V_o N \\ &= \frac{4}{3} \pi R_o^3 N \end{aligned} \quad (8)$$

The total inter phase mass transfer rate per unit volume is:

$$\begin{aligned} \dot{M} &= N \frac{d m_o}{dt} \\ &= \frac{3 r \rho_g}{R_o} \sqrt{\frac{2}{3} \frac{p_v - p}{\rho_f}} \end{aligned} \quad (9)$$

The above expression (9) has been derived assuming bubble growth, vaporisation. For condensation the rate varies as it is slower than vaporisation.

A.D.2 Vibratory Cavitation Model

One cycle of the transducer vibration was modelled to calculate the resulting liquid conditions between the transducer and the test specimen. A transient mode simulation is required for this to implement this one cycle of vibration over time. The in-built cavitation model in the software uses Rayleigh-Plesset model and was used for this simulation. The vibration of the transducer was achieved using a mesh deformation option which allow modelling a moving mesh and is detailed in the following sections. Cavitation bubble may contain air or water vapour or even both. For this work, it was assumed that the bubble contains only water vapour with appropriate volume fraction values defined in the model domain. This multi-phase model was assumed to be homogenous and the turbulence was also modelled using k-epsilon turbulence model. The following sections details the approach and assumption made to build this model.

A.D 2.1 Geometry and Grid Generation

The vibratory cavitation system simulated is shown in Figure A.D.3. The fluid domain shown in Figure A.D.2 is the region of interest to analyse the flow conditions caused by transducer vibration. The modelled transducer is of 12.7 mm diameter same as the test material, and due to its cylindrical structure, advantage on the geometric symmetry was taken. This has lead to model only a small segment of 15 degrees without loosing the overall system behaviour by applying appropriate boundary conditions. The simulated system geometry only consists of a fluid region as the transducer and test specimen were modelled as walls on both top and bottom side.

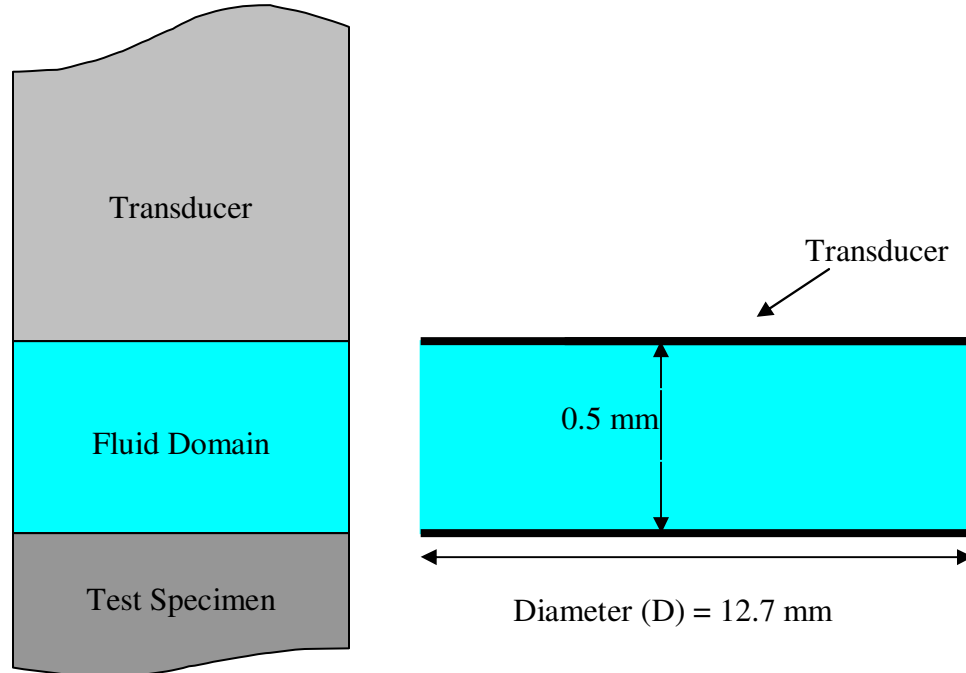


Fig: A.D.2 Schematic of the region of interest.

This geometry was generated using a CAD program and the grid generation was done using the CFX mesh method. This geometry is a collection of few faces which should be defined as composite regions before generating mesh in order to specify the corresponding locations for the boundary conditions. These composite regions form a collection of nodes or elements in the grid output for the physics definition. Here as

shown in Figure A.D.3, the top, bottom and side face 2D regions are modelled as opening boundaries, where the fluid can enter or leave the fluid domain. The region of interest is the transducer, test material and the fluid region in between. Transducer and the test material were modelled as solid wall boundaries. The two faces on the Z-axis are symmetry regions. Further details on these regions are described in the next section.

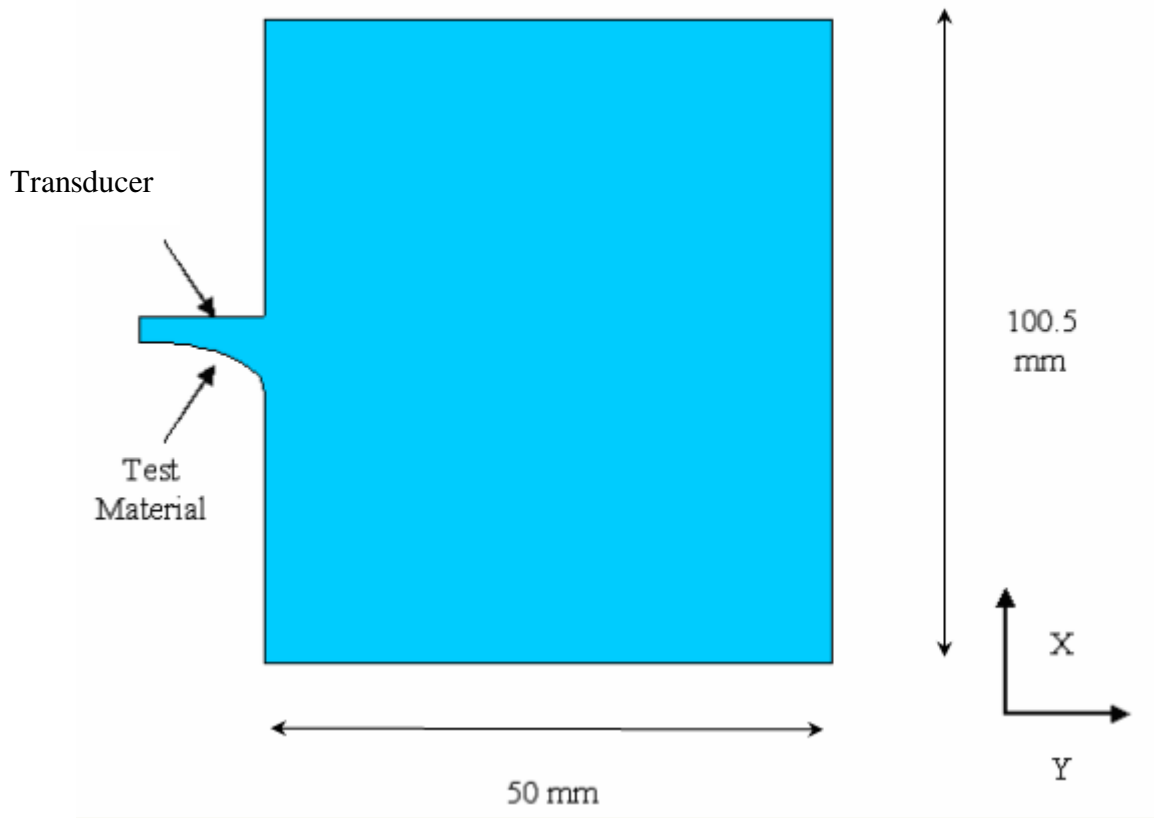
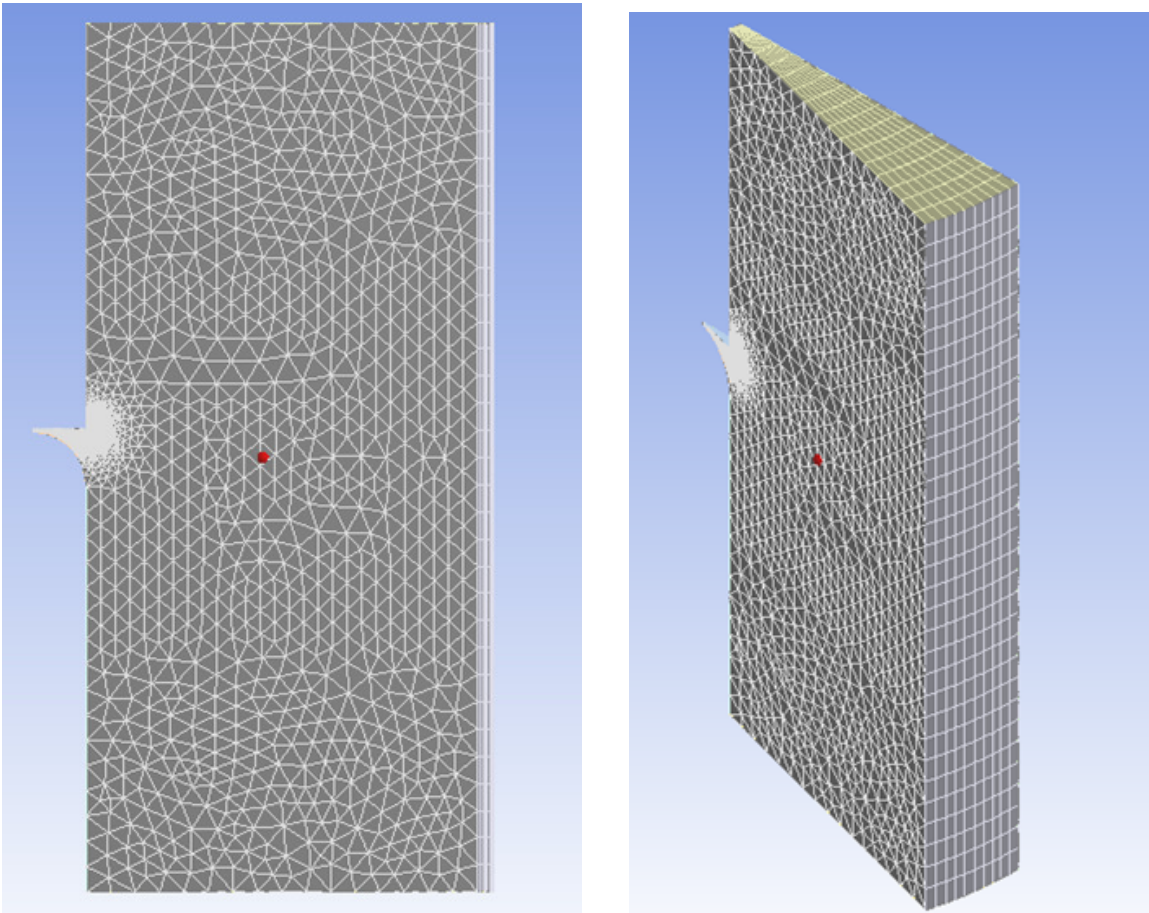


Fig: A.D.3 schematic of the CFD model.

An extruded 2D mesh was used as meshing strategy; this creates mesh which is more aligned with the flow. This method requires specifying the periodic pairs in the model to define the grid transformation. Symmetry faces in the system were specified as periodic pairs with rotation as the type and the resulting mesh is shown in Figure A.D.4. The surface mesh is made of quadrilaterals, but the volume mesh is a mixture of hexahedra and triangular prisms. Mesh refinement had to be performed at the region of interest to allow several element formations. This was achieved by using “point spacing” and “line control” options to specify the required number of divisions for the region. The element

length size and the volume adjustment near the faces were achieved using the “face spacing” option to specify the required maximum and minimum edge lengths. The outcome of this meshing is shown in the below Figure A.D.4. The top image in the Figure shows the complete model and the bottom images show the mesh refinement at the region of interest. Several iterations of simulation were carried out to find the right level of mesh density required at this region. This was done by increasing the elements in the region until no difference in the results was noted. The below structure consists of about 170,000 elements, which for 150 solver iterations, with 40 steps for a single vibration cycle took approximately 1 day of computational time on a normal desktop computer.



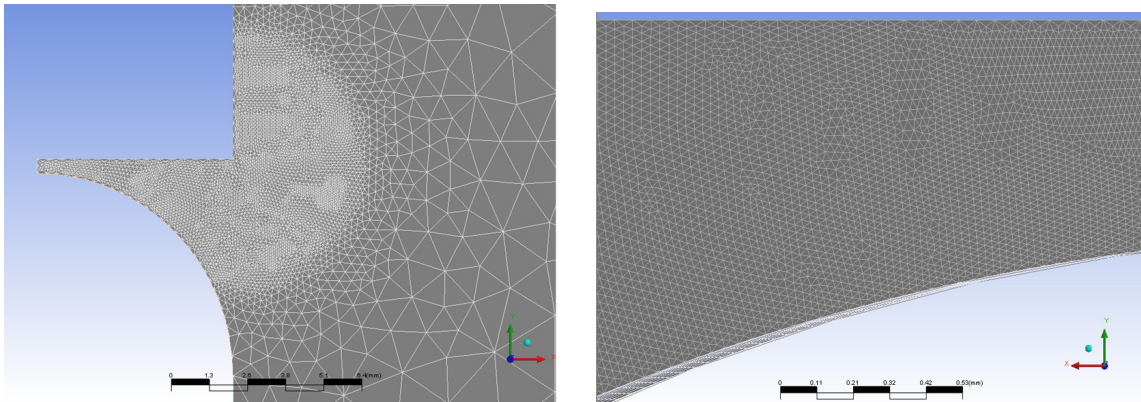


Fig: A.D.4 Meshed structure with refinement at the region of interest

A.D.2.2 Fluid Domain Definition

The fluid domain is a mixture of two fluids namely, water and vapour. So the materials used for the domain were liquid water at 25 °C and water vapour at 25 °C. As homogenous multiphase model was used, both these fluids share same fluid flow conditions such as same velocity and turbulence. Thermal effects of the model should be included in the domain description. For cavitation modelling this is often assumed as isothermal because of the characteristic time required for the bubble nuclei to evolve. This bubble evolution time is much larger than the time required for heat transfer and hence temperature equilibrium is continuously achieved (Franc 2008, Brennan 1995, Leighton 1994). But for larger bubbles the heat transfer behaviour tends to be adiabatic (Franc 2004). This model was assumed to be isothermal with the temperature of 25 °C as it is reasonable for water cavitation due to the less thermal-sensitive fluid properties (Utturkar 2008).

In order to include cavitation in the model, the mass transfer between the fluids pairs was specified as due to cavitation. The program in-built cavitation model, Rayleigh-Plesset was used for this simulation and is proven to be a simple and powerful tool to understand various aspects of cavitation (Agostino 2008). The mean nucleation site diameter and saturation pressure must be specified and a reasonable default value of 2e-06 m was used. Turbulence must be included in model, as applying acoustic cavitation leads to turbulent

motion of the liquid (Ashokkumar 2007, Leighton 1994, Bertodano 1994). The k-epsilon turbulence model was used for turbulence modelling as it is shown to be stable, numerically robust and produces accurate results (CFX 2007). The initial domain was set with a volume fraction of continuous fluid liquid water as 100 % as is the case in real conditions.

A.D.2.3 Boundary Conditions

As only a section of the vibratory cavitation test setup was modelled, which includes the transducer horn, the test specimen and the interface and surrounding fluid region. Boundary conditions must be properly defined to specify that the model is a part of the real fluid domain. Any under defined boundary condition will lead to an insufficient data input for CFD solver and any over defined boundary condition will form an unrealistic physical model causing solution convergence problems. This cavitation model consists of two major parts: solid and fluid. The solid part, being boundary regions constitute the transducer and silicon nitride, the fluid part constitutes the opening and symmetry regions.

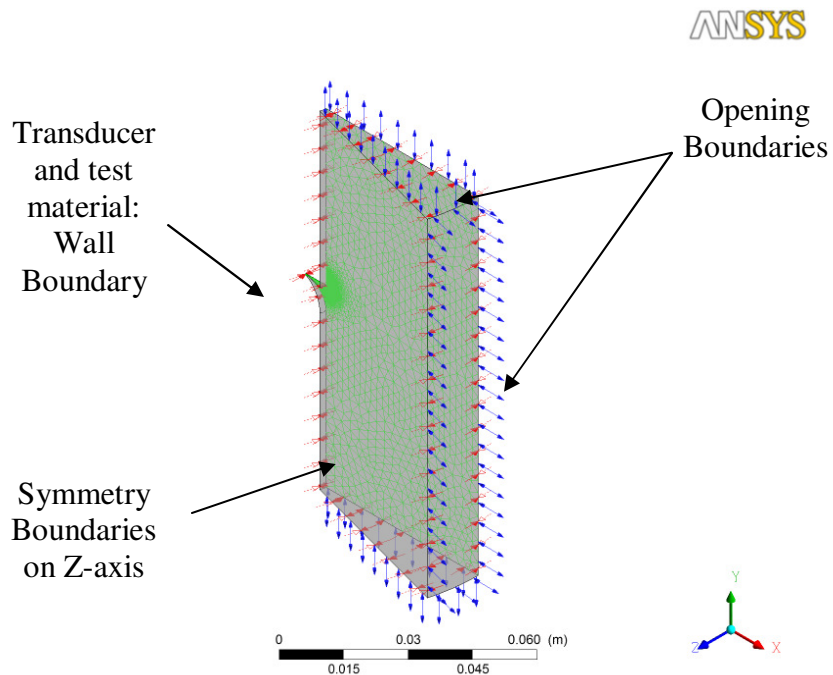


Fig: A.D.5 Boundary conditions for the CFD model

The transducer was set as wall boundary condition which is defined as fluid-solid interface, where the transducer horn interfaces with the fluid domain. The wall influence on the flow was defined as relative to the motion of the transducer. Silicon nitride or test specimen in this case, which is the bottom face, was modelled as fixed wall boundary. The flow at this boundary was specified as free slip, which means the shear stresses at this wall is zero and the velocity of the fluid is not retarded by any wall friction effects. These wall boundaries act as impenetrable boundaries for the fluid flow. The open surfaces in the model were specified as an “opening boundary”, which allows the fluid to leave or enter the domain as per the flow conditions. No data on pressure at these openings is available and hence these boundaries were moved far away from the cavitating regions by 50 mm and the reference pressure was assumed to be 0. The symmetry faces in the Z-axis were specified as planar boundary surface, due to the reason that all aspects of the flow are symmetric to the plane as shown in Figure A.D.5. Also the mesh motion for the opening and symmetry boundaries were set as “unspecified”. Volume fractions at all these boundaries were specified as 100% for water and 0 for water vapour, however the solver consider this water vapour value as a minimum level of 10^{-13} .

A.D.2.4 Transducer Motion

In order to incorporate the vibration of piezoelectric transducer in the CFD model, it is necessary to clearly define the motion of the transducer; this can be done by using mesh deformation method. This is achieved by modelling the transducer as a moving wall with the displacement specified using an expression as required. The transducer vibrates at amplitude of 16 and 60 microns peak-to-peak with a frequency of 20 kHz. As shown in the Figure A.D.6, the vibration of the transducer was set as a function of time (t) in y direction. The co-ordinate system shows the initial position of the transducer is 0. The motion of the transducer is sinusoidal with a rarefaction and compression cycle. During the rarefaction cycle the transducer moves positive in Y-direction to a maximum distance of 16 or 60 microns causing mechanical tension in the fluid and returns back to its initial position in the subsequent cycle exerting pressure on the test specimen.

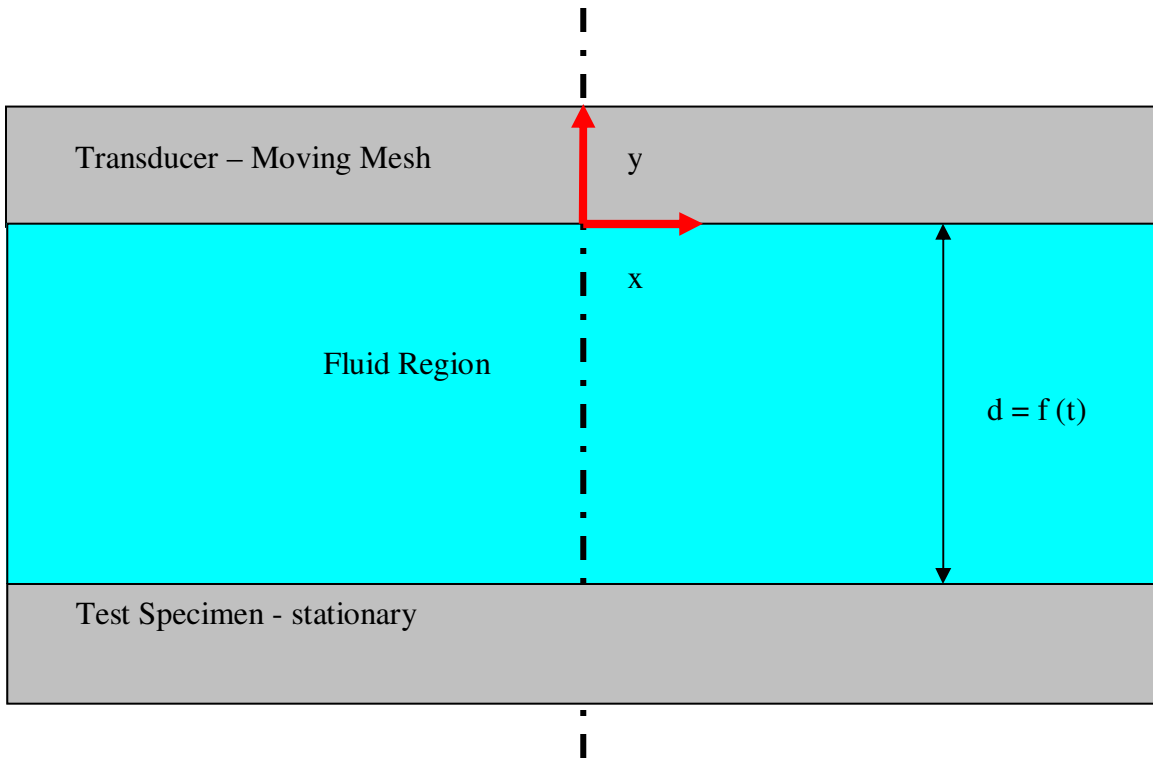


Fig: A.D.6 Schematic of transducer motion as a function of time

The parameters which govern the motion of the transducer are given in the Table A.D.1. One vibration cycle of the transducer motion was simulated. The time period of 50 micro seconds was calculated from the frequency and was used as the total simulation time with 40 time steps. Cosine function used to define the motion of the transducer begins at the negative amplitude of $-8.0 \mu\text{m}$ and required an offset to specify that the motion starts at 0 in the coordinate system. This offset value of $8.0 \mu\text{m}$ is hence added in the displacement expression. The motion plot of the transducer is shown in the Figure A.D.7.

Parameter	Value
Initial distance (d_i)	0
Final distance (d_f)	16 μm
Amplitude (a)	$\frac{d_f - d_i}{2}$
Frequency (ν)	20,000 Hz
Angular Frequency (ω)	125663.706 rad/s
Time period (T_p)	0.00005 s
Displacement in Y direction (d_y)	$-a * \cos(\frac{2\pi t}{T_p}) + a$
Total time (T_{tot})	T_p
Time step (T_{step})	$\frac{T_p}{100}$

Table: A.D.1 Transducer motion parameters

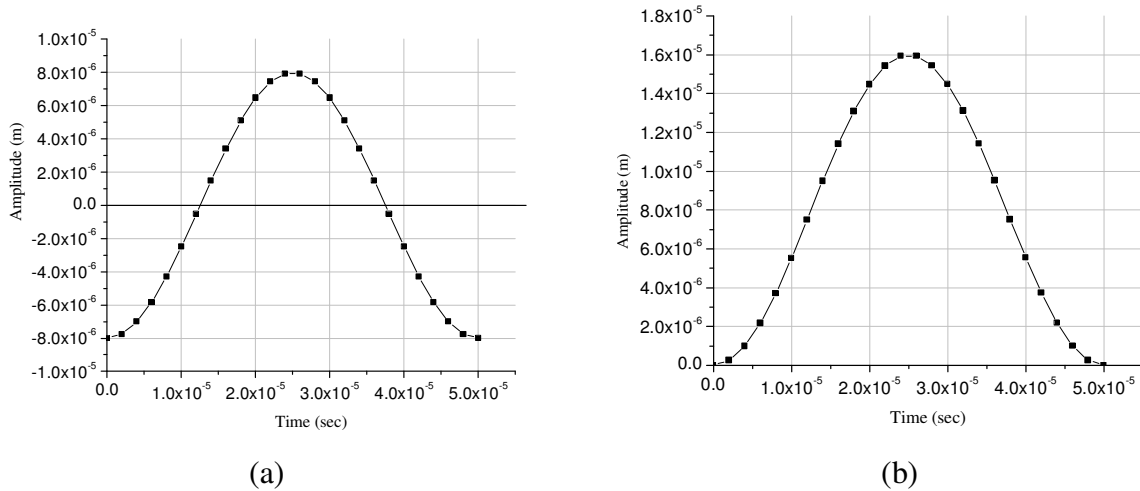


Fig: A.D.7 (a) Actual mesh displacement and (b) with distance offset for simulation.

A.D.2.5 Results and Discussion

A.D.2.5.1 Impact pressure

The following sections details the results obtained from these simulations. Initially simulations were run without implementing the cavitation model which showed huge negative pressures confirming cavitation occurrence. Results shown here are with cavitation model implemented. The pressure contour plot at time step 25 for both low and high powered transducer is shown in Figure A.D.8. Simulation result of low powered transducer showed a maximum pressure of 1.3 MPa and high powered transducer of about 4 MPa. Okada measured the amplitude of impact wave on the target material and reported to be about 1.2 to 1.4 MPa (Okada, 1999). This was measured by the pit number on surface of metal materials induced by cavitation .These values are very close to the results obtained in these simulations. However, they are very low compared to other pressure values of single bubble collapse reported in the literature, which are about hundreds of MPa or even in some GPa range (Pecha 2000, Brujan 2005, Momma 1995, Holzfuss 1998, Brennen 1995, Young 1999, Leighton 1994). It should be noted that pressures arising from single bubble collapse cannot be a substitute for actual flow cavitation.

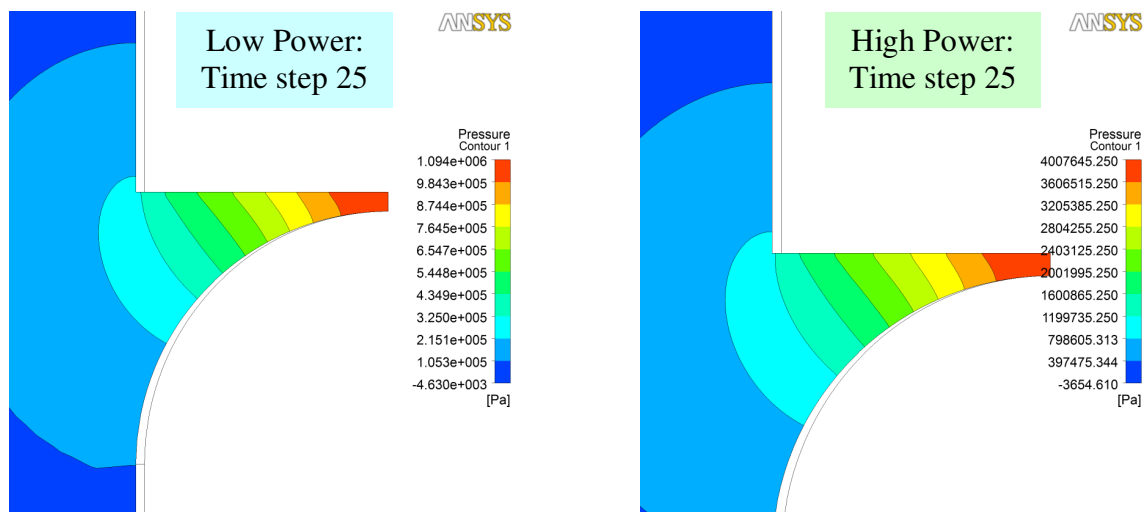


Fig: A.D.8 Pressure contour at time step 25 for low and high powered transducer

The maximum pressure values for both transducers obtained from these simulations are plotted as is shown in Figure A.D.9. The pressure values of these two transducers show that high pressures are generated by the high powered transducer, approximately by a factor of 4 compared to the other. Also, the results show that the pressure on the test material remains at a very low level or close to 0 until the midway of the vibration cycle; this is because the bubble volume increases with drop in pressure. The sudden increase in pressure begins when the transducer reverses its direction during the compression cycle, the time when the bubble volume decreases. At the final stages of the transducer motion, the pressure values on the test material return back to low level or close to 0, implying that the loading of cavity pressures on the test material occurs only between 50 and 75% of the vibration cycle. There are even variations in this time for tow transducers and can be seen in the result at times $2e-5$ and $4.5e-5$.

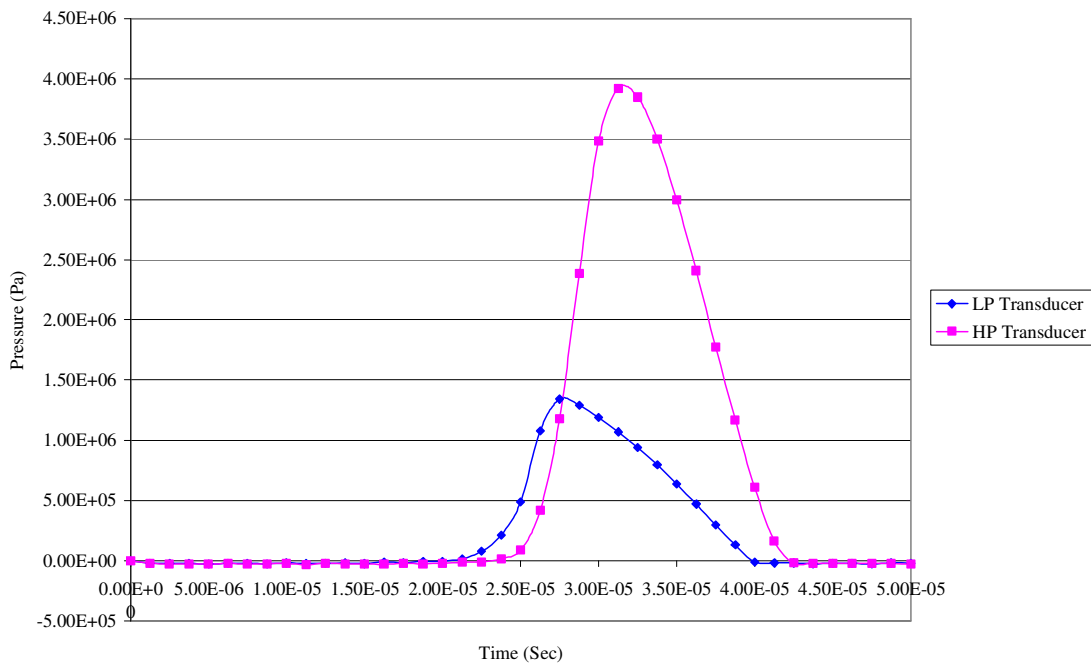


Fig: A.D.9 Pressure plot comparison for low and high powered transducer

A.D.2.5.2 Fluid Velocity

The fluid velocity generated by the transducer motion at time steps 10 and 40 is shown in Figure A.D.10. During the rarefaction cycle, the fluid is driven inside the cavitation region as seen in time step 10 and at the compression time steps it is forced to leave the cavitation zone. High velocities are generated by the high powered transducer which vibrates at 60 μm peak-to-peak at the same frequency of 20 KHz as the low powered transducer

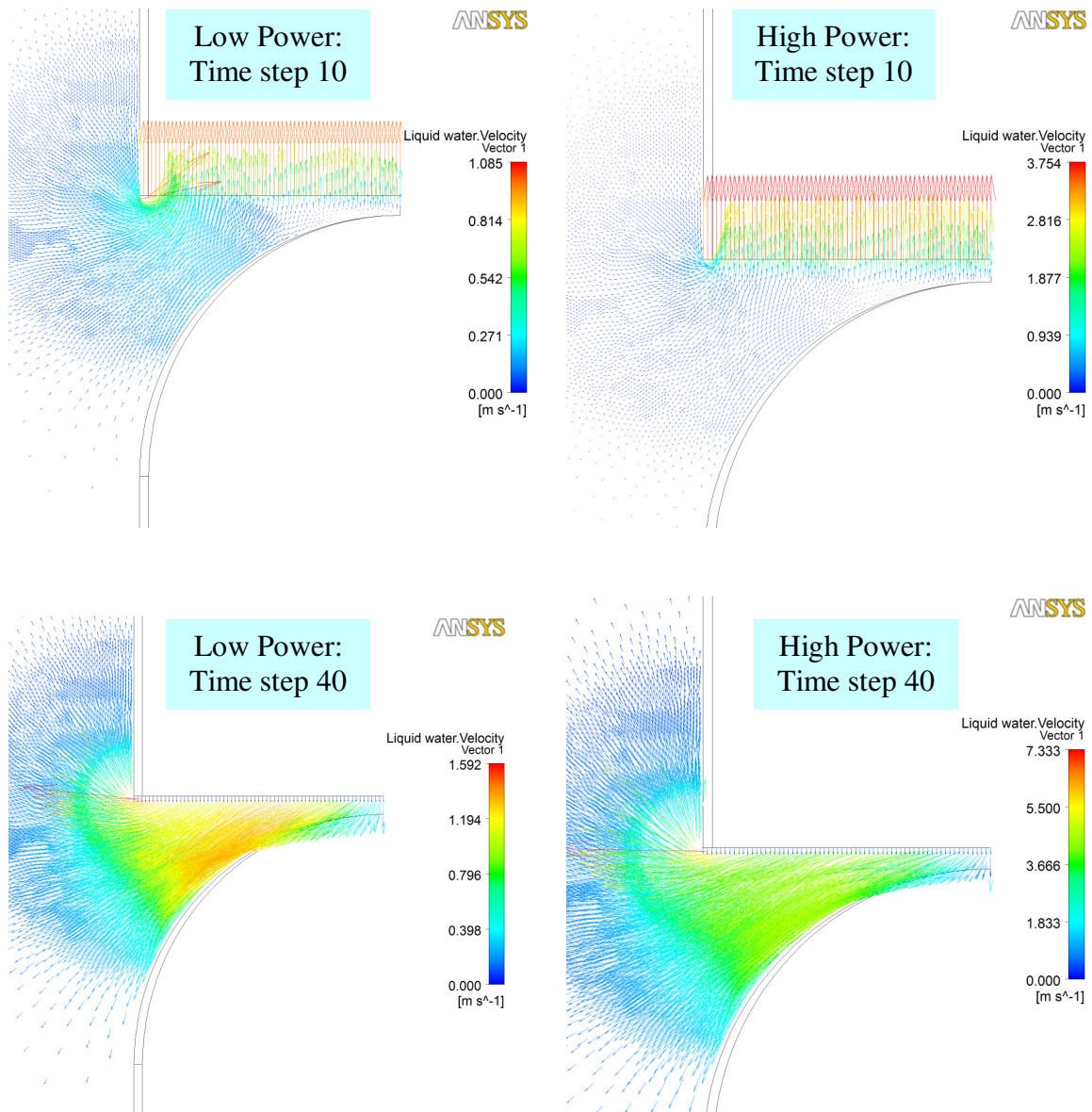


Fig: A.D.10 Vector plots of velocity at varying time steps

Velocity plot at the cavitation region is shown in Figure A.D.11. The velocity increases steadily until the first 10 time steps which is the quarter of the vibration cycle. During the first half cycle the fluid moves inside the cavitation region, but the velocity increases steadily only until the quarter of the cycle and gradually reduces in the next quarter cycle. This reaches a minimum level when the transducer moves to the maximum displacement of 16 or 60 μm . During the compression cycle, the velocity peaks to the maximum in the 3rd quarter of the total vibration cycle. This could be due to the fact that fluid is forced to move out of the cavitation region by the downward motion of the transducer. Also, the velocity retards during the final quarter but remain at high velocity. The maximum velocities of 2.7 m/s and 10.2 m/s are obtained for the low and high powered transducers, which imply that high powered transducer generates fluid velocity of nearly 4 times compared to the other.

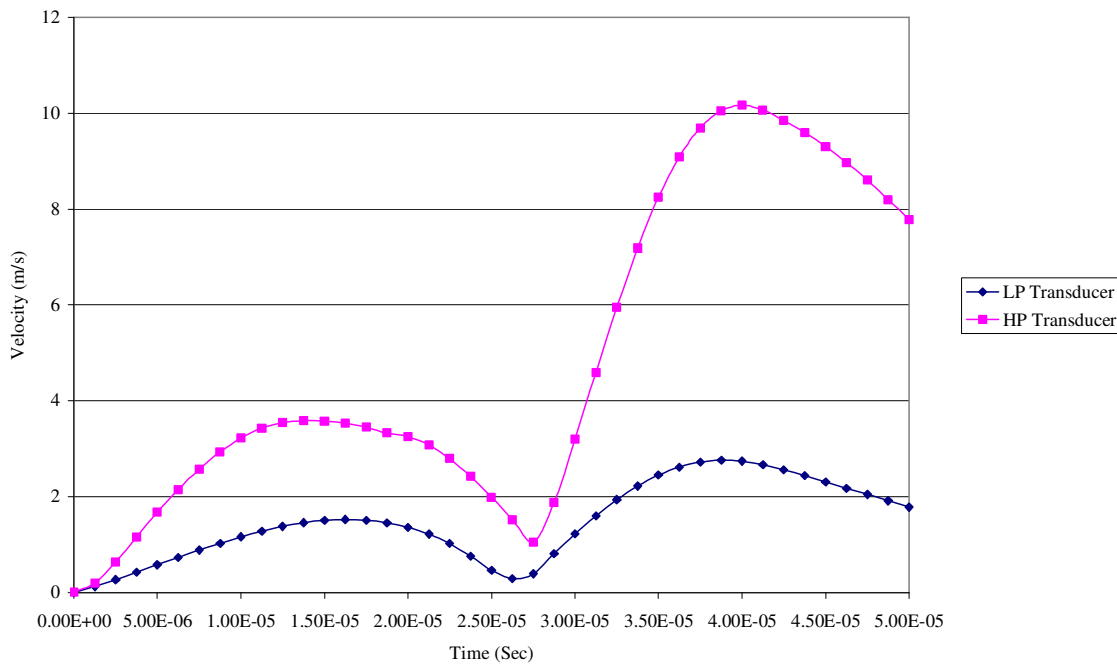


Fig: A.D.11 Velocity plot comparison of low and high powered transducer

A.D.2.5.3 Volume Fraction

The main purpose of any cavitation modelling is to determine the volume fraction of fluids as a function of time. The change in density of the fluid during the vibration cycle is modelled by volume fraction of liquid water and water vapour. This would help understand the occurrence of cavitation in a system. The CFD solver determines this fraction value by solving its transport equations with appropriate source to regulate mass transfer between liquid water and water vapour. Also the shape of the cavity is indicated by the phase volume fractions as shown in the Figure A.D.12 below.

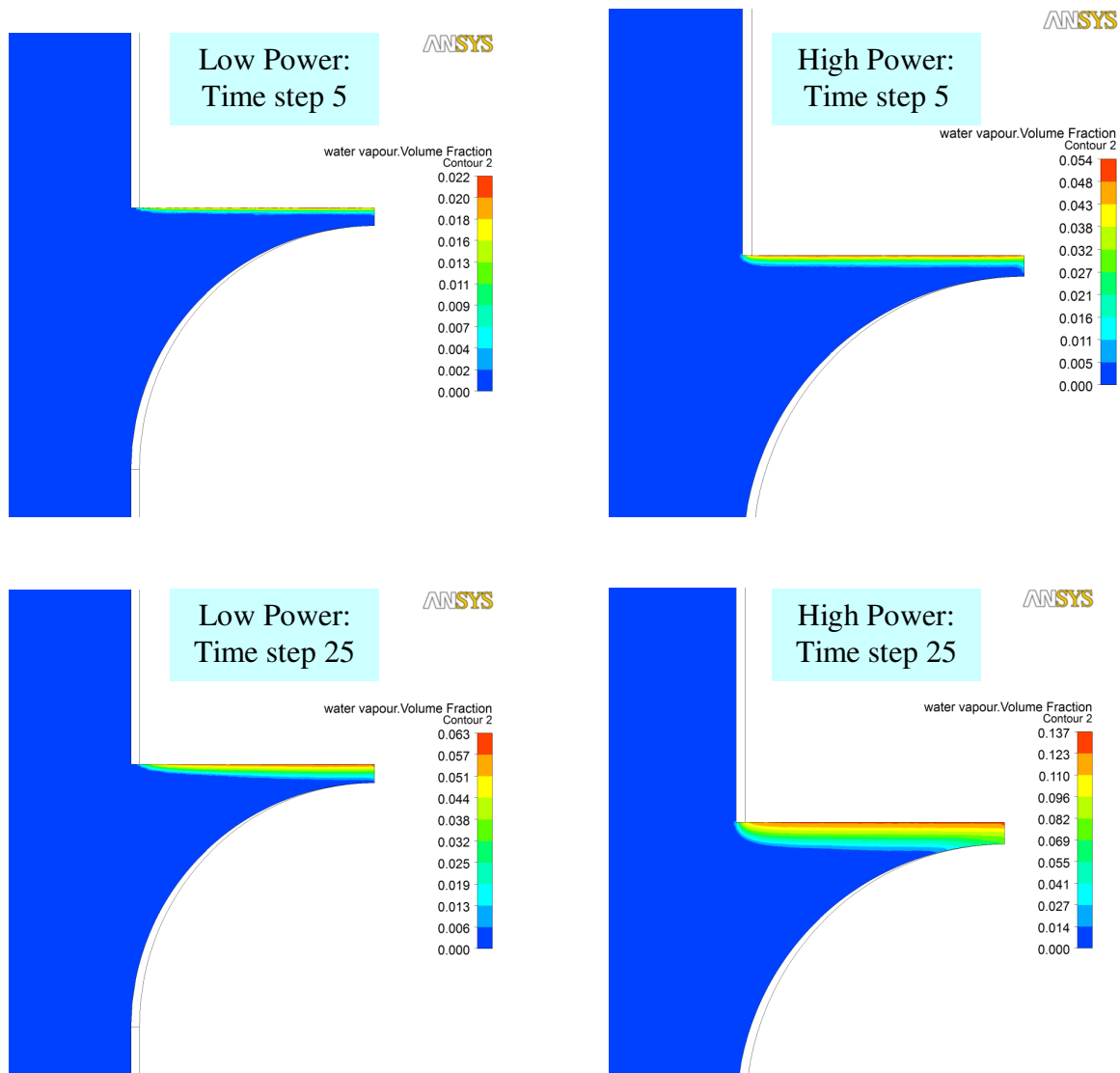


Fig: A.D.12. Water vapour volume fraction contour at different time steps.

The water vapour volume fractions of both transducers are plotted below in the Figure A.D.13. This was done by the same method as followed for pressure and velocity, and plotted against time by creating a graph. The fraction values for water vapour increases steadily from 0 and reaches the maximum at the end of the half vibration cycle i.e when the transducer reaches the maximum displacement. The refraction cycle causes huge tension in the liquid which results in bubble formation merely by cavity expansion. This expansion of cavities is slightly larger than the compression of cavities due to the fact that surface area on expansion is larger than the surface area on compression. During the second half cycle vibration, the volume fraction reduces gradually and reaches the maximum at the end. This may be due to the decrease in surface area during high compression, which was noted in pressure changes that the maximum pressures arise in the 3rd quarter of the vibration cycle. As the compression level decreases at the final stages, the volume fraction returns to the maximum. Also shown in this Figure that nearly 4 times higher values for high powered transducer is seen compared to the other, which is same as what was observed for pressure and velocities.

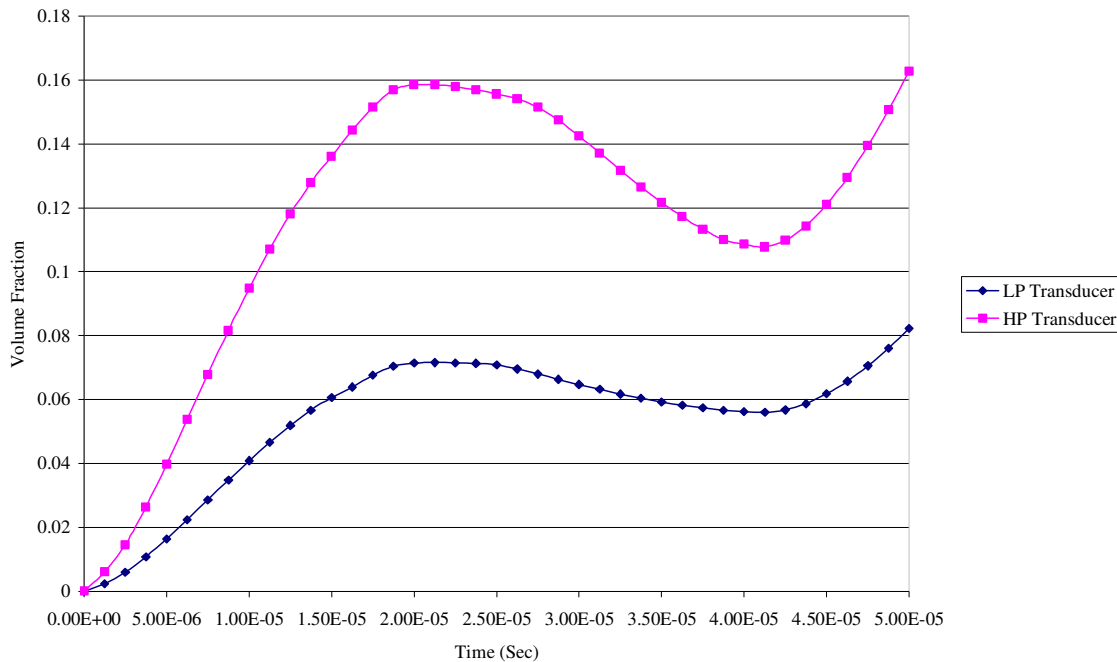


Fig: A.D.13 Volume fraction plot of low and high powered transducer.

A.D.2.5.4 Bubble collapse impact loads:

The liquid/ water vapour force exerted on the test material over one vibration cycle is shown in Figure A.D.14. This was calculated by selecting the force in y-direction acting on the test material location. In order to plot the force against time steps, an expression must be created. This was done by creating a new variable called F_v denoting force in vertical direction. The force value in Y-direction calculated by the solver was selected at the preferred location; here in this case, is the test material. These values were plotted against time for both low and high powered transducer. Exporting these two plots to a spreadsheet and were combined as shown in the Figure A.D.13

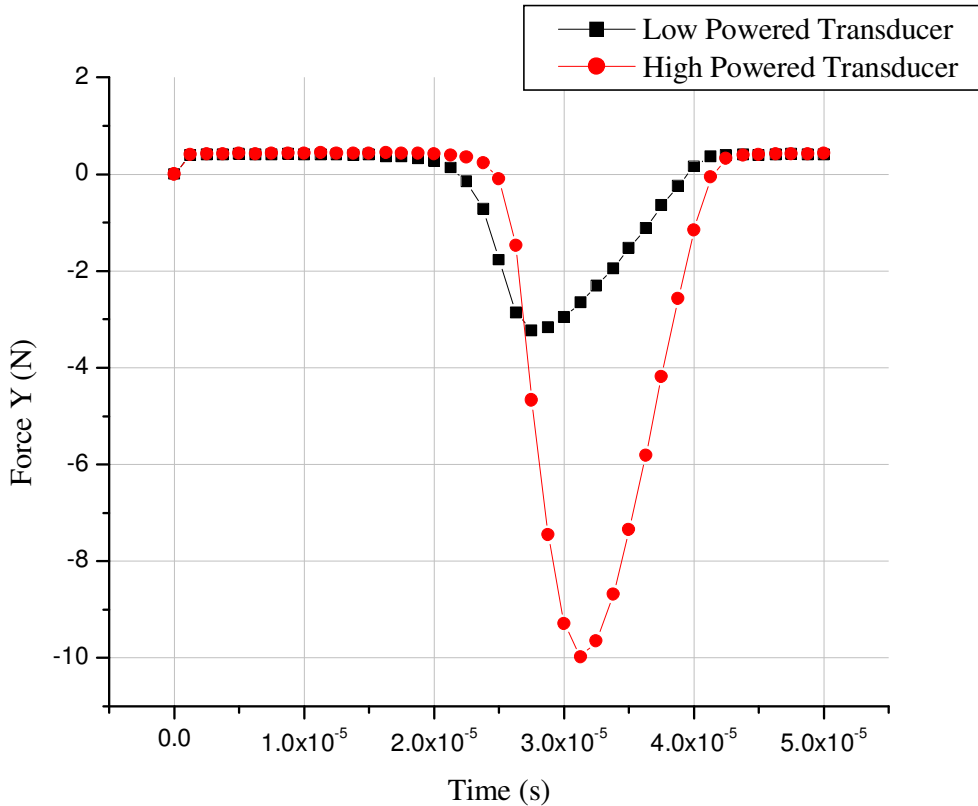


Fig: A.D.14 Bubble collapse impact loads on test material

The maximum force exerted by the fluid for low powered transducer is 3.5 N and high powered transducer is about 10 N. The variation between the two transducers is approximately 3 times. Okada reported on the measurement of impact loads due to bubble collapse (Okada 1995). They used a magnesium oxide single crystal mounted on a piezoelectric pressure detector and a relation between the impact load F (Newton) and the output voltage V (volts) was obtained. With varying force values for different cavity impacts, they produced a distribution of force with a range of 0 to 9.5 Newton. These values are very identical to what is reported here as the outcome of simulation results.

A.D.3 Fluid-Structural Interaction

To perform a structural analysis on the test specimen, the pressure loads must be imported from the fluid simulation results. This is a one-way fluid structural simulation, where the resulting pressure values obtained from the fluid analysis are transferred to a new structural analysis. This structural analysis is a transient one which simulates the structural response for each time step of a full vibration cycle of the transducer. The geometry remains the same as used for fluid cavitation simulation, but only the solid part is taken into account. This was achieved by suppressing the fluid regions and other wall boundaries in the model and only generating mesh on the test material. Structural or mechanical mesh was generated on the model using the same program. Body constraints need to be specified and was appropriately applied by fixing the bottom of the test material as in the experiments. The regions on the z-axis were modelled as symmetry boundaries.

There is no established routine to directly import the pressure results for transient analysis from CFD for all load steps. This required writing a program code called as “Macro” to transfer all the pressure values corresponding to each load steps. The flow structure is shown in Figure A.D.15. This was done in 3 steps by inserting the relevant commands. First the structural mesh was generated, followed by exporting the mesh to the working directory in .cdb format. This second command was issued without a solving

the simulation in order to only export the required mesh. This mesh was imported in the CFD post processing by inserting a program file, which also exports the corresponding pressure loads for each load step. The third command in the mechanical simulation was then unsuppressed to read the imported load file and subsequently to solve the simulation.

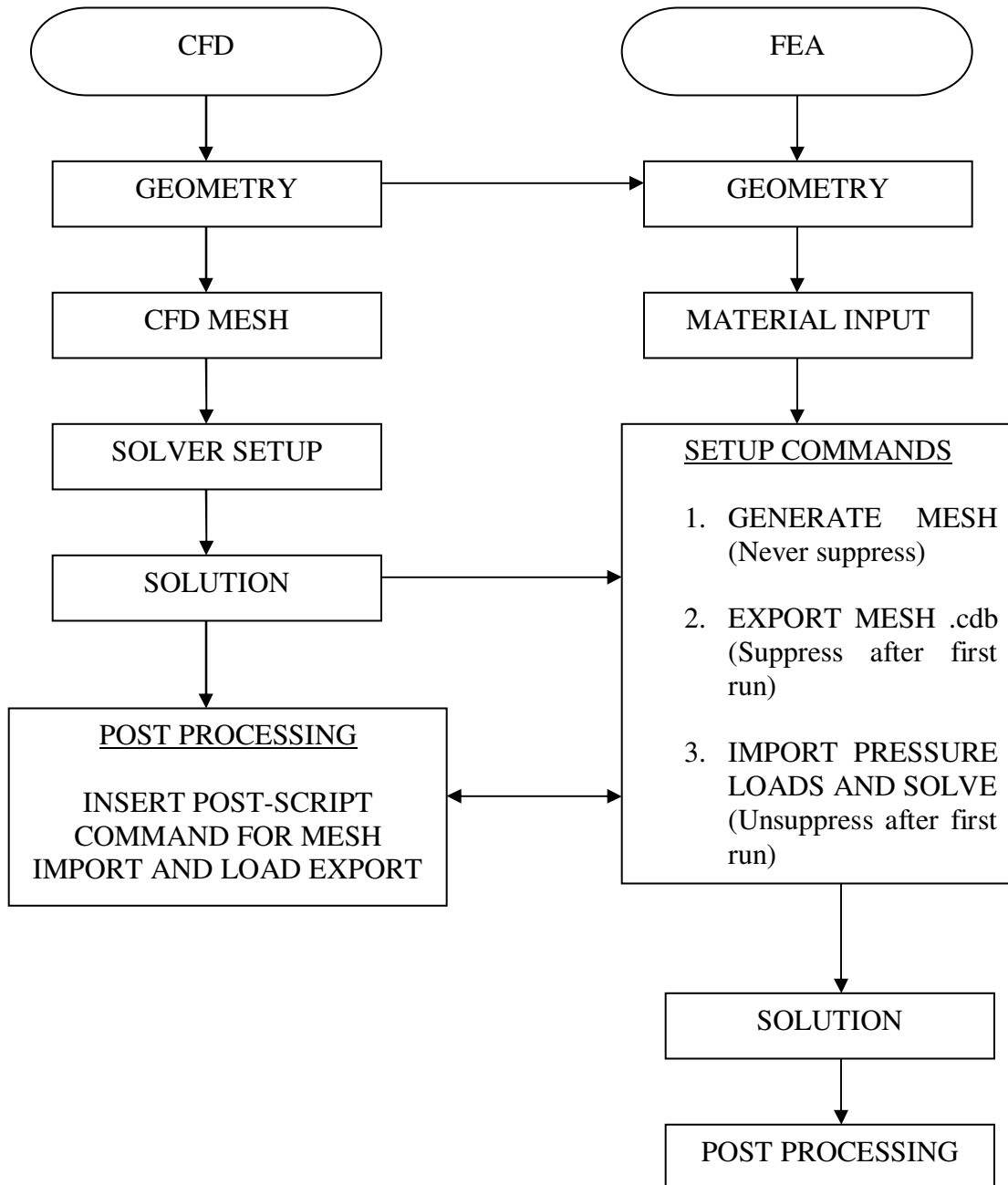


Fig: A.D.15 Flow chart of fluid-structural simulation

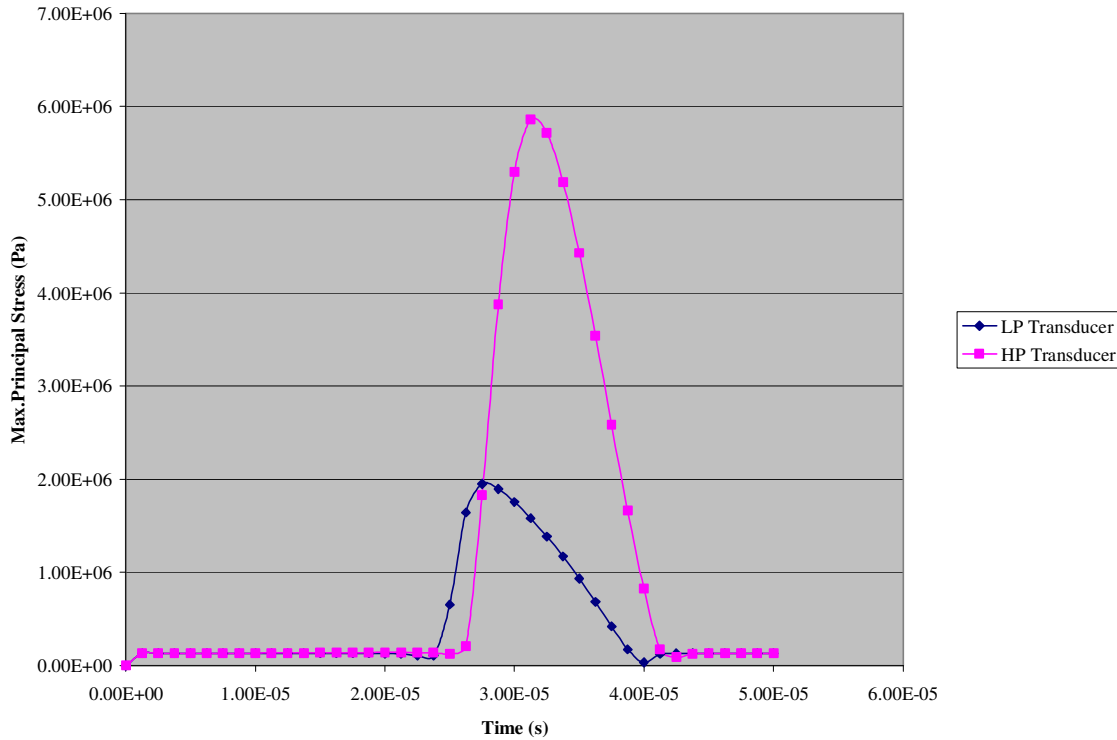


Fig: A.D.16 Stress plot on the test material

The resulting stress curves resemble the pressure values exerted on the test material during the vibration cycle. High powered transducer shows a maximum of 6 MPa and the low powered transducer show a maximum stress value of 2 MPa. This is less by a factor of 3 compared to the other. Also, the stress values remains near zero during most of the vibration cycle as shown in the Figure A.D.16. For the time steps until the midway of the cycle i.e during the rarefaction cycle the stress values calculated stay close to the minimum. These values peak to the maximum just when the compression cycle begins, where the transducer exerts huge pressures on the test material. During the final stages of the cycle, the stress values return the minimum, suggesting that cavitation loads are generated on the test material only during the last quarter of the vibration cycle.

REFERENCES

- Agostino L, Salvetti M V (2008). *Fluid Dynamics of Cavitation and Cavitating Turbopumps*. CISM International Centre for Mechanical Sciences series , ISBN: 978-3-211-76668-2.
- Armstrong, S Elizabeth, Coe H.H (1988). Computer-Aided Design Analysis of 57-mm Angular-Contact. Cryogenic Turbopump Bearings. *NASA Tech Paper 2816*.
- Andreas S L (2000). Cavitation in Liquid film bearings, From lecture notes, Texas A&M University, USA.
- Andrews, P., Illson, T. F. and Matthews, S. J. (1999) Erosion-corrosion studies on 13 Cr steel in gas well environments by liquid jet impingement. *Wear*, 233-235, 568-574.
- ANON, (2005). *CERBEC Product Catalogue*. East Granby, Connecticut USA, *Saint-Gobain ceramics*
- Anon. (2006) Product catalogue. Delray Beach FL 33445 U.S.A., *Boca Bearing Company*.
- Ashokkumar M, Lee J, Kentish S, Grieser F (2007). Bubbles in an acoustic field: An overview. *Ultrasonics Sonochemistry*, vol.14, pp.470-475
- ASTM G32-06 (2006). Standard test method for cavitation erosion using vibratory apparatus. West Conshohocken, PA, ASTM International, www.astm.org.
- Auref, J. G., O.F.R.A. Damm., G.J. Wright and F.P.A. Robinsonbp (1993). The pressure and velocity dependence of flow-type cavitation erosion. *Wear*, 170, 185-190.

- Khanna R., Basu B., (2006) Low friction and severe wear of alumina in cryogenic environment: A first report. *Journal of materials research*, 21.
- Berthe (1975) Cavitation and film rupture in a lubricated contact and its relation to surface degradations, *Cavitation and related phenomena in lubrication, Proceedings of the first Leeds-Lyon symposium*, Dowson et al. (editor), pp. 185–188
- Bertodano M L, Jones O C (1994). Development of a k-Epsilon Model for Bubbly Two-Phase Flow, *Trans. ASME, J. of Fluids Engineering*, Vol. 116, No. 1, pp. 128-134,
- Bingley, M. S. and O'flynn, D. J. (2005) Examination and comparison of various erosive wear models. *Wear*, 258, 511-525.
- Bitter, G. A. (1963) A study of erosion phenomena: Part II. *Wear*, 6, 169-190.
- Bitter, G. A. (1963) A study of erosion phenomena: part I. *Wear*, 6, 5-21.
- Blake, J. R., Giles S. Keen, Robert P. Tong., Miles Wilson (1999) Acoustic cavitation: the fluid dynamics of non-spherical bubbles. *Philosophical Transactions of Royal Society of London (A)*, 357, 252-267.
- Blazek J, (2001) Computational fluid dynamics: Principles and Applications. Elsevier Science publication. ISBN-10: 0080430090
- Boca Bearing Company (2006). *Product catalogue*, Delray Beach, FL 33445 U.S.A.
- Bosson, R., Edeline, E. and Collongeat, L. (1999) High Performance Cryogenic Ball Bearing Demonstration. *Proc. 35nd AIAA/ASME/SAE/ASEE Joint Propulsion Conf. And Exhibit*.
- Bower, F. (1988) The influence of crack face friction and trapped fluid on surface initiated rolling contact fatigue cracks *Journal of Tribology, ASME*, 110, 704–711.

- Bregliozzi, G., A. Di Schino, S.I.-U. Ahmed, J.M. Kenny, H. Haefke (2005) Cavitation wear behaviour of austenitic stainless steels with different grain sizes. *Wear*, 258, 503-510.
- Brennen, C. E. (1995). *Cavitation and Bubble Dynamics*, Oxford University Press
- Brewe David E and Khonsari M. M (1987). Effect of shaft frequency on cavitation in a journal bearing for noncentered circular whirl, Presented at the 1987 Annual Meeting of the American Society of Lubrication Engineers, California, USA, 11-14.
- Brujan, E. A., T. Ikeda and Y. Matsumoto (2004). Dynamics of ultrasound-induced cavitation bubbles in non-Newtonian liquids and near a rigid boundary. *Physics of Fluids*, 16, 2402-2410.
- Brujan E.A, Ikeda T, Matsumoto Y, (2005). Jet formation and shock wave emission during collapse of ultrasound-induced cavitation bubbles and their role in the therapeutic applications of high-intensity focused ultrasound. *Phys. Med. Biol.* Volume 50, pp. 4797-4809
- Bryant M.D, Miller G.R, Keer L.M., Line contact between a rigid indenter and a damaged elastic body, *Quarter. J. Mechanics Appl. Math.* 37 (1984) 468–478.
- Burrill, L. C. (1951). Sir Charles Parsons and Cavitation. *Trans. Inst. of Marine Engineers*, 63, 149 - 167.
- Burse, R. W., Jr., Chin, H. A., Olinger, J. B., Moore, L. C., Thom, R. L., Moore, J. D. and Marty, D. E. (1996). Advanced Hybrid Rolling Element Bearings for the Space Shuttle Main Engine High Pressure Alternate Turbopumps,. *32nd AIAA/ASME/SAE/ASEE Joint Propulsion Conf.*
- CERAM (2005). Silicon Nitride: An Overview. *AZo Journal of Materials Online*.

- CFX (2007). *CFX user manual*. ANSYS Inc, USA.
- Chao, L., Lakshminarayanan R, Iyer N, Lin Gy, Shetty Dk (1998). Transient wear of silicon nitride in lubricated rolling contact. *Wear*, 223, 58-65.
- Chen, Y.M. (2002). Cavitation Erosion. *ASM Handbook, Failure Analysis and Prevention*, 11, 1002-1012.
- Chen Y.M and Mongis J (2005). Cavitation wear in plain bearing: case study, *Mécanique & Industries* 6, 195–201
- Cheng, F. T., Shi. P, Man. H C, (2003). Cavitation erosion resistance of heat-treated NiTi. *Material Science and Engineering A*, 339, 312-317.
- Coe, H. H and Zaretsky E.V (1978). Predicted and Experimental Performance of Jet-Lubricated 120-Millimeter Bore Ball Bearings Operating to 2.5 Million DN. *NASA TP-1196*.
- Crum, L. (1995). Bubbles hotter than the sun. *New Scientist*, 146, 36-41.
- Crum, L and Mao Y (1996). Acoustically enhanced bubble growth at low frequencies and its implications for human diver and marine mammal safety. *Journal of Acoustic society of America*, 99, 2898-2907
- Dalal, H. M., Chiu Y P, Rabinowicz E (1975). Evaluation of hot pressed silicon nitride as a rolling bearing material. *ASLE Transactions*, 18, 211-221.
- Dee, C. W. (1970). Silicon Nitride —Tribological Applications of a Ceramic Material. *Tribology* 3, 89-92.
- DIEHL BGT Defence (2006). A German supercavitating Torpedo, *company news letter*.

- Dietrich, M. W., Townsend, D.P And Zaretsky (1969). Rolling-Element Lubrication with Fluorinated Polyether at Cryogenic Temperatures (160° to 410° R). *NASA TN D-5566*.
- Dietrich, M. W., Townsend, D.P And Zaretsky (1970). Rolling-Element Fatigue and Lubrication with Fluorinated Polyether at Cryogenic Temperatures. *ASME Paper-70, Lub-17*.
- Dietrich, M. W and Zaretsky (1975). Effect of viscosity on Rolling Element Fatigue Life at Cryogenic Temperatures with Fluorinated Ether Lubricants. *NASA TN D-7953*.
- Dieval, L., Marcer, R., and Arnaud, M. (1998). Modélisation de poches de cavitation par une méthode de suivi d'interfaces de type VOF (In French). *Proceedings of the 3rd International Symposium on Cavitation*. Grenoble, France
- Dowson, D., and Taylor, C.M. (1974) Fundamental Aspects of Cavitation in Bearings: Cavitation and Related Phenomena in Lubrication. *ImechE. England*.
- Dowson, D. Taylor C. M. (1979). Cavitation in Bearings. *Annual Review of Fluid Mechanics*, 11.
- Dupont P, Okamura T, (2003). Cavitating flow calculations in industry, *International Journal of Rotating Machinery*, 9(3): 163–170.
- Effner, U., Woydt M (1998). Importance of machining on tribology of lubricated slip-rolling contacts of Si₃N₄, SiC, Si₃N₄-TiN and ZrO₂. *Wear*, 216, 123-130.
- Elrod, H.G., Adams, M.L. (1974), A Computer Program for Cavitation and Starvation Problems, *Cavitation and Related Phenomena in Lubrication*, Mechanical Engineering Publications, New York, pp.37–41.
- Elrod, H.G. (1981). A Cavitation Algorithm, *ASME Journal of Lubrication Technology*, Vol. 103 pp.350–4.

- Feller, H. G., Kharrazi, A.G (1984). Cavitation erosion of metal and alloys. *wear*, 93, 249-260.
- Feng N S and Hahn E J (1989). Inlet pressure and cavitation boundary effects on the orbit jump phenomenon in squeeze film damper operation, *Proc. I.Mech.E., Part C, J. of Mechanical Engineering Science*, Vol 203, pp 209-217.
- Fernandes, P. J. L. (1997). Contact Fatigue in Rolling-Element Bearings. *Engineering Failure Analysis*, 4, 155-160.
- Finnie, I. (1960) Erosion of surfaces by solid particles: Oberflächenerosion durch feste teilchen. *Wear*, 3, 87-103.
- Fischbach L Daniel, Tetreault R, Harvey C Andrew, Leary W, Longo N, and Walker David H. (2007). Rolling-Piston Compressor with Flow-Through Lubrication. *Work done for Johnson Space Centre*.
- Flannigan J David and Suslick S Kenneth (2005). Plasma Line Emission during Single-Bubble Cavitation, *Phys. Rev. Lett.* 95, issue 4.
- Flint B. Edward and Kenneth S. Suslick (1991). The Temperature of Cavitation, *Science*, 253, 1397-1399.
- Floberg L (1961). Boundary Conditions of Cavitation Regions in Journal Bearings *Tribology Transactions*, 1547-397X, Volume 4, Issue 2, Pages 282 – 286.
- Franc J.-P. and Michel J.-M. (2004) Fundamentals of Cavitation (Fluid mechanics and its applications). Springer, ISBN-10: 1402022328.
- Franc J P, (2008). The Rayleigh-Plesset equation: a simple and powerful tool to understand various aspects of cavitation, Published in *Fluid Dynamics of Cavitation and Cavitating Turbopumps*. CISM International Centre for Mechanical Sciences series , Editors:

d'Agostino, Luca; Salvetti, Maria Vittoria ISBN: 978-3-211-76668-2

- Fu, W. T., Yang, Y.B, Jing, T.F, Zhang, Y.Z, Yao, M (1998) The resistance to cavitation erosion of CrMnN stainless steels. *Journal of Materials Engineering and Performance*, 7, 801-804.
- Galbato, A., Cundil Rt, Harris Ta (1992). Fatigue life of silicon nitride. *Journal of lubrication engineering*, 48, 886-894.
- Gandhi, B. K., Singh, S. N. & Seshadri, V. (1999). Study of the parametric dependence of erosion wear for the parallel flow of solid-liquid mixtures. *Tribology International*, 32, 275-282.
- Garner D.R, James R.D, Warriner J.F (1980). Cavitation erosion damage in engine bearing: Theory and Practice, *Journal of Engineering for Power*, 102, 847-857.
- Gibson, H., Chip Moore, Robert Thorn (2000). Marshall Space Flight Center High Speed Turbopump Bearing Test Rig. 34th *Aerospace Mechanisms Symposium*. Goddard Space Flight Center, USA.
- Grinchenko, V. 1998 High-speed body motion and sound generation. *AGARD Report 827*, 34-1–34-5.
- Gong, C. (1999) *Ultrasound Induced Cavitation and Sonochemical Effects*. PhD thesis, Department of Mechanical Engineering. Massachusetts Insitute of Technology, USA.
- Hamrock, B.J., 1994, *Fundamentals of Fluid Film Lubrication*, CRC Press, 2nd Edition. ISBN-10: 0824753712
- Hadfield, M. (1992) Rolling Contact Fatigue of Ceramics. *PhD Thesis, Brunel University*.

- Heshmat H, Experimental studies in cavitation, *Current Research in Cavitation Fluid Films. STLE Special Publications* (1988), pp. 4–8 SP-28.
- Hirschi, R., Dupont, P., Avellan, F., Favre, J.-N., Guelich, J.-F., Handloser, W., and Parkinson, E. (1998). Centrifugal pump performance drop due to leading-edge cavitation: numerical predictions compared with model tests. *Journal of Fluids Engineering* 120, pp. 705– 711.
- Hoffmann, M. J. (1995) Relationship between microstructure and mechanical properties of silicon nitride ceramics. *Pure and Applied Chemistry*, 67, 939-946.
- Holfuss J, Rüggeberg M, and Billo A (1998). Shock Wave Emissions of a Sonoluminescing Bubble, *Physics review letters*, Vol.81, No:24, pp. 5434-5437.
- Hussainova, I., Kubarsepp, J. & Shcheglov, I. (1999). Investigation of impact of solid particles against hard metal and cermet targets. *Tribology International*, 32, 337-344.
- Hyeon-Ju Choi, D.-H. H., Dong-Soo Park, Hai-Doo Kim, Byung-Dong Han, Dae-Soon Lim, Il-Soo Kim (2003). Erosion characteristics of silicon nitride ceramics. *Ceramics International* 29, 713-719.
- Huang J.L, Lee M, Lu H, Lii D (1996). Microstructure, fracture behaviour and mechanical properties of TiN/Si₃N₄ composites. *Materials Chemistry and Physics* 45, 203-210
- Jacobson, B.O., Hamrock, B.J., Vapor Cavitation in Dynamically Loaded Journal Bearings, *Second international conference on Cavitation*, Mechanical Engineering Publications, 1983, pp. 133-140.
- Kaneta, M., Yatsuzuka, H, Murakami, Y (1985). Mechanism of crack growth in lubricated rolling/sliding contact *ASLE Transactions*, 28, 407-414.

- Kang, J., M Hadfield (2003). Comparison of four-ball and five-ball rolling contact fatigue tests on lubricated Si₃N₄/steel contact. *Materials and Design*, 24, 595-604.
- Karimi, A. (1988). Modele mathematique poru la prediction de la vitesse d'erosion Mathematical model predicting cavitation erosion rate. *Houille Blanche*, 571-576.
- Karimi, A. & Schmid, R. K. (1992). Ripple formation in solid-liquid erosion. *Wear*, 156, 33-47.
- Karunamurthy, B., Hadfield, M (2007) Mechano-Erosion: A novel Test Methodology to Accelerate Erosion in Rolling Contact Fatigue Experiments. *The Annals of 'Dunarea de Jos, university of Galati, Fascicle IX Metallurgy and Materials Science. ISSN 1453-083X*.
- Keer, L. M., Bryant, M.D. (1983). A pitting model for rolling contact fatigue *Journal of Lubrication Technology, ASME*, 105, 198-205.
- Khalil, Y. F., Rosner, D.E (1996). Erosion rate prediction and correlation technique for ceramicsurfaces exposed to high speed flows of abrasive suspensions *Wear*, 201, 64-79.
- Khan, Z. A., Hadfield M, Ying Wang (2005). Pressurised Chamber design for conducting Rolling contact Experiments. *Materials and Design*, 26, 680-689.
- Khan, Z. A. (2005). Rolling contact wear of hybrid with refrigerant lubricant. *PhD Thesis, Bournemouth University, UK*.
- Khan, Z. A., Hadfield M, Shogo Tobe, Ying Wang (2006). Residual stress variations during rolling contact fatigue of refrigerant lubricated silicon nitride bearing elements *Ceramics International*, 32, 751-754.
- Kirschner I. N., N. E. Fine, J. S. Uhlman, D. C. Kring, B. J. Rosenthal, T. A. Gieseke, R. Kuklinski, A. N. Varghese, D. R. Stinebring, J. E. Dzielski, J. W. Lindau, and R. F.

- Kunz, (2001). "Supercavitation research and development," in *Anteon Corporation - Engineering Technology Center, Naval Undersea Warfare Center Division, Applied Research Laboratory/Penn State University, Waikiki, HI.*
- Lathabai, S. (2000). The effect of grain size on the slurry erosive wear of Ce-TZP ceramics. *Scripta Materialia*, 43, 465-470.
- Leibensperger R (2003). The conquest of friction. *Mechanical Engineering New York: American Society of Mechanical Engineers*, pp. 46–49.
- Leighton T.G. (1994). *The acoustic bubble. Academic Press, ISBN: 0124419216.*
- Lim.D.-S, Cho H. C., Park D S (2003). Effect of microstructural orientation on erosion behavior of self-reinforced silicon nitride. *Wear*, 255, 110-114.
- Lin, C. J., He, J.L (2005). Cavitation erosion behavior of electroless nickel-plating on AISI 1045 steel. *Wear*, 259, 154-159.
- Lindau, Olgert, Lauterborn and Werner (2001). Investigation of the counter jet developed in a cavitation bubble that collapses near a rigid boundary. *Fourth International Symposium on Cavitation Pasadena, USA*
- Man, H. C., Kwok,C.T, Yue, T.M. (2000) Cavitation erosion and corrosion behaviour of laser surface alloyed MMC of SiC and Si N on Al alloy AA6061. *Surface and coatings technology*, 132, 11-20.
- Manoj, V., .K. Manohar Shenoy, K Gopinath (2007) Developmental studies on rolling contact fatigue test rig. *Wear*, 264, 708-718.
- Masataka Nosaka, S. T., Masataka Kikuchi, Takayuki Sudo And Makoto Yoshida (2004) Ultra-High-Speed Performance of Ball Bearings and Annular Seals in Liquid Hydrogen at Up

- to 3 Million DN (120,000 rpm). *Tribology Transactions*, 47, 43-53.
- Mikalonis, D. (2003) New hybrid bearings enable maximum pump performance with minimum lubrication. *World Pumps*, 37-39.
- Mitchell, D. J., John J. Mecholsky Jr, James H. Adair (2000). All-steel and Si N -steel hybrid rolling contact fatigue under contaminated conditions. *Wear*, 239.
- Miyoshi K, Sutter K J, Mondry R J, Bowman (2003). Measurements of erosion wear volume loss on bare and coated polymer matrix composites, *NASA/TM – 212628*.
- Momma T, Lichtarowicz A. (1995). A study of pressures and erosion produced by collapsing cavitation, *Wear*, 186-187, pp. 425-436.
- MORGEN (2005). Silicon Nitride. *Product catalogue, Morgen Technical Ceramics*.
- Morton H.T (1965). Anti-friction bearings, Ann Arbor, MI.
- Niebhur David (2007). Cavitation erosion behaviour of ceramics in aqueous solution. *Wear*. Volume 263, Issues 1-6, , Pages 295-300
- Nixon, H. P., H. Zantopulos, (1995) Fatigue life comparisons of tapered roller bearings with debris-damaged raceways. *STLE Lubrication Engineering*, 51, 732-736.
- Nosaka, M., Kikuchi, M., Oike, M. and Kawai, N (1999). Tribo-Characteristics of Cryogenic Hybrid Ceramic Ball Bearings for Rocket Turbopumps: Bearing Wear and Transfer Film. *Tribology Transactions*, 42, 106-115.
- Nosaka, M., Takada S, Kikuchi, M., Sudo T and Yoshida M (2004) Ultra-High-Speed Performance of Ball Bearings and Annular Seals in Liquid Hydrogen at Up to 3 Million DN (120,000 rpm). *Tribology Transactions*, 47, 43-53.

- Osborne, R. (1886). On the flow of gases, *Philosophical Magazine*.
- Okada T, Hattori S, Shimizu M. (1995). A fundamental study of cavitation erosion using a magnesium oxide single crystal (intensity and distribution of bubble collapse impact loads), *Wear*, 186-187, pp. 437-443.
- Okada Y and S. Hattori, Erosion induced by cavitation. In: H. Kato, Editor, *Basic theory and recent progress on cavitation*, Makisyoten Press, Tokyo (1999), pp. 189–249.
- Parker, R. J., Zaretsky E V (1975). Fatigue life of high speed bearing with silicon nitride balls. *Journal of Lubrication Technology*, 350-357.
- Pasaribu, H. R. (2005) Friction and Wear of Zirconia and Alumina Ceramics Doped with CuO. PhD Thesis, University of Twente, The Netherlands.
- Patella R F, Rebound J-L, Archer A, (2000). Cavitation damage measurement by 3D laser profilometry. *Wear* , 246, 59-67.
- Pecha R, Gompf B (2000). Microimplosions: cavitation collapse and shock wave emission on a nanosecond time scale, *Physics review letters*, volume84, pp. 1328-1330
- Popovici G (2005). Effects of Lubricant Starvation on Performance of Elasto-Hydrodynamically Lubricated Contacts. *PhD Thesis*, University of Twente, The Netherlands.
- Preece, C. M. & Brunton, J. H. (1980). A comparison of liquid impact erosion and cavitation erosion. *Wear*, 60, 269-284.
- Pryakhin, V. V., Panarin, A. I., Polykhin, V. P. & Romanov, L. M. (1986) Mathematical Model of Erosion of Turbine Blades. *Fluid Mechanics, Soviet Research*, 15, 105-109.
- Rapposelli E, Agostino L, 2001. A modified isenthalpic model of cavitation in plane journal

- bearings, *CAV2001: Fourth International Symposium on Cavitation*, June 20-23, 2001, California Institute of Technology, Pasadena, CA USA.
- Rebound J. L., Stutz, B., and Coutier O. (1998). Two-phase flow structure of cavitation: experiment and modelling of unsteady effects. *Proceedings of the 3rd international symposium on cavitation*, Grenoble, France
- Reidal, R. (Ed.) (2000) *Handbook of Ceramic Hard Materials*, John Wiley and Sons Ltd.
- Richerson, D. W. (1997). Evolution of Ceramics for Turbines. *Mechanical Engineering Magazine*.
- Rowe G, D (2000). Faster than a speeding bullet, *NewScientist*, 167, 26-30.
- Savchenko, Y. N. (2001). Supercavitation – Problems and Perspectives. IN BRENNEN, C. E. (Ed.) *Fourth International Symposium on Cavitation* pasadena, california, USA, California Institute of Technology.
- Sayles, R. S., P.B. Macpherson (1982). Rolling Contact Fatigue Testing of Bearing Steels. *ASTM STP 771, American Society for Testing and Materials*.
- Sayles, R. S., E. Ioannides (1988). Debris damage in rolling bearings and its effects on fatigue life. *ASME Journal of Tribology*, 110, 26-31.
- Scibbe, H. W. (1967). Bearings and seals for cryogenic fluids. *SAE Paper 680550*.
- Scibbe, H.W.; Brewe, D.E.; and Coe, H.H.(1968). Lubrication and Wear of Ball Bearings in Cryogenic Hydrogen. *NASA TM X-52476*.
- Scott, D., G. H. Mills (1973). Spherical Particles formed in Rolling Contact Fatigue. *Nature*, 241, 115-116.

- Sentence, B. (2004). *Ceramics: A World Guide to Traditional Techniques*, Thames & Hudson publication.
- Sonic Systems (2005). High intensity Ultrasonic power systems. *Product catalogue*, Ilminster, Somerset. UK.
- Stanisa, B. & Ivusic, V. (1995). Erosion behaviour and mechanisms for steam turbine rotor blades. *Wear*, 186-187, 395-400.
- Steller, J. (1999). International Cavitation erosion test. GDAŃSK, Poland Polish Academy Of Sciences Institute of Fluid-Flow Machinery, Poland.
- Stephanis, C. G., Hatiris, J. G. & Mourmouras, D. E. (1997). The process (mechanism) of erosion of soluble brittle materials caused by cavitation. *Ultrasonic Sonochemistry*, 4, 269-71.
- Stewart, S., Ahmed R (2002) Rolling contact fatigue of surface coatings - a review. *Wear*, 253, 1132-1144.
- Subramonian, B., Basu Bikramjit (2006) Development of a high-speed cryogenic tribometer: Design concept and experimental results. *Materials Science and Engineering A*, 415, 72-79.
- Sundararajan, G. & Shewmon, P. G. (1983) A new model for the erosion of metals at normal incidence. *Wear*, 84, 237-258.
- Suresh, S. (1998) *Fatigue of Materials*, Cambridge University Press, ISBN-10: 0521578477
- Tamura, Y., Sugiyama, K., and Matsumoto, Y. 2001. Physical modeling and solution

- algorithm for cavitating flow simulations, 2001–2652. *15th AIAA Computational Fluid Dynamics Conference*. Anaheim, CA. AIAA.
- Tao, F. F., Appeldoorn, J.K (1971) Cavitation erosion in a thin film as affected by the liquid properties. *Journal of Lubrication Technology, Transactions of the ASME*, 93, 470.
- Thornycroft, J I, Barnaby S W. (1895). Torpedo- boat destroyers, *Minutes of the Proceedings of Inst. Civil Engrs*, 50.
- Tichler, J. W. & Scott, D. (1970) A note on the correlation between cavitation erosion and rolling contact fatigue resistance of ball bearing steels. *Wear*, 16, 229-233.
- Tomlinson, W. J. & Matthews, S. J. (1994) Cavitation erosion of structural ceramics. *Ceramics International*, 20, 201-209.
- Touret, R., Wright Ep (1977) *Rolling contact fatigue: Performance testing of lubricants*, London, Heyden & Son Ltd.
- Trunev, A. P. & Fomin, V. M. (1985) Continuum Model of Impact Erosion. *Journal of Applied Mechanics and Technical Physics (English translation of PMTF, Zhurnal Prikladno*, 26, 860-866.
- TWI, Cambridge, England (2007). Hardness Testing.
- Utturkar Y, Wu J, Wang G, Shyy W (2005). Recent progress in modeling of cryogenic cavitation for liquid rocket propulsion, *Progress in Aerospace Sciences* 41, pp.558-608.
- Vincent B, Maspeyrot P and Frene J (1996). Cavitation in dynamically loaded journal bearings using mobility method, *Wear*, Volume 193, Issue 2, Pages 155-162
- Vyas, B., Inge L.H. Hansson (1990). The cavitation erosion-corrosion of stainless steel.

Corrosion Science, 30, 761-770.

Wakuda, M. Y., Y. Kanzaki, S (2003) Material response to particle impact during abrasive jet machining of alumina ceramics. *Journal of Material Processing Technology*, 132, 177-183.

Wallin H Hans and Guillermo Morales Espejel (2002). Hybrid Bearings in Oil-free air conditioning and refrigeration compressors. *Evolution*. SKF.

Wang, D. F., Mhao, Y.Z (1996) A study for erosion of Si₃N₄ ceramics by solid particles. *Wear*, 199, 283-286.

Wang, L., Snidle, R,W.,Gu, L (2000) Rolling contact silicon nitride bearing technology: a review of recent research. *Wear*, 246, 159-173.

Wang, Y., Hadfield, M (1999) Rolling contact fatigue failure modes of lubricated silicon nitride in relation to ring crack defects. *Wear*, 225-229, 1284-1292.

Wang, Y., Hadfield,M (2000) The influence of ring crack location on the rolling contact fatigue failure of lubricated silicon nitride: experimental studies. *Wear*, 243, 167-174.

Wang, Y. (2001) Failure modes of silicon nitride rolling elements with ring crack defects. *PhD thesis*, Bournemouth University, UK.

Wang, Y., Hadfield M (2002) Rolling contact fatigue of ceramics. *American Society of Testing Materials* 11, Section 6E.

Wikipedia, 2007. www.wikipedia.com

Williams, J. A., A.M. Hyncica (1992) Mechanisms of abrasive wear in lubricated contacts. *Wear*, 152, 57-74.

Young, F. R. (1999) *Cavitation*, Imperial College press, ISBN: 1860941982

Zaretsky, V. E. (1971). Palmgren Revisited - A Basis for bearing life prediction. *STLE Annual Meeting sponsored by the Society of Tribologists and Lubrication Engineers*. Kansas City, Missouri, USA.

Zaretsky, V. E., Brian L. Vlcek, Robert C. Hendricks (2005) Effect of Silicon Nitride Balls and Rollers on Rolling Bearing Life. *Report at John H. Glenn Research Center at Lewis Field Cleveland, NASA, USA*.

Zeiden F. Y and Vance J. M., (1989). Cavitation Leading to a Two Phase Fluid in a Squeeze Film Damper,” *STLE Tribology Transactions*, Vol. 32, 1, pp. 100-104.

Zhao, P., Hadfield. M, Y Wang, C. Vieillard (2004) The influence of test lubricants on the rolling contact fatigue failure mechanisms of silicon nitride ceramic. *Wear*, 257, 1047-1057.

Zhao, P. (2006). Three-Dimensional Boundary Element and Experimental Analysis of Lubricated Ceramic Surface Ring Cracks in Rolling Contact. PhD Thesis, Bournemouth University, UK.